



# THE UNIVERSITY *of* EDINBURGH

This thesis has been submitted in fulfilment of the requirements for a postgraduate degree (e.g. PhD, MPhil, DClinPsychol) at the University of Edinburgh. Please note the following terms and conditions of use:

This work is protected by copyright and other intellectual property rights, which are retained by the thesis author, unless otherwise stated.

A copy can be downloaded for personal non-commercial research or study, without prior permission or charge.

This thesis cannot be reproduced or quoted extensively from without first obtaining permission in writing from the author.

The content must not be changed in any way or sold commercially in any format or medium without the formal permission of the author.

When referring to this work, full bibliographic details including the author, title, awarding institution and date of the thesis must be given.



# **Title: Mass Spectrometry Imaging of Steroids**

Diego Federico Cobice, BSc (hons), MSc

A THESIS SUBMITTED FOR THE DEGREE OF DOCTOR OF  
PHILOSOPHY

SCHOOL OF CLINICAL SCIENCE

FACULTY OF MEDICINE AND VETERINARY MEDICINE

THE UNIVERSITY OF EDINBURGH

January 2015

# Declaration

I declare that this thesis was composed by myself and that the work contained therein is my own, except where explicitly stated otherwise in the text

(Diego. F. Cobice)

# Acknowledgments

This thesis is dedicated to my father who always believed in me and supported me in everything. It is also dedicated to Alicia, my future wife, for her patience and support in everything.

I would like to thank MS Core Laboratory Team for all the support. Logan MacKay (SIRCAMS) for giving me the opportunity to learn a fantastic new technique (MALDI-FTICR-MSI) and for being so supportive in all aspects. Carolyn Cairns, Lynne Ramage and June Noble for their contribution in histology and steroids analysis. Scott Webster for providing me with the novel 11 $\beta$ HSD-1 inhibitor (UE2316), Andrew McBride, Karen Sooy for their contribution and fruitful discussion about UE2316 pharmacodynamic data. Special thanks to Ruth Andrew and Brian Walker for their excellent supervision and Matt Bailey for organising the 4 years BHF Core PhD programme. Finally, I would like to mention the British Heart Foundation for its support through funding.

# Publications

1. Cobice DF, Mackay CL, Goodwin RJ, McBride A, Langridge-Smith PR, Webster SP, *et al.* (2013). Mass spectrometry imaging for dissecting steroid intracrinology within target tissues. *Analytical Chemistry* **85**(23): 11576-11584.
2. Swales JG, Tucker JW, Strittmatter N, Nilsson A, Cobice D, Clench MR, *et al.* (2014). Mass spectrometry imaging of cassette-dosed drugs for higher throughput pharmacokinetic and biodistribution analysis. *Analytical Chemistry* **86**(16): 8473-8480.
3. Tijana Mitić, Steven Shave, Nina Semjones, Iain McNae, Diego F Cobice, Gareth Lavery, Scott P. Webster, Patrick W.F. Hadoke, Brian R. Walker, Ruth Andrew. 11b-Hydroxysteroid dehydrogenase type 1 contributes to the balance between 7-keto- and 7-hydroxy-oxysterols in vivo. *Journal of Biochemical Pharmacology*, Volume 86, Issue 1, 1 July 2013, Pages 146–153.

Publication reprints are included in Appendix II at the end of this Thesis.

# Abstract

Glucocorticoids are steroid hormones involved in the stress response, with a well-established role in promoting cardiovascular risk factors including obesity and diabetes. The focus of glucocorticoid research has shifted from understanding control of blood levels, to understanding the factors that control tissue steroid concentrations available for receptor activation; it is disruption of these tissue-specific factors that has emerged as underpinning pathophysiological mechanisms in cardiovascular risk, and revealed potential therapeutic targets. However, the field is hampered by the inability at present to measure concentrations of steroid within individual tissues and indeed within component cell types. This research project explores the potential for steroid measurements using mass spectrometry-based tissue imaging techniques combining matrix assisted laser desorption ionization with on-tissue derivatisation with Girard T and Fourier Transform Ion Cyclotron Resonance Mass Spectrometry (OTCD-MALDI-FTICRMS).

A mass spectrometry imaging (MSI) platform was developed and validated to quantify inert substrate and active product (11-dehydrocorticosterone (11DHC), corticosterone (CORT) respectively) of the glucocorticoid-amplifying enzyme 11 $\beta$ -hydroxysteroid dehydrogenase type 1 (11 $\beta$ -HSD1) in rodent tissues. A novel approach to derivatising keto-steroids in tissue sections using Girard T reagent was developed and validated. Signals were boosted ( $10^4$  fold) by formation of GirT hydrazones compared to non-derivatised neutral steroids. Active and inert glucocorticoids were detected in a variety of tissues, including adrenal gland and brain; in the latter, highest abundance was found in the cortex and

hippocampus. The MSI platform was also applied to human biopsies and murine tissues for the analysis of other ketosterols such as androgens and oxysterols.

Proof-of-principle validation that the MSI platform could be used to quantify differences in enzyme activity was carried out by following *in vivo* manipulation of 11 $\beta$ -HSD1. Regional steroid distribution of both substrate and product were imaged at 150-200 $\mu$ m resolution in mouse brain sections, and the identification confirmed by collision induced dissociation/liquid extraction surface analysis (CID-LESA). To validate the technique, the CORT/11DHC ratios (active/inert) were determined in 11 $\beta$ -HSD1 deficient mice and found to be reduced (KO vs WT; cortex (49 %\*); hippocampus (46 %\*); amygdala (57 %)). Following pharmacological inhibition by administration of UE2316, drug levels peaked at 1 h in tissue and at this time point, a reduction in CORT/11DHC ratios were also determined, although to a lesser degree than in KO mice, cortex (22%), hippocampus (25 %) and amygdala (33 %). The changes in ratios appeared driven by accumulation of DHC, the enzyme substrate. In brains of mice with 11 $\beta$ -HSD1 deficiency or inhibition, decreases in sub-regional CORT/11DHC ratio were quantified, as well as accumulation of an alternative 11 $\beta$ -HSD1 substrate, 7-ketocholesterol. MSI data correlated well with the standard liquid chromatography tandem mass spectrometry (LC-MS/MS) in whole brain homogenates.

Subsequently, the MSI platform was also applied to measure the dynamic turnover of glucocorticoids by 11 $\beta$ -HSD1 in metabolic tissues using stable isotope tracers (Cortisol-D<sub>4</sub> (9,11,12,12-D<sub>4</sub>) (D<sub>4</sub>F). D<sub>4</sub>F was detected in plasma, liver and brain after 6 h infusion and after 48 h in adipose. D<sub>3</sub>F generation was detected at 6 h in plasma and liver; at 24 h in brain specifically in cortex, hippocampus and amygdala; and at 48 h in

adipose. The spatial distribution of  $d_3F$  generation in brain by MSI closely matched enzyme localisation. In liver, an  $11\beta$ -HSD1-riched tissue, substantial generation of  $d_3F$  was detected, with a difference in  $d_4F/d_3F$  ratios compared with plasma ( $\Delta TTR$   $0.18 \pm 0.03$  (6 h),  $0.27 \pm 0.05$  (24 h) and  $0.38 \pm 0.04$  (48 h)). A smaller difference in TTR was also detected between plasma and brain ( $\Delta TTR$   $0.09 \pm 0.03$  (24 h),  $0.13 \pm 0.04$  (48 h)), with no detectable regeneration in adipose. After genetic disruption of  $11\beta$ -HSD1,  $d_3F$  generation was not detected in plasma or any tissues, suggesting that  $11\beta$ -HSD1 is the only enzyme carrying out this reaction. After pharmacological inhibition, a similar pattern was seen. The circulating concentration of drug peaked at 2 h and declined towards 4 h, with same pattern in liver and brain. The  $\Delta TTR$  ratios 2HPD between plasma and liver ( $0.27 \pm 0.08$  vs.  $0.45 \pm 0.04$ ) and brain ( $0.11 \pm 0.2$  vs.  $0.19 \pm 0.04$ ) were smaller following drug administration than vehicle, indicating less  $d_3F$  generation. Extent of enzyme inhibition in liver responded quickly to the declining drug, with  $\Delta TTR$  returning to normal by 4 h ( $0.38 \pm 0.06$ ).  $\Delta TTR$  had not normalised 4HPD in brain ( $0.12 \pm 0.02$ , suggesting buffering of this pool. In adipose, UE2316 was not detected and nor were rates of  $d_3F$  altered by the drug. Two possible phase I CYP450 metabolites were identified in the brain differing in spatial distribution.

In conclusion, MSI with on-tissue derivatisation is a powerful new tool to study the regional variation in abundance of steroids within tissues. We have demonstrated that keto-steroids can be studied by MALDI-MSI by using the chemical derivatisation method developed here and exemplified its utility for measuring pharmacodynamic effects of small molecule inhibitors of  $11\beta$ -HSD1. This approach offers the prospect of many novel insights into tissue-specific steroid and sterol biology.



# Table of Contents

<b>Declaration</b>	i
<b>Acknowledgements</b>	ii
<b>Publications</b>	iii
<b>Abstract</b>	iv
<b>Table of Contents</b>	vii
<b>List of Tables</b>	xvii
<b>List of Figures</b>	xxiii
<b>Glossary</b>	xxiv
<b>Chapter 1: Introduction</b>	<b>1</b>
1.1 Steroids	1
1.1.1 Structure and function	1
1.1.2 Steroid and the adrenal cortex	2
1.1.3 Steroidogenesis	4
1.1.4 Cortisol	5
1.2 Intracrinology	7

vii

1.2.1	Intracrinology of glucocorticoids	8
1.2.2	Intracrinology of androgens	8
1.2.3	11 $\beta$ -HSDs	9
1.2.3.1	Structure and functions	9
1.2.3.2	11 $\beta$ -HSD type 1	11
1.2.3.3	11 $\beta$ -HSD type 2	13
1.2.3.4	11 $\beta$ -HSDs in the brain	14
1.2.4	Measuring glucocorticoids action at tissue level	16
1.2.4.1	Whole body: 24 hour cortisol and cortisone and urinary metabolites	19
1.2.4.2	Tritiated tracers not labelled on 11 position	20
1.2.4.3	Arteriovenous sampling of endogenous corticosteroids	22
1.2.4.4	<i>Ex vivo</i> biopsies	23
1.2.4.5	11 $\alpha$ -tritiated cortisol	24
1.2.4.6	Stable isotope tracers	25
1.2.4.7	New approaches	33
<b>1.3</b>	<b>Mass Spectrometry Imaging</b>	<b>34</b>
1.3.1	Introduction	34
1.3.2	Principle and instrumentation	35
1.3.3	Ionisation techniques	38
1.3.3.1	Liquid extraction surface analysis (LESA)	38
1.3.3.2	Matrix assisted laser desorption ionisation (MALDI)	40
1.3.3.3	Secondary Ion Mass Spectrometry (SIMS)	43
1.3.3.4	Desorption Electrospray Ionisation (DESI)	45

1.3.4	Tissue preparation for MALDI-MSI analysis	44
1.3.4.1	Preparation of Tissue Sections	46
1.3.4.1.1	Pre-sectioning steps	47
1.3.4.1.2	Sectioning and tissue pre-treatment	48
1.3.4.2	Matrix deposition	49
1.3.5	Mass Analysers	52
1.3.5.1	Quadrupole Mass Analysers	53
1.3.5.2	Time of flight (TOF) analysers	54
1.3.5.3	Trapped-Ion Mass analysers	55
1.3.5.4	Fourier Transform Ion Cyclotron Resonance	
	Mass Spectrometry (FTICRMS)	56
1.3.6	Data processing	59
1.3.7	Ion Suppression	60
1.3.8	Broadening the spectrum of MSI by on-tissue derivatisation	60
1.3.9	Quantitation	62
1.3.10	MSI of steroids	63
1.4	Aims and hypothesis	64
	<b>Chapter 2: Material and Methods</b>	<b>65</b>
2.1	Chemicals	65
2.2	Animals tissue	65
2.3	Sectioning of tissues	66
2.4	Histological staining	67
2.5	On-tissue chemical derivatisation (OTCD)	67
2.6	Matrix application	68

2.7	Instrumentation for Mass Spectrometry	68
2.8	MALDI-FTICR analysis	69
2.8.1	MSI	69
2.8.2	Tissue spotting	70
2.9	Liquid extraction surface analysis (LESA)-ESI-FTICRMS	71
2.10	Statistical analysis	72
<b>Chapter 3: Development and Optimisation of a</b>		
<b>MALDI-FTICRMS MSI Platform for Glucocorticoids</b>		<b>73</b>
3.1	Introduction	73
3.2	Methods	75
3.2.1	Biological tissue sections	75
3.2.2	Imaging of un-derivatised steroids in tissues	75
3.2.2.1	Comparison of responses of standards measured off and on-tissue	75
3.2.2.2	Adrenal gland and murine brain imaging	75
3.2.3	Screening of matrices	76
3.2.4	Derivatisation screening	76
3.2.5	Optimising On-tissue derivatisation conditions	77
3.2.6	Limits of Detection (LODs) of GirT derivatives of glucocorticoids applied to the surface of tissue	77
3.2.7	Stability of derivatised steroids	78
3.2.8	Screening of matrix solvents for TLC-based matrix deposition methods	78

3.2.9	Optimisation of derivatisation reagent application and saturation studies	79
3.2.10	Sublimation as a matrix deposition methodology	79
3.2.11	Tissue washing	80
<b>3.3</b>	<b>Results</b>	<b>82</b>
3.3.1	Characterisation of MALDI-FTICRMS spectra of neutral steroids	82
3.3.2	MALDI-FTICRMS of neutral steroids enriched in tissue homogenates	83
3.3.3	Tissue imaging of un-derivatised steroids in murine adrenal gland	84
3.3.4	Attempts to improve imaging of un-derivatised steroids	86
3.3.4.1	MALDI matrix screening	86
3.3.5	MSI imaging of derivatised corticosteroids	90
3.3.5.1	Screening of derivatisation reagents	91
3.3.5.2	Optimisation of formation of Girard T derivatives	96
3.3.5.3	Limits of detection and quantitation of derivatised corticosteroids on tissue sections	98
3.3.5.4	Stability of Girard-T derivative	99
3.3.5.5	Detection of endogenous steroids in adrenal glands following derivatisation with GirT	100
3.3.5.6	Confirmation of identity of molecular species by LESA	105
3.3.5.7	Solvent optimisation of method to detect endogenous steroids	107
3.3.5.8	Investigation of approaches to limit analyte diffusion	109

3.3.5.8.1	Saturation studies	109
3.3.5.8.2	Pre-coating of slides	111
3.3.5.9	Application of matrix by sublimation	111
3.3.5.10	Tissue washing to limit ion suppression	115
<b>3.4</b>	<b>Discussion</b>	<b>116</b>
<b>3.5</b>	<b>Conclusion</b>	<b>121</b>
<b>Chapter 4: Application of the MALDI-FTICR-MSI for the Assessment of the Spatial Distribution of Endogenous Steroids in Biological Tissues</b>		<b>122</b>
<b>4.1</b>	<b>Introduction</b>	<b>122</b>
4.1.1	Androgens	122
4.1.2	Oxysterols	124
<b>4.2</b>	<b>Methods</b>	<b>127</b>
4.2.1	Screening of tissues for suitability to detect glucocorticoids	127
4.2.2	Detection of androgens	127
4.2.2.1	Standards on-tissue	127
4.2.2.2	Imaging of androgens on prostate tissue sections	128
4.2.3	Simultaneous imaging of glucocorticoids and androgen in human tissue section	128
4.2.4	Detection of keto-oxysterols	128
4.2.4.1	Standards on-tissue	128
4.2.4.2	Imaging of keto-oxysterols on rat brain tissue sections	129
<b>4.3</b>	<b>Results</b>	<b>130</b>
4.3.1	MSI of glucocorticoids	130
4.3.1.1	Murine liver	130

4.3.1.2	Murine brain	131
4.3.1.3	Human placenta	132
4.3.2	Imaging of androgens	131
4.3.2.1	Standards	134
4.3.2.2	Imaging androgens in prostate	135
4.3.2.3	Androgens and glucocorticoids	136
4.3.3	Imaging of oxysterols	137
4.3.3.1	Standards	137
4.3.3.2	Imaging Oxysterols in Rat Brain	139
4.4	Discussion	141
4.5	Conclusion	145
<b>Chapter 5: Monitoring effects of 11<math>\beta</math>-hydroxysteroid dehydrogenase-type 1 Deficiency or Inhibition on Region-Specific Corticosteroid Regeneration in Brain by MALDI/LESA FTICRMS-MSI</b>		<b>146</b>
5.1	Introduction	146
5.2	Methods	148
5.2.1	Biomatrix	148
5.2.2	MSI	148
5.2.2.1	Steroids	148
5.2.2.2	UE 2316	149
5.2.3	Approaches to validate quantitation	149
5.2.3.1	Extraction of steroids from whole brain	149
5.2.3.2	Extraction of steroids from plasma	150
5.2.3.3	Quantitative analysis of steroids by LC-MS/MS	150

5.2.4	Extraction of UE2316 from whole brain	151
5.2.4.1	Quantitative LC-MS/MS UE2316 analysis	152
5.2.5	Data analysis	152
<b>5.3</b>	<b>Results</b>	<b>153</b>
5.3.1	Studies of genetic manipulation of 11 $\beta$ -HSD1	154
5.3.1.1	Absolute CORT and 11DHC quantitation in plasma and brain by LC/MS	155
5.3.2	Studies of pharmacological inhibition of 11 $\beta$ -HSD1	155
5.3.3	Agreement between methods of quantitative analysis	158
5.3.4	Quantitation of alternative substrates of 11 $\beta$ -HSD1	159
<b>5.4</b>	<b>Discussion</b>	<b>161</b>
<b>5.5</b>	<b>Conclusions</b>	<b>164</b>
<b>Chapter 6: 11<math>\beta</math>-Hydroxysteroid dehydrogenase-1 Activity by Measuring Cortisol Turn-Over Using Tracer Infusion</b>		<b>165</b>
<b>6.1</b>	<b>Introduction</b>	<b>165</b>
<b>6.2</b>	<b>Methods</b>	<b>168</b>
6.2.1	Biomatrices	168
6.2.2	FTICRMS spectral characterisation of deuterated glucocorticoids (standard on tissue)	169
6.2.3	Detection of d <sub>4</sub> F and d <sub>3</sub> F in an infused murine brain (control) section	169
6.2.4	Structural confirmation of d <sub>4</sub> F and d <sub>3</sub> F in a brain (control) section from a mouse infused with d <sub>4</sub> F analysed by CID experiments using LESA-nanoESI-FTIRMS	170



6.2.5	Time-dependent cortisol turn-over using stable isotope tracers in metabolic tissues	170
6.2.5.1	Plasma analysis	171
6.2.5.2	Extraction of steroids from liver tissue	171
6.2.5.3	Whole brain analysis	171
6.2.5.4	Extraction of steroids from adipose tissue	171
6.2.5.5	MSI of deuterium labelled cortisol metabolites in murine brain	172
6.2.6.	PK/PD study of UE 2316 using stable isotope tracer	173
6.2.6.1	Extraction and analysis of plasma UE2316	173
6.2.6.2	Extraction and analysis of UE2316 in whole liver, adipose and brain	173
6.2.6.3	MSI of UE2316 in murine brain.	174
6.2.6.4	MSI of deuterium labelled cortisol metabolites in murine brain	174
6.2.6.5	MSI of UE2316 and its metabolites	174
6.2.7	Data analysis	175
<b>6.3.</b>	<b>Results</b>	176
6.3.1	FTICR Spectra of deuterated glucocorticoids	176
6.3.1.1	Spectral characterisation	176
6.3.1.2	Implementation of CASI <sup>TM</sup> for MSI	177
6.3.1.3	Detection of d <sub>4</sub> F and d <sub>3</sub> F using CASITM in a tissue section following <i>in vivo</i> administration of d <sub>4</sub> F	178
6.3.1.4	Structural confirmation by CID experiments using LESA-nanoESI-FTICRMS	179

6.3.2	Cortisol turn-over using stable isotope tracers	181
6.3.2.1	Tracer enrichment in plasma	181
6.3.2.2	Tracer enrichment in tissues	183
6.3.2.3	Tracer enrichment in murine brain assessed by MSI	185
6.3.2.4	Cortisol regeneration in tissues	187
6.3.2.5	D <sub>3</sub> F regeneration in mice with genetic disruption of 11β-HSD1	189
6.3.3	PK/PD study of UE 2316 using stable isotope tracers	191
6.3.3.1	PK profile of UE2316	191
6.3.3.2	PD assessment of glucocorticoid regeneration after UE2316 treatment	193
6.3.3.3	Tissue PD assessment of glucocorticod regeneration after UE2316 treatment	194
6.3.3.4	Tissue-cortisol regeneration suppression in tissues upon pharmacological inhibition	197
6.3.3.5	UE2316 metabolism	199
<b>6.4</b>	<b>Discussion</b>	<b>201</b>
<b>6.5</b>	<b>Conclusion</b>	<b>210</b>
	<b>Chapter 7: Overall Summary and Future Perspectives</b>	<b>211</b>
<b>7.1</b>	<b>Overall summary</b>	<b>211</b>
<b>7.2</b>	<b>Future perspective</b>	<b>212</b>
	<b>Appendix I</b>	<b>215</b>
	<b>References</b>	<b>221</b>
	<b>Appendix II</b>	<b>241</b>

# List of Tables

<b>1.1:</b> Principal characteristics of the two isozymes of 11 $\beta$ -HSD	10
<b>1.2:</b> MSI ionisation methods	38
<b>1.3:</b> Traditional MALDI matrices	51
<b>1.4:</b> Matrix deposition techniques	52
<b>1.5:</b> Characteristic performances of different mass analysers for MSI	53
<b>2.1:</b> Molecular weights and masses of ions of steroids and Girard-T derivatives	71
<b>3.1:</b> Proton affinity calculation of standard MALDI matrices	88
<b>3.2:</b> Potential derivatisation reagents	92
<b>3.3:</b> Intensity of responses and LOD of corticosteroids derivatives following analysis by MALDI-FTICRMS	94
<b>3.4:</b> Limits of detection and quantitation of Girard T derivatives of corticosteroids by MSI	99
<b>6.1:</b> Full mass Vs. CASI <sup>TM</sup>	177

# List of Figures

<b>1.1:</b> Steroid core and nomenclature	1
<b>1.2:</b> Adrenal gland steroidogenesis	4
<b>1.3:</b> Representation of endocrine, paracrine, autocrine and intracrine secretion	7
<b>1.4:</b> 11 $\beta$ -HSD in rodents and humans.	10
<b>1.5:</b> Structures of [1,2] $^3\text{H}_2$ (a) and [1,2,6,7] $^3\text{H}_4$ cortisol tracer	22
<b>1.6 :</b> Structure of 11 $\alpha$ -3H-cortisol tracer	25
<b>1.7 :</b> Schematic of metabolism of deuterated cortisol tracer by 11 $\beta$ -HSD	26
<b>1.8 :</b> Mass spectrometry imaging (MSI) workflow	37
<b>1.9:</b> Liquid Extraction Surface Analysis workflow	40
<b>1.10:</b> A schematic diagram of the mechanism of MALDI	41
<b>1.11:</b> A schematic diagram of the mechanism of SIMS	45
<b>1.12:</b> DESI mechanism	46
<b>1.13:</b> Representative FT-ICRMS	57
<b>3.1:</b> MALDI-FTICR-MS of neutral steroids standards	82
<b>3.2:</b> MALDI-FTICR-MS of neutral steroids standards spiked into a murine mouse brain	83
<b>3.3:</b> MALDI-FTICR-MS imaging (MSI) of neutral steroids in rat adrenal gland and mouse brain sections	85
<b>3.4:</b> Screening of matrices for detection of neutral corticosteroids	87

<b>3.5:</b> Proton affinity (PA) using Cook's kinetic method	88
<b>3.6:</b> 4-chloro- $\alpha$ -cyanocinnamic acid (Cl-CCA) vs $\alpha$ -cyano-4-hydroxycinnamic	89
<b>3.7:</b> MALDI-FTICRMS spectra of neutral corticosteroids in a section of adrenal gland using CCA matrices	90
<b>3.8:</b> Molecular structure of corticosteroid core	91
<b>3.9:</b> Girard-T (GirT) derivatization reaction scheme	94
<b>3.10:</b> MALDI-FTICRMS of Girard T (GirT)-derivatives (standards)	96
<b>3.11:</b> Optimisation of time and catalytic conditions	97
<b>3.12:</b> On-tissue stability of Girard T corticosterone (GirT-CORT)	99
<b>3.13:</b> On-tissue chemical derivatisation mass spectrometry imaging (OTCD-MSI) platform	101
<b>3.14:</b> Derivatisation reaction chamber	102
<b>3.15:</b> Molecular imaging of corticosteroid in rat adrenal gland sections	103
<b>3.16:</b> Molecular imaging of corticosterone derivative in rat adrenal gland sections at different spatial resolution	104
<b>3.17:</b> Liquid extraction surface analysis (LESA) with nanoESI-FTICR collision induced dissociation (CID) mass spectra of Girard T (GirT) derivatives of corticosteroids	106
<b>3.18:</b> Screening of solvents	108
<b>3.19:</b> Optimisation of derivatisation reagent application for MALDI-FTICRMS	

of corticosteroids Girard T (GirT) hydrazones in adrenal gland tissue sections	110
<b>3.20:</b> Comparison of pre and post-coating application of derivatisation reagent	111
<b>3.21:</b> Glass sublimator used for MALDI matrix deposition	112
<b>3.22:</b> Photograph (25 x magnifications) of a rat adrenal gland tissue	113
<b>3.23:</b> Sublimation of CHCA matrix in rat adrenal gland tissue	114
<b>3.24:</b> The effect of washing the tissue surface prior to MALDI-FTICR-MS	115
<b>4.1:</b> Biosynthetic pathways and interconversion of the major androgens	123
<b>4.2:</b> Cholesterol metabolism pathway	125
<b>4.3:</b> Molecular imaging of corticosteroid in murine liver sections	130
<b>4.4:</b> Molecular imaging of corticosteroid in murine brain sections	132
<b>4.5:</b> Molecular imaging of corticosteroid in human placenta section	133
<b>4.6:</b> Androgens GirT derivatisation reaction scheme	135
<b>4.7</b> MALDI-FTICR-MS of androgen derivatives (standards)	135
<b>4.8:</b> Molecular imaging of androgens in a rat prostate tissue section	136
<b>4.9:</b> Extended TIC FTMS spectra of androgens and glucocorticoids	137
<b>4.10:</b> Reaction scheme for derivatisation of keto-oxysterols with Girard T	138
<b>4.11:</b> MALDI-FTICRMS of Girard T of keto-oxysterols standards	138
<b>4.12 :</b> Molecular imaging of oxysterols in a rat brain section	140
<b>5.1:</b> Effect of 11 $\beta$ -hydroxysteroid dehydrogenase type 1 deficiency on	

proportions of active and inactive glucocorticoids in regions of murine brain	154
<b>5.2:</b> Absolute quantitation of corticosterone (CORT) and 11-dehydrocorticosterone (11DHC) in plasma and brain homogenate	155
<b>5.3:</b> Molecular structure of UE 2316	156
<b>5.4:</b> Effect of pharmacological inhibition of 11 $\beta$ -hydroxysteroid dehydrogenase type 1 (11 $\beta$ -HSD1) with UE2316 in C57BL/6 mice	157
<b>5.5:</b> Agreement between MSI and alternative methods for corticosteroids	159
<b>5.6:</b> MSI detection of 7-ketocholesterol, an alternative substrate for 11 $\beta$ -HSD1	160
<b>6.1:</b> Cortisol turnover at the tissue level using stable isotope tracers.	167
<b>6.2:</b> MALDI-FTICRMS of deuterium labelled glucocorticoid standards	176
<b>6.3:</b> CASIT <sup>M</sup> of labelled glucocorticoids in brain from a mouse infused with d <sub>4</sub> F for 48h.	177
<b>6.4:</b> Mass spectra of Girard T derivatives of deuterium labeled cortisol	178
<b>6.5:</b> CID Mass spectra of Girard T derivatives of deuterium labeled cortisol	180
<b>6.6:</b> Indices of circulating tracer and tracee in plasma from wild-type mice	182
<b>6.7:</b> Estimation of d <sub>4</sub> F, d <sub>3</sub> E, d <sub>3</sub> F and CORT in tissues from wild-type mice.	184
<b>6.8:</b> MALDI-FTICR-MSI in regions of interest in murine brain.	185
<b>6.9:</b> Estimation of d <sub>4</sub> F, d <sub>3</sub> E, d <sub>3</sub> F and CORT d <sub>3</sub> E/d <sub>8</sub> CORT ratios in regions of interest in murine brain.	186

<b>6.10:</b> Cortisol regeneration measured as TTR and $\Delta$ TTR in tissues and plasma from wild-type mice	188
<b>6.11:</b> Concentrations of d <sub>4</sub> F, d <sub>3</sub> E and d <sub>3</sub> F in plasma from mice with genetic disruption of 11 $\beta$ -HSD1 (KO), after 48h d <sub>4</sub> F infusion	189
<b>6.12:</b> Estimation of absolute levels of d <sub>4</sub> F, d <sub>3</sub> E and $\Delta$ TTR <sub>(T)</sub> normalized to internal standard (d <sub>8</sub> CORT), expressed as ratios in liver, brain and adipose tissue of mice with genetic disruption of 11 $\beta$ -HSD1 (KO) following 48h d <sub>4</sub> F infusion	190
<b>6.13:</b> Cortisol turnover by measuring the proportions of active and inactive deuterium labelled cortisol and metabolites in regions of brain from mice with genetic disruption of 11 $\beta$ -HSD1 (KO) following 48h d <sub>4</sub> F infusion	191
<b>6.14:</b> UE2316 levels in plasma during time dependent PK study	191
<b>6.15:</b> Levels of UE2316 in brain and liver tissues during d <sub>4</sub> F infusion	192
<b>6.16:</b> MS image distribution of UE2316 in murine brain after dosing	192
<b>6.17:</b> Concentrations of d <sub>4</sub> F, d <sub>3</sub> E, d <sub>3</sub> F and Ra in plasma during timed inhibition of 11 $\beta$ -hydroxysteroid dehydrogenase type 1 by UE2316	193
<b>6.18:</b> Estimation of levels of d <sub>4</sub> F, d <sub>3</sub> E and d <sub>3</sub> F normalized to internal standard in liver, brain, adipose tissues and plasma during UE2316 treatment	194
<b>6.19:</b> MS image distribution of d <sub>4</sub> F, d <sub>3</sub> E and d <sub>3</sub> F in murine brain after dosing	195
<b>6.20:</b> Estimation of d <sub>4</sub> F, d <sub>3</sub> E and d <sub>3</sub> F ratios in regions of interest	



in murine brain during UE2316 treatment	196
<b>6.21:</b> Suppression of d3F regeneration measured as TTR and $\Delta$ TTR (T) in different regions across the brain by MALDI-FTICRMS upon enzyme inhibition by UE2316	198
<b>6.22:</b> Proposed metabolic pathway for UE2316 in the liver	199
<b>6.23:</b> Proposed metabolic pathway for UE2316 in the brain	200
<b>6.24:</b> Metabolite identification MSI in mouse brain of UE2316 4 hours post-dose	200

# Glossary

11DHC	11-dehydrocorticosterone
11 $\beta$ -HSD	11 $\beta$ hydroxysteroid dehydrogenase
11 $\beta$ -HSD-1	11 $\beta$ hydroxysteroid dehydrogenase type I
11 $\beta$ -HSD-2	11 $\beta$ hydroxysteroid dehydrogenase type 2
A4	Androstenedione
ACN	Acetonitrile
ACTH	Adrenocorticotropic hormone
AME	Apparent mineralocorticoid excess
APCI	Atmospheric pressure chemical ionisation
CID	Collision induced dissociation
CORT	Corticosterone
cps	count per second
CYP	Cytochrome P450 enzymes
DESI	Desorption Electrospray Ionisation
DMSO	Dimethyl sulfoxide
E	Cortisone
ESI	Electrospray ionisation
F	Cortisol

FTICRMS	Fourier Transform Ion Cyclotron Resonance Mass Spectrometry
ICR	Ion Cyclotron Resonance
KO	Knock out
LC-MS	Liquid chromatography-Mass Spectrometry
LC-MS/MS	Liquid chromatography-Tandem Mass Spectrometry
LESA	Liquid extraction surface analysis
MALDI	Matrix assisted laser desorption ionisation
MeOH	Methanol
MRM	Multiple reaction monitoring
MS	Mass Spectrometry
MSI	Mass Spectrometry Imaging
NAD	Nicotinamide adenine dinucleotide
NADP	Nicotinamide adenine dinucleotide phosphate
<i>m/z</i>	<i>mass/charge</i>
OTCD	On-tissue chemical derivatisation
PD	Pharmacodynamics
PK	Pharmacokinetics
SIMS	Secondary Ion Mass Spectrometry
WT	Wild type

# Chapter 1

## Introduction

### 1.1. Steroids

#### 1.1.1. Structure and function

The steroid hormones are all derived from cholesterol. Moreover, with the exception of vitamin D, they all contain the same cyclopentanophenanthrene ring and atomic numbering system as cholesterol. The conversion of C<sub>27</sub> cholesterol to the 18-, 19-, and 21-carbon steroid hormones (designated by the nomenclature C with a subscript number indicating the number of carbon atoms, e.g. C<sub>19</sub> for androstanes) involves the rate-limiting, irreversible cleavage of a 6-carbon residue from cholesterol, producing pregnenolone (C<sub>21</sub>) plus isocaproaldehyde (Lednicer, 2011).

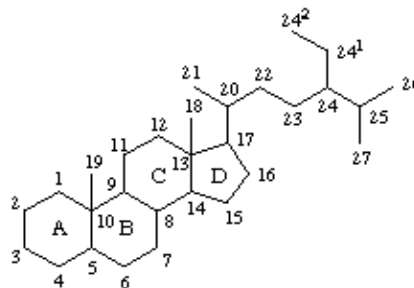


**Figure 1.1:** Steroid core and nomenclature. Adapted from (Lednicer, 2011)

Common names of the steroid hormones are widely recognized, but systematic nomenclature is gaining acceptance and familiarity with both nomenclatures is

increasingly important. Steroids with 21 carbon atoms are known systematically as pregnanes, whereas those containing 19 and 18 carbon atoms and aromatic rings are known as androstanes and estranes, respectively (Carson-Jurica *et al.*, 1990). Most of the steroid hormones exert their action by passing through the plasma membrane and binding to intracellular receptors, although in some cases, they may act directly on membrane receptors (Puia *et al.*, 1990). Steroids exert their genomic action by their corresponding receptor which binds to specific nucleotide sequences in the DNA of responsive genes. These DNA sequences are identified as hormone response elements, (HREs). The interaction of steroid-receptor complexes with DNA leads to altered rates of transcription of the associated genes (Beato *et al.*, 1995). The particular steroid hormone class synthesised by a given cell type depends upon its complement of peptide hormone receptors, its response to peptide hormone stimulation and enzymes transcribed and translated. The following indicates which glycoprotein is mainly responsible for stimulating the synthesis of which steroid hormone: *Luteinizing Hormone (LH)*: progesterone and testosterone, *adrenocorticotrophic hormone (ACTH)*: cortisol and corticosterone, *follicle stimulating hormone (FSH)*: estradiol and *angiotensin II/III*: aldosterone (Leake *et al.*, 1987).

### **1.1.2. Steroids and the adrenal cortex**

The adrenal cortex is responsible for production of three major classes of steroid hormones critical for health: glucocorticoids, which regulate carbohydrate metabolism; mineralocorticoids, which regulate the body levels of sodium and potassium; and androgens, whose actions are similar to that of steroids produced by the male gonads (Baxter, 1976). Primary adrenal insufficiency is known as Addison's disease, and in the

absence of steroid hormone replacement therapy can rapidly cause death. The adrenal cortex is composed of three main tissue regions: zona glomerulosa, zona fasciculata, and zona reticularis. Although the pathway to pregnenolone synthesis is the same in all zones of the cortex, the zones are histologically and enzymatically distinct, with the exact steroid hormone product dependent on the enzymes present in the cells of each zone (James, 1992). Many of the enzymes of adrenal steroid hormone synthesis are of the class called cytochrome P450 enzymes. These enzymes all have a common, standardised nomenclature, using the abbreviation CYP. For example the P450 enzyme (also called 20, 22-desmolase or cholesterol desmolase) is identified as CYP11A1. In order for cholesterol to be converted to pregnenolone in the adrenal cortex, it must be transported into the mitochondria where CYP11A1 resides (Hanukoglu, 1992b). This transport process is mediated by steroidogenic acute regulatory protein (StAR). This transport process is the rate-limiting step in steroidogenesis (Hanukoglu, 1992a). The steroidogenic pathway is shown in **Figure 1.2**.

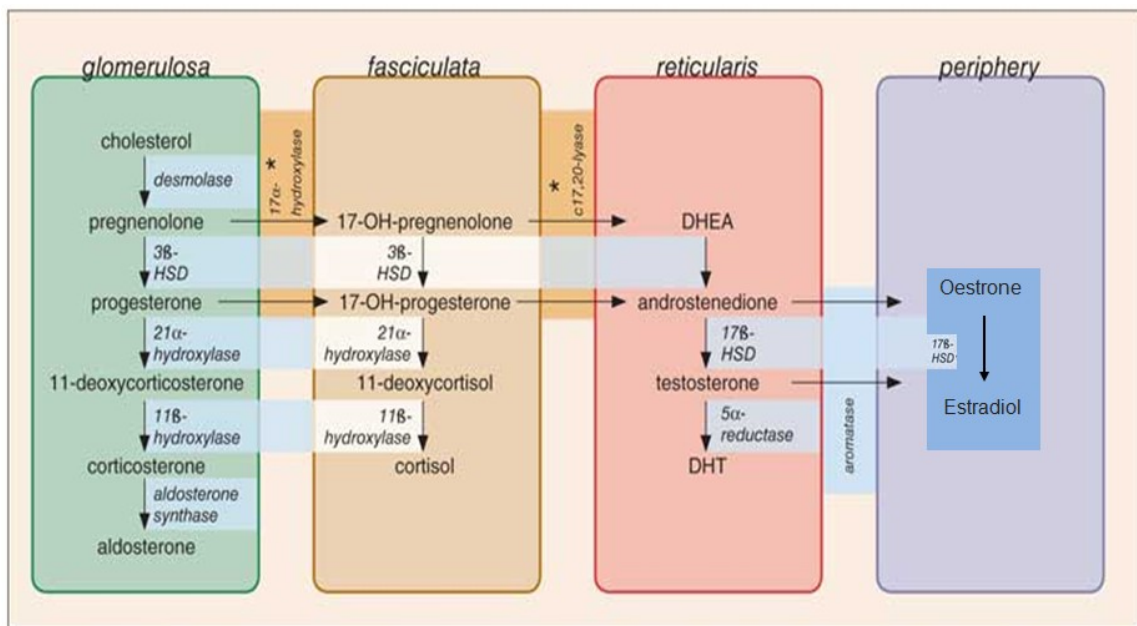


**Figure 1.2:** Adrenal gland steroidogenesis. (Adapted from Miller et al., 2011). DHT: Dihydrotestosterone, 3β-HSD: 3β-hydroxysteroid dehydrogenase, 17β-HSD: 17β-hydroxysteroid dehydrogenase

### 1.1.3. Steroidogenesis

Steroidogenic enzymes fall into two superfamilies. Most belong to the CYP-P450 monooxidase gene family and are thus referred to as CYPs. These enzymes are located either in the inner mitochondrial matrix, where they use molecular oxygen and a flavoprotein electron donor, or in the smooth endoplasmic reticulum, where they use a different flavoprotein for electron transfer. Different CYP enzymes act as hydroxylases, lyases (desmolases), oxidases, or aromatases (Miller *et al.*, 2011). Two of these enzymes have multiple functions. CYP17 has both a 17-hydroxylase function and a 17,20-lyase (desmolase) function. CYP11B2, also called aldosterone synthase, has three functions: 11-hydroxylase, 18-hydroxylase, and 18-oxidase. The other enzymes involved in steroidogenesis belong to three hydroxysteroid dehydrogenase (HSD)

families (Gonzalez, 1988).  $3\beta$ -HSDs have two isoforms that convert the hydroxyl group on carbon 3 of the cholesterol ring to a ketone and shift the double bond from the 5-6 ( $\Delta^5$ ) position to the 4-5 ( $\Delta^4$ ) position. All active steroid hormones must be converted to  $\Delta^4$  structures by  $3\beta$ -HSD (Lorence *et al.*, 1990). The  $17\beta$ -HSDs have at least five members and can act as either oxidases or reductases.  $17\beta$ -HSDs primarily act on sex steroids and can be activating or deactivating (Moghrabi *et al.*, 1998).

#### **1.1.4. Cortisol**

The zona fasciculata produces the glucocorticoid hormones, for example cortisol in humans. This zone is an actively steroidogenic tissue composed of straight cords of large cells. These cells have a "foamy" cytoplasm because they are filled with lipid droplets that represent stored cholesterol esters (Strain *et al.*, 1980). These cells make some cholesterol *de novo* but also import cholesterol from blood in the form of low-density lipoprotein (LDL) and high-density lipoprotein (HDL) particles. Free cholesterol is then esterified and stored in lipid droplets (Olson, 1998). The stored cholesterol is continually turned back into free cholesterol by a cholesterol ester hydrolyase, a process that is increased in response to the stimulus of cortisol synthesis (e.g., adrenocorticotrophic hormone [ACTH]). In the zona fasciculata, cholesterol is converted sequentially to pregnenolone, progesterone, 17-hydroxyprogesterone, 11-deoxycortisol, and cortisol (**Figure 1.2**) (Stocco *et al.*, 1996). A parallel pathway in the zona fasciculata involves the conversion of progesterone to 11-deoxycorticosterone (DOC) and then to corticosterone. This pathway is minor in humans, but corticosterone is the principle glucocorticoid in mice and rats. In the absence of active CYP11B1 (11-



hydroxylase activity), the production of DOC is significant. Because DOC acts as a weak mineralocorticoid, elevated levels of DOC cause hypertension (Costanzo, 2006).

Cortisol is transported in blood to its sites of action predominantly bound to corticosteroid-binding globulin [CBG] (also called transcortin), which binds about 90%, and albumin, which binds 5- 7% of the circulating hormone (Zhou *et al.*, 2006). The liver is the predominant site of steroid inactivation. It both inactivates cortisol and conjugates active and inactive steroids with glucuronide or sulfate so that they can be excreted more readily by the kidney (Basu *et al.*, 2009). However pathways also exist in the liver to regenerate active cortisol.

Cortisol has a broad range of actions and is often characterised as a "stress hormone." In general, it maintains blood glucose levels, CNS function, and cardiovascular function during fasting and increases blood glucose during stress at the expense of muscle protein (Andrews *et al.*, 1999; Maclulich *et al.*, 2005; Walker, 2007; Walker *et al.*, 1995). Also, it protects the body against the self-injurious effects of unbridled inflammatory and immune response (Carmichael *et al.*, 1981) and has several other effects on bone, skin, connective tissue, the GI tract (Mitchell *et al.*, 1990), and the developing foetus (Lindsay *et al.*, 1996) that are independent of its stress-related functions. Cortisol reinforces its effects on blood glucose by its positive effects on the cardiovascular system. It is permissive for the actions on catecholamines (Brust *et al.*, 1951) and thereby contributes to cardiac output and blood pressure (Connell *et al.*, 1987). Cortisol stimulates erythropoietin synthesis and hence increases red blood cell production. Anaemia occurs when cortisol is deficient, and polycythaemia occurs when cortisol levels are excessive (Kelly *et al.*, 2000).

## 1.2. Intracrinology

Hormones form in specialised glands, called endocrine glands, and are released into the general circulation and transported to distant target cells. On the other hand, hormones released from one cell can influence neighbouring cells (paracrine activity) or can exert a positive or negative action on the cell of origin (autocrine activity) (Labrie *et al.*, 1988). The term Intracrinology was coined in 1991 by Labrie *et al* to focus our attention on the synthesis of active steroids in peripheral target tissues where steroid action is exerted in the same cells where synthesis takes place without release of the active hormones in the extracellular space and in the general circulation (Labrie, 1991)(Figure 1.3).

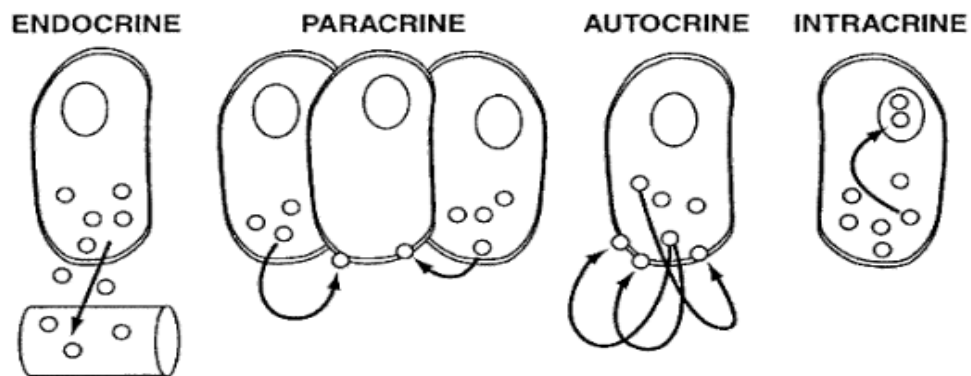


**Figure 1.3:** Representation of endocrine, paracrine, autocrine and intracrine secretion. Adapted from (Labrie, 1991).

### **1.2.1. Intracrinology of Glucocorticoids**

It is now viewed as very important to elucidate by factors that determine intracellular glucocorticoid concentrations available for action. Access of glucocorticoids to corticosteroid receptors (MR or GR) is determined not only by the plasma pool of glucocorticoid but also by local metabolism of glucocorticoids (e.g. by  $11\beta$ -hydroxysteroid dehydrogenases ( $11\beta$ -HSDs) and  $5\alpha$ -reductases) (Livingstone *et al.*, 2014; Walker, 2007; Yang *et al.*, 2011), and potentially by active transport of glucocorticoids across the cell membrane (Webster *et al.*, 2002) and/or by the control of storage of glucocorticoids in the inert triglyceride pool in some tissues (Hughes *et al.*, 2010).

### **1.2.2. Intracrinology of androgens**

Adrenal androgens contribute 40% of total androgens in adult men. The inactive precursor steroids dehydroepiandrosterone (DHEA) and DHEA-sulphate are secreted in large amounts by the adrenals and reach the prostate and other peripheral target tissues, where they are transformed into the potent androgen dihydrotestosterone (DHT) (Labrie, 2004). In other hands, testosterone is taken up from the systemic circulation by the prostatic glandular and stromal cells. Once within the prostate, testosterone is rapidly and irreversibly converted to dihydrotestosterone (DHT) by the enzyme 5AR. This leads to a five-fold higher concentration of DHT versus testosterone within the intracellular prostate, versus an eleven-fold higher concentration of testosterone within the circulation (Bartsch *et al.*, 2002). DHT then binds to the androgen receptor within the cytosol, is actively transported into the nucleus, and serves as a transcription factor for prostatic gene expression and thus prostatic cellular function. The higher

concentration of intracellular DHT, in addition to its higher affinity for the androgen receptor, support the importance of 5AR in normal and pathologic prostate physiology (Labrie *et al.*, 1993). The 5AR enzyme is responsible for converting testosterone into DHT. DHT is a prevalent and potent androgen in prostate tissue and is responsible for embryologic development of the prostate (Walsh *et al.*, 1974), growth of the prostate and promotion of prostate cancer (McConnell, 1995). Finasteride inhibits 5-AR type 2, and dutasteride inhibits 5AR types 1 and 2. Both finasteride and dutasteride were designed and approved for the treatment of benign prostatic hyperplasia (BPH) and have proven efficacy in this regard.

### **1.2.3. 11 $\beta$ -Hydroxysteroid dehydrogenase (11 $\beta$ -HSDs)**

#### **1.2.3.1. *Structure and functions***

The interconversion of active cortisol and inert cortisone is mediated by the two isozymes of 11 $\beta$ -HSD (**Figure 1.4**) (White *et al.*, 1997). Both enzymes are hydrophobic, membrane-bound proteins that bind cortisol/cortisone and corticosterone (CORT)/ 11-dehydrocorticosterone (11DHC), but otherwise their properties and physiological roles differ substantially (White *et al.*, 1997) (**Table 1.1**). Interest in these enzymes extends far beyond their deficiency states because they play central roles in regulating metabolism (Morton, 2010; Seckl *et al.*, 2004b; Wake *et al.*, 2003).

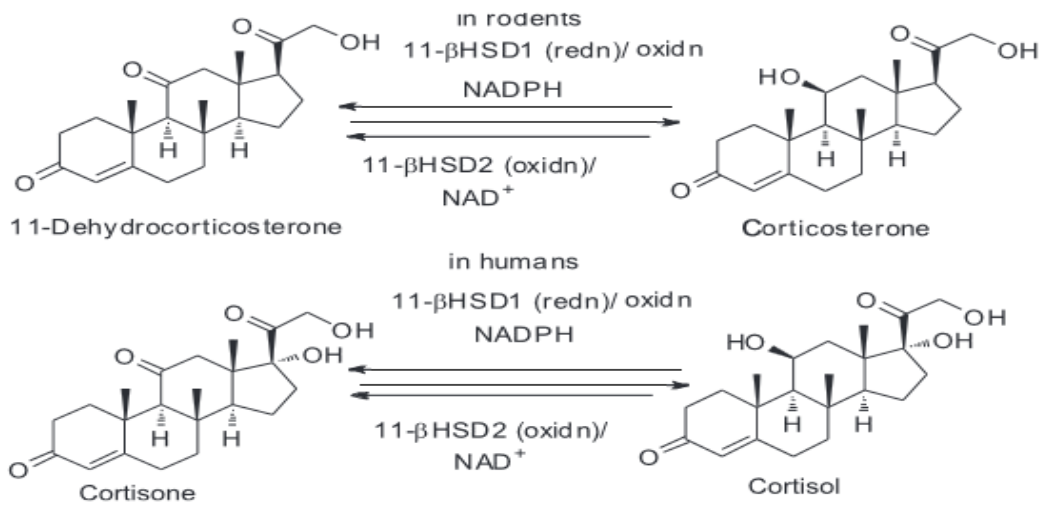


**Figure 1.4:** 11β-HSD in rodents and humans. Adapted from (White *et al.*, 1997). **NADP:** nicotinamide adenine dinucleotide phosphate, **NAD:** nicotinamide adenine. **Oxid n:** Oxidation. **Red n:** reduction.

**Table 1.1:** Principal characteristics of the two isozymes of 11βHSD

	11β-HSD type 1	11β-HSD type 2
Tissues	Liver, testis, lung, fat, proximal nephron, CNS.	Distal nephron, placenta, colon
Location	Endoplasmic reticulum, facing lumen	Endoplasmic reticulum, facing cytoplasm
Reaction	Reduction/Oxidation	Oxidation
Substrates	Cortisone, 11-dehydrocorticosterone, cortisol, corticosterone, synthetic steroids, oxysterols and bile acids	Cortisol, corticosterone, synthetic steroids
Cofactor	NADPH/NADP <sup>+</sup>	NAD <sup>+</sup>
Coenzyme	H6PDH	
K <sub>m</sub>	0.1–0.3/1-2 μM	0.01–0.1 μM

**K<sub>m</sub>:** Michaelis constant, **NADP:** nicotinamide adenine dinucleotide phosphate, **NAD:** nicotinamide adenine dinucleotide, **H6PDH:** Hexose-6-phosphate dehydrogenase **CNS:** central nervous system.

### 1.2.3.2. *11 $\beta$ -HSD type 1*

11 $\beta$ -HSD type 1 enzyme (11 $\beta$ -HSD1) (Tannin *et al.*, 1991) is a dimer of 34-kDa subunits expressed mainly in glucocorticoid-responsive tissues such as the liver, testis, lung, fat, and proximal convoluted tubule (Morton, 2010; Seckl *et al.*, 2004a). The type 1 enzyme catalyzes both the oxidation of cortisol to cortisone using NADP<sup>+</sup> as cofactor ( $K_m$  1–2  $\mu$ M) and the reduction of cortisone to cortisol using NADPH cofactor ( $K_m$  0.1–0.3  $\mu$ M), with cortisone reduction being the dominant reaction in transfected cells (Agarwal *et al.*, 1989; Moore *et al.*, 1993); the reaction catalysed depends on which cofactor is available (Agarwal *et al.*, 1990). Many synthetic glucocorticoids (*e.g.*, prednisone and cortisone) are 11-ketosteroids that must be reduced to their 11 $\beta$ -hydroxy derivatives to attain biological activity; these transformations are performed mainly in the liver by 11 $\beta$ -HSD1. However, when recombinant 11 $\beta$ -HSD1 is expressed *in vitro*, oxidation of cortisol with NADP<sup>+</sup> is more efficient, and cortisone reduction is only achieved if NADP<sup>+</sup> is removed by an enzymatic NADPH regeneration system (Walker *et al.*, 2001). Thus, the net flux of steroid driven by 11 $\beta$ -HSD1 depends on the relative concentrations of available NADPH and NADP<sup>+</sup>, which usually favours reduction in cells, especially given the high  $K_m$  of the enzyme for cortisol. The discrepancy between the prominent oxidative preference *in vitro* and the reductive dominance *in vivo* derives from the localisation of 11 $\beta$ -HSD1 in the lumen of the endoplasmic reticulum (Albiston *et al.*, 1994). In the endoplasmic reticulum, the ratio of NADPH to NADP<sup>+</sup> is maintained by hexose-6-phosphate dehydrogenase (H6PDH), rather than by cytoplasmic NADP<sup>+</sup>-coupled dehydrogenases (*e.g.*, glucose-6-phosphate dehydrogenase) (Bujalska *et al.*, 2003). Furthermore, a balance of activities has been found by *in vivo* observations in adipose and muscle tissues (Hughes *et al.*, 2012).

Early studies had addressed the hypothesis that 11 $\beta$ -HSD1, like 11 $\beta$ -HSD2, was a predominant dehydrogenase enzyme, which protected glucocorticoid receptors, e.g. in testis. However, it appears that there is an ample supply of inert substrate that can be reactivated by predominant 11 $\beta$ -reductase activity of 11 $\beta$ -HSD1 in many tissues *in vivo*. To explore this further, 11 $\beta$ -HSD1 “knock-out” mice (11 $\beta$ -HSD1<sup>-/-</sup>) have been generated following genetic disruption of the *Hsd1b1* allele; homozygous mice had no detectable 11 $\beta$ -HSD1 mRNA and also no 11-reductase activity as demonstrated by the failure to convert 11-DHC to corticosterone. The knockout mice thrived, were fertile, and basally did not exhibit any overt phenotypical abnormalities (Kotelevtsev *et al.*, 1997). However, upon closer examination, it was determined that glucocorticoid-induced responses were attenuated in the 11 $\beta$ -HSD1<sup>-/-</sup> mice, consistent with the hypothesis that 11 $\beta$ -HSD1 activity contributes significantly to the active intracellular glucocorticoid pool. For example, the 11 $\beta$ -HSD1 null mice are less able to induce phosphoenolpyruvate carboxykinase (PEPCK) and glucose-6-phosphatase (key glucocorticoid-inducible gluconeogenic and glycolytic enzymes) following a fast, compared to wild-type controls (Paterson *et al.*, 2005). Furthermore, after 4 weeks fat feeding or following an acute stressor, the 11 $\beta$ -HSD1 knockout mice had lower levels of fasting plasma glucose. More detailed analysis of these mice suggest that 11 $\beta$ -HSD1 deficiency produces a “cardioprotective” lipid profile due, at least in part, to increased beta oxidation in the liver, hepatic insulin sensitization, and reduced fibrinogen synthesis (Kipari *et al.*, 2013) .

### 1.2.3.3. *11 $\beta$ -HSD type 2*

The 41 kDa type 2 enzyme (11 $\beta$ -HSD2) has only 21% sequence identity with 11 $\beta$ -HSD1, whereas 11 $\beta$ -HSD2 and 17 $\beta$ -HSD2 share 37% identity and favour steroid oxidation *in vivo*. Thus, 11 $\beta$ -HSD1 and 2 are only distantly related members of the short-chain dehydrogenases/reductases (SDR) family, yet they perform physiologically related but opposite functions. 11 $\beta$ -HSD2 catalyzes only the oxidation of cortisol to cortisone using NAD<sup>+</sup> and functions with low (nM) concentrations of steroid (K<sub>m</sub> 10–100 nM) (Brown *et al.*, 1993; Rusvai *et al.*, 1993); an ability of 11 $\beta$ -HSD2 to catalyse reduction has not been demonstrated for endogenous steroids, although *in vitro* it can be demonstrated to catalyse reduction of synthetic keto-steroids (Heirholzer *et al.*, 1966). 11 $\beta$ -HSD2 is expressed in mineralocorticoid-responsive tissues and thus serves to “defend” the mineralocorticoid receptor by inactivating cortisol to cortisone, so that only “true” mineralocorticoids, such as aldosterone can exert a mineralocorticoid effect. 11 $\beta$ -HSD2 is inactive against aldosterone and 9 $\alpha$ -fludrocortisol. Thus, 11 $\beta$ -HSD2 prevents cortisol from overwhelming renal mineralocorticoid receptors (Funder, 1993), and in the placenta and other foetal tissues 11 $\beta$ -HSD2 (Krozowski *et al.*, 1995) also inactivates cortisol. The placenta also has abundant NADP<sup>+</sup> favouring the oxidative action of 11 $\beta$ -HSD1, so that in placenta both enzymes may protect the foetus from high maternal concentrations of cortisol.

11 $\beta$ -HSD2 disruption on an out bred background revealed mice with an apparently normal phenotype at birth but within 48 h, half of them exhibit motor deficiencies, perhaps due to hypocalcaemia, and die (Kotelevtsev *et al.*, 1999). Survivors are fertile, but exhibit severe hypertension and polyuria, all typical characteristics of apparent



mineralocorticoid excess (AME) and thus apparent mineralocorticoid actions of corticosterone were revealed by 11 $\beta$ -HSD2 deficiency. The original strain of modified mice did not exhibit reduced foetal weight although this was clearly apparent in later studies on a 11 $\beta$ -HSD2 knock-out model congenic on a C57BL/6 J background (Holmes *et al.*, 2006). This raises the intriguing possibility of gene interaction effects on fetoplacental 11 $\beta$ -HSD2 function.

In addition to the AME symptoms, 11 $\beta$ -HSD2<sup>-/-</sup> mice revealed a key role for 11 $\beta$ -HSD2 in brain function. Heterozygous mating have shown 11 $\beta$ -HSD2<sup>-/-</sup> offspring have heightened anxiety in comparison to their wild type littermates (Wyrwoll *et al.*, 2013), demonstrating a key role of fetoplacental 11 $\beta$ -HSD2 in prenatal glucocorticoid ‘programming’ (Kotelevtsev *et al.*, 1999).

#### **1.2.3.4. *11 $\beta$ -HSDs in the brain***

Glucocorticoids have profound effects on pre- and post-natal brain development. They are essential for normal maturation in most regions of the developing CNS, initiating terminal maturation, remodelling axons and dendrites, and affecting neuronal and glial cell survival. Either inadequate or excessive glucocorticoid levels cause abnormalities in neuronal and glial structure and function that often impact throughout the lifespan (Moisan *et al.*, 1990a). Similarly in adulthood either excessive or deficient glucocorticoid action affects a myriad of brain functions, altering biochemistry, neurotransmission and cell structure (Joels *et al.*, 2009a; Joels *et al.*, 2009b; Sapolsky *et al.*, 1986). Thus accurate control of glucocorticoid levels and cellular action is critical for brain development and function. 11 $\beta$ -HSD1 is the main isozyme found in the adult mammalian CNS. It was originally described in neuronal and glial cell lines.

Using biochemical techniques, 11-keto oxidation of steroids was found in mouse, rat, dog and primate whole brain extracts, as well as foetal brain and the C6 glioma cell line (Moisan *et al.*, 1990b). 11 $\beta$ -HSD1 is widely distributed in the CNS, albeit with an uneven pattern of expression. Studies have clearly demonstrated the 11 $\beta$ -HSD activity in rat cerebellum (Moisan *et al.*, 1990b) and a broad range of CNS regions, including the hippocampus and neocortex, with levels some 10–30% of those in kidney and liver. There were higher levels in specific cells types, for instance Purkinje cells of the cerebellum, CA3 pyramidal cells of the hippocampus and layer V neurons of the neocortex (Moisan *et al.*, 1990b). 11 $\beta$ -HSD is also clearly detectable in most other brain sub regions, including the hypothalamus, amygdala and brain stem (Lakshmi *et al.*, 1991). The enzyme mRNA, protein and activity are found in neurons and in glia. . Whilst there is some discordance in the earlier literature on the expression of 11 $\beta$ -HSD2 mRNA, and perhaps confusion generated by highly sensitive PCR-based methods which inevitably detect occasional transcripts, the vast majority of 11 $\beta$ -HSD mRNA and activity in the adult mammalian CNS is 11 $\beta$ -HSD1. The exception may be a few discrete nuclei in the hind brain/brain stem, notably the nucleus of the tractus solitarius (NTS), which expresses 11 $\beta$ -HSD2 mRNA in adult rodents.

Nevertheless, manipulation of 11 $\beta$ -HSD1 does not always have the anticipated effects as studies have shown cognitive improvement with 11 $\beta$ -HSD1 deficiency or inhibition (Yau *et al.*, 2011). However, the effects in man have been disappointing, as clinical trials of 11 $\beta$ -HSD1 inhibitors have not demonstrated any improvements in dementia.

These observations raise the question of how much 11 $\beta$ -HSD1 really contributes to GR activation in different tissues in mouse and in man and if there is a better way to document the pharmacodynamic effects of 11 $\beta$ -HSD1 inhibition.

The importance to measure effects of intracrinology on tissue steroid levels, is to understand the relative contributions of local metabolism versus circulating levels in determining the concentration of steroid available to receptors

#### **1.2.4. Measuring glucocorticoids action at the tissue level**

An elevated exposure to glucocorticoids at tissue level may influence metabolism, fat distribution and mass. Predisposition to type 2 diabetes and excess accumulation of abdominal fat has been clearly demonstrated in patients with Cushing's syndrome (Walker *et al.*, 1992c; Wei *et al.*, 2004). Similar features as seen in idiopathic obesity (a component of the metabolic syndrome) are associated with increased risk of cardiovascular disease including insulin resistance and hypertension (Walker *et al.*, 1992b) (Wei *et al.*, 2004). It has been shown in several studies that cortisol synthesis rate is increased in obese subjects. Despite the attractive hypothesis of activation of the hypothalamic pituitary-adrenal (HPA) axis in obesity, this is not evident when studying steroids in the circulation, as plasma levels of cortisol are not consistently high, being normal, slightly elevated or lower (Praveen *et al.*, 2011; Rask *et al.*, 2001) throughout the day (Rosmond *et al.*, 1998). Furthermore, after administration of dexamethasone, the feedback regulation of the HPA axis does not seem to differ between lean and obese. Furthermore, Mattson and colleagues has demonstrated that a combined receptor antagonist stimulation of the HPA axis revealed redundancy of MR and GR in negative feedback in humans. The group have found that obese men have impaired responses to

combined receptor antagonist stimulation, suggesting impaired negative feedback by endogenous cortisol (Mattson *et al.*, 2009). Therefore, it remains unclear whether overweight/moderate obesity is related with a primary alteration in the HPA axis activity.

An alternative hypothesis has been proposed in which an increased cortisol production rate in obesity reflects normal HPA axis function compensating for changes in peripheral cortisol clearance. This hypothesis is sustained by an increased in cortisol metabolic clearance rates seen in obese subject measured by isotope dilution (Strain *et al.*, 1980). Data have also confirmed that an increased cortisol metabolite excretion in urine, as a combination of excretion of A ring reduced (especially 5 $\alpha$ -reduced) cortisol metabolites (Andrew *et al.*, 1998; Fraser *et al.*, 1999) together with impaired hepatic regeneration of cortisol from cortisone, at least in men (Rask *et al.*, 2001; Stewart *et al.*, 1999) and in women is associated with obesity (Rask *et al.*, 2002). Therefore, the compensatory activation of the HPA axis to maintain normal levels of circulating cortisol by decreasing the negative feedback may be due to a combination of increased hepatic cortisol inactivation and impaired regeneration of cortisol. However, in contrast in adipose glucocorticoid regeneration may be enhanced locally by increased activity of 11 $\beta$ -HSD1 – the goal of a number of studies has been to quantify the contribution of different tissues to glucocorticoid clearance and activation in metabolic disease.

In rodents, the levels of glucocorticoids in tissues have been measured primarily by LC/MS using tissue homogenate (Livingstone *et al.*, 2003; Sooy *et al.*, 2010). In a study conducted by Livingstone, glucocorticoids were measured in liver, adipose and skeletal muscle of obese and lean rats to evaluate the effects of Carbenoxolone. The

study shown that Carbenoxolone inhibited 11 $\beta$ -HSD1 activity in liver but not in adipose tissue or skeletal muscle.

Glucocorticoids were also measured in murine brain homogenate (Sooy *et al.*, 2010; Joyce *et al.*, 2011) to test whether lifelong or short-term decreases in 11 $\beta$ -HSD1 activity are sufficient to alter cognitive function in aged mice (Sooy *et al.*, 2010) and to determine which brain receptors [high-affinity mineralocorticoid receptors (MRs) or low-affinity glucocorticoid receptors (GRs)] are involved in the memory deficit with aging (Joyce *et al.*, 2011). The latter study supports the notion that 11 $\beta$ -HSD1 deficiency in aging mice leads to lower intracellular GC concentrations in brain, particularly in the hippocampus, which activate predominantly MRs to enhance memory (Yau *et al.*, 2011).

Active glucocorticoid activity at corticosteroid receptors is controlled by tissue-specific pre-receptor metabolism primarily by 11 $\beta$ -HSD1. These changes happened independently of changes in circulating levels. In male leptin-resistant Zucker obese rats (Livingstone *et al.*, 2000) and in men with idiopathic obesity (Rask *et al.*, 2001), 11 $\beta$ -HSD1 activity was increased in adipose tissue potentially contributing to some features of obesity. Therefore, a focus of research has been to measure glucocorticoid regeneration in metabolic tissues by 11 $\beta$ -HSD1. However finding techniques to discriminate inactivation from regeneration of glucocorticoids in tissues has been challenging.

#### 1.2.4.1. *Whole body: 24 hour cortisol and cortisone and urinary metabolites*

There has been extensive interest in the control of local activation and inactivation of cortisol by the 11 $\beta$ -HSD enzymes in patients with common disorders, e.g. hypertension and obesity. One approach to measure the activity of these enzymes in human cohorts is based on whole-body measurements of both cortisol and cortisone in blood or the concentrations of their major metabolites in urine. These approaches provide limited information on the activities of the individual 11 $\beta$ -HSD as the measurements merely reflect the balance of their dehydrogenase and reductase activities. Typical readouts include the ratio of cortisol:cortisone or the same ratio of their tetrahydro metabolites (5 $\alpha$ +5 $\beta$  tetrahydrocortisol vs tetrahydrocortisone).

The ratio does change predictably upon inhibition of the enzymes. Glycyrrhetic acid inhibits cortisol inactivation by 11 $\beta$ -HSD2 in vivo and increases the ratios of cortisol to cortisone metabolites (Best *et al.*, 1997; Stewart *et al.*, 1990). In subjects unable to reduce cortisone to cortisol through genetic mutation in either 11 $\beta$ HSD1 (Jamieson *et al.*, 2000) or H6PDH (Draper *et al.*, 2003; Lavery *et al.*, 2006), the opposite change is seen. By way of example of the use of this approach, in some clinical studies, subjects with AME presented with elevated urinary 11 $\beta$ -hydroxy metabolites of cortisol (cortols, tetrahydrocortisol (THF) and C19 steroids) while the 11-oxo metabolites (cortolones and tetrahydrocortisone THE) were diminished (Stewart *et al.*, 1988). From this information, however, it cannot be interpreted whether the change lies with 11 $\beta$ -HSD 1 or 2.

Urinary metabolite ratios may therefore give false negative results. Carbenoxolone (a non-selective inhibitor), which inhibits both isozymes does not alter the ratio of metabolites of cortisol and cortisone due to inhibition of both cortisol inactivation and reactivation (Stewart *et al.*, 1990). However, carbenoxolone results in marked inhibition of turnover in the 11 $\beta$ -HSD pathways, with increased cortisol concentrations in kidney and decreased cortisol levels in the liver and in the brain (Stewart *et al.*, 1990). As the isozymes possess distinct physiological roles and are altered in different pathologies, determination of their separate activities is desirable (Stewart *et al.*, 1990). A number of more refined approaches has been attempted

#### **1.2.4.2. Tritiated tracers not labelled on C11 position**

Approaches using tritium labelled cortisol (**Figure 1.5**) to tackle the selectivity issues found during determination of cortisol metabolites have been presented. Several radio labelled isotopomers of cortisol have been used to measure cortisol metabolism and to further evaluate 11 $\beta$ -HSD activities. These may be infused or injected and clearance of the endogenous pool assessed.  $^3\text{H}$  radio labelled corticosteroids were used to study either 11 $\beta$ -HSD1 (conversion of [1,2]  $^3\text{H}_2$  cortisone to [1,2]  $^3\text{H}_2$  cortisol) or 11 $\beta$ -HSD2 (conversion of [1,2]  $^3\text{H}_2$  cortisol to [1,2]  $^3\text{H}_2$  cortisone) usually detected by liquid scintillation counting but, as with endogenous steroids, these are not truly selective as they can be interconverted and only initial rates may be discriminatory. [1,2]  $^3\text{H}_2$  cortisol was applied to measure the conversion in normal and inflamed human gingiva biopsies and detection of other 20- $\alpha/\beta$  dehydrogenation metabolites (Leloup-Hatey, 1976). *In vivo* human studies conducted by Sandeep and colleagues (Sandeep *et al.*, 2005) used [1,2]  $^3\text{H}_2$  cortisone to infer the differences in 11 $\beta$ -HSD1 activity in adipose

obese subjects using microdialysis. In this study the infusion of substantial concentrations of [1,2] <sup>3</sup>H cortisone (50 nmol/L; similar to normal blood cortisone levels) was required to ensure reliable detection. Under these conditions, the [1,2] <sup>3</sup>H<sub>2</sub> cortisone infused was not a “tracer” because it contributed substantially to the local substrate concentration (Sandeep *et al.*, 2005). Furthermore, since high concentrations are needed to achieve a reliable detection, this restricts the use for *in vivo* experiments in humans due to ethical and safety concerns.

In order to increase the sensitivity in the assessment of cortisol metabolism another tracer [1,2,6,7] <sup>3</sup>H<sub>4</sub> cortisol, with higher specific activity was used, but this still lacks selectivity due to regeneration. Klemcke and colleagues used this approach while conducting an *in vivo* experiment in pigs to evaluate the foetal cortisol metabolism during gestation. The study found that the major contribution of maternal cortisol to fetal cortisone strongly suggested the presence of porcine placental hydroxysteroid dehydrogenase. However, accurate assessment of 11β-HSD2 activity could not be achieved as [1,2,6,7] <sup>3</sup>H<sub>4</sub> cortisone can be also formed in the foetus may also be derived from the plasma [1,2,6,7] <sup>3</sup>H<sub>4</sub> cortisone pool (Klemcke *et al.*, 1996). Moreover, the placenta also expresses some 11β-HSD1 confounding quantitation of rates. Another study conducted by Bocchi attempted to provide evidence of 11β-HSD2 deficiency in aldosterone-sensitive sweat gland ducts biopsies from subject with essential hypertension (Bocchi *et al.*, 2004). The [1,2,6,7] <sup>3</sup>H<sub>4</sub> tracer has been extensively used by others (Bujalska *et al.*, 2008). However, as with previous tracers, the main drawbacks is the lack of selectivity due to cross-reactivity with other metabolites in radioactivity measurement using liquid scintillation counting, lack of discrimination of reductase and dehydrogenase and ethical and safety concerns for *in vivo* human studies.



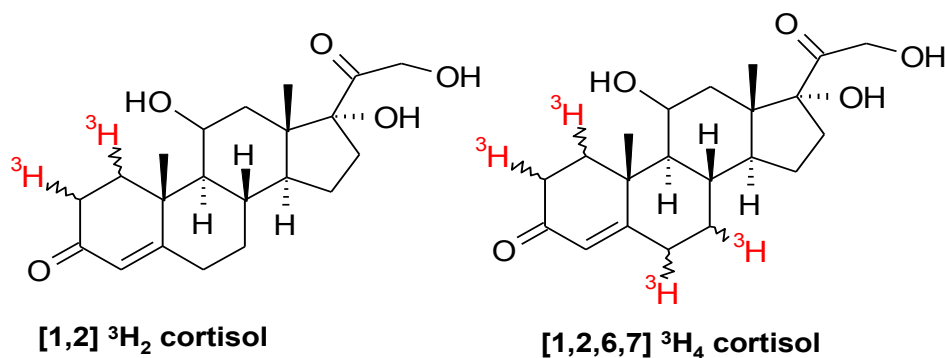


**Figure 1.5:** Structures of [1,2] <sup>3</sup>H<sub>2</sub> (a) and [1,2,6,7] <sup>3</sup>H<sub>4</sub> cortisol tracer. Radioactive tritium labelled is highlighted in red.

#### 1.2.4.3. *Arteriovenous sampling of endogenous corticosteroids*

Another approach to measure enzyme 11 $\beta$ -HSDs activity was by measuring both endogenous cortisol and cortisone by arteriovenous (A-V) sampling; this approach measures the change in substrate and product in blood entering and leaving a tissues. An *in vivo* study of the cortisol–cortisone shuttle in subcutaneous abdominal adipose tissue was conducted by Katz et al in where (A-V) differences in serum cortisol and cortisone across subcutaneous human abdominal adipose tissue and forearm muscle were measured. In this study, serum cortisol and cortisone were measured in samples from a radial artery, superficial epigastric vein and deep forearm vein and 11 $\beta$ -HSD oxo-reductase activity in subcutaneous abdominal adipose tissue was inferred from and increased cortisol/cortisone ratio, which increased in obesity (Katz *et al.*, 1999a). Walker and co-workers applied A-V measurements of cortisol and cortisone in patients with valvular or ischaemic heart disease and with Cushing's syndrome to evaluate if 11 $\beta$ -HSD is inhibited by ACTH, and prove that cortisol induces hypokalaemic alkalosis in ectopic ACTH syndrome (Walker *et al.*, 1992a). In this study, the principal sources

of plasma cortisone were assessed by selective venous catheterisation with measurement of cortisol and cortisone by radioimmunoassay. The study found that peripheral conversion of cortisol to cortisone occurs mainly in the kidney and is inhibited by ACTH. In ectopic ACTH syndrome the characteristic mineralocorticoid excess can be accounted for by a combination of increased secretion of cortisol, corticosterone and of 11-deoxycorticosterone and decreased inactivation of cortisol and corticosterone by 11 $\beta$ -HSDs, but this approach did not distinguish activity in the liver from the contribution of visceral adipose tissue which in vitro studies suggested is substantial (Bujalska *et al.*, 1997). Unfortunately, measuring cortisol in the portal vein is only achievable during surgery, when high stress would probably obscure the local regeneration (Aldhahi *et al.*, 2004). Furthermore, the errors associated with A-V measurement are wide and A-V is an invasive methodology. Most importantly again dehydrogenase and reductase activities could not be separately measured.

#### **1.2.4.4. *Ex vivo biopsies***

*Ex vivo* studies have been conducted on tissue homogenate biopsies to measure the velocities and transcript abundance of the individual isozymes of 11 $\beta$ -HSD1. This is achievable since 11 $\beta$ -HSD2 accepts NAD<sup>+</sup> as a co-factor, whereas 11 $\beta$ -HSD1 requires NADPH, allowing harnessing of either isozyme through experimental conditions. Cortisol metabolism within different adipose tissue depots was studied by (Bujalska *et al.*, 1997) in cultured omental and subcutaneous adipose stromal cells from 16 patients undergoing elective abdominal surgery. By analysing activity of the two isozymes of 11 $\beta$ -HSDs, the study found that adipose stromal cells from omental fat, but not subcutaneous fat, generated active cortisol from inactive cortisone through the

expression of 11 $\beta$ -HSD1. Another group studied the tissue-specific disruption of cortisol metabolism in subcutaneous fat biopsies, showing that enhanced reactivation of cortisone to cortisol in subcutaneous adipose tissue was observed (Rask *et al.*, 2001). The approach reports on the amount and activity of protein present but does not account for the availability and concentration of enzyme substrate. Although tissue-specific, this method does not usually provide spatial localisation information within different cell population, without cell sorting. This is very important in tissue like brain in which the enzyme expression varies across the tissue.

#### **1.2.4.5. *11 $\alpha$ -tritiated cortisol***

To allow specific dehydrogenation of cortisol to be assessed, other studies were conducted using a tritiated labelled cortisol tracer, 11 $\alpha$ -<sup>3</sup>H-cortisol (**Figure 1.6**), which is metabolised by 11 $\beta$ -HSD2, yielding unlabeled cortisone and tritiated water. This tracer is more selective than those mentioned previously in **section 1.1.1.2** as the radioactive tag is strategically place on the C11 position (site of enzyme dehydrogenation). Therefore clearance of this tracer reflects dehydrogenation. The clearance of this tracer is more rapid than with cortisol alone (Hellman *et al.*, 1971). Using this tracer *in vivo*, Walker and co-workers showed impaired clearance of the radio tracer, in spite of no change in endogenous plasma steroids. Furthermore, normal ratios were observed after carbenoxolone administration in patient with essential hypertension against healthy volunteers (controls) suggesting that 11 $\beta$ -reductase conversion of cortisone to cortisol was also defective (Walker *et al.*, 1993). The tracer was also use by Stewart and colleagues in patients with 11 $\beta$ -HSD2 deficiency (Stewart, 1988). The downside of this method is that is only provides information about

dehydrogenation and is again less desirable due to the ethical and safety concerns of radiochemicals as previously discussed above.

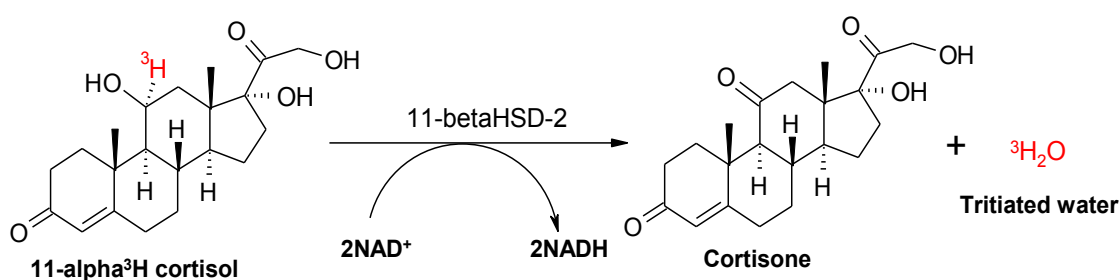
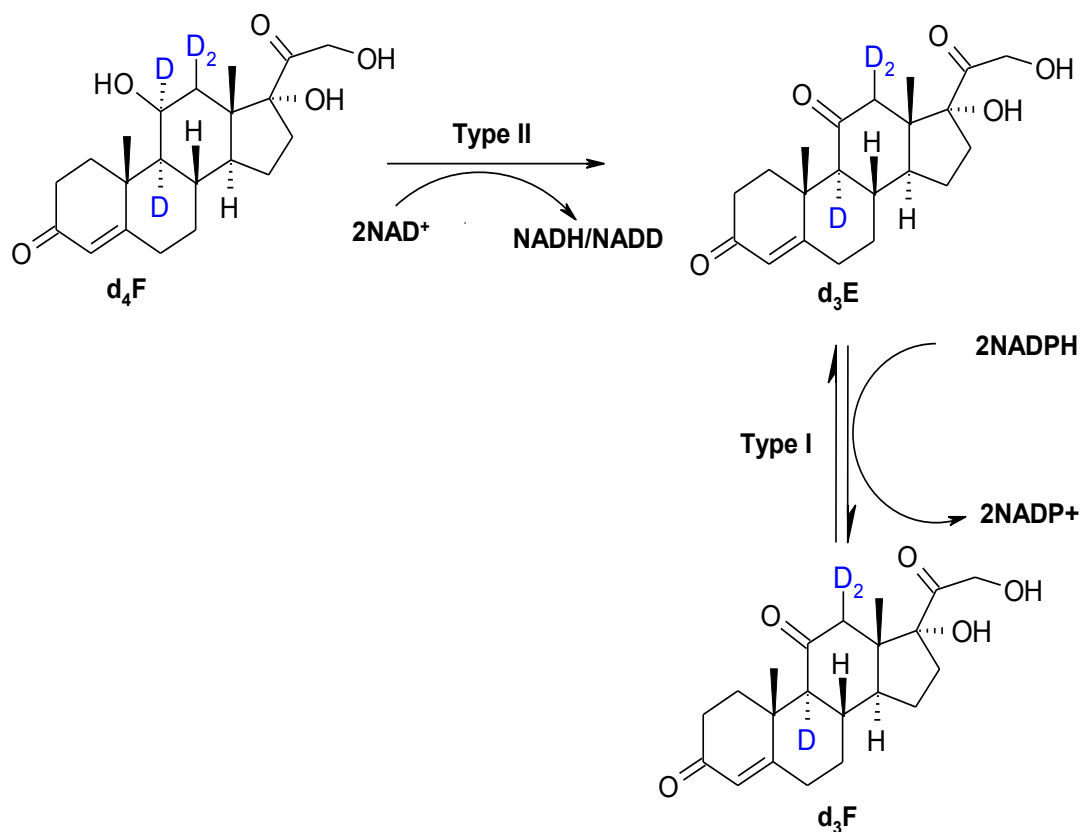


Figure 1.6: Structure of 11 $\alpha$ - $^3\text{H}$ -cortisol tracer. Radioactive tritium labelled is highlighted in red.

#### 1.2.4.6. *Stable isotope tracers*

To tackle the aforementioned issues of non-selectivity and radiolabelling, Andrew and colleagues developed a novel, approach to measure the turnover of the 11 $\beta$ -HSDs pathways and further distinguish dehydrogenase and reductase activities using a stable isotope tracer of cortisol (9,11,12,12- $^2\text{H}_4$ -cortisol ( $\text{d}_4\text{F}$ )) (**Figure 1.7**). The tracer, analogous to that prepared by Ulick *et al* (Ulick *et al.*, 1991), contains four deuteriums in the steroid skeleton, one of which is in the 11 position. By using this tracer, cortisol and other metabolites can be distinguished from the endogenous contribution by their respective molecular masses. The deuterium at the 11 position is lost on metabolism by dehydrogenation, yielding a labelled cortisone molecule [trideuterated cortisone ( $\text{d}_3\text{E}$ )] with a mass 3 greater than that of the endogenous cortisone. Then on reactivation by 11 $\beta$ -HSD1/reductase,  $\text{d}_3\text{E}$  is converted to a labelled cortisol species [trideuterated cortisol ( $\text{d}_3\text{F}$ )], which can be distinguished from the [9,11,12,12- $2\text{H}_4$ ]cortisol ( $\text{d}_4\text{F}$ )

infused. Therefore, by using this approach it was possible to distinguish “cortisol” generated from the substrate of 11 $\beta$ -HSD1 from adrenal secreted cortisol.



**Figure 1.7:** Schematic of metabolism of deuterated cortisol tracer (9,11,12,12-<sup>2</sup>H<sub>4</sub>-cortisol (d<sub>4</sub>F) by 11 $\beta$ -HSD. Deuterium labelled in blue. 9,12,12-<sup>2</sup>H<sub>4</sub>-cortisone (d<sub>3</sub>E), 9,12,12-<sup>2</sup>H<sub>4</sub>-cortisol (d<sub>3</sub>F).

The first *in vivo* application of the tracer in humans to distinguish the dehydrogenase and reductase activities following carbenoxolone administration was presented by Andrew and colleagues (Andrew *et al.*, 2002). D<sub>4</sub>F and its metabolites were measured in plasma and urine during a steady state infusion. Inhibition of 11 $\beta$ -HSDs by carbenoxolone was measured by increased steady state concentrations of d<sub>4</sub>F and a fall in the rate of appearance of d<sub>3</sub>F. 11 $\beta$ -HSD1 reductase activity was measured as dilution

of d<sub>4</sub>F by d<sub>3</sub>F whereas 11 $\beta$ -HSD2 was measured by initial rates of appearance of d<sub>3</sub>E or from urinary ratios of d<sub>4</sub>F/(d<sub>3</sub>E + d<sub>3</sub>F). This study confirms that carbenoxolone inhibits both isozymes of 11 $\beta$ -HSD (Andrew *et al.*, 2002) and that d<sub>3</sub>F was a useful measure of 11 $\beta$ -HSD1 activity. Using this approach in combination with tissue-specific sampling can be used to elucidate tissue-specific changes in 11 $\beta$ -HSD1 activity in a disease context.

In a subsequent application, *in vivo* whole body kinetics of cortisol using d<sub>4</sub>F tracer infusion, were examined in obesity. The study found that the obese men had no difference in their whole-body rate of regenerating cortisol. Possibly the contribution of subcutaneous adipose 11 $\beta$ -HSD1 to d<sub>3</sub>F generation was too small to cause a significant change in measured whole body rates of appearance. Again carbenoxolone inhibited whole-body cortisol regeneration, but did not significantly inhibit adipose 11 $\beta$ -HSD1. Therefore, this study suggested that efforts in the development of selective 11 $\beta$ -HSD1 inhibitors should address drug delivery in order to inhibit the enzyme more effectively in adipose tissue (Sandeep *et al.*, 2005).

Following with *in vivo* applications, the magnitude of regeneration of cortisol in different tissues in humans several studies have been inferred by sampling arterio-venous blood across tissue beds. In one study, d<sub>4</sub>F was infused in men and tracer enrichment in the hepatic vein compared with that in arterialised blood as an indicator of total splanchnic cortisol generation. Modelling from this study suggested that tissues draining into the hepatic vein contribute substantially to the regeneration of cortisol. Thus, the hepatic vein may deliver cortisol to the liver (Andrew *et al.*, 2005). Basu and colleagues likewise found that the splanchnic production of cortisol occurs in

nondiabetic humans at rates approximating that which occurs in the remainder of the body (Basu *et al.*, 2004).

From whole-body to tissue-specific regeneration, a study has been conducted in adipose to directly studying the release of cortisol by 11 $\beta$ -HSD1 from visceral adipose tissue and its effect on portal vein concentrations. D<sub>4</sub>F infusion was conducted on both healthy and stable chronic liver disease subjects and blood samples were taken from superficial epigastric vein (healthy) and from the portal, hepatic and peripheral veins (liver disease). Significant cortisol and d<sub>3</sub>F release from subcutaneous adipose tissue was detected, but with splanchnic release of cortisol and d<sub>3</sub>F accounted entirely by the liver (Stimson *et al.*, 2009). This finding was supported by another study in which it was found that the liver accounts for all splanchnic production; cortisol from visceral tissues into portal vein was not detected (Basu *et al.*, 2006). Therefore, visceral adipose 11 $\beta$ -HSD1 activity appears insufficient to increase portal vein cortisol concentrations and hence is unlikely to influence intrahepatic glucocorticoid signalling or be an effective drug target (Stimson *et al.*, 2009).

Another study was carried out to evaluate the dynamics of turnover of cortisol within adipose tissue and the circulating pool, Hughes *et al* (Hughes *et al.*, 2010) measured the rate of exchange of cortisol and d<sub>3</sub>F between plasma and adipose for comparison with rates of intracellular cortisol generation by 11 $\beta$ -HSD1, using adipose biopsies. In plasma, d<sub>4</sub>F concentrations and appearance rates of cortisol and d<sub>3</sub>E (reflecting 11 $\beta$ -HSD1 activity) did not change during the experiments. In both omental and sc adipose, the tracer was detected later than plasma and enrichment with d<sub>4</sub>F in the adipose cortisol pool was low. The contribution of 11 $\beta$ -HSD1 to this turnover could not be

quantified because very little substrate  $d_3E$  accumulated in adipose during infusion, but can be considered slow. The slow turnover observed in the adipose glucocorticoid pool demonstrated that the rapid acute fluctuations in circulating cortisol are not likely to be reflected in adipose (Hughes *et al.*, 2010).

Stable isotope tracer approaches have also allowed evaluation of effects of factors regulating metabolism (nutrition/insulin sensitivity) on cortisol generation. Wake and colleagues have demonstrated that hyperinsulinemia increased the rate of appearance of  $d_3F$ , indicating increased whole-body  $11\beta$ -HSD1. Within adipose, the predominant reaction was reductase conversion of cortisone to cortisol and insulin increased reductase activity (Wake *et al.*, 2006). The effects of dietary macronutrients (high fat-low carbohydrate (HF-LC) vs. moderate fat-moderate carbohydrate (MF-MC)) on cortisol metabolism have been evaluated in obese men. This study found that both HF-LC and MF-MC diets induced weight loss. During  $d_4F$  infusion, HF-LC but not MF-MC increased  $11\beta$ -HSD1 activity (measured as rates of appearance of cortisol and  $d_3F$ ) along with a reduction in urinary excretion of  $5\alpha$ - and  $5\beta$ - reduced  $d_4F$  metabolites and clearance. Nevertheless, in sub-cutaneous abdominal adipose tissue,  $11\beta$ -HSD1 mRNA and activity were unaffected by diet implicating the liver source of enzyme in the findings (Stimson *et al.*, 2007).

A recent study conducted by the same group showed that plasma cortisol was similarly increased after all macronutrient meals compared with placebo. With carbohydrate-based diet the adrenal secretion and extra-adrenal regeneration of cortisol was stimulated to a similar degree. The adrenal cortisol secretion following protein and fat meals was greater than extra-adrenal cortisol regeneration with postprandial cortisol



rise not accounted for by decreased cortisol clearance. Therefore, food-induced circadian variation in plasma cortisol is mediated by adrenal secretion and extra-adrenal regeneration of cortisol (Stimson *et al.*, 2014).

Isotope traces have also been applied to assess drug-efficacy on several targets. In one study, peroxisome proliferator-activated receptor (PPAR) agonists (rosiglitazone (PPAR $\gamma$ ) and fenofibrate (PPAR $\alpha$ ) was tested to see whether cortisol secretion and peripheral regeneration by 11 $\beta$ -HSD1 were altered in humans receiving these drugs and whether reduced cortisol action contributes to metabolic effects of PPAR $\gamma$  agonists. Neither PPAR $\alpha$  nor PPAR $\gamma$  agonists down-regulate 11 $\beta$ -HSD1 or cortisol secretion acutely in humans and the early insulin-sensitizing effect of rosiglitazone was not dependent on reducing intracellular glucocorticoid concentrations (Wake *et al.*, 2007).

Another application by (Sigurjonsdottir *et al.*, 2009) evaluated the acute effects of growth hormone (GH) on 11 $\beta$ -HSD1 in liver and adipose tissues *in vivo* in men with benign pituitary disease. Cortisol kinetics during d<sub>4</sub>F infusion was measured. In this study, subjects on stable GH replacement therapy for >6 months were studied after GH withdrawal for 3 weeks, and after either placebo or GH injections were reintroduced for another 3 weeks. Results found that d<sub>3</sub>F appearance was not changed after GH withdrawal and reintroduction and d<sub>4</sub>F clearance increased after GH withdrawal, hence, GH did not regulate 11 $\beta$ -HSD1 rapidly *in vivo* in humans (Sigurjonsdottir *et al.*, 2009).

In a disease context, single nucleotide polymorphisms (SNPs) in HSD11B1, the gene encoding 11 $\beta$ -HSD1, have been associated with type 2 diabetes and hypertension and with hyperandrogenism in patients with the polycystic ovary syndrome (PCOS). The functional consequences of these single nucleotide polymorphisms (SNPs) in 11 $\beta$ -

HSD1 expression and activity were evaluated using d<sub>4</sub>F in patient with polycystic ovary syndrome (PCOS). Using an *in vivo* setting, the study shown that women with and without PCOS, alleles of *HSD11B1* containing the two SNPs rs846910 A and rs12086634 T confer increased 11 $\beta$ -HSD1 expression and activity (Gambineri *et al.*, 2011). Another study conducted by (Boonen *et al.*, 2013) used d<sub>4</sub>F cortisol to measure the plasma cortisol clearance and production in critically ill patients in the intensity care unit (ICU). In the patients, as compared with the controls, endogenous cortisol and rate of appearance were increased and no significant difference in cortisol production between patients was found in patients who were treated with catecholamines and those who were not treated. By using isotope tracer, cortisol production in patients with adrenal insufficiency could be evaluated and levels were indistinguishable from that in controls, whereas it was elevated in patients with a normal response to corticotropin. Tracer analysis also allowed dissection of the contribution of 11 $\beta$ -HSD enzymes to altered cortisol clearance. The patients had a lower net rate of appearance of cortisone than the controls). However, there was no significant between-group difference in the level of regeneration of cortisol by 11 $\beta$ -HSD1, as measured by the rate of appearance of d<sub>3</sub>F (Boonen *et al.*, 2013)

As the development of novel and selective 11 $\beta$ -HSD1 inhibitors has focussed on treatment of type 2 diabetes and the pharmacological effects may be reduced if hepatic 11 $\beta$ -HSD1 is similarly decreased in obese patients with type 2 diabetes (Stimson *et al.*, 2011) evaluated this hypothesis by quantifying *in vivo* whole-body, splanchnic, and hepatic 11 $\beta$ -HSD1 activity in obese type 2 diabetic subjects by infusion of both cortisol and d<sub>4</sub>F. D<sub>3</sub>F appearance rate in the arterialised blood was increased, splanchnic d<sub>3</sub>F production was not reduced and cortisol appearance in the hepatic vein after oral

cortisone was unchanged. These data supported the concept that inhibitors of 11 $\beta$ -HSD1 are likely to be most effective in obese type 2 diabetic subjects (Stimson *et al.*, 2011).

While d<sub>4</sub>F infusion has allowed measurement of 11 $\beta$ -reductase activity, a strand of literature has suggested that this enzyme may also proceed as dehydrogenase under given circumstances. Further tracers may be employed to address this. *In vivo* assessment of the bidirectionality activity of 11 $\beta$ -HSD1 in human metabolic tissues was carried out by (Hughes *et al.*, 2012). In this study, 1,2-[<sup>2</sup>H]<sup>2</sup>-cortisone (d<sub>2</sub>E) was used to measure 11 $\beta$ -dehydrogenase activity and d<sub>4</sub>F for 11 $\beta$ -reductase activity. 11 $\beta$ -Reductase and -dehydrogenase activities were detected in muscle and splanchnic circulation and in adipose, dehydrogenase was higher readily detected than reductase (Hughes *et al.*, 2012).

However, in these studies the glucocorticoid turnover in individual tissues was inferred from measurements either *in vivo* (whole-body, AV sampling) or *ex vivo* (enzyme activities/mRNA and tissue steroid concentrations in whole tissue homogenates), therefore, the reliability to measure tissue- or cell-specific steroid concentrations is still needed for understanding tissue-specific pharmacodynamics of novel enzyme inhibitors, interactions between 11 $\beta$ -HSD1 and other determinants of intracellular glucocorticoid concentrations, and the relative importance of 11 $\beta$ -HSD1 in specific cells in complex tissues such as brain.

#### 1.2.4.7. *New approaches*

Ongoing efforts are being focused in the development of non-invasive tools of tissue-specific activity of 11 $\beta$ -HSD1, Magnetic resonance spectroscopy (MRS) has been explored using fluorinated steroids for *in vivo* studies. Coherent anti-Stokes Raman spectroscopy (CARS) microscopy is being investigated for *in vitro* measurements of steroid trafficking at sub-cellular level in cell cultures using deuterated steroids and the technique has the potential for *in vivo* imaging application by incorporation in multiphoton *in vivo* confocal microscopy.

However, a limiting factor for all of the above is sensitivity, requiring either large samples (from mass spectrometry analysis stable isotope tracer), high non-physiological tracer concentrations (for MRS and CARS microscopy) and synthesis of radioactive tags (tritiated steroids). Furthermore, standard tissue-homogenate analysis assumes homogeneity across the tissue section and in most of the cases (e.g. tumour tissue biopsies) this assumption is incorrect, as tissues have different histological features due to different cell population. Therefore, our research group in Edinburgh has continued to explore alternative technological solutions such as mass spectrometry imaging (MSI) as an approach to overcome current limitations. The main advantage of using MSI over conventional tissue-based analysis is that MSI can generate molecular distribution maps across the tissue section based on the mass/charge ( $m/z$ ) of molecules with acceptable spatial resolution (100-10 $\mu$ m) and great sensitivity (up to femtomole). The methodology is also capable of performing both targeted (e.g. drugs) and untargeted (endogenous metabolites) multiplex analysis. This technique may potentially be used to study steroid molecular histology in the tissue microenvironment,

as biochemical-based assays (e.g. immunohistochemistry) lack of reproducibility and multiplex identification. Thus, in this thesis, MSI will be explored as a potential technique to study steroid biology at the tissue level.

### **1.3. Mass Spectrometry Imaging**

#### **1.3.1. Introduction**

The concept of MSI has its origins in the field of physics, where it was used to study semiconductor surfaces (Benninghoven *et al.*, 1978). The introduction of matrix assisted laser desorption ionization (MALDI)-MSI in 1997 by Caprioli *et al.* (Caprioli *et al.*, 1997) led to a significant development and optimisation of instrumentation and data analysis platforms for the analysis of biological samples. The technologies were rapidly applied to the fields of biology, chemistry and pharmaceutical analysis using the label-free strategy to generate molecular maps aligned with histology images (Heeren *et al.*, 2010; Nilsson *et al.*, 2010; Stoeckli *et al.*, 2007). MSI has the ability to detect endogenous and exogenous analytes across a wide mass range. The analysis of lower molecular weight drugs and endogenous compounds through to lipids, peptides and large proteins directly from tissue samples (Castellino *et al.*, 2011; Falth *et al.*, 2006; Groseclose *et al.*, 2008) is leading to an important contribution in fields such as molecular histology, drug distribution, lipidomics and proteomics (Fletcher *et al.*, 2011). It is important to again reiterate that as MSI can, by accurate mass measurement, differentiate between molecular species such as drugs and their metabolites; hence the technique overcomes the limitations of non-specificity encountered with using radioactive analogues. In addition, as labelled compounds are not required, it is possible to dose test animals with multiple compounds (cassette dosing) (White *et al.*,

2001) increasing the throughput of compounds in discovery or enabling the study of combination therapies. To successfully, accurately, and reproducibly analyse the abundance and distribution of a molecules directly from tissue sections, a robust workflow is required. Variations and fluctuations in technical aspects can affect subsequent stages leading to erroneous or misleading data. The following section will describe the commonly available ionisation processes and mass analysers. Also the steps in sample preparation (focus primarily on MALDI-MSI), processing and analysis required for successful MSI analysis will be reviewed.

### **1.3.2. Principle and instrumentation**

MSI is a multi-step process, involving sample preparation, analyte desorption and ionisation, mass analysis, and image registration (**Figure 1.8**). Briefly, tissue cryosections are placed, commonly under vacuum, into an MS instrument and analyte molecules are desorbed and ionised from the surface (Zimmerman *et al.*, 2008). With ionisation being performed from known positions across a sample, the collated mass spectral information can be used to generate distribution data on the molecules present. The resulting ion distributions are typically presented as 2D ion images showing relative abundance of selected molecular masses. The sample processing pipeline for MSI, while simple, does offer multiple stages for optimisation and modification. In MSI, spatial resolution is determined by the size of the probe beam (affected by laser spot size and sample positioning) and mass resolving power is defined by  $(m/\Delta m)_{50\%}$  where  $\Delta m$  is the resolution (The minimum peak separation  $\Delta M$  which allows to distinguish two ion species: at 50% peak height) and  $m$  is the mass of the second peak. Another important aspect is the pixel size, which is defined by the speed of the stage

movements, acquisition rate of the mass spectra and distance between two lines of acquisitions (Heeren *et al.*, 2010).

There are two major types of MALDI-TOF MSI; microprobe and microscope mode experiments. In MALDI microprobe MSI, a highly focused pulsed desorption/ionization laser beam probes the sample surface. A full mass spectrum is generated at every raster point. An image is reconstructed after the experiment with a pixel resolution equivalent to the beam size (provided the stepping size/accuracy of the sample/beam movement is not limiting) (Spengler *et al.*, 2002). Disadvantages of small surface probe areas include long measurement times and loss of sensitivity due to low laser fluence for desorption and ionization. (Bradshaw *et al.*, 2009)

MALDI microscope mode MSI is an alternative approach to microprobe mode imaging (Luxembourg *et al.*, 2004). In the microscope mode, a large surface probe desorbs and ionizes surface molecules over a large sample area, typically 200-300  $\mu\text{m}$  in diameter. The large field of view in microscope mode MSI enables fast, large area image acquisition at high spatial resolution (Luxembourg *et al.*, 2004). An ion microscope uses ion optics to project the desorbed/ionized surface compounds onto a position-sensitive detector. Importantly, the initial ion distribution is magnified and the lateral spatial organization of the surface molecules is retained on the flight path to the detector. While the ionization spot size determines the obtainable spatial resolution in microprobe mode, the spatial resolution in microscope mode is decoupled from the ionization spot size. Rather, the spatial resolution is determined by the quality and the capabilities of the ion optics in combination with a position- (and time-) sensitive detector. Spatial resolving powers on the order of 4  $\mu\text{m}$  have been achieved where a 10

$\mu\text{m}$  charge-coupled device (CCD) camera pixel probed  $1\ \mu\text{m}$  on the sample surface pot size has been demonstrated by over-sampling (Jurchen *et al.*, 2005). Presented here is an overview of several key stages for MALDI-MSI, the focus of this thesis.

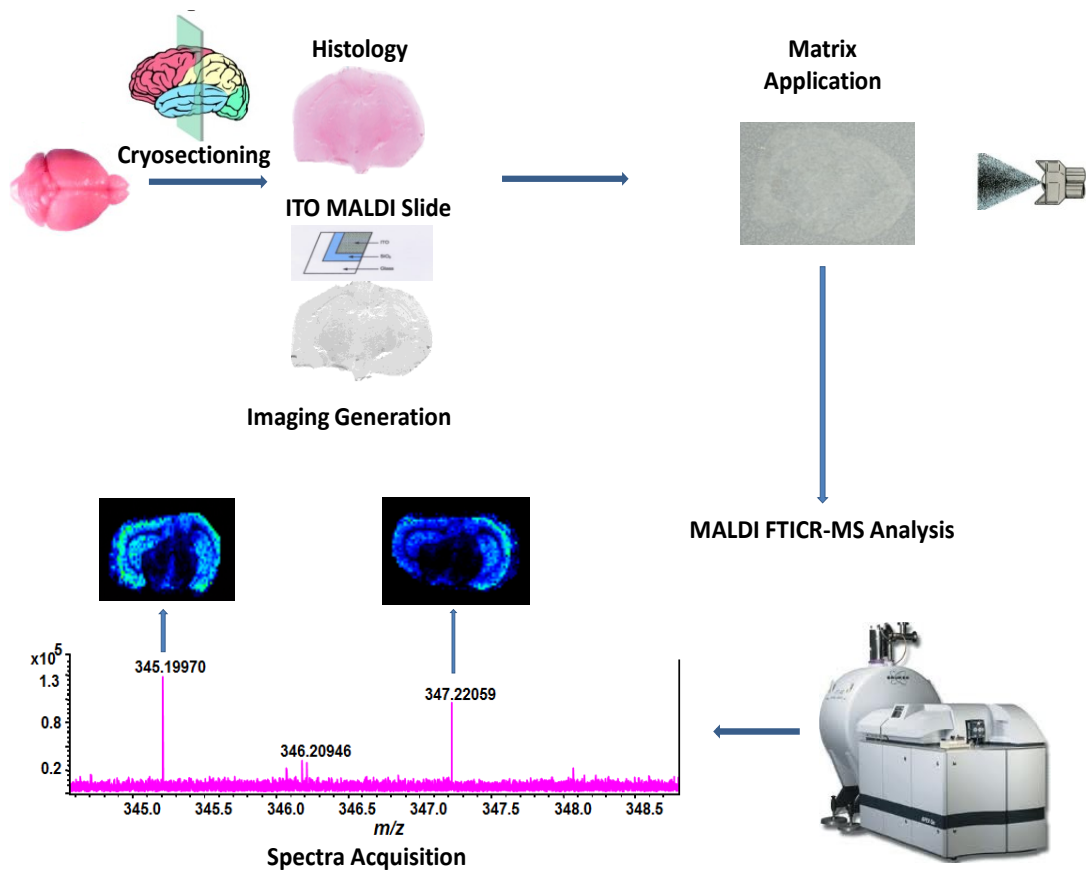


**Figure 1.8:** Mass spectrometry imaging (MSI) workflow. MSI involves sample preparation, analyte desorption and ionization, mass analysis, and image registration. In briefly, cryo-sections of tissue of interest are coated with a suitable MALDI matrix and then introduced into an MSI instrument. A specified area of the tissue section is analysed and mass spectral information collected. The resulting ion distributions are presented in the form of ion images. **ITO** = Indium Titanium oxide; **MS** = Mass Spectrometry; **MALDI** = Matrix assisted laser desorption ionisation.



### 1.3.3. Ionisation techniques

There are a number of ionisation methods capable of performing MSI, with MALDI the most commonly used and the primary focus of this thesis. The next most commonly utilised are secondary ion mass spectrometry (SIMS) and more recently desorption electrospray ionisation (DESI) and Liquid extraction surface analysis (LESA) all described briefly (**Table 1.2**). The alternative ionisation methods prove advantageous for certain studies depending on target analyte, abundance of analyte, or spatial resolution of analysis. Detailed reviews have been published that compare the advantages and optimisation of the various methods (Klinkert *et al.*, 2007).

**Table 1.2:** MSI ionisation methods adapted from (Caprioli, 2007)

<b>Ionisation Techniques</b>	<b>Ionisation Source</b>	<b>Matrix</b>
LESA	Nano-ESI	Direct Analysis
LDI/MALDI	Laser beam	MALDI Matrices
Me-nSIMS (HV)	Ion beam	(Ag,Au,Pt) + MALDI
DESI (AP)	Charged electro-sprayed droplets	Direct Analysis

**MALDI:** Matrix assisted laser desorption ionisation, **Me-nSIMS:** Metal-nano secondary ion mass spectrometry, **DESI:** Desorption electrospray ionisation **AP:** Atmospheric pressure. **LDI:** Laser desorption ionisation. **LESA:** Liquid extraction surface analysis. **Nano-ESI:** nano-electrospray ionisation

#### 1.3.3.1. *Liquid extraction surface analysis (LESA)*

A recent development in the context of MSI is Liquid Extraction Surface Analysis Mass Spectrometry (LESA-MS) (Kertesz *et al.*, 2010) which obtains information from biological tissue sections via liquid extraction of analytes from the solid surface

followed by nano-electrospray ionisation (**Figure 1.9**). The LESA-MS approach has potential advantages over other MSI approaches in that no additional sample preparation is required (which compared to e.g. MALDI could also eliminate potential low molecular weight MALDI matrix mass interferences), the ionisation process is soft, potentially revealing labile molecules or metabolites and it allows analysis of negatively or positively charged analytes by simple exchange of the modifier used in the extraction solvent. However, LESA is a fairly new analysis tool available for ambient surface analysis and its extraction process on thin tissue sections is not well characterised or understood. Its sensitivity might be compound-dependent and affected by ion suppression of co-extracted matrix molecules. Differences in extraction and ion suppression from different tissues might also limit the ability for relative quantification across a thin section. Another limiting factor of LESA is the spatial resolution, as it can only be optimised to approximately 1 mm not suitable for high resolution tissue imaging (Eikel *et al.*, 2011).

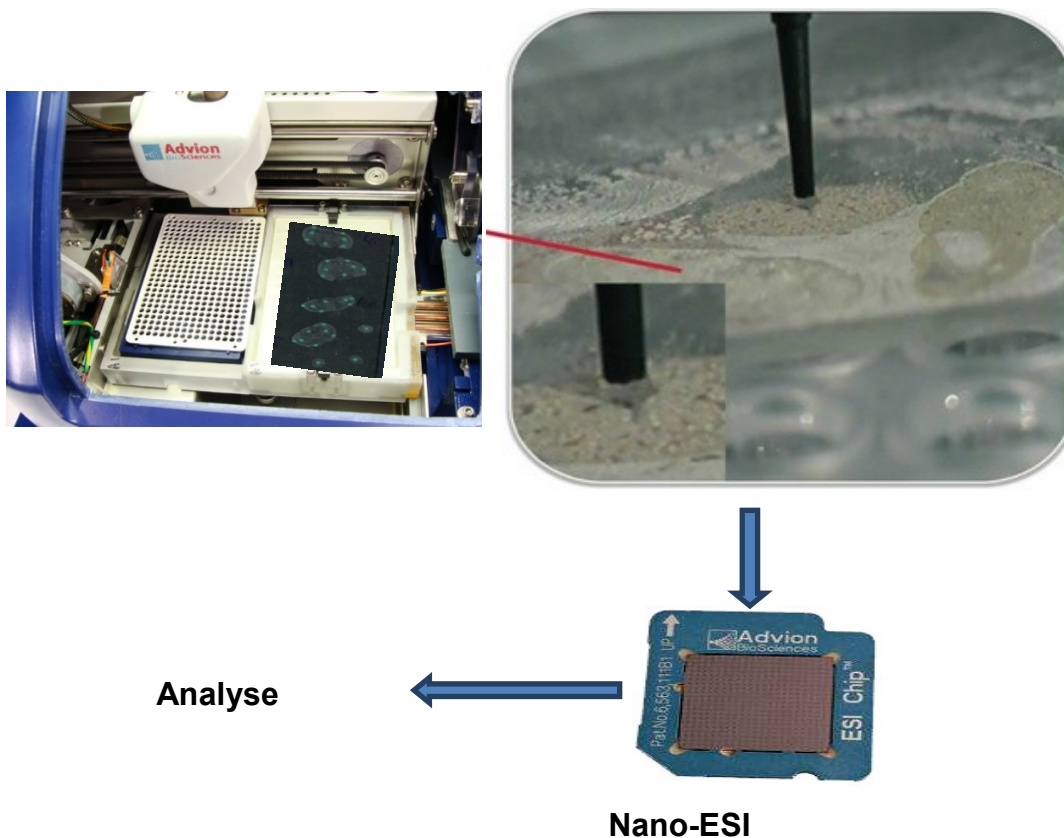


**Figure 1.9:** Liquid Extraction Surface Analysis workflow. Solvent is deposited using a precise micro pipette into an area of interest of the tissue (spot), the spot is then extracted several times and transferred to an Electrospray nano-chip device in which the tissue components and analyte ionised and ions are finally guided to the mass analyser.

### 1.3.3.2. *Matrix assisted laser desorption ionisation (MALDI)*

MALDI is a development of the established laser desorption/ionization mass spectrometry (LDI-MS) introduced in 1988 by Karas and Hillenkamp (Karas *et al.*, 1988). It is a powerful technique that allows the analysis and detection of a wide range of molecules directly from a surface, including from a tissue section. MALDI-MSI has the ability to detect multiple biomolecules generated as intact ions directly from individual, localised pulsed laser spots in matrix-coated tissue sections. In traditional MALDI analysis, the analyte is mixed with an excess of chemical matrix at a molar

matrix to analyte ratio of 100-1000:1 (Dreisewerd, 2003), whereas for MALDI-MSI, the matrix is coated as an even surface layer as described above. MALDI possesses low femtomole to attomole sensitivity and can ionise molecules across a wide mass range up to 300 kDa, lending itself to applications from large biomolecules down to small molecular weight drugs. As such, it has been used for the analysis of proteins, peptides, lipids and pharmaceutical compounds (Franck *et al.*, 2009).

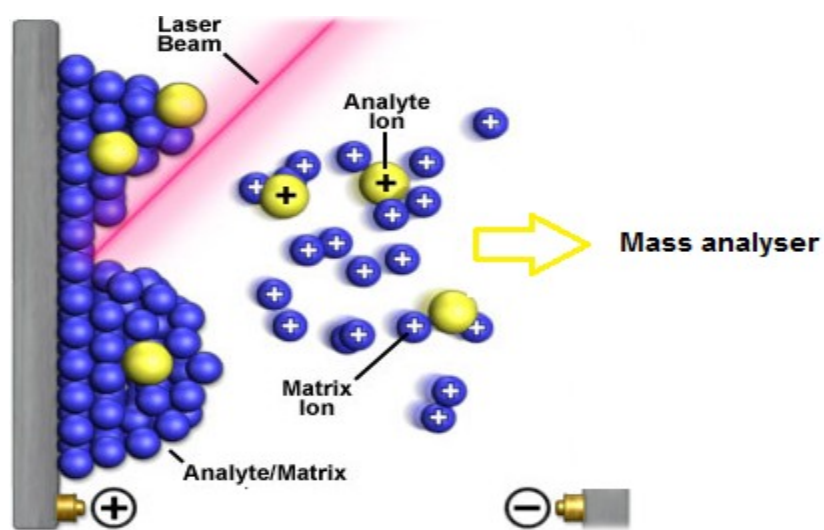


**Figure 1.10:** A schematic diagram of the mechanism of MALDI. Adapted from (Nygren *et al.*, 2007)

In a MALDI-MSI experiment the laser beam is rastered across the surface of the matrix covered tissue. The matrix crystal surface is irradiated with pulsed laser light of sufficient fluence (Karas *et al.*, 2003) and the matrix molecules absorb the laser energy, resulting in the explosive desorption of matrix and analyte molecules (**Figure 1.10**). This phenomenon can be explained and quantified by using the Coupled Physical and Chemical Dynamics (CPCD) model. This name is intended to reflect the fact that it explicitly covers everything from the condensed phase, through a very dense fluid, and the expansion of that fluid, to the state of isolated ions. In particular, it

includes the way chemical and physical processes interact to determine the final result. The concepts of CPCD model can be cast into quantitative form, making them much more useful for prediction and understanding of MALDI spectra (Knochenmuss, 2002). The unimolecular and bimolecular (pooling) processes involved can be quantified using one order differential equations as described in **equation 1**. The bimolecular processes are scaled by D (expansion factor), the rate of collisions in the expanding plume. Because the plume begins at very high pressures and the external environment is vacuum (or at most 1 atm), it is can be well described as an isentropic expansion (Knochenmuss, 2002).

$$\begin{aligned}
\frac{d[S_0]}{dt} &= -I(t)\sigma_{01}(\lambda)[S_0] + \frac{[S_1]}{\tau_1} + I(t)(\sigma_{01}(\lambda)/5)[S_1] + Dk_{11}[S_1]^2 + Dk_{1n}[S_1][S_n] + Dk_{I_0}[I_+][I_-] \\
\frac{d[S_1]}{dt} &= I(t)\sigma_{01}(\lambda)[S_0] - \frac{[S_1]}{\tau_1} - I(t)(\sigma_{01}(\lambda)/5)[S_1] - I(t)\sigma_{1n}(\lambda)[S_1] + k_{n1}[S_n] - 2Dk_{11}[S_1]^2 - Dk_{1n}[S_1][S_n] \\
\frac{d[S_n]}{dt} &= I(t)\sigma_{1n}(\lambda)[S_1] - k_{n1}[S_n] - k_{therm}[S_n] + Dk_{11}[S_1]^2 - Dk_{1n}[S_1][S_n] \\
\frac{d[I_+]}{dt} &= \frac{d[I_-]}{dt} = k_{therm}[S_n] + Dk_{11}[S_1]^2 - Dk_{1n}[S_1][S_n] - Dk_{I_0}[I_+][I_-] \\
\frac{d[E]}{dt} &= I(t)\sigma_{01}(\lambda)[S_0](h\nu - E(S_1)) + \frac{1}{\tau_1}([S_1]E(S_1)(1 - \Phi(S_1)) + k_{n1}[S_n](E(S_n) - E(S_1))) \\
&+ Dk_{1n}[S_1][S_n](E(S_n) + E(S_1) - IP) + Dk_{I_0}[I_+][I_-]IP \\
\text{Temperature} &= E/(kf) \\
k_{n1} &= 9 \times 10^{15} e^{(E(S_1) - IP)/kT}
\end{aligned}
\tag{Equation 1}$$

**Equation 1: MALDI ionization mechanism: IP (free molecule);IP (large clusters) S1 state energy starting temperature  $\sigma$ :S0→S1 absorption coefficient;  $\sigma$ : S0←S1 stimulated emission;  $\sigma$ : S,→S, absorption coefficient;  $\sigma$ : S,→S decay rate;  $\tau_1$ :(t=0)= solid state lifetime;  $\tau'$ : limiting plume S1 lifetime;(I)(t)= fluorescence quantum yield; f= internal degrees of freedom;  $\gamma$ = C/CV for plume expansion density; Kf = Ion recombination Fraction clusters in plume laser spot diameter. Pooling rate constants: K11 = S, + S1→Sn + 80K1n = S, + S,,→Ions + 80; D: expansion scaling factor**

The depth of the ablation crater is estimated around 1  $\mu\text{m}$  or more, depending on laser fluence (Knochenmuss, 2014). Although this has traditionally been a slow process, the introduction of the new  $\text{N}_2$  (337 nm) or neodymium-doped yttrium aluminium garnet

(Nd:YAG) (355 nm) lasers with repetition rates of 200-5000 Hz and typical pulse lengths of 3 ns or less has shortened the data acquisition process (Dreisewerd, 2003). To make MALDI-MSI a more practical application for biological cellular imaging the lasers spot size have been reduced from >100 to <20  $\mu\text{m}$ . Focusing of the laser beam to the diameter of a single cell (approximately 7  $\mu\text{m}$ ) has also been reported by Holle et al. (Holle *et al.*, 2006). However, although such improvements greatly enhance spatial resolution, they also dramatically decrease the sensitivity and are only suitable for high abundance species (e.g. membrane lipids (Fuchs *et al.*, 2007))

### 1.3.3.3. *Secondary Ion Mass Spectrometry (SIMS)*

SIMS is a desorption-ionisation technique which has been used for the characterisation of biomaterials by physicists and now is being extended into biomedicine.

$$I_m = I_p y_m \alpha^+ \theta_m n \quad (\text{Equation 2})$$

The basic equation (**Equation 2**) for the SIMS phenomena is described by equation 1 where  $I_m$  is the secondary ion current of species  $m$ ,  $I_p$  it is the primary particle flux,  $y_m$  is the sputter yield,  $\alpha$  is the ionisation probability to positive ions,  $\theta$  is the fractional concentration of the chemistry in the surface layer and  $\eta$  is the transmission of the analysis system. Ionisation occurs at, or close to, emission of the particles from the surface with the consequence that the matrix participates in the electronic processes involved. This means that the yield of secondary ions is strongly influenced by the electronic state of the material being analysed with consequent complications for quantitative analysis. (John C. Vickerman and David Briggs, 2nd edition, IM Publications, 2013)

Its key benefit over MALDI is in achieving higher spatial resolution and a matrix is not required, reducing opportunities for diffusion and analyte delocalisation. SIMS uses a primary ion beam (e.g. metal ions) capable of producing secondary ions from the surface of the sample (**Figure 1.11**) (Jones *et al.*, 2007). An ion column is used to produce, accelerate and steer a primary ion beam onto the tissue surface, can be focussed as sharply as 50 nm, depending on the primary ion beam current, molecular weight, and its charge state (Altelaar *et al.*, 2005). The energy of the primary ions is substantially higher than the energy of a MALDI laser beam; SIMS thus often yields extensive fragmentation of surface molecules. However, as ion beams can be focused with higher precision than lasers, SIMS offers a unique tool for high spatial resolution MSI of abundant inorganic elements and small organic molecules in cellular organelles (Altelaar *et al.*, 2007). Furthermore, the depth of SIMS imaging can be refined to nm as opposed to  $\mu\text{m}$  layers (Chandra *et al.*, 2002).

However, since 2001, the introduction of cluster and polyatomic ion beams has resulted in a sea change in the technique of molecular SIMS. The wide introduction of polyatomic ion beams such  $\text{C}_{60}^{+}$  and  $(\text{H}_2\text{O})^{n+}$  cluster ions ( $n= 500\text{-}10,000$ ) has had an even more dramatic effect on molecular SIMS (Sheraz *et al.*, 2015). Not only did these beams increase ion yield, it was also discovered that, for many materials, the degree of observable bombardment-induced damage was very significantly reduced, so that analysis could be carried out well beyond the static limit; indeed, in some cases, the whole sample could be consumed during analysis and the chemical information was not compromised. This was a revolutionary development for molecular SIMS because, in principle, it allowed molecular depth profiling of organic materials (John C. Vickerman and David Briggs, 2013).

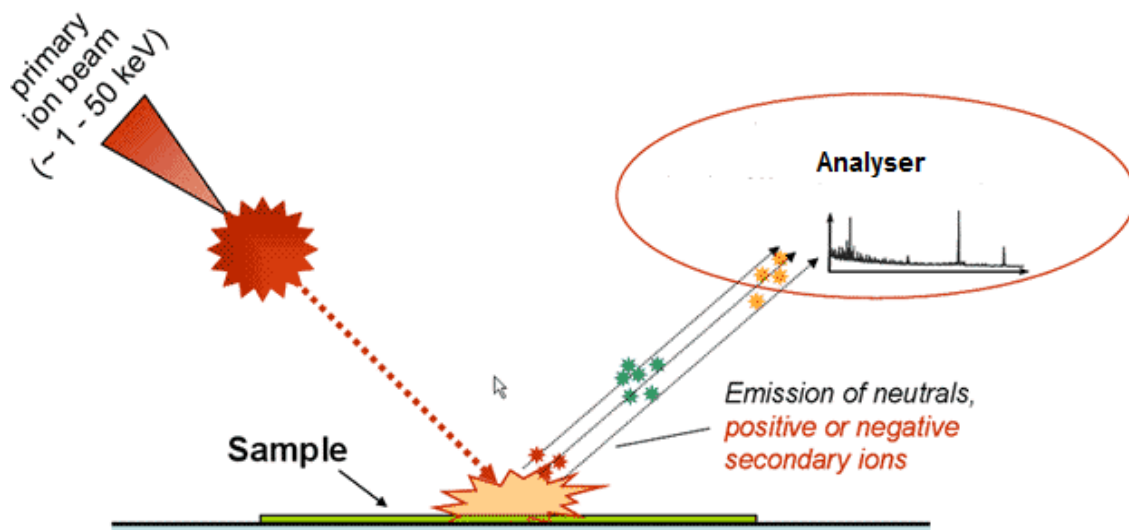


**Figure 1.11:** A schematic diagram of the mechanism of SIMS. Adapted from (Vickerman *et al.*, 2005). SIMS is used to analyze solid surfaces and thin films by sputtering the surface with a focused primary ion beam and collecting and analysing ejected secondary ions.

#### 1.3.3.4. *Desorption Electrospray Ionisation (DESI)*

DESI, an atmospheric pressure ionisation method developed by R.G. Cooks in 2004 (Takats *et al.*, 2004), has been suggested as an alternative MSI platform. In contrast to MALDI and SIMS, DESI operates under atmospheric pressure (AP), being derived from a combination of two MS ionisation methods: electrospray ionisation (ESI) and desorption ionization (DI). Instead of a laser beam or a primary ion beam, DESI uses energetic, charged electrosprayed solvent droplet to release the molecules from the surface (Takats *et al.*, 2004). Molecular ion formation from secondary droplets occurs either by ion emission (ion evaporation model) (Parvin *et al.*, 2005) or by evaporation of neutral solvent molecules (charged residue model) (**Figure 1.12**). Solid samples analysed by DESI produce multiply charged ions like pure ESI. For DESI imaging, the



sample can be placed onto a target (e.g. microscope glass slide). The main advantage of DESI over the others MSI ionisation techniques is that it offers the unique possibility of *in situ* analysis (Dill *et al.*, 2009). In terms of spatial lateral resolution, an study conducted using DESI achieved 400  $\mu\text{m}$  in rat brain (Ifa *et al.*, 2007). However; a recent spray design theoretically predicts an improvement in achievable lateral resolution of 40  $\mu\text{m}$ . Although improvements are still required for this, it holds the promise of soft, local, liquid atmospheric desorption and ionisation, already being applied to study lipids, endogenous molecules, and drug metabolites (Wiseman *et al.*, 2006).

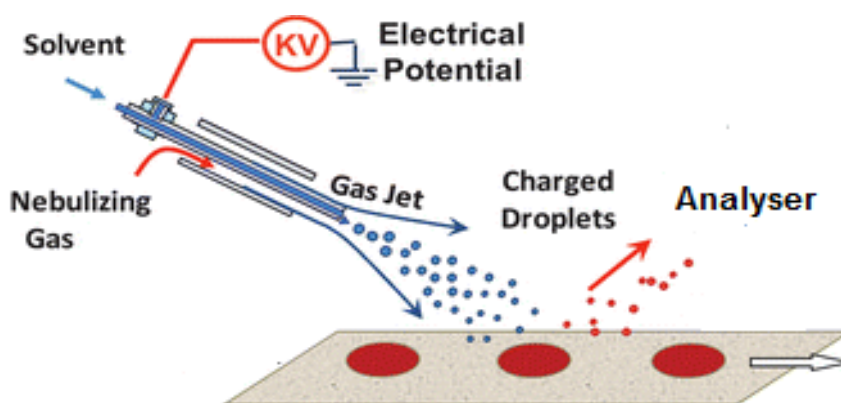


**Figure 1.12:** DESI mechanism. Adapted from (Takats *et al.*, 2004). DESI is a combination of electrospray (ESI) and desorption (DI) ionisation methods. Ionisation takes place by directing an electrically charged mist to the sample surface that is a few millimetres away. The electrospray mist is attracted to the surface by applying a voltage on the sample holder and transfer to the mass analyser.

#### 1.3.4. Tissue preparation for MALDI-MSI analysis

Sample collection and preparation are the first stages of any MSI experiment. The protocols must ensure that histological integrity of the tissue sections are retained so

that spatial localisation of any target molecule is uncorrupted by analyte degradation/diffusion (rapid proteolytic activity has been reported in tissue sections when analysed by MSI (Goodwin, 2012; Goodwin *et al.*, 2008). Put simply, the quality of an MSI image is only ever as good as the starting tissue section. To achieve the highest quality sections, the following steps need to be optimised for the particular target tissues being analysed: sectioning, sample transfer, and washing and application/deposition of the MALDI matrix.

#### **1.3.4.1.        *Preparation of Tissue Sections***

##### **1.3.4.1.1.     *Pre-sectioning steps***

It is most common to conduct MSI using snap-frozen cryosections cut from dissected tissues or organs, rather than conventionally embedded/fixed tissues. For analysis of small drug molecules, it is important to avoid processes which delocalise the analytes, specifically lengthy soaking in fixative or washing with graded ethanol, although these processes may be compatible with analysis of structural components such as proteins. Even so, proteomic analysis from formalin-fixed paraffin embedded tissues is fraught with difficulty, involving multistage process to reverse cross-linking and remove paraffin (Groseclose *et al.*, 2008). An alternative procedure using RCL2/CS100, a non-volatile and non-cross-linking fixative reagent, has been reported as suitable for tissue MSI of proteins and peptides, introduced by Mange and colleagues (Mange *et al.*, 2009); however this is not suitable for small molecules, again due to washing out of analyte. Ideally tissues are collected by rapid freezing in liquid nitrogen, and cryosections prepared specifically for MSI analysis. It is worth collecting consecutive tissue sections for traditional histology, allowing MSI and histology images to be

aligned. If the morphological assessment is performed using the same MSI sample, histological staining must be performed with MSI-compatible stains such as methylene blue or cresyl violet (Chaurand *et al.*, 2004a), i.e. stains not causing ion suppression.

“Ion suppression” is a common problem encountered in biological mass spectrometric analyses, whereby high abundance analytes (e.g. fixative embedding agents) ionise preferentially to low abundance species, masking the signal and swamping mass analyser detectors. Haematoxylin and eosin staining can also be performed after MSI analyses by washing off the MALDI matrix with a suitable solvent, as the histological features of the tissue remain intact (Heeren *et al.*, 2010). In conventional histology, tissues are usually mounted using an optimal cutting temperature polymer (OCT) to allow easier and precise cryosectioning. However, the presence of OCT causes suppression of the MS ion signal (Todd *et al.*, 2001). If samples cannot be mounted with just a small drop of water on the reverse side of the sample, then mounting the sample in gelatine or ice, rather than OCT, can be attempted.

#### **1.3.4.1.2.**      *Sectioning and tissue pre-treatment*

During sectioning, the sample stage temperature is maintained between -10 and -25°C and sections are usually cut at 10-20µm, comparable to the thickness of a mammalian cell diameter, so that the majority of cells are cut open. This allows MALDI matrix (described below) to co-crystallise with cell contents. For some MALDI mass spectrometers, the sample must be ionised from a conductive surface, either a metal plate or a metal coated microscope slide. If tissue sections are much thicker than 30-50 µm then the tissue surface can start to become insulated from the underlying electrical field and hence ionisation will be less efficient. Tissue attachment can be carried out by

the use of an adhesive double-sided conductive tape or by thaw-mounting (Schwartz *et al.*, 2003). Multiple sections from different tissues can be placed on the same MALDI target to allow inter-sample comparison e.g. with vehicle controls. Cell debris, compounds, and salts from the surface of the tissue (Todd *et al.*, 2001) that can cause ion suppression or formation of unstable adducts can be removed by washing. Several solvents have been used, ethanol being preferred due to the fixative dehydration properties (Lemaire *et al.*, 2007). This approach is suitable for proteins or structural components of the tissue, but in the case of small molecular weight drugs care must be taken, as washing with ethanol may lead to the removal of small molecules, particularly hydrophobic ones (e.g. steroids). Therefore, the washing step is target compound-dependent and usually avoided for all small molecule analysis unless optimised specifically. Samples and sections should be stored at -80°C prior to analysis, with all transfers performed on dry ice. Prior to matrix application, samples should be removed from storage and dried using a stream of nitrogen or under vacuum in a desiccator.

#### **1.3.4.2. *Matrix deposition***

The role of the MALDI matrix is to absorb laser energy in the MALDI source, leading to the explosive desorption of analytes (often neutral species) held within matrix crystals, into the gas-phase without significant degradation (Karas *et al.*, 1988). Matrix application must enable homogenous co-crystallisation of the analytes from the tissue within the matrix on the section surface, without causing any diffusion or disruption of the tissue morphology. This step is crucial for achieving reproducible high quality data. Non-optimal matrix selection can obviate detection of target analytes. Furthermore, poorly applied matrix can prevent effective high spatial resolution analysis as analytes

may delocalise in the matrix solvent during deposition and prior to matrix crystallisation. The matrix solution consists of: (a) an organic solvent (commonly ethanol, methanol or acetonitrile), (b) an organic acid (matrix) and (c) trifluoroacetic acid (TFA) or another strong organic acid (when performing positive mode ionisation). The function of the organic solvent is to rapidly extract target compounds from the tissue, followed by fast solvent release by evaporation at room temperature. This allows co-crystallisation of the molecules of interest within the growing crystals of the matrix at the tissue surface (Goodwin *et al.*, 2008). The addition of TFA promotes the ionisation of analytes by enriching the media with available protons, thus, allowing protonated mass formation (ions formed by gain of a proton). The choice of matrix depends on the mass range and physicochemical properties of the target compounds: those most commonly used are listed in **Table 1.3**.

**Table 1.3:** Traditional MALDI matrices. Adapted from (Chaurand *et al.*, 2004b)

Matrix	Abbreviation	Applications	Type
2,5-Dihydroxybenzoic acid	DHB	Sugars, peptides and nucleotides,	crystalline
$\alpha$ -Cyano-4-hydroxycinnamic acid	CHCA	Peptide and small proteins	crystalline
3,5-Dimethoxy-4-hydroxycinnamic	SA	Oligonucleotides	crystalline
2,4,6-Trihydroxyacetophenone	THAP	Oligonucleotides and glycoprotein	crystalline
3-Hydroxypicolinic acid	3-HPA	Phospholipids	crystalline
2,6-Dihydroxyacetophenone	DHA	FFPE tissues	reactive
2,4-Dinitrophenylhydrazine	2,4 DNPH	Peptides	ionic solid

The size of the droplets and subsequent crystals formed by the different matrices influences the spatial resolution possible. Matrix deposition can be performed as individual droplets (spotted) or as a homogeneous layer (coated). The coating can be performed by either spray-based (e.g. TLC-sprayer) or solvent-free (e.g. sublimation) based methods dependent on the spatial resolution that is required. The advantages and disadvantages of the most commonly used deposition techniques are summarised in **Table 1.4** (Kaletas *et al.*, 2009). To limit diffusion of the analyte molecules during matrix deposition, alternative solvent-free matrices have been developed and successfully applied for small molecule MSI analysis (Goodwin *et al.*, 2010). However, the main issue of the “dry-coating” technique is the lack of sensitivity of the low abundance molecules due to poor extraction of analytes from the tissue (Goodwin

*et al.*, 2011). The formation of matrix adducts can mask the detection of a target mass and therefore the use of a deuterated matrix can help in avoiding interference while retaining the ionisation efficient of the MALDI matrix (Shariatgorji *et al.*, 2012).

**Table 1.4:** Matrix deposition techniques adapted from (Kaletas *et al.*, 2009)

<b>Technique</b>	<b>Advantages</b>	<b>Disadvantages</b>
Acoustic multi-spotter	Uniform, fast, good reproducibility	Droplet application, limited spatial resolution
Electrospray deposition	Homogenous	Limited time for analyte matrix interaction
Pneumatic Sprayer	Homogenous	Droplet size not constant
Image Prep <sup>®</sup>	Controlled conditions, automated	Droplet size not constant, expensive
Dry-coating	Cheap, high purity matrix	Poor analyte–matrix extraction
Sublimation	Homogenous, reproducible, fast	Poor analyte–matrix extraction
Desktop inkjet printer	Uniform droplets, (multichannel)	Slow and poor solvent compatibility

### 1.3.5. Mass Analysers

Technological improvements in MS instrumentation started with high throughput peptide and protein screening applications, followed by the innovative technological improvement in the field of proteomics. MSI has applied these technological developments in tissue analysis and imaging. **Table 1.5** provides an overview of the most commonly used mass spectrometers for MSI together with their characteristic performance indicators. The ions generated by the different ions sources are then detected by their mass/charge ratios ( $m/z$ ) and a range of potential detection systems are

available. Each mass analyser has its own special characteristics and applications, benefits and limitations (Jaroslav *et al.*, 2010) and the choice is based upon the application and cost. A single imaging experiment in the MS-mode can yield multiple ion images within a narrow mass range of only a few hundred Da and therefore mass analysers with high mass accuracy and resolving power are desirable. This contrasts with tandem quadrupole systems commonly used for targeted analysis but only resolving to unit mass. In terms of sensitivity, hybrid configuration of ion traps such as Qtraps, orbitraps<sup>®</sup> or triple quadrupoles in MRM mode offers great sensitivity in particular for small molecules MSI.

**Table 1.5:** Characteristic performances of different mass analysers for MSI. Adapted from (Heeren *et al.*, 2010).

<b>Analyser</b>	<b>MRP</b>	<b>Mass range</b>	<b>detection</b>	<b>PAF</b>
Quadrupoles	$10^2$ - $10^3$	0-5KDa	MRM/Sequential	>100Hz
Time of flight	$10^3$ - $10^4$	0-150KDa	Parallel	>10Hz
Trapped MS	$10^2$ - $10^3$	50Da-5KDa	Sequential	< 10Hz
FTICR-MS	$10^4$ - $10^6$	20Da-10KDa	Parallel	>1Hz

**PAF:** Pixel acquisition frequency, **TOF:** Time of flight, **FTICR:** Fourier transform ion cyclotron resonance, **MRM:** Multiple Reaction Monitoring, **MRP:** Mass Resolving Power.

### 1.3.5.1. *Quadrupole Mass Analysers*

A quadrupole mass spectrometer consists of an ioniser, an ion accelerator, and a mass filter consisting of four parallel metal rods. Two opposite rods have an applied potential of  $(U+V\cos(\omega t))$  and the other two rods have a potential of  $-(U+V\cos(\omega t))$ , where U is



a direct current (DC) voltage and  $V\cos(\omega t)$  is an alternative current (AC) voltage. The applied voltages affect the trajectory of ions travelling down the flight path centered between the four rods. For given DC and AC voltages, only ions of a certain  $m/z$  pass through the quadrupole filter and all other ions are ejected from their original path (Hoffmann *et al.*, 2001). A mass spectrum is obtained by monitoring the ions passing through the quadrupole filter as the voltages on the rods are varied. There are two methods: varying  $\omega$  and holding U and V constant, or varying U and V with (U/V) fixed for a constant angular frequency,  $\omega$ . Quadrupole mass analysers are low resolution systems often used for quantitation, with high reliability. However, their data collection at a nominal mass may be confounded by the presence of multiple species with the same average integer mass (Chernushevich *et al.*, 2001). To improve specificity in the quantitative arena, triple quadrupole and tandem mass spectrometers have been developed. These allow Selected Reaction monitoring (SRM) where a precursor ion is selected by the first quadrupole, fragmented in the second and a particular product ion selected for detection in the third quadrupole. Quadrupole systems are limited in mass range (<4000 Da), and hence suitable for imaging most drugs but not large biomolecules. If further confidence in structural identity is required or large analytes of interest, mass analysers of higher mass accuracy are used (Steen *et al.*, 2001).

#### **1.3.5.2.        *Time of flight (TOF) analysers***

In a linear mode, a time of flight mass spectrometer measures the mass-dependent time it takes ions of different masses to move from the ion source to the detector. This requires that the starting time (the time at which the ions leave the ion source) is well-

defined. Therefore, ions are either formed by a pulsed ionisation method (usually MALDI), or various kinds of rapid electric field switching are used as a 'gate' to release the ions from the ion source in a very short time (Wiley, 1956). In a reflectron mode, the ions leaving the ion source of a TOF mass spectrometer have neither exactly the same starting times nor exactly the same kinetic energies phenomena calls "chromatic aberrations". Various TOF spectrometer designs have been developed to compensate for these differences. A reflectron is an ion optic device in which ions in a TOF mass spectrometer pass through a "mirror" or "reflectron" and their flight is reversed. A linear-field reflectron allows ions with greater kinetic energies to penetrate deeper into the reflectron than ions with smaller kinetic energies. The ions that penetrate deeper will take longer to return to the detector if a packet of ions of a given  $m/z$  contains ions with varying kinetic energies, then the reflectron will decrease the spread in the ion flight times, and therefore improve the resolution of the time-of-flight mass spectrometer (Vestal *et al.*, 2005). A curved-field reflectron ensures that the ideal detector position for the TOF mass spectrometer does not vary with  $m/z$  ratio. This also results in improved resolution for time-of-flight mass spectrometers. ToF analysers offer excellent  $m/z$  resolution, with high repetition rates, ideally suited for pulsed ionisation techniques like MALDI (Laiko, 2006).

### **1.3.5.3. *Trapped-Ion Mass analysers***

This analyser employs similar principles as the quadrupole analyser mentioned above; it uses an electric field for the separation of the ions by  $m/z$ . The analyser is constructed of a ring electrode of a specific voltage and grounded end cap electrodes. The ions enter the area between the electrodes through one of the end caps. After entry, the

electric field in the cavity due to the electrodes causes the ions of certain  $m/z$  values to orbit in the space. As the radio frequency voltage increases, heavier mass ion orbits become more stabilised and the light mass ions become less stabilised, causing them to collide with the wall, and eliminating the possibility of travelling to and being detected by the detector (Stafford, 2002). The quadrupole ion trap usually runs a mass selective ejection, where selectively it ejects the trapped ions in order of increasing mass by gradually increasing the applied radio frequency voltage. This approach provides some unique capabilities, such as extended MS/MS experiments, very high resolution, and high sensitivity (Michalski *et al.*, 2011).

A relative new trapping analyser has been introduced by Makarov and co-workers called Orbitrap®. The Orbitrap® mass analyser is the first high-performance mass analyser which employs trapping of ions in electrostatic fields. Originating from an ideal Kingdon trap, Orbitrap® analyser can provide high performance analytical characteristics such as speed, mass accuracy and dynamic range, only when it is highly integrated to the ion introduction process (Zubarev *et al.*, 2013 and Makarov *et al.*, 2000).

#### **1.3.5.4. *Fourier Transform Ion Cyclotron Resonance Mass Spectrometry (FTICRMS)***

In this research, FTICR was chosen as an ultra-high resolution mass spectrometry analyser for measuring steroids and drug distribution in the targeted tissues. FTICRMS offers a unique accurate mass measurement in contrast with most triple quadrupole mass spectrometer that can only achieved integer mass accuracy leading to potential selectivity issues.

FTICRMS technique is determined by the cyclotron frequencies of ions trapped in a Penning trap. The  $m/z$  of the ions is calculated from this frequency in first approximation by the equation  $\omega = qB/m$ , where  $\omega$  is the reduced cyclotron frequency in rad/s,  $q$  the elemental charge in Coulomb,  $B$  the magnetic field in T, and  $m$  the molecular weight in kg. In FTICRMS, the ions can be generated directly inside the ion trap or externally and then transported to the ion trap. The ion trap (or ICR cell) generally consists of two trap electrodes, two excitation electrodes, and two detection electrodes **Figure 1.13** (Marshall *et al.*, 1998).

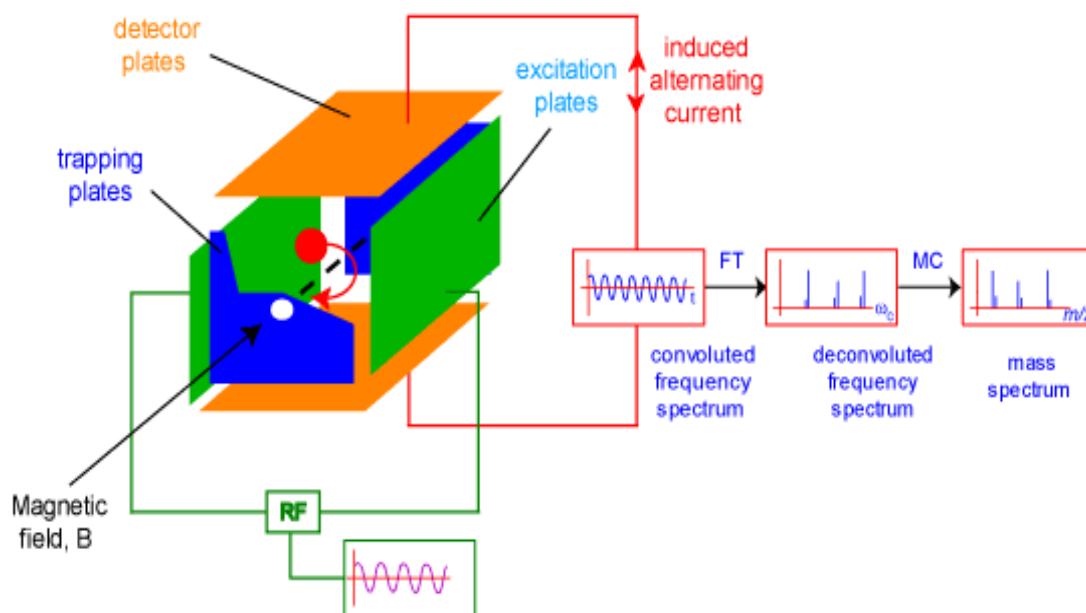


**Figure 1.13:** Representative FT-ICR-MS showing the ion trapping, detection and signal generation. Adapted from (Hendrickson *et al.*, 1996)

The trap electrodes confer the parabolic trapping potential in order to confine the ions in an axial plane. After the trapping step (which can vary from milliseconds to a few hours), the ion cyclotron motion is then excited by the application of a Rf (radio frequency) excitation pulse on the excitation electrodes. As a result, the ions experience a net outward force which causes the ions to increase their cyclotron radius. Moreover, the ion motion also becomes coherent (Yin *et al.*, 1992). The coherently orbiting ions induce a corresponding image charge in the detection electrodes. The ICR signal is measured by digitising the voltage difference between the two detection electrodes as a function of time. This signal is referred to an ICR transient. Fourier transformation of the time-domain transient results in the cyclotron frequency spectra, this frequency is then converted into mass spectra. Fourier transform mass spectrometers (FTMSs) offer several unique advantages including high mass resolving power and multistage MS/MS capabilities (Guan *et al.*, 1994).

FTICRMS has been gaining popularity in tissue imaging analysis due to the ability to trap and store ions while allowing additional ones to be introduced into the ion cyclotron resonance (ICR) cell. This phenomenon makes it possible to accumulate ions from multiple MALDI ionization events in the ICR cell during an imaging analysis prior to detection leading to an ultra-high resolution power. This increment in resolution (up to 2M) increases the selectivity of the mass accuracy down to sub-ppm levels allowing an almost unique monoisotopic mass measurement (Marto *et al.*, 1995). Continuous accumulation of selected ions (CASI<sup>TM</sup>) has been introduced by Bruker Daltonics showing very promising results with an increased in sensitivity up to 10 times in comparison with the broadband acquisition mode. This continuous mode of operation successfully separates the targeted ions (e.g. drug, metabolite, etc.) from the

intense chemical background which is generated by MALDI of tissue, thereby lowering the limit of detection for the targeted species (Ruh *et al.*, 2013). FTICRMS delivers a unique combination of high mass spectral resolution and tandem mass spectrometric capabilities. The resolution offered by FTICRMS allows the visualization of spatial details that remain hidden under lower mass spectral resolution conditions (Marshall *et al.*, 1998) .

### **1.3.6. Data processing**

Specialised software programs are used to generate distribution images of ions of specific masses from MSI data. Each sample position/spot (or pixel) on the tissue irradiated by the laser, contributes a mass spectrum containing information about the species desorbed (Caprioli, 2007). The relative intensity of a specific target molecule is plotted in each pixel, producing a molecular map. Several software packages have been used and mostly are commercially available, including Biomap® (Novartis, Basel, Switzerland) and FlexImaging® (Bruker Daltonics, GmbH) among others. The data collated can then be aligned with histological information, commonly using an adjacent tissue section.

It should be again reiterated that the displayed image is of a specified mass window, with summed abundance within that window displayed as a 2D relative abundance image. To confirm that the image generated is representative of the distribution of a target mass the most effective method is to reanalyse the samples in MS/MS fragmentation mode. This allows the parent compound to be fragmented and then relative abundance distribution of the fragments ions mapped over the sample.

### **1.3.7. Ion Suppression**

The term ion suppression was introduced originally by Buhrmann (Buhrmann *et al.* 1996). The authors described it quantitatively as  $(100 - X)/(Y \times 100)$ , where  $X$  and  $Y$  are the unsuppressed and suppressed signals, respectively (Buhrman *et al.*, 1996). Ion suppression occurs in the early stages of the ionisation process in the MALDI source. Disregarding sample cleanup, especially when complex matrices are involved, will lead to poor performance. The origin and mechanism of matrix effects are not fully understood. There are many possible sources for ion suppression, including the MALDI matrices, endogenous compounds from the tissue sections as well as exogenous substances, molecules not present in the original sample but from contamination with polymers during tissue embedding and fixation. Some other factors make a compound a prime candidate for inducing ion suppression, for example, concentration, mass, and physicochemical properties such as basicity and hydrophobicity (Goodwin, 2012).

### **1.3.8. Broadening the spectrum of MSI by on-tissue derivatisation**

It is an absolute requirement to effectively detect compounds directly from tissue sections by MALDI-MSI and the drug/analyte of interest must be ionised by the desorption and ionisation processes. However, not all drugs are amenable to ionisation as they lack chargeable moieties. Careful matrix selection and solvent composition can help to achieve the desired sensitivity, however, some drugs of interest are recalcitrant to these processes, e.g. many steroids are examples of difficult analytes to detect by MS. Derivatisation is a technique used in chemistry to transform a chemical compound into a product (the derivative) of similar chemical structure, called

a derivative. Generally, a specific functional group of the compound participates in the derivatisation reaction and transforms the precursor to a derivative of distinct reactivity, solubility, boiling point or chemical composition. The new chemical properties that result can be used for quantification or separation of the precursor. Derivatisation has been extensively used as a strategy for improving the detection of poorly ionisable molecules such as steroids for both atmospheric pressure chemical ionisation (APCI) and ESI analysis in LC/MS analysis (Higashi *et al.*, 2007; Higashi *et al.*, 2004). However, MSI in combination with on-tissue chemical derivatisation (OTCD) is still in its infancy with few cases reported (Chacon *et al.*, 2011; Manier *et al.*, 2011).

Chacon and co-workers have demonstrated the use of OTCD of a small molecule, 3-methoxysalicylamine (3-MoSA). The molecule 3-methoxysalicylamine (3-MoSA) is a scavenger of levuglandins (LGs). LGs are highly reactive towards primary amines, and form adducts with proteins and DNA, a process linked to oxidative injury, inflammation and the progression of Alzheimer's disease. Therefore, molecules such as 3-MoSA, which can scavenge LGs and prevent the formation of LG adducts, are of great interest. The study of the distribution of 3-MoSA on intact tissue by MALDI-MSI is very limited by matrix ion interference and low sensitivity. Derivatisation of 3-MoSA with 1,1'-thiocarbonyldiimidazole (TCDI) resulted in a readily ionisable oxothiazolidine derivative. TCDI treatment of tissue from mice dosed with 3-MoSA allowed pharmacokinetic profiling of this drug in different organs (Chacon *et al.*, 2011). Further OTCD approaches are required to broaden the spectrum of analytes currently readily detected by MALDI-MSI.



### 1.3.9. Quantitation

Imaging by mass spectrometry has been generally considered as a qualitative method though fundamentally, the signal generated by MSI is proportional to the relative abundance of the analyte. Therefore, with the use of properly controlled sample preparation it is possible to obtain quantitative data. The challenges arise in generating robustly prepared samples and achieving homogenous matrix application as both factors influence signal intensity. The application of a quantitation calibration curve onto vehicle control tissue, processed and analysed within the same experiment, is the simplest way to obtain quantitative information (Nilsson *et al.*, 2010). However, as localised ion suppression of analyte signal can vary across a complex tissue due to varying composition, the analysis may be improved by the use of an internal standard (e.g. stable isotope labelled analyte) within the matrix or applied to the tissue surface. The signal of the internal standard can be used to reflect the changes in ion extraction and ionisation efficiency at micrometre scale resolutions (Kallback *et al.*, 2012). For whole body tissue analysis the use of tissue-specific correction factors can also prove useful (Hamm *et al.*, 2012). Currently, data generated by MSI is cross-referenced to a gold-standard quantitative technique; drug concentrations measured by LC-MS/MS in adjacent tissue sections following homogenisation have been shown to correlate well with data generated by MALDI-MSI in several studies (Reyzer *et al.*, 2003). A quantitative method for elemental bio-imaging by laser ablation-inductive plasma MS (LA-ICP-MS) has been proposed by Becker and colleagues, using the 'matrix-matched' approach where quantitation is carried out using certified standards in the corresponding biological matrix; this approach compensates for any matrix ion

suppression effects (Becker *et al.*, 2007). Such approaches can be anticipated to be more readily accepted by regulatory authorities.

### **1.3.10. MSI of steroids**

MS is widely used for steroid quantification in plasma. Regarding MSI, the distribution of cholesterol, chemically similar to steroids, has been imaged in brain (Malmberg *et al.*, 2013) and in liver (Winograd *et al.*, 2010), while corticosteroids and androgens have been detected in a non-biological matrix by cation-enhanced nanostructure-initiator mass spectrometry (CA-NIMS) (Patti *et al.*, 2010). However, localisation of endogenous neutral steroids in biological tissues by MSI has not been yet reported. MSI of steroids is challenging, not only because of their relatively low abundance, but also because of their lack of either hydrogen donor or acceptor moieties, resulting in poor ionization yields during MALDI. Furthermore, steroids are susceptible to ion suppression by tissue components, such as lipids and proteins. Although steroids can be ionised by conventional ESI or atmospheric pressure chemical ionisation (APCI) (Singh G, 2000), detection in the low sub-pg range in tissues is largely out of reach, and these quantitative approaches do not offer two-dimensional imaging. For ESI, derivatisation (Higashi *et al.*, 2004) enhances the ionisation efficiency of neutral corticosteroids, for example using Girard reagents (Higashi *et al.*, 2007) . Similar approaches have allowed Girard P (GirP) derivatives of oxysterols to be detected with fmole sensitivity in rat brain homogenates using MALDI (Griffiths *et al.*, 2011). The recent innovation of OTCD (Chacon *et al.*, 2011; Manier *et al.*, 2011) has paved the way for application of derivatisation techniques to MSI for investigation of tissue steroids.

## 1.4 Aims and hypothesis

### *Hypothesis*

We hypothesise that tissue imaging using mass spectrometry allows high-resolution dissection of tissue steroid levels, potentially at near cell-type-specific resolution, that will provide a step change in our understanding of the consequences of altered glucocorticoid metabolism.

### *Aims*

The overall aim of this Thesis is to optimise the MALDI-FTICR-MSI for steroid analysis and provide proof of principle for its utility for pharmacodynamics and for investigating the pathophysiology of disrupted glucocorticoid metabolism. The specific aims during this work were:

**Chapter 3:** To develop and optimise a MALDI-FTICRMS MSI platform for detection of endogenous glucocorticoids in tissue.

**Chapter 4:** To apply the optimised MALDI-FTICR-MSI platform for the assessment of the spatial distribution of endogenous steroids in murine and human tissue sections.

**Chapter 5:** To monitor the effects of 11 $\beta$ -hydroxysteroid dehydrogenase-1 (11 $\beta$ -HSD1) deficiency or inhibition on region-specific corticosteroids concentration in brain.

**Chapter 6:** To apply the OTCD-MSI platform to measure the contribution of tissue-specific cortisol regeneration in the brain using a stable isotope tracer, 9,11,12,12[<sup>2</sup>H]<sub>4</sub>-cortisol (d<sub>4</sub>F).

**Chapter 7:** Summary of finding and future perspectives

# Chapter 2

## Material and Methods

### 2.1 Chemicals

All chemicals used were analytical reagent grade and from Sigma-Aldrich (UK) unless otherwise stated. Isotope tracer ( $^4\text{H}$ -9,11,12,12)<sub>4</sub>-cortisol ( $\text{d}_4\text{F}$ ) (purity 98-99%), ( $^3\text{H}$ -9,12,12)<sub>3</sub>-cortisol ( $\text{d}_3\text{F}$ ) and Internal standard (ISTD) corticosterone ( $^8\text{H}$ -2,2,4,6,6,17 $\alpha$ ,21,21)<sub>8</sub> ( $\text{d}_8\text{-CORT}$ ) (purity 95-97%) were from Cambridge Isotopes; MA, USA and 11DHC from Steraloids Inc (PA, USA), UE 2316, [4-(2-chlorophenyl-4-fluoro-1-piperidinyl) [5-(1H-pyrazol-4-yl)-3-thienyl]-methanone and UE 2346 [4-(4-chlorophenyl-4-fluoro-1-piperidinyl) [5-(1H-pyrazol-4-yl)-3-thienyl]-methanone were synthesised by High Force Ltd, York, UK (Sooy *et al.*, 2010). Conductive indium tin-oxide (ITO)-coated glass slides were from Bruker Daltonics (Bremen, GmbH). Solvents were glass-distilled HPLC grade (Fisher Scientific, Loughborough, UK). 4-Chloro- $\alpha$ -cyanocinnamic acid (Cl-CCA) was synthesized in-house as explained in **Appendix I** (Jaskolla *et al.*, 2008).

### 2.2 Animals tissue

All animals were housed in the Biological research facility, University of Edinburgh, Edinburgh, UK and studied under protocols approved by the UK home office. Licensed procedures were performed under the UK Animals (Scientific Procedures) Act, 1986 by either Dr A Livingstone (PIL 60/5467) or Dr A McBride (PIL 60/1344) and under Project license PPL60/3962 JR Seckl Sept 2009. In all studies, animals were killed by

decapitation at 9.00 am; plasma was prepared from trunk blood, collected in EDTA and stored at -80°C until analysis. Tissues were snap frozen in liquid nitrogen and stored (-80°C).

### **2.3 Sectioning of tissues**

Sections of tissues was carried out using cryostat cleaned to ensure the absence of optimum cutting temperature (OCT) mountant (Leica Microsystems Inc, Bannockburn, IL, USA) and tissues were embedded in gelatine solution (50%w/v). Rodent brain (coronal/horizontal); adrenal, kidney, testis, prostate and human biopsies (horizontal cryosections (10 µm) were cut and frozen (-80°C). For quantitation, a sampling protocol to combine MSI, histology and quantitation was used as previously described by Koeniger (Koeniger *et al.*, 2011). Briefly: (1) fifteen tissue sections (50 µm thick) were collected for confirmatory quantitation; (2) two adjacent sections were thaw mounted onto glass slides (Superfrost, Thermo Scientific, Braunschweig, Germany) and retained for histological examination; (3) four adjacent sections for MSI/LESA (10 µm) were thaw mounted onto a conductive indium tin-oxide (ITO)-coated glass slides (Bruker Daltonics, Bremen, GmbH) pre-coated with Girard-T (GirT) reagent (0.15 mg/cm<sup>2</sup>) and further sections for histology (x 2) and confirmatory quantitation (x 15) were harvested as above. Tissue sections for confirmatory quantitation were combined, weighed at room temperature (RT) and stored at -80°C until LC-MS/MS analysis. Tissue sections for MSI were stored in a vacuum desiccator (RT, 1 h) and then at -80°C.

## **2.4 Histological staining**

Cryosections were stained using haematoxylin and eosin as follows: Tissues were fixed in cold acetone (chilled with wet/ice for 60 min). After fixation, tissues were rehydrated with ethanol (EtOH) 70 % (3 min), then rinsed in distilled water (5 min), stained using haematoxylin (10 % alcoholic Harris hematoxylin solution) (6 min) and rinsed in running tap water for 20 min. Tissues were submerged in acid alcohol (70 % ethanol, 1 % hydrochloric acid) (1 second (s)) for decolourisation, rinsed well in tap water (5 min) and counterstained in Eosin (1% in water) for 15 s. Tissues were then dehydrated using EtOH 95 % (3 min) (twice) and finally EtOH 100 % (3 min). Tissues were then cleared in xylene (2 x 5 min), and mounted with cytooseal in a fume hood prior to histological evaluation. Tissue sections were examined using an optical microscope (40 X, Leica Microsystems Inc, Bannockburn, IL, USA) with CCD camera (Hitachi model 3969, Japan).

## **2.5 On-tissue chemical derivatisation (OTCD)**

From -80°C, tissues were allowed to dry in a vacuum desiccator (20 min). ITO glass slides were coated with (GirT) solution (20 mg/mL) in methanol (approx. 10 mL per slide with a nitrogen flow of 7.5 L/min at a distance of 7 cm from the slide) using an artistic airbrush (Nozzle diameter 0.3 mm; AirArt, London, UK). Each manual pass took approximately 1 s and the process was repeated with 5-10 s between passes until a uniform coating of derivatisation reagent ( $0.15 \text{ mg/cm}^2 \sim 2.1 \text{ mg per slide}$ ) (pre-coated slides). For post-coating, GirT (5 mg/mL) in methanol + 0.2 % v/v TFA containing 0.1  $\mu\text{g}$  of  $d_8\text{CORT}$  (ISTD) was applied by an artist's airbrush (AirArt, model highT40, London, UK) (4 mL per slide with a nitrogen flow of 5.5 L/ min at a distance of 10 cm

from the MALDI target). Each manual pass took approximately 1 sec and the process was repeated with 2-5 s between passes until a uniform matrix coating was achieved on the tissue section. For pre-coated, slide was sprayed with 3 mL of methanol+ 0.2 % v/v of trifluoroacetic acid (TFA) containing 0.1 µg of d<sub>8</sub>CORT (ISTD). Then, for both pre-coated and post-coated, the slide was placed in a sealed container (reaction chamber) containing a saturated solution of potassium chloride to create a moisturising-controlled reaction environment. The tissue was incubated (60 min, 40 °C) in an oven or water bath and then allowed to cool and dry in a vacuum desiccator (RT, 15 min) to remove the condensed water prior to matrix deposition. For tissue homogenate/plasma analysis, the extract was re-constituted in 100 µL of GirT (5 mg/mL) in methanol and derivatised by incubation (60 min, 40 °C) in an oven or water bath.

## **2.6 Matrix application**

Matrix (CHCA; 10 mg/mL) in acetonitrile (80 % + 0.2 % v/v TFA) was applied by a pneumatic TLC sprayer (20 mL per slide with a nitrogen flow of 7.5 L/ min at a distance of 20 cm from the MALDI target). Each manual pass took approximately 1 s and the process was repeated with 5-10 s between passes until a uniform matrix coating was achieved on the tissue section. The tissue section was then allowed to dry at RT and stored in a desiccator until analysis.

## **2.7 Instrumentation for Mass Spectrometry**

MSI was performed using a 12T SolariX MALDI-FTICRMS (Bruker Daltonics, MA, US) employing a Smartbeam 1 kHz laser, with instrument control using SolariX control v1.5.0 (build 42.8), Hystar 3.4 (build 8) and FlexImaging version 3.0 (build 42).

On-tissue collision-induced dissociation was carried out by Liquid extraction surface analysis (LESA)-nanoESI-FTICRMS using Triversa nanomate<sup>®</sup> (Advion, NY, USA) using software chip-soft version 3.0 (build 18). Cl-CCA synthesis was monitored using a ZMD single Quad (Micromass, Mancehester, UK) with MassLynx version 3.1 Build 324. Confirmatory liquid chromatography-tandem MS (LC-MS/MS) analysis was performed using a triple-quadrupole linear ion trap mass spectrometer (QTRAP 5500, AB Sciex, Cheshire, UK) coupled with an ACQUITY ultra high pressure liquid chromatography (UPLC; Waters, Manchester, UK). Data was acquired using Analyst software version 1.5.1 Build 5218.

## **2.8 MALDI-FTICR analysis**

### **2.8.1 MSI**

Optical images were taken using a flatbed scanner (Canon LiDE-20, Canon, UK). MSI analysis was performed using 250 laser shots, with a laser spot diameter of ~50  $\mu\text{m}$  and laser power was optimized for consistent ion production. Ions were detected between  $m/z$  250 and 1500, yielding a 1 Mword time-domain transient, and with a laser spot raster spacing of 100 – 300  $\mu\text{m}$  unless otherwise stated. For constant accumulation of selected ion (CASI<sup>TM</sup>) MSI analysis was conducted using 1000 laser shots with a frequency of 1000 Hz. Ions were detected at  $m/z$  470 using an isolation window of 50 Da, yielding a 2 Mword time-domain transient. MSI data were subject to vector normalization method (RMS) for broadband detection (250 to 1500 Da) mode and window normalization using d<sub>8</sub>CORT protonated mass at  $m/z$  468.36726 with 0.9995 as ICR noise reduction threshold. Mass precision was typically  $\pm$  0.025 Da. Internal calibration was performed using a (CHCA) matrix cluster ion at  $m/z$  417.04834



(broadband) and  $d_8$ CORT quasimolecular ion (CASI<sup>TM</sup>). Average abundances were determined by defining specific regions of interest (ROI). A measure of the average abundance was then assigned from the summed spectra. Neutral, derivatised steroids and drug-like molecules were monitored at the corresponding protonated mass described in the **Table 2.1**

### **2.8.2 Tissue spotting**

CHCA (20  $\mu$ L, 10 mg/mL in 6:4, ACN: H<sub>2</sub>O containing 0.2% TFA) was added to the sample extract and vortex-mixed and 1  $\mu$ L applied onto a MALDI stainless steel plate. MALDI analysis was performed at 2 Mword time-domain transient in broadband mode (neutral steroids) and in isolation mode (470.3 $\pm$ 50 Da) for 10 s at 500 laser shots at 800 Hz for GirT-derivatised steroids. Corresponding ratios of ion intensity were calculated from the sum of 10 spectra.

**Table 2.1:** Molecular weights and masses of ions of steroids and Girard-T derivatives

<b>Compound</b>	<b>Mw</b>	<b><i>m/z</i> (<i>M+H</i>)<sup>+</sup></b>
Corticosterone (CORT)	346.219	347.222
11-dehydrocorticosterone (11DHC)	344.199	345.206
UE2316	389.080	390.084
<b>Charged Girard-T (GirT) derivatives</b>	<b><i>m/z</i> (<i>M</i><sup>+</sup>)</b>	
GirT-CORT	460.317	
GirT-11DHC	458.301	
GirT-7ketocholesterol (GirT-7KC)	514.437	
GirT-Cortisol (GirT-F)	476.312	
GirT-Cortisone (GirT-E)	474.296	
GirT-Androstenedione(GirT-A4)	400.292	
GirT-dehydroepiandrosterone ( GirT-DHEA)	402.312	
GirT-testosterone (GirT-TESTO)	402.312	
GirT-dihydrotestosterone (GirT-DHT)	404.322	
GirT-d <sub>4</sub> Cortisol (d <sub>4</sub> F)	480.337	
GirT-d <sub>3</sub> Cortisol (d <sub>3</sub> F)	479.331	
GirT-d <sub>4</sub> Cortisone (d <sub>3</sub> E)	477.298	
GirT-7 $\alpha$ ,27-dihydroxy-4-cholesten-3-one (GirT-(VII))	530.432	
GirT-7 $\alpha$ -hydroxy-4-cholesten-3-one one (GirT-(IV))	514.444	

## 2.9 Liquid extraction surface analysis (LESA)

Steroids within tissue sections were derivatised as previously described in **section 2.5** and analysed immediately using LESA-nanoESI-FTICRMS as follows: solvent (methanol: water, 50:50 with 0.1% v/v of formic acid); pick-up volume, 1.5  $\mu$ L; dispense volume, 1.2  $\mu$ L at 0.2 mm away for surface; droplet rest time (delay), 5 s; and aspiration volume of 1.4  $\mu$ L at 0.1 mm away from surface. ESI-FTICRMS was

performed using the 12T SolariX dual source (ESI-MALDI) with SolariX control v1.5.0 (build 42.8). Ions were isolated at  $m/z$  470.3 $\pm$ 50Da (11 $\beta$ -HSD-1 manipulation studies) and  $m/z$  470.3 $\pm$ 20Da (deuterated tracer studies) for 30 s yielding a 2 Mword time-domain transient. Collision induced dissociation (CID) fragmentation was carried out at 28 eV.

## **2.10 Statistical analysis**

Data are expressed as mean  $\pm$  SEM and differences were analyzed using two-way ANOVA with Bonferroni's post-hoc test. Statistical significance was accepted at  $p < 0.05$ . Statistical calculations were performed using Statistica® version 8.0, StatSoft, Inc. Tulsa, OK, USA.

## Chapter 3

# Development and optimisation of a MALDI-FTICRMS MSI platform for glucocorticoids

### 3.1. Introduction

Mass spectrometry imaging (MSI) has emerged as a new modality that allows the rapid detection, localisation, and identification of many species, identified by the mass of the free ions in high vacuum, originating from the most complex biological sample surfaces (Caprioli *et al.*, 1997). To date, the distribution of cholesterol, chemically similar to steroids, has been imaged in brain and in liver while corticosteroids and androgens have been detected in a non-biological matrix by cation-enhanced nanostructure-initiator mass spectrometry (Patti *et al.*, 2010). However, localisation of endogenous neutral steroids in biological tissues by MSI is challenging, not only because of their relatively low abundance, but also because of their lack of either hydrogen donor or acceptor moieties, resulting in poor ionisation yields. Furthermore, in biological tissues, steroids are susceptible to ion suppression by more abundant molecules, such as lipids and proteins. Although steroids can be ionised by conventional electrospray or APCI, detection in the low sub-pg range in tissues is largely out of reach, and these quantitative approaches do not offer two-dimensional imaging. For electrospray ionization (ESI), derivatization enhances the ionisation efficiency of neutral corticosteroids, achieved for example using Girard reagents

(Higashi *et al.*, 2007). Similar approaches have allowed Girard P (GirP) derivatives of oxysterols to be detected with fmole sensitivity in rat brain homogenates using MALDI (Griffiths *et al.*, 2011) and have enhanced sensitivity for cholesterol analysis using N-alkylpyridinium isotope quaternisation in analysis of human hair homogenate by (MALDI-FTICRMS) (Fuchs *et al.*, 2007). The recent innovation of on-tissue chemical derivatization (OTCD) has paved the way for application of derivatisation techniques to MSI for investigation of tissue steroids (Chacon *et al.*, 2011).

In this chapter, the application and method development of OTCD for the detection of CORT and 11DHC, active product and inert substrate of the enzyme, 11 $\beta$ -HSD-1, in biological tissue sections will be described. MALDI-FTICRMS was used as the MSI platform of choice due to its unique selectivity and sensitivity achieved by its high mass resolution power. Tissue preparation, matrix selection, derivatisation screening, reaction conditions, deposition techniques and MS parameters were optimised to achieve the best possible sensitivity.

## **3.2. Methods**

### **3.2.1. Biological tissue sections**

Adrenal glands (horizontal section) from Sprague Dawley male rats (5-7 weeks, ~175-200 g) and murine brains (horizontal sections) from C57Bl/6j (12 weeks) ~25-30 g mice were prepared as described in section 2.3.

### **3.2.2. Imaging of un-derivatised steroids in tissues**

#### **3.2.2.1. Comparison of responses of standards measured off- and on-tissue**

Standards of both CORT and 11DHC (10 µg 1 µg/µL) of each steroid were mixed with CHCA solution (10 µL of 10 mg/mL in 50:50 (acetonitrile: water) + 0.2 % v/v TFA) and 1 µL was spotted on a MALDI ITO slide (n=3) (**standards off-tissue**). Sample preparation was carried out using the standard dried droplet method. The sample (steroid standard) was mixed with the matrix solution, deposited on the ITO MALDI slide and dried. Following the same procedure, 1 µL of the (steroid: matrix) solution was spotted onto a murine mouse brain section (n=3) (**Standards on-tissue**) and analysed by MALDI-FTICRMS as described in **section 2.8.2**.

#### **3.2.2.2. Adrenal gland and murine brain imaging**

MSI was performed on rat adrenal gland and murine brain tissue sections. After preparing a cryosection (10 µm), tissue was thaw-mounted on an ITO-MALDI slide and coated with CHCA as described in **section 2.6**. FTICRMS was used in broadband mode and heat maps of both CORT and 11DHC were generated extracting the ions of both steroids at  $m/z$  345.20826 and 347.22385 respectively.

### 3.2.3. Screening of matrices

$\alpha$ -Cyano-4-hydroxycinnamic acid (CHCA), 4-chloro- $\alpha$ -cyanocinnamic acid (Cl-CCA), 2,5-dihydroxybenzoic acid (DHB), 2-(4'-cydroxybenzeneazo) benzoic acid (HABA): 3-indole acetic acid (IAA), ferulic acid and Buckminsterfullerene (C<sub>60</sub>) were screened as potential matrices for neutral corticosteroids. Matrix assessment was carried out by quantifying signal from spots of steroids. In this case, d<sub>8</sub>CORT (1  $\mu$ g, 0.1 mg/mL) in methanol: water (1:1) (n=3 per matrix) was mixed with the selected MALDI matrices (300  $\mu$ g, 10 mg/ml in 50:50 (acetonitrile: water) with 0.2 % TFA except for C<sub>60</sub> where toluene was used. 1  $\mu$ L was manually spotted on a MALDI stainless steel plate and allowed to dry at RT (dried-droplet technique) and analysed by MALDI-FTICRMS as described in **section 2.8.2**.

### 3.2.4. Derivatisation screening

Derivatisation screening was performed off- and on-tissue using CORT and 11DHC as control standards. CORT (10 ng, 1  $\mu$ g/mL) and ISTD (d<sub>8</sub>CORT) (10 ng, 1  $\mu$ g/mL) were added to a 2 mL Eppendorf tube containing 100  $\mu$ L of derivatisation reagents (aminoguanidine, dansyl chloride, sulfonyl chloride, isonicotinoyl chloride, ferrocene azide, dansyl hydrazine, GirT and GirP (5 mg/mL in methanol with 1% of TFA), the solution was mixed and allowed to react (3 h, 40 °C) using a rotating water bath. After derivatisation, an aliquot of 30  $\mu$ L was mixed with of CHCA (50  $\mu$ L, 10 mg/mL, 0.2% TFA); 1  $\mu$ L was used for MALDI-FTICRMS analysis using a dried-droplet technique as described in **section 2.8.2**. The intensity was normalised against that of derivatised d<sub>8</sub>CORT.

### **3.2.5. Optimising on-tissue derivatisation conditions**

Optimisation of reaction conditions was performed using a control tissue section with spots (5 ng, 10 µg/mL; methanol: water (1:1) of d<sub>8</sub>CORT applied to the surface manually (n=3 per condition). CORT and 11DHC were also applied as spots to a tissue-free region as controls. Spots were allowed to dry, then GirT (1 µL; 5 mg/mL) in different solvent systems (methanol and ethanol with TFA 0.2 % v/v, formic acid (FA) 0.2 %v/v, acetic acid (HA) 10 %v/v (freshly prepared)) was deposited on top. The MALDI glass slide was placed in the reaction chamber and incubated (20, 60 or 120 min, 40 °C), then allowed to cool and dry in a vacuum desiccator (RT, 20 min). Matrix CHCA (10 mg/mL; (80 %)) in acetonitrile + 0.2 % v/v TFA) was applied by a pneumatic TLC sprayer (20 mL per slide) and allowed to dry (RT) and stored in a desiccator until MALDI-FTICRMS analysis as described in **section 2.8.2**.

### **3.2.6. Limits of Detection (LODs) of GirT derivatives of glucocorticoids applied to the surface of tissue**

LODs were assessed using standards (CORT, 11DHC) applied to slides "off-tissue" and deuterated standard (d<sub>8</sub>CORT) applied to the tissue (murine brain, kidney and liver) surface as spots "on-tissue" using a dilution series of both steroids in methanol to achieve a range of 10 µg to 100 pg/spot for neutral steroids and 1 ng to 0.01 pg/spot for GirT-derivatives (n=3 spots per concentration). Matrix was applied and slides imaged by MALDI-FTICRMS as described in **section 2.8.1**. The ratios (CORT/11DHC) were estimated. The estimated LODs and LODs of GirT derivatives were estimated using the S/N (signal/noise) criteria of (S/N>3) for LOD and (S/N>10) for LOQ.



### **3.2.7. Stability of derivatised steroids**

The GirT-CORT standard was prepared as reported previously by reaction of GirT and the corresponding steroid in a 1:1 molar ratio, in a 10 % v/v acetic acid solution in methanol. The reaction was incubated (3 h, RT). The derivative was extracted in toluene: dichloromethane (1:1) and the solvent evaporated to dryness. The residue was reconstituted in methanol, characterised using accurate mass measurement and storage until MALDI-FTICRMS analysis. On-tissue stability studies were performed using a control tissue section manually spotted with GirT-CORT standard solution (10 µg/mL, 5 ng) in methanol: water (1:1). Spots (n=3, per time) were allowed to dry at RT. The matrix CHCA was applied using a pneumatic TLC sprayer (25 mL per slide) immediately after reaction (T= 0, 10, 20 and 30 min, RT) to evaluate the stability of the hydrazone derivative on the tissue. MALDI-FTICRMS analysis was performed as described in **section 2.8.2**.

### **3.2.8. Screening of matrix solvents for TLC-based matrix deposition methods**

Screening of solvents for the matrix was conducted in order to evaluate analyte extraction during matrix deposition by spray coating. Immediately after the derivatisation, matrix was applied using acetonitrile: water or methanol: water in proportions ranging from 1:1 to 9:1 with 0.2 % v/v TFA as solvents. Matrix deposition was performed as described in **section 2.7**. MALDI-FTICRMS analysis was performed as described in **section 2.8.1**.

### **3.2.9. Optimisation of derivatisation reagent application and saturation studies**

Pre-coating and saturation studies were performed to assess diffusion of the GirT derivatives, ion suppression and reaction yields using adrenal gland sections. Adrenal gland sections (10  $\mu\text{m}$ ) were cut (horizontal) from frozen ( $-80\text{ }^{\circ}\text{C}$ ) as previously and thaw-mounted on an ITO-MALDI target previously coated (pre-coated) with GirT reagent (0.08, 0.15, 0.30 and 0.60  $\text{mg}/\text{cm}^2$ ). Post-coating (controls) was carried out as described in **section 2.5** with 2, 4, 6, 8 mL of a 5  $\text{mg}/\text{L}$  of GirT. Steroids within tissues were derivatised followed matrix deposition a (**section 2.6**) described in **section 2.5**. MALDI-FTICRMS analysis was performed as described in **section 2.8.1**.

### **3.2.10. Sublimation as a matrix deposition methodology**

Sublimation was performed in Sublimation apparatus 8023 (Ace Glass, Vineland, NJ). A key component of the device was the flat bottom condenser to which the glass cover slips or MALDI plate inserts could be fixed using double sided thermally conductive tape (3M, St. Paul, MN). Matrix CHCA (300 mg) was added to the bottom section of the apparatus; the two pieces were assembled with an O-ring seal and connected to a direct drive vacuum pump (8  $\text{m}^3/\text{h}$ ). After 15 min at reduced pressure, the condenser was filled with cold water ( $15\text{ }^{\circ}\text{C}$ ). After five additional min, heat was applied to the base of the sublimator via a heating mantle covered with a sand bath, the temperature was monitored using a thermocouple, and time was measured from the onset of heat application. The sublimation of the solid matrix gradually progressed upon application of heat. The variable voltage regulator was set to 200 V and the temperature of the heating mantle increased gradually from 25 to  $120\text{ }^{\circ}\text{C}$  over 25 min. The deposition of

matrix was visually observed to slowly move up the sides of the glassware to the level of the sample plate. Optimization of the amount of matrix that condensed onto the tissue was empirically determined by adjusting the following parameters: temperature at the condenser, amount of matrix, heat applied to matrix, and time of sublimation. The optimal amount of matrix recommended by Hankin *et al.*, 2007 and Caprioli *et al.*, 2005 is 0.17-0.22 mg/cm<sup>2</sup>. Use of a period of 20–25 min from the onset of heat application resulted in a thin uniform layer of matrix. Adrenal gland tissue sections were coated with CHCA (n=4) with 0.18 mg/cm<sup>2</sup>. Adjacent tissue sections were post-coated as described in **section 2.5** as controls. After this time, the heat and condenser coolant were both removed, and the system was allowed to return to room temperature while still under vacuum. Once equilibrated (RT), the system was returned to ambient pressure, opened, and the sample plate was carefully removed from the sublimation condenser and transferred to a MALDI plate holder for analysis by MALDI-FTICRMS. After sublimation, one slide was placed in a recrystallisation chamber (same as for derivatisation, **section 2.5**) containing 3 ml, 1:1 methanol: water with 1 % v/v FA for 5 s at 90 °C and then stored in a desiccator prior to MALDI-FTICRMS analysis as per **section 2.8.1**.

### **3.2.11. Tissue washing**

From -80 °C, control tissues (adrenal gland) were allowed to dry in a vacuum desiccator (20 min). The tissue contours were highlighted using a hydrophobic pen (Steindler, CT, USA) to hold the washing solution on top of the tissue sections. Targeted tissue sections were covered with chilled solutions of ammonium formate (5 mM, pH4) and ammonium acetate (5 mM, pH7) using a glass pipette. The solution was

retained (3 s) and the content drained using a small glass pipette. This procedure was repeated ten times and then the tissues were allowed to dry in a vacuum desiccator (15 min) prior on-tissue derivatisation as in **section 2.5**, followed by matrix application as described in **section 2.6**.

### 3.3. Results

#### 3.3.1. Characterisation of MALDI-FTICRMS spectra of neutral steroids

Method development started with characterisation of the mass spectra of CORT and 11DHC by MALDI-FTICRMS. Standards were manually applied onto a stainless-steel MALDI plate by the dried-droplet technique using CHCA as MALDI matrix. For both steroids, protonated masses  $[M+H]^+$  ions were the most abundant species detected at  $m/z$  347.22889 and  $m/z$  345.20385 respectively, in close agreement with the monoisotopic theoretical masses at  $m/z$  347.22169 and  $m/z$  345.20604 respectively. Fragment ions such as those formed by water loss  $[M-H_2O+H]^+$  and alkaline (A) adducts  $[M+A]^+$  were not observed (**Figure 3.1**).

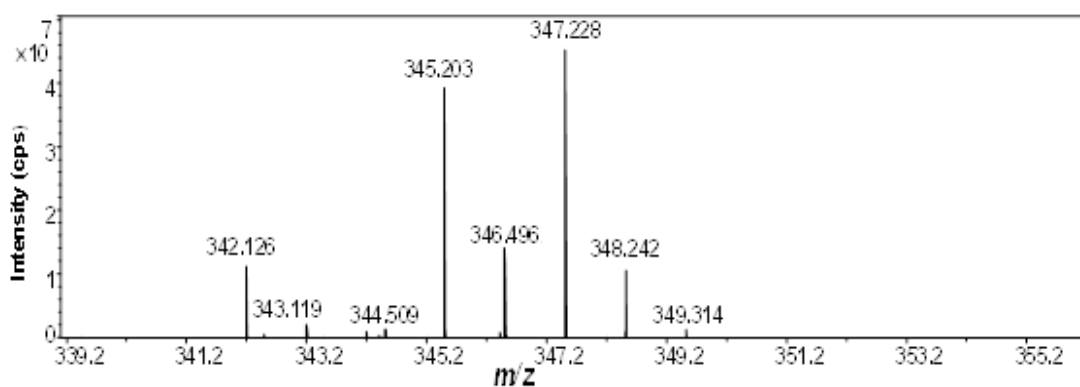


**Figure 3.1:** MALDI-FTICRMS of neutral steroids standards. Both steroids showed their corresponding protonated masses  $[M+H]^+$  as the most abundant species detected at  $m/z$  347.228 (CORT) and  $m/z$  345.203 (11DHC) respectively **cps**: count per second.

### 3.3.2. MALDI-FTICRMS of neutral steroids enriched in tissue homogenates

Murine brain homogenates were enriched with steroid standards and compared with standards in matrix only for evaluation of the ion-suppression effects and specificity. When standards of steroids were added to murine brain homogenates followed by matrix application as described in **section 2.6** the same spectra were observed as standards alone and interferences of isobaric ions from the matrix were not observed (**Figure 3.2**)

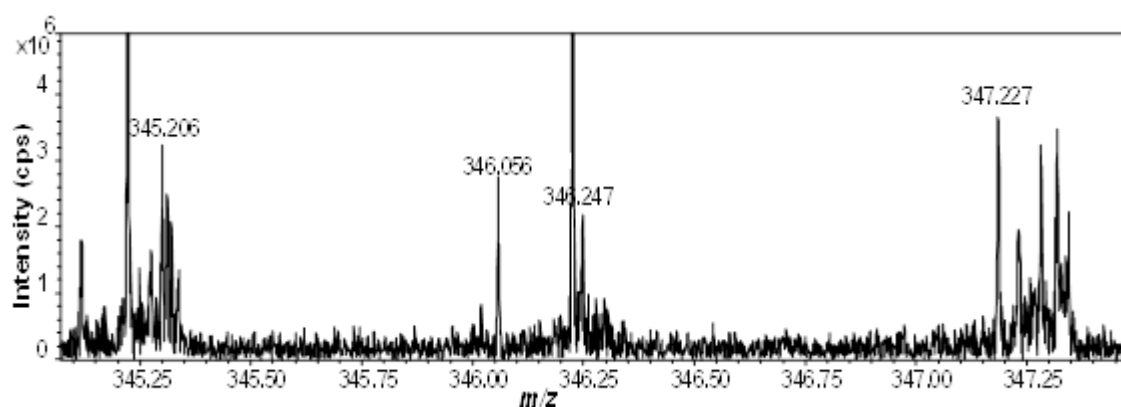


**Figure 3.2:** MALDI-FTICRMS of neutral steroids standards spiked into a murine mouse brain. Both steroids showed their corresponding protonated masses  $[M+H]^+$  as the most abundant species detected at  $m/z$  347.227 (CORT) and  $m/z$  345.206 (11DHC). Interferences from isobaric ion were not observed. cps: count per second.

The LODs on- and off-tissue were found to be  $\sim 30$  ng (off-tissue) and  $1\mu\text{g}$  (on-tissue) for both steroids, as the response factor for CORT and 11DHC was close to 1. However, the signal of the standard was considerably suppressed by the presence of tissue. These LODs were considered to be well in excess of the anticipated endogenous physiological levels (nM range).

### 3.3.3. Tissue imaging of un-derivatised steroids in murine adrenal gland

An attempt was made to detect endogenous CORT and its 11-dehydro metabolite directly from a tissue section by MALDI-MSI. Adrenal glands from Sprague-Dawley rats and murine brains were selected as representative tissue sections, with the adrenal gland anticipated to possess the highest levels of steroids at their sites of synthesis. Moreover, the adrenal gland is a good tissue to use as a control tissue section to detect diffusion, as it has defined histological zones where steroids would be expected to cluster. Initial attempts at imaging corticosteroids in rat adrenal gland, and murine brain, monitoring the  $[M+H]^+$  ions of the glucocorticoids of interest, yielded ions with mass accuracy of -3.2 ppm (CORT) and -18.3 ppm (11DHC) (**Figure 3.3 (a-c)**) but with signal/noise (S/N) values of 5 and 7 respectively, reflected in a poor quality MS image for adrenal gland (**Figure 3.3 e,f**) and for brain (**Figure 3.3 h,i**).

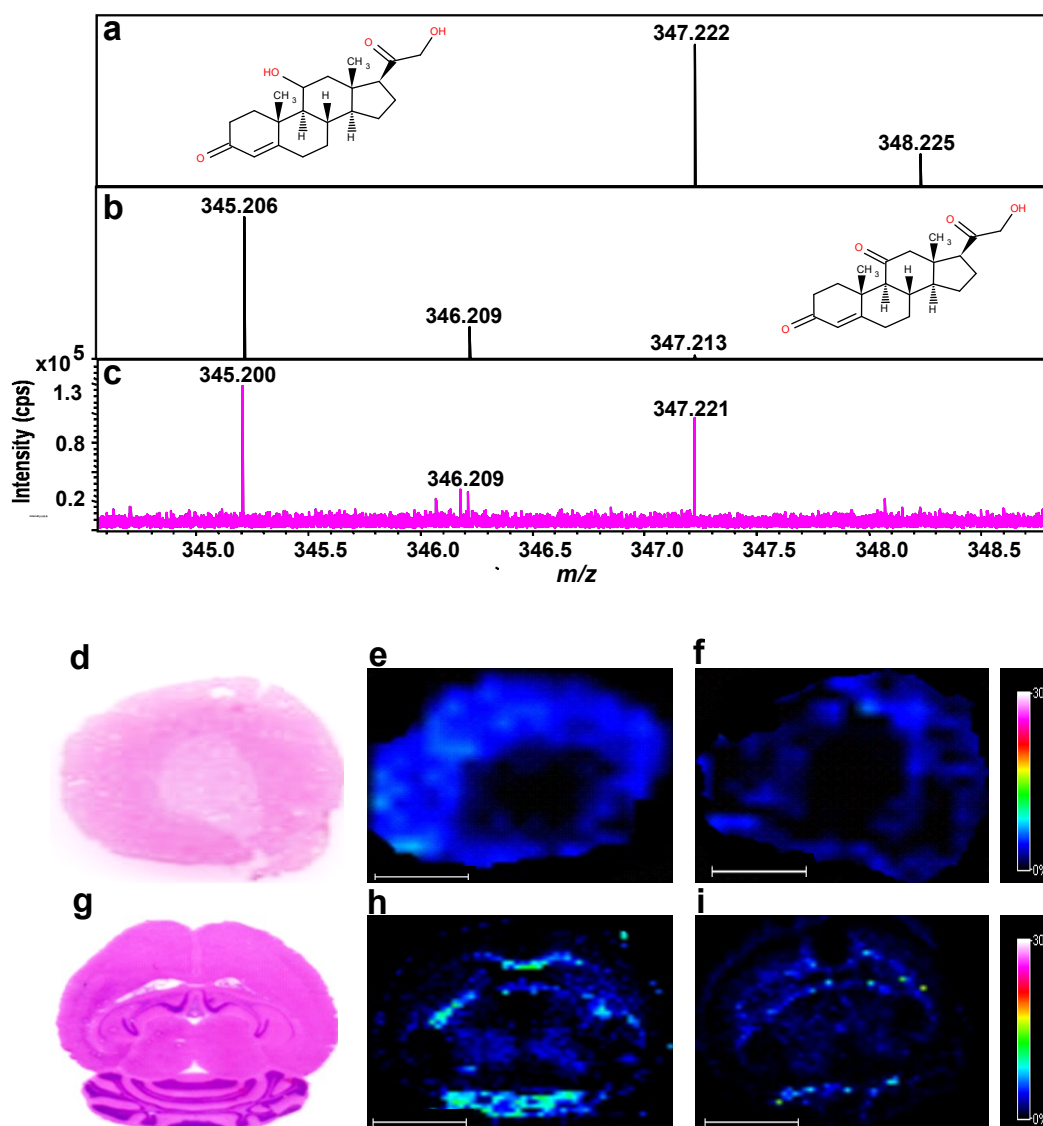


**Figure 3.3:** MALDI-FTICR-MS imaging (MSI) of neutral steroids in rat adrenal gland sections. MSI of neutral glucocorticoids using  $\alpha$ -cyano-4-hydroxycinnamic acid (CHCA) as matrix showed very low ionisation yields in both adrenal and brain tissue sections. Simulated theoretical isotopic distribution pattern of: (a) corticosterone (CORT); and (b) 11-dehydrocorticosterone (11-DHC). (c): MALDI-FTICRMS spectra of adrenal gland of neutral corticosteroids of corticosterone at  $m/z$  347.221 Da and 11-dehydrocorticosterone at  $m/z$  345.200 Da. (d) Histological image of adrenal gland stained with haematoxylin and eosin. MSI heat map distribution of: (e) CORT at  $m/z$  347.222 Da; and (f) 11DHC at  $m/z$  345.206 Da in rat adrenal gland. (g) Histological image of murine brain stained with haematoxylin and eosin. MSI heat map distribution of: (h) CORT at 347.222 Da; and (i) 11DHC at  $m/z$  345.206 Da in murine brain. Signal intensity is depicted by colour as per the scale shown. cps: count per second. Scale bar (2 mm) for adrenal section and (5 mm) for brain section.



### **3.3.4. Attempts to improve imaging of un-derivatised steroids**

To improve images of neutral steroids in tissues, a number of approaches were pursued to enhance their low intensity signal.

#### **3.3.4.1. *MALDI matrix screening***

Screening was performed using both standard and novel matrices, to identify reagents which may enhance energy transfer and facilitate desorption and ionisation efficiency. To improve the quality of the MS image, alternative matrices must possess better qualities in terms of spatial resolution (crystal size), sensitivity, noise, tolerance for contaminants and energy absorption compared with CHCA. In term of solid state characteristics, the alternative matrix should have a good covering capacity, homogeneity and fast crystallisation, also possess better vacuum stability and be more resistant to laser irradiation especially for high frequency lasers.

Substantial differences in signal intensity were observed between matrices; the maximum signal intensity and desorption yield however was still achieved using CHCA (**Figure 3.4**).

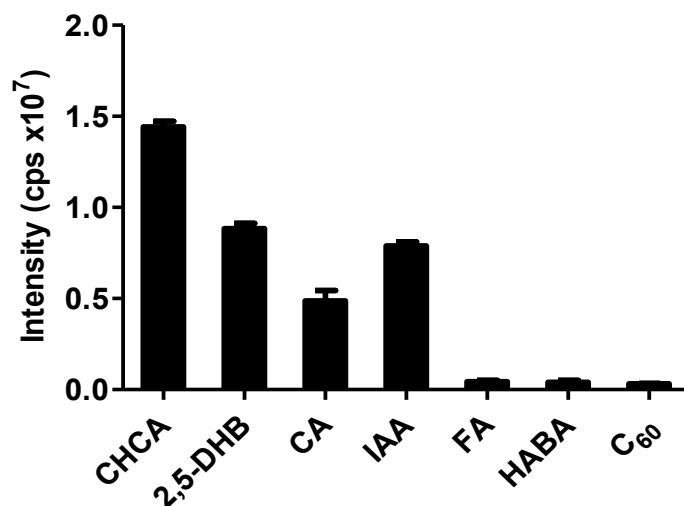


**Figure 3.4:** Screening of matrices for detection of neutral corticosteroids by MALDI-FTICR-MSI. A solution of d<sub>8</sub>-corticosterone (1 µg) in of methanol: water (50:50) was spotted on a control tissue sections (brain) (n=3/matrix) using the dried-droplet technique. A best yield of ions was achieved using CHCA as a matrix. Data are mean ± SEM. **cps**: count per second. **CHCA**: α-cyano-4-hydroxycinnamic acid, **2,5-DHB**: 2,5-dihydroxybenzoic acid, **CA**: cinnamic acid, **IAA**: 3-indole acetic acid, **FA**: ferulic acid **HABA**: 2-(4'-hydroxybenzeneazo) benzoic acid, **C<sub>60</sub>**: Buckminsterfullerene.

As the best sensitivity was achieved using CHCA, the relationship of the desorption and ionisation mechanism and its chemistry was further investigated, with a view to proposing structural modifications which may be beneficial. In the CHCA core, the free carboxylic acid function is essential for good matrix performance. Also, it becomes possible that proton affinity (PA) may play a key role in the ionisation process. Matrices with lower PA have a faster proton transfer reaction constant leading to a more efficient ionisation. Proton affinities of some of the tested matrices were calculated based on the kinetic method (Brodbelt-Lustig *et al.*, 1989). As shown in **Table 3.1**, the CHCA which had the lowest PA also led to the higher signal intensity

(Figure 3.5), confirming the hypothesis that matrices with lower PA have higher ionisation efficiency.

**Table 3.1:** Proton affinity calculation of standard MALDI matrices

Matrix	PA (kJ/mol)
CHCA	864
2,5 DHB	890
CA	885
IAA	987
FA	876
HABA	908

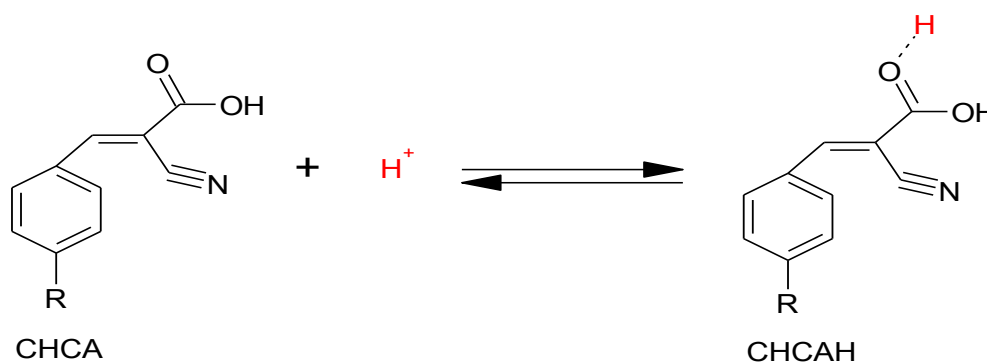


**Figure 3.5:** Proton affinity (PA) using the kinetic method.  $\Delta_r$ : Enthalpy of reaction.  $\Delta_f$ : Enthalpy of formation. Adapted from (Brodbelt-Lustig *et al.*, 1989).

On this basis Karas and co-workers designed a halogenated cyanocinnamic acid derivative, the novel 4-chloro- $\alpha$ -cyanocinnamic acid (Cl-CCA), which possess a lower proton affinity (846 kJ/mol) than its hydroxyl analogue (864 kJ/mol). Use of this matrix had increased the signal of poorly ionisable peptides. To investigate if use of a

matrix with lower PA would be of benefit in imaging underivatised steroids, the Cl-CCA matrix was synthesised and tested (**Appendix I**). Interestingly, the novel Cl-CCA, demonstrated lower intensity signals in combination with steroids than CHCA (**Figure 3.6**), however, the background signal was noticeably lower in the low mass range (200-400 Da) (**Figure 3.7**).

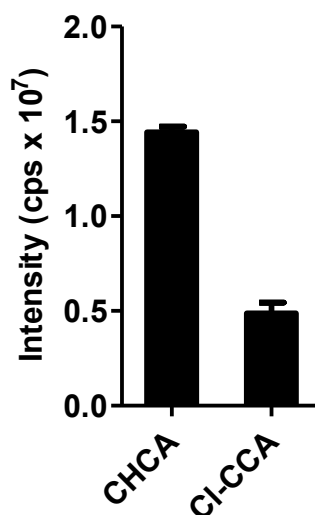


**Figure 3.6:** Use of 4-chloro- $\alpha$ -cyanocinnamic acid (Cl-CCA) vs  $\alpha$ -cyano-4-hydroxycinnamic acid as matrix for detection of neutral corticosteroids by MSI.  $d_8$ -corticosterone ( $1\mu\text{g}$ ) in of methanol: water (50:50) was spotted on a control tissue sections (brain) ( $n=3/\text{matrix}$ ) using the dried-droplet technique as described in **section 3.2.3**. The greater intensity of signal of ions was achieved using CHCA as a matrix. Data are mean  $\pm$  SEM. cps: count per second.

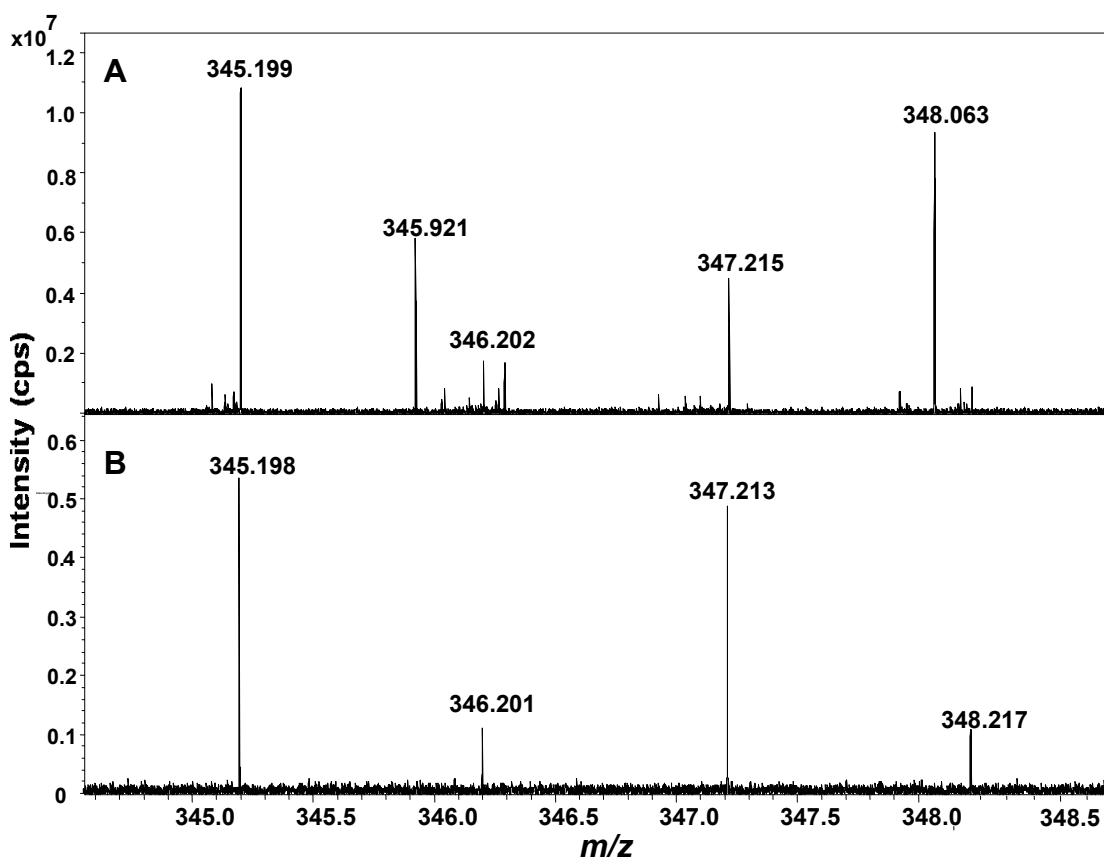


**Figure 3.7:** MALDI-FTICRMS spectra of neutral corticosteroids in a section of adrenal gland using CCA matrices. Corticosterone at  $m/z$  347.215 Da and 11-dehydrocorticosterone at  $m/z$  345.198 Da using (a)  $\alpha$ -cyano-4-hydroxycinnamic acid (b) chloro- $\alpha$ -cyanocinnamic acid (Cl-CCA) as matrices. Signal intensity could not be improved by use of Cl-CCA; however, the matrix clusters contribution was noticeably lower. cps: count per second. CCA: cyanocinnamic acid.

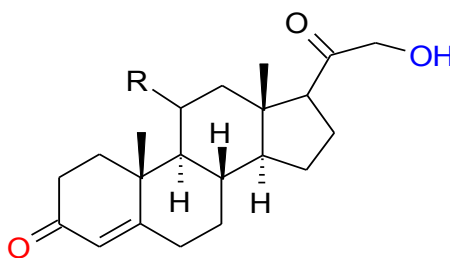
### 3.3.5. MSI imaging of derivatised corticosteroids

It is well known in approaches to analyse steroids by LC/MS that sensitivity can be improved using chemical derivatisation by the incorporation of readily charged or charged moieties (Higashi *et al.*, 2007). The conversion of low proton affinity native

steroids to readily charged derivatives may increase the proton affinity (or proton displacement, in negative ion-mode) leading to a more efficient ionisation.

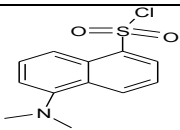
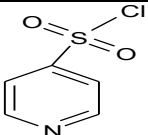
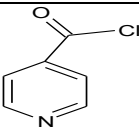
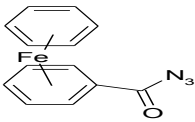
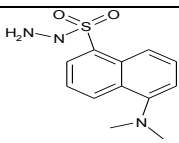
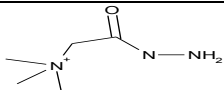
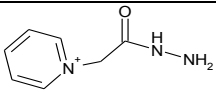
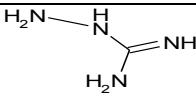
### 3.3.5.1. *Screening of derivatisation reagents*

Several derivatisation reagent were screened (**Table 3.2**) targeting both ketone at C3 in the A ring (**Figure 3.8**, in red) and the primary alcohol at C21 (in blue) of the steroid molecule.



**Figure 3.8:** Molecular structure of corticosteroid core. Targetable derivatisation moieties: A,  $\beta$ -unsaturated ketone group (in red) and primary alcohol at C21 (in blue).

**Table 3.2:** Potential derivatisation reagents

Reagents	Structure	functionality	Mechanism
Dansyl chloride		alcohols	Substitution Elimination
Pyridine-sulphonyl chloride			
Isonicotinoyl chloride			
Ferrocene azide			
Dansyl hydrazine		ketones	Substitution condensation
Girard T			
Girard P			
Aminoguanidine			

The screening was carried out by spotting experiments on- and off-tissue using a labelled corticosteroid ( $d_8$ CORT) rather than endogenous steroids to avoid any background contribution.

Poor desorption or ionization by MALDI analysis was found using derivatives targeting the primary (C21) alcohol moiety with acyl and sulfonyl chlorides. Screening derivatization reactions, targeting the  $\alpha$ - $\beta$  unsaturated ketone at C3 in the steroid A-ring (**Table 3.3**) improved signal intensity in positive mode when the corticosteroids were converted to derivatives either permanently charged or easily protonated. In particular, formation of a quaternary ammonium derivative, by a hydrazine-type condensation reaction of the ketone at C3 using Girard-T (GirT) reagent (**Figure 3.9**) forming water soluble hydrazones group, greatly enhanced response up to  $10^4$  fold more than the un-derivatised steroid (**Table 3.3**).



**Table 3.3:** Intensity of responses of corticosteroids derivatives following analysis by MALDI-FTICRMS.

Derivatisation reagent	Corticosterone	11-dehydrocorticosterone	LOD
	Intensity (cps)		
None (underivatised)	$1.3 \times 10^4$	$0.9 \times 10^4$	0.1 $\mu$ g
Aminoguanidine	ND	ND	N/A
Dansyl chloride	ND	ND	N/A
Sulfonyl chloride	$2 \times 10^4$	$1 \times 10^4$	20 ng
Isonicotinoyl chloride	$3.1 \times 10^5$	$5.4 \times 10^5$	4 ng
Ferrocene azide	ND	ND	N/A
Dansyl hydrazine	$8.1 \times 10^6$	$6.7 \times 10^6$	0.2 ng
Girard T	$8.5 \times 10^8$	$8.7 \times 10^8$	1 fg
Girard P	$2.1 \times 10^7$	$1.7 \times 10^7$	10 fg

**ND:** not detectable, **N/A:** no applicable **cps:** Count per second.

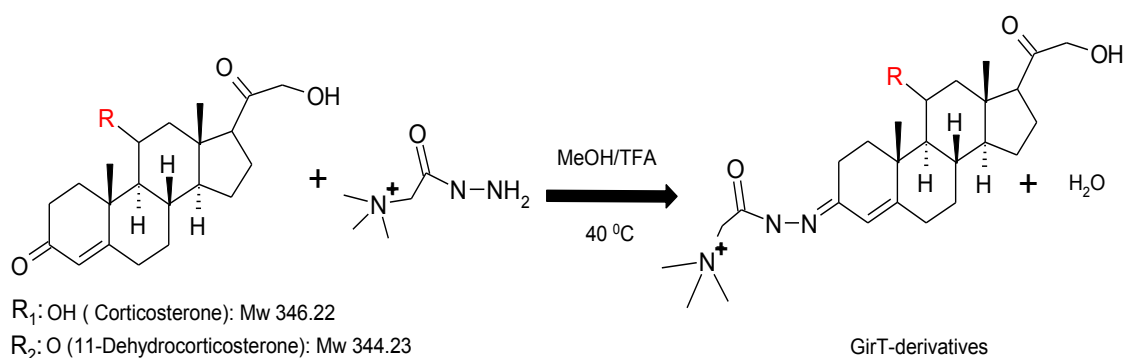


**Figure 3.9:** Girard-T (GirT) derivatization reaction scheme. **MeOH:** Methanol. **TFA:** trifluoroacetic acid.

In terms of reactivity, derivatisation was only observed at the C3 in the steroid A-ring as the  $\pi$  electrons are delocalised across the conjugated system leaving the carbonyl group more susceptible to a nucleophilic attack. Moreover, double or triple charged species were not detected suggesting that double or triple (in case of DHC) tagged derivatives were not formed to any significant degree.

Upon derivatisation the average molecular weight of the CORT derivative was 460.4 Da and for the corresponding 11DHC was 458.3 Da, in both cases, greater than the untagged steroid due to the introduction of the GirT tag. The monoisotopic masses of both GirT-derivatives were confirmed by accurate mass measurement with a mass deviation of  $\pm 10$  ppm from their theoretical values as it shown in **Figure 3.10**. Moreover, upon derivatisation, the ionisation of both derivatives was driven by the positive-charged quaternary amine tag, therefore similar intensities of responses were found for both steroids derivatives; the observed response factor (abundance of GirT-CORT/abundance GirT-11DHC at same amount) was  $\sim 1.07$ .

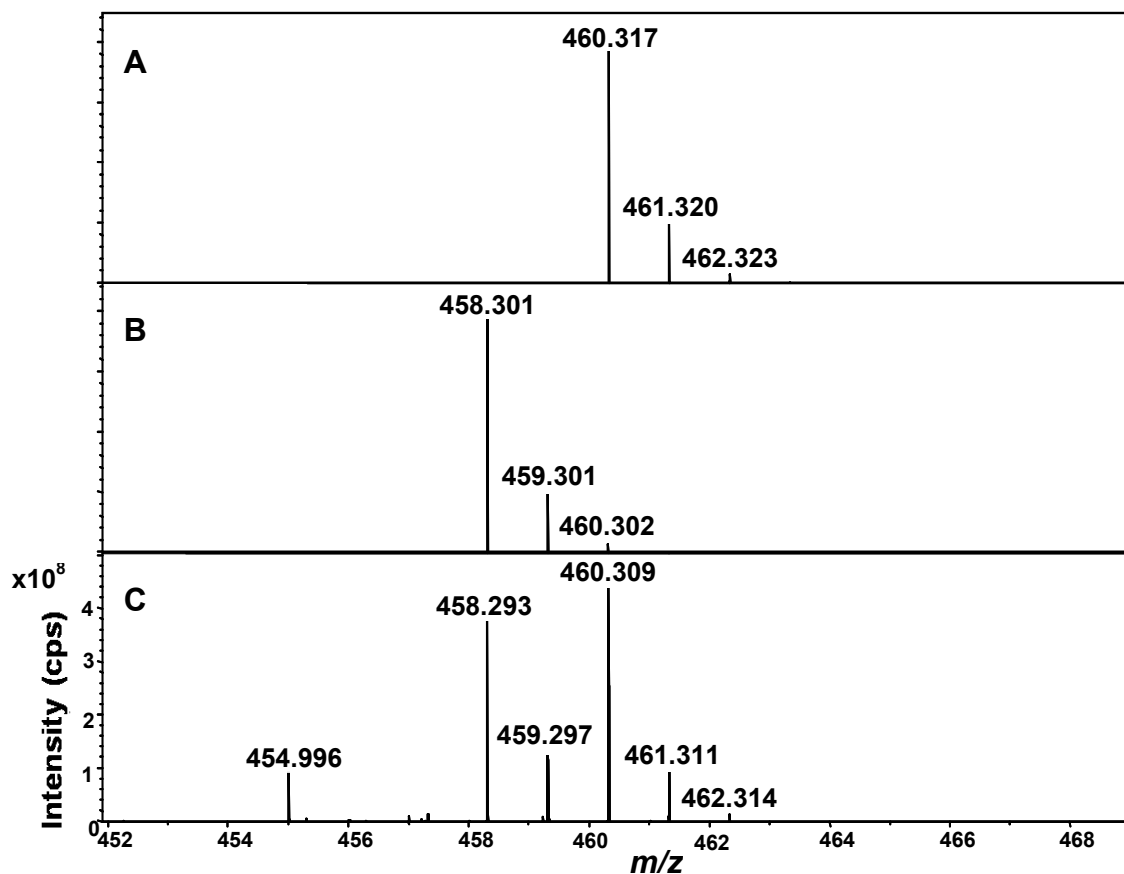


**Figure 3.10:** Representative MALDI-FTICRMS of Girard T (GirT)-derivatives of corticosteroids standards at same amount (5 ng) each. Observed response factor was 1.07. Theoretical monoisotopic pattern (a: GirT-corticosterone (GirT-B).(b) GirT-11-dehydrocorticosterone (GirT-11DHC). C: Mass spectrum of GirT-(11DHC&CORT) derivatives (5 ng). cps: counts per second.

### 3.3.5.2. *Optimisation of formation of Girard T derivatives*

GirT condensation is generally carried out using protic solvents in weak acid media at RT with reaction times around 10-18 h achieving 60-80 % of conversion of ketones to hydrazones. Recent studies have shown that the reaction can be carried out in 30 min at 70 °C (Wu *et al.*, 2010). However, this was not appropriate for the method developed here as such high temperatures may cause disruption of tissue morphology due to an

increase of water vapour in the reaction chamber and may also lead to diffusion of the water soluble GirT derivatives and ion suppression effects due to protein cleavage and tissue component degradation. Screening using different with MSI compatible solvents (ethanol/methanol) and acidic catalysts (formic acid, acetic acid and TFA) as described in **section 3.2.6** was conducted. The best signal intensity was achieved in 1 h at 40 °C, in a moisturizing environment using methanol/TFA as solvent/catalyst system (**Figure 3.11**).

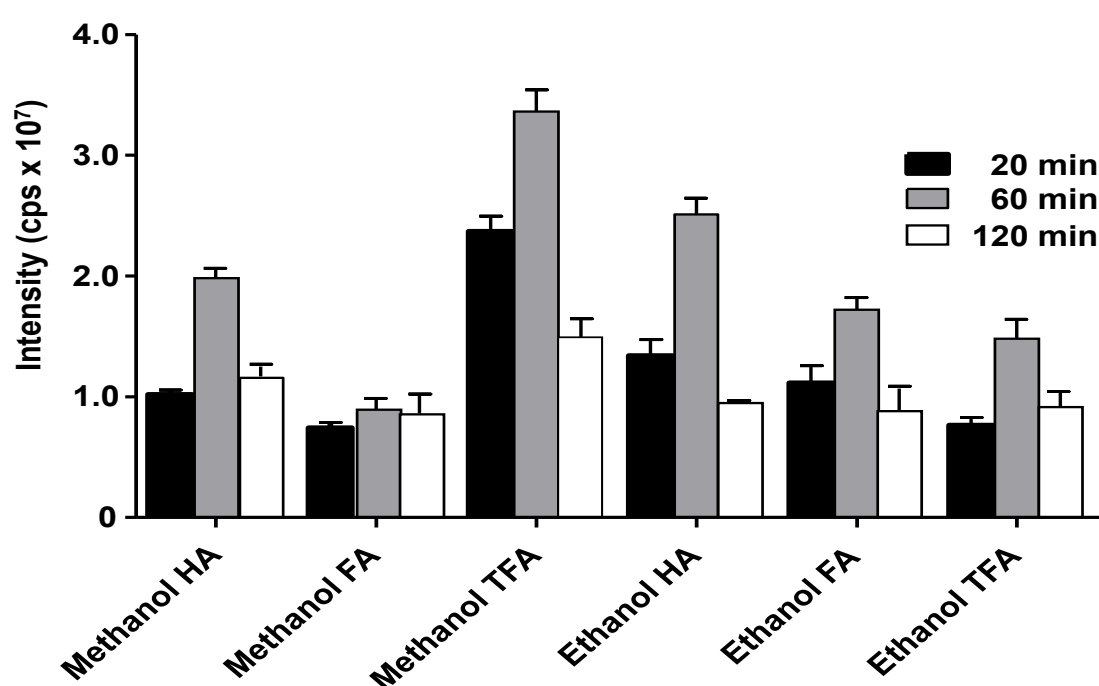


**Figure 3.11:** Optimisation of time and catalytic conditions. A solution of  $d_8$ -corticosterone (5 ng) in methanol: water (50:50) was spotted onto a control tissue section (murine brain (n=3)). The spots were allowed to dry, then solutions of Girard T (GirT; 0.5  $\mu$ L, 5 mg/mL) applied using different solvent systems: Methanol or ethanol with HA, FA and TFA, respectively. Spots of reagent were deposited directly on top of the  $d_8$ -CORT standard spots. The slide was placed in the reaction chamber and incubated (40°C for 20, 60 and 120 min). Matrix (CHCA (10mg/mL in 60:40 acetonitrile: water + 0.25 %v/v TFA)) was applied to the tissue by a pneumatic TLC sprayer (20 mL per slide). The best signal intensity was achieved at 60 min using methanol/TFA as solvent/catalyst system. Data are mean  $\pm$  SEM (n=3/per condition). **cps**: counts per second. **HA**: Acetic acid, **FA**: Formic acid **TFA**: Trifluoroacetic acid.

Accordingly MALDI-FTICR parameters were optimised for maximum sensitivity of detection and quantification of GirT derivatives using CHCA as a MALDI matrix and following derivatisation using the optimised reaction conditions (methanol/TFA solvent system at 40°C for 60 min).

### 3.3.5.3. *Limits of detection and quantitation of derivatised corticosteroids on tissue sections*

The LODs and LOQs were evaluated in different tissue sections by standard spotting experiment as described in section 3.2.7. Results are shown in Table 3.4.

**Table 3.4:** Limits of detection and quantitation of Girard T derivatives of corticosteroids by MSI

Tissue	LOQ (pg)		LOD (pg)		ΔM LOQ (ppm)	
	11DHC	CORT	11DHC	CORT	11DHC	CORT
<b>Brain</b>	5-10	0.5-1	1	0.1	3	2
<b>Liver</b>	12-15	12-15	1-2	1	2	3
<b>Kidney</b>	50-60	50-60	10	8-10	16	15

**LOQ:** limit of quantitation; **LOD:** limit of detection; **11DHC:** 11-dehydrocorticosterone-derivative, **CORT:** corticosterone-derivative **ΔM:** Mass accuracy against the theoretical isotopic distribution. **ppm** = parts per million.

LODs at pg levels were achieved in brain and liver sections with very good mass accuracy (less than 10 ppm). An improvement of approximately 10<sup>4</sup>-fold in signal intensity was achieved in comparison with non-derivatised steroids. However, higher values were found in kidney, possibly due to the high ion suppression caused by endogenous tissue composition and high levels of alkaline cations.

### 3.3.5.4. *Stability of Girard-T derivative*

As previously reported, proteolysis and tissue degradation during sample preparation may cause ion-suppression. With the optimized protocol in place, stability was evaluated temporally by assessing the intensity of signal from GirT-CORT applied on and off tissue sections as described in section 3.2.8. Only 13 % reduction in signal suppression/degradation was observed after 20 min at RT, within the necessary limit of tissue handling times before matrix coated (**Figure 3.12**).

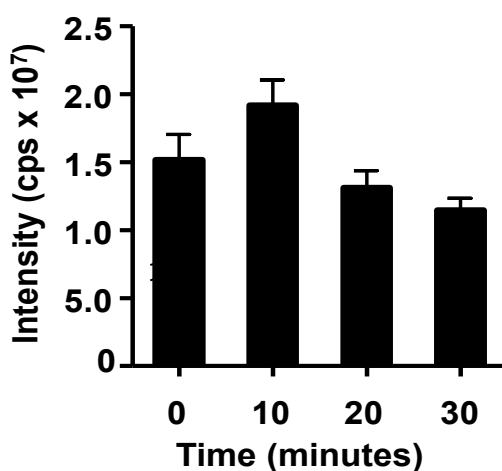


**Figure 3.12:** On-tissue stability of Girard T corticosterone (GirT-CORT). A solution of GirT-CORT (5 ng) was spotted on a control tissue section in duplicate. Matrix (CHCA (10 mg/mL in 60:40 acetonitrile: water + 0.25 %v/v TFA) was applied to the tissue by a pneumatic TLC sprayer (6ml per slide) immediately after reaction (T=0) and after 10, 20 and 30 min at RT (n=3 per time point). The observed decline in signal intensity was less than the acceptable cut-off for stability of the original signal (20 %). Data are mean  $\pm$  SEM (n=3/per time point). **cps**: count per second.

### **3.3.5.5.      *Detection of endogenous steroids in adrenal glands following derivatisation with GirT***

After optimisation of the derivatisation reaction, a feasibility study was conducted to establish whether endogenous cortico steroids could be detected in biological tissue sections as their GirT- hydrazones with greater intensity than without derivatisation (**section 3.3.3**). Again rat adrenal glands were selected as a model tissue for method development, due to the anticipated high abundance of corticosteroids and well know distribution pattern. The on-tissue chemical derivatisation (OTCD) MALDI-MSI platform protocol was applied as summarised in **Figure 3.13**. Derivatisation reagent was applied using an artist's air brush and ITO-slice with the tissue sections was incubated in the derivatisation chamber (**Figure 3.14**).

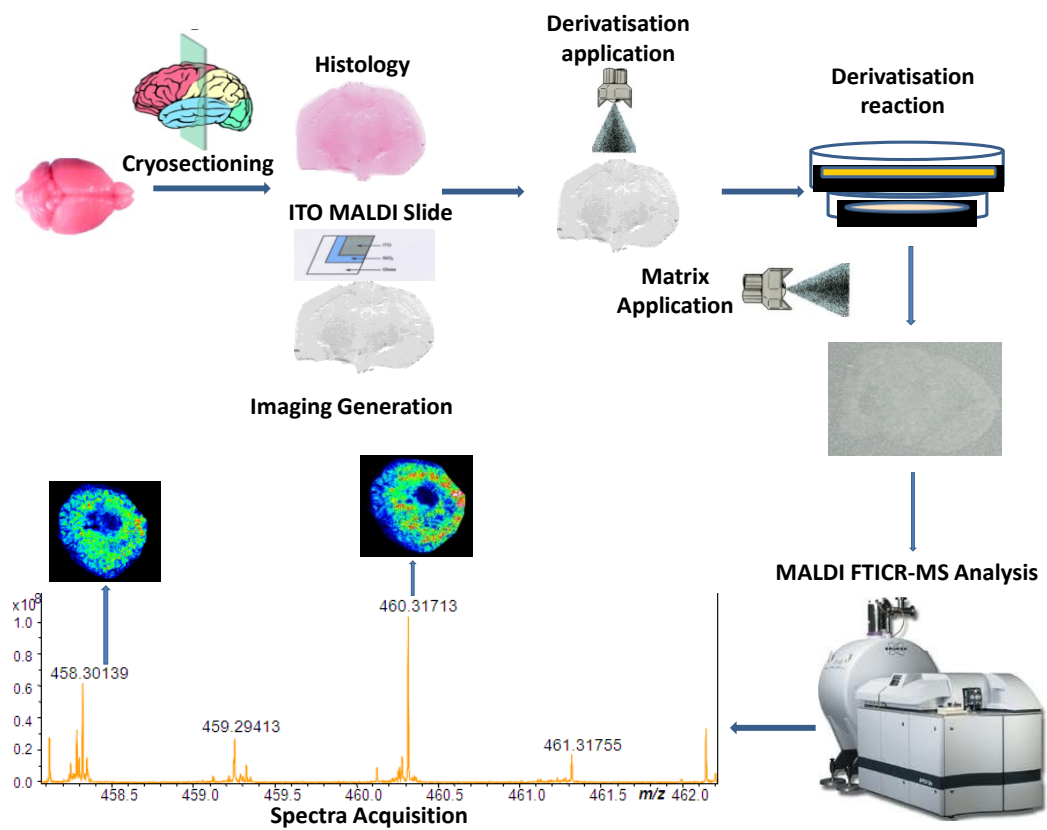


**Figure 3.13:** On-tissue chemical derivatisation mass spectrometry imaging (OTCD-MSI) platform. Mass Spectrometry imaging workflow: after sectioning, tissue were coated with GirardT (GirT) by spray-based techniques, incubated in a temperature and humidity-controlled chamber and further coated with MALDI matrix before MALDI-FTICRMS analysis.



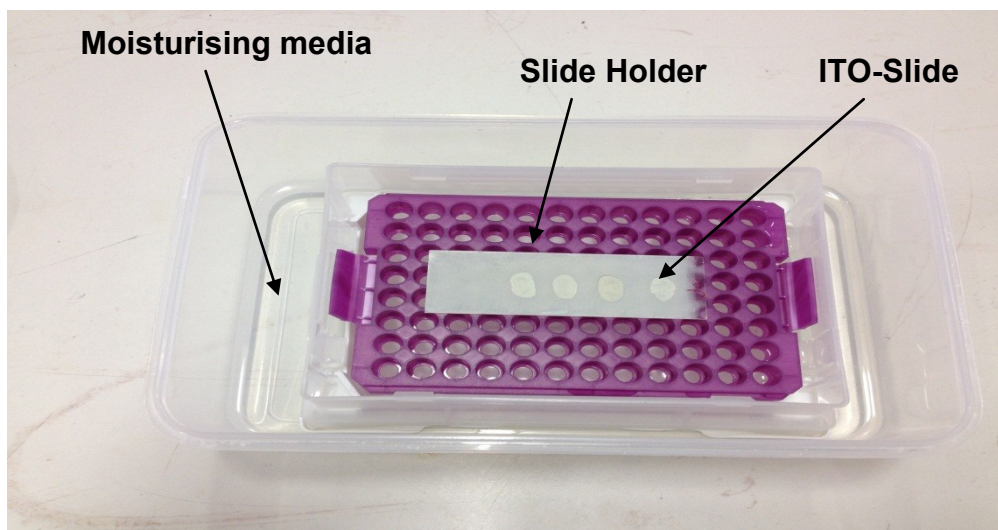


**Figure 3.14:** Derivatisation reaction chamber. After coating with Girard T (GirT), slides were placed in a sealed container containing a moisturising-controlled solution (saturated potassium chloride) and incubated at 40°C for 60 min in a temperature-controlled oven.

Both steroids were identified as hydrazone derivatives within adrenal tissue and molecular distribution maps were generated, showing GirT-CORT ( $m/z$  460.317) and GirT-11DHC ( $m/z$  458.301) in high abundance in the zona fasciculata/reticularis (**Figure 3.15 b and a**) respectively, with mass accuracy of  $\pm 5$  ppm from their theoretical monoisotopic masses (**Figure 3.15 d-f**) and signal to noise ratios  $>100$ .

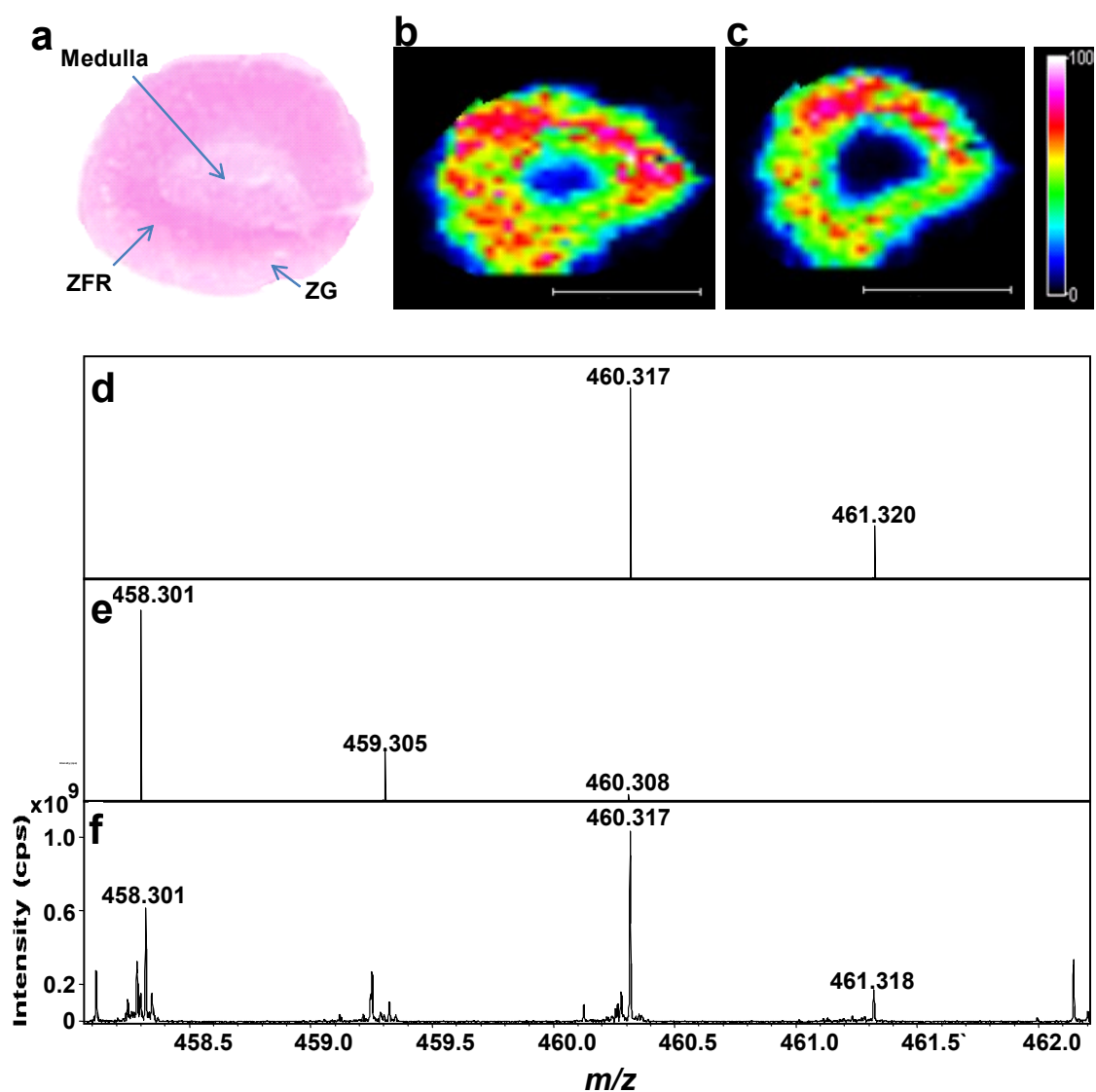


**Figure 3.15:** Molecular imaging by MALDI-FTICR-MSI of corticosteroid derivatives prepared with Girard T reagent (GirT) in representative rat adrenal gland sections. Molecular regional distribution maps showed GirT-corticosterone (GirT-CORT;  $m/z$  460.31713) and GirT-11-dehydrocorticosterone (GirT-11DHC;  $m/z$  458.30139) in high abundance in the zona fasciculata/reticularis (site of glucocorticoids synthesis) with mass accuracy of  $\pm 5$  ppm from their theoretical monoisotopic masses and (S/N) signal to noise ratios above 100. (a) Histological image of a cryosection of rat adrenal gland stained with haematoxylin and eosin **ZG** = zona glomerulosa; **ZFR** = zona fasciculata/reticularis). Heat map of GirT derivatives of: (b) GirT-CORT at  $m/z$  460.31698 Da and (c) GirT-11DHC at  $m/z$  458.30133 Da, collated by MALDI-FTICRMS. Signal intensity is depicted by color on the scale shown. Scale bar (2 mm). Simulated theoretical isotopic distribution pattern of: (d) GirT-CORT; and (e) GirT-11DHC. (f) Representative FTICRMS spectrum of corticosteroid hydrazones in rat adrenal gland, showing excellent agreement with theoretical mass. **cps** = counts per second.

In the adrenal gland, GirT derivatives yielded spectra dominated by the molecular ion (**Figure 3.15, f**) and high resolution MS was used to overcome the challenge of selecting specific analytes of interest from the many high abundance ions in the low mass range.

Glucocorticoids were visualised and most abundant in the zona fasciculata and reticularis, the major site of glucocorticoid synthesis, with lower signal in the outer zona glomerulosa, where CORT is further metabolised to aldosterone. This suggested that unwanted diffusion of analytes was constrained by the tissue processing method. Spatial resolution of the laser is adjustable, but increasing the spatial resolution decreases sensitivity as the spot size sampled is smaller (**Figure 3.16**). In the adrenal, collecting data at 200  $\mu\text{m}$  resolution generated sufficient spatial information with adequate signal (signal/noise  $>100$ ) as when the resolution was changed to 50  $\mu\text{m}$  a considerable decline in signal intensity was observed.

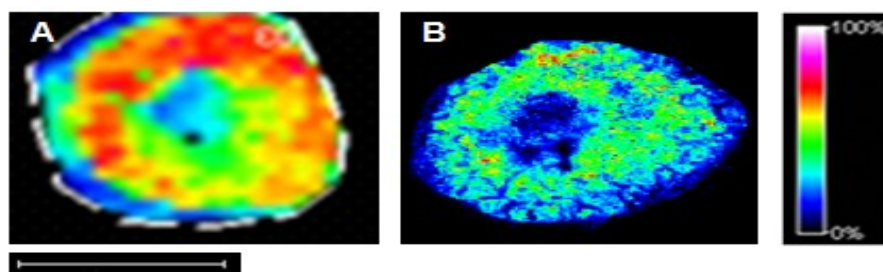


**Figure 3.16:** Molecular imaging by MALDI-FTICR-MSI of corticosterone derivative prepared with Girard T reagent (GirT-CORT) in representative rat adrenal gland sections at different spatial resolution. Increasing the spatial resolution of the image caused a decline in signal intensity due to the smaller spot size. Heat map of GirT-CORT at  $m/z$  460.317Da. (a) at 200  $\mu\text{m}$  lateral resolution. (b) at 50  $\mu\text{m}$  lateral resolution. Signal intensity is depicted by color on the scale shown. Scale bar (1 mm).

### 3.3.5.6. *Confirmation of identity of molecular species by LESA*

Structural confirmation by fragmentation using LESA-electrospray ionisation (ESI)-FTICR-MS followed by CID, allowed isolation of the precursor ions in the ICR cell, increasing both sensitivity and selectivity in comparison to MALDI. The experimental procedure can be found in **section 2.9**. This process provided fragmentation patterns typical of GirT hydrazones (**Figure 3.17**), concordant with the structures of steroid hydrazones, extrapolating from GirP analogues, which may form a stable five member ring as previously reported. CID of the GirT derivatives generated a series of fragment ions characteristic of the loss of the quaternary amine tag  $[M-59]^+$  and carbon monoxide  $[M-87]^+$  of the derivatised group at  $m/z$  399,  $m/z$  371 (GirT-11DHC) and  $m/z$  401,  $m/z$  373 (GirT-CORT), respectively. Also, a GirT-CORT selective fragment was observed at  $m/z$  383 corresponding to the neutral loss of water at C11 of the  $m/z$  401 GirT-CORT fragment ion.

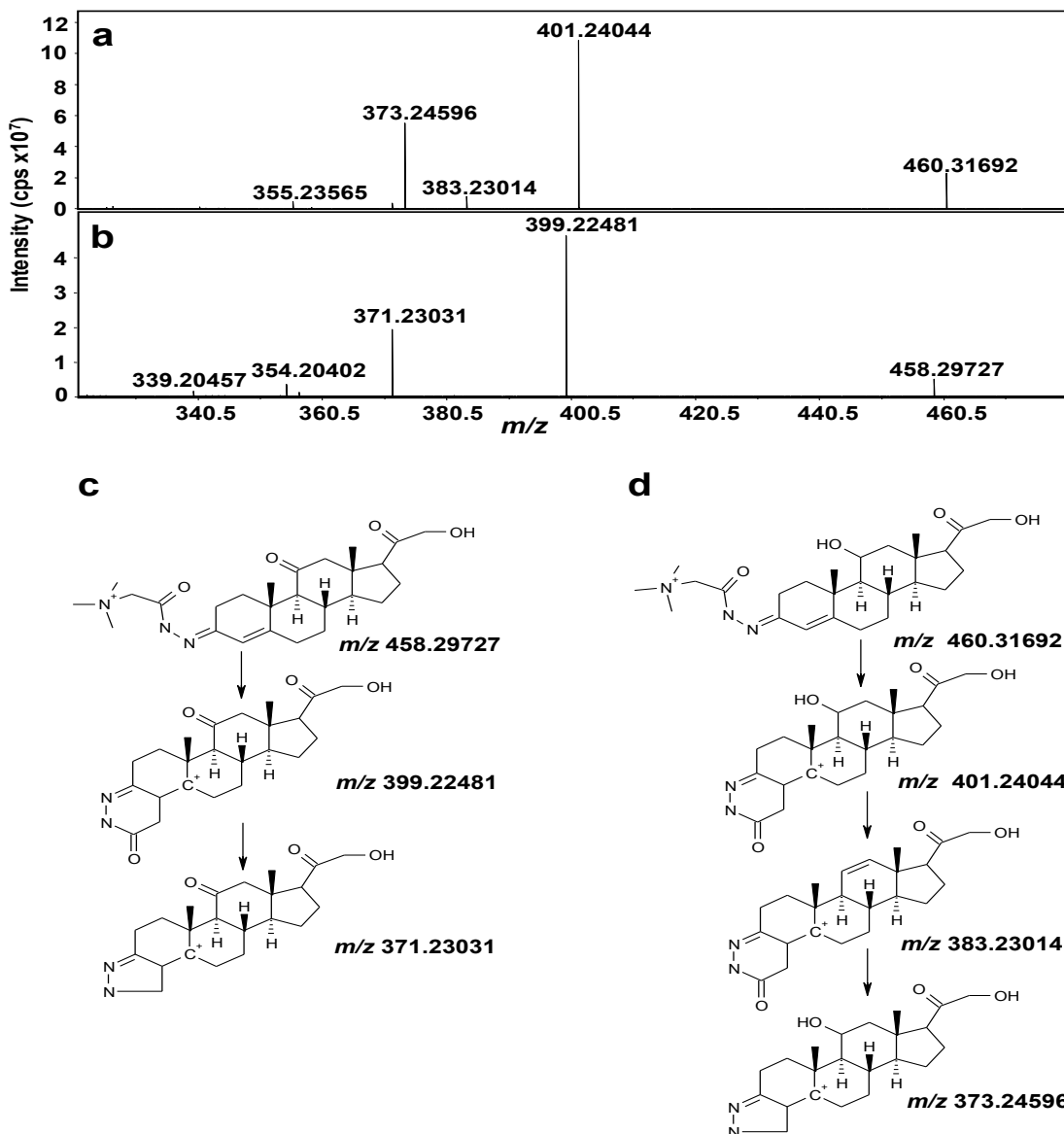


**Figure 3.17:** Liquid extraction surface analysis (LESA) with nanoESI-FTICR collision induced dissociation (CID) mass spectra of Girard T (GirT) derivatives of corticosteroids. CID mass spectra and proposed fragmentation patterns of GirT derivatives were in agreement with the structures of steroid hydrazones, extrapolating from Girard P (GirP) analogues. Precursors (a) at  $m/z$  460.31692 Da (GirT-corticosterone) and (b) at  $m/z$  458.29727 Da (GirT-11-dehydrocorticosterone) (d) Proposed fragmentation patterns for GirT-CORT (c) and GirT-11DHC. cps = counts per second. Cell isolation was 20 s and collision energy was set to 28eV.

### 3.3.5.7. *Solvent optimisation of method to detect endogenous steroids*

To further optimise the MSI platform specifically for detection of endogenous steroids in tissue, matrix solvents were screened to evaluate the extraction efficiency from the tissue surface. Due to solubility properties of the MALDI matrix, only methanol/water and acetonitrile/water in acidic media (TFA, 0.2 % v/v) were evaluated as solvents. The mixture 6:4 with 0.2 % v/v TFA has been used for all MSI experiments and therefore it was selected as a control solvent system. As shown in **Figure 3.18**, the highest signal intensity for GirT-CORT was achieved using acetonitrile: water, 8:2 with 0.2 % v/v.

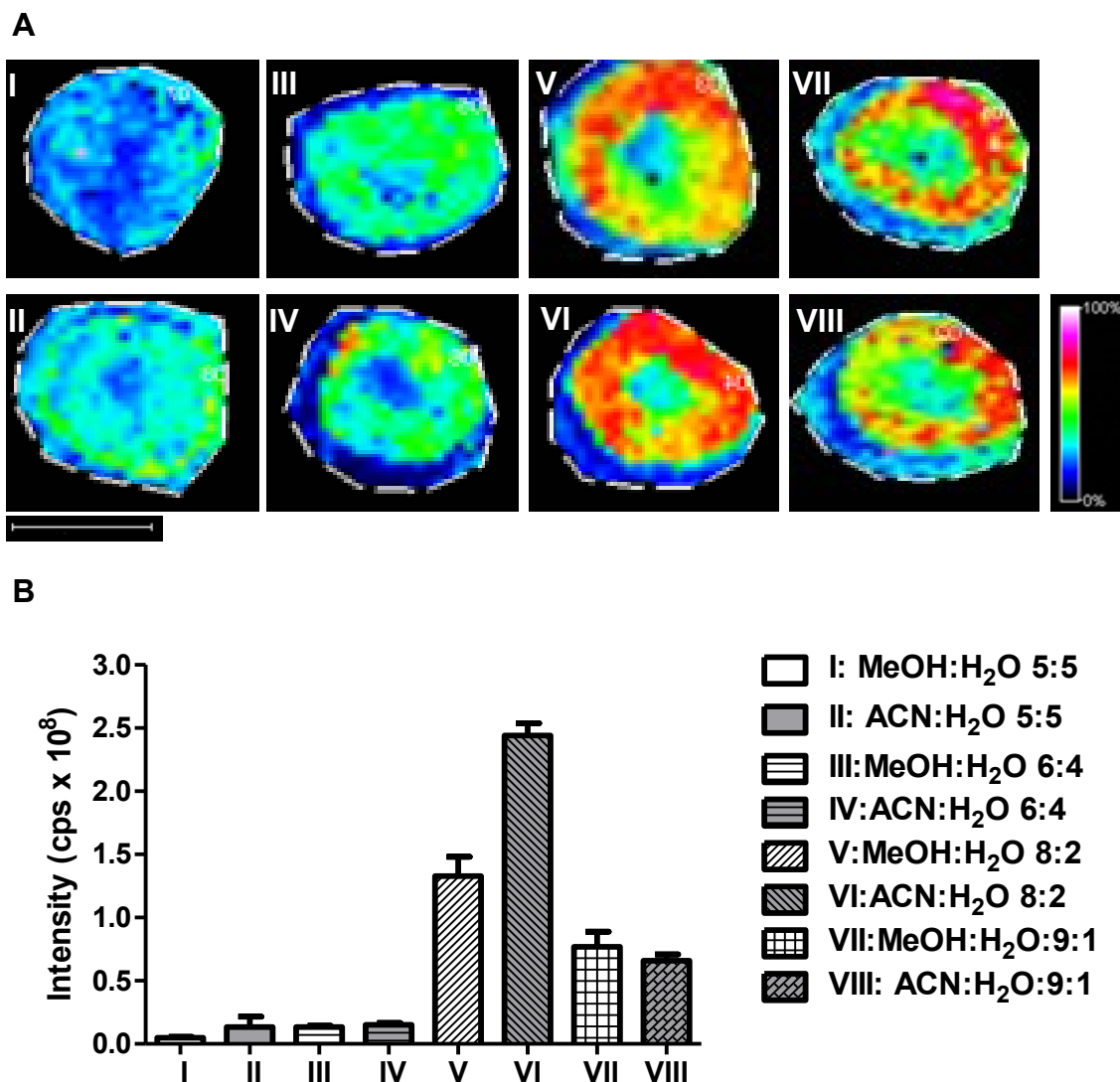


**Figure 3.18:** Screening of solvents using  $\alpha$ -cyano-4-hydroxycinnamic acid (CHCA) for MALDI-FTICR-MSI analysis of endogenous corticosteroids as Girard T (GirT) hydrazones extracted from rat adrenal gland tissue sections. The greatest signal intensity was achieved using acetonitrile: water 80:20 as matrix solvent system during matrix deposition by pneumatic TLC sprayer (a) Gradient distribution of corticosterone GirT derivative (GirT-CORT) detected at  $[M]^+$ ;  $m/z$  460.317 Da in rat adrenal gland. Lateral resolution was set at 150  $\mu$ m. Signal intensity is depicted by colour as per the scale shown. Scale bar (2 mm). Methanol (MeOH): H<sub>2</sub>O I 5:5, III 6:4, V 8:2, VII 9:1. Acetonitrile (ACN): H<sub>2</sub>O II 5:5, IV 6:4, VI 8:2, VIII 9:1. (b) Relative intensity of the GirT-CORT ion under different conditions. Data are mean  $\pm$  SEM (n=3/per solvent condition). **cps**: count per second.

### **3.3.5.8.        *Investigation of approaches to limit analyte diffusion***

Analyte delocalisation is a well-known problem in MALDI-MSI, caused primarily by the matrix co-solvent during application by spray-based techniques. Therefore a number of approaches were explored to limit this process.

#### **3.3.5.8.1.        *Saturation studies***

Studies were conducted to find out the amount of GirT generating the best and most rapid reaction yields on tissue, achieving completion for endogenous steroids conversion into the corresponding GirT hydrazones. This had to be balanced against using too much derivatisation reagent which could lead to ion suppression. Controlling the amount of reagent was crucial to achieve good MS images. The assessment was carried out using a rat adrenal gland. The derivatisation was carried out using GirT pre-coated (pre-coated) MALDI slides and also applied by spray-based techniques (post-coated) as previously described in section **3.2.10**. The greatest signal intensity was achieved using 4 mL (post-coating) and 0.15 mg/cm<sup>2</sup> (pre-coated) (**Figure 3.19**).



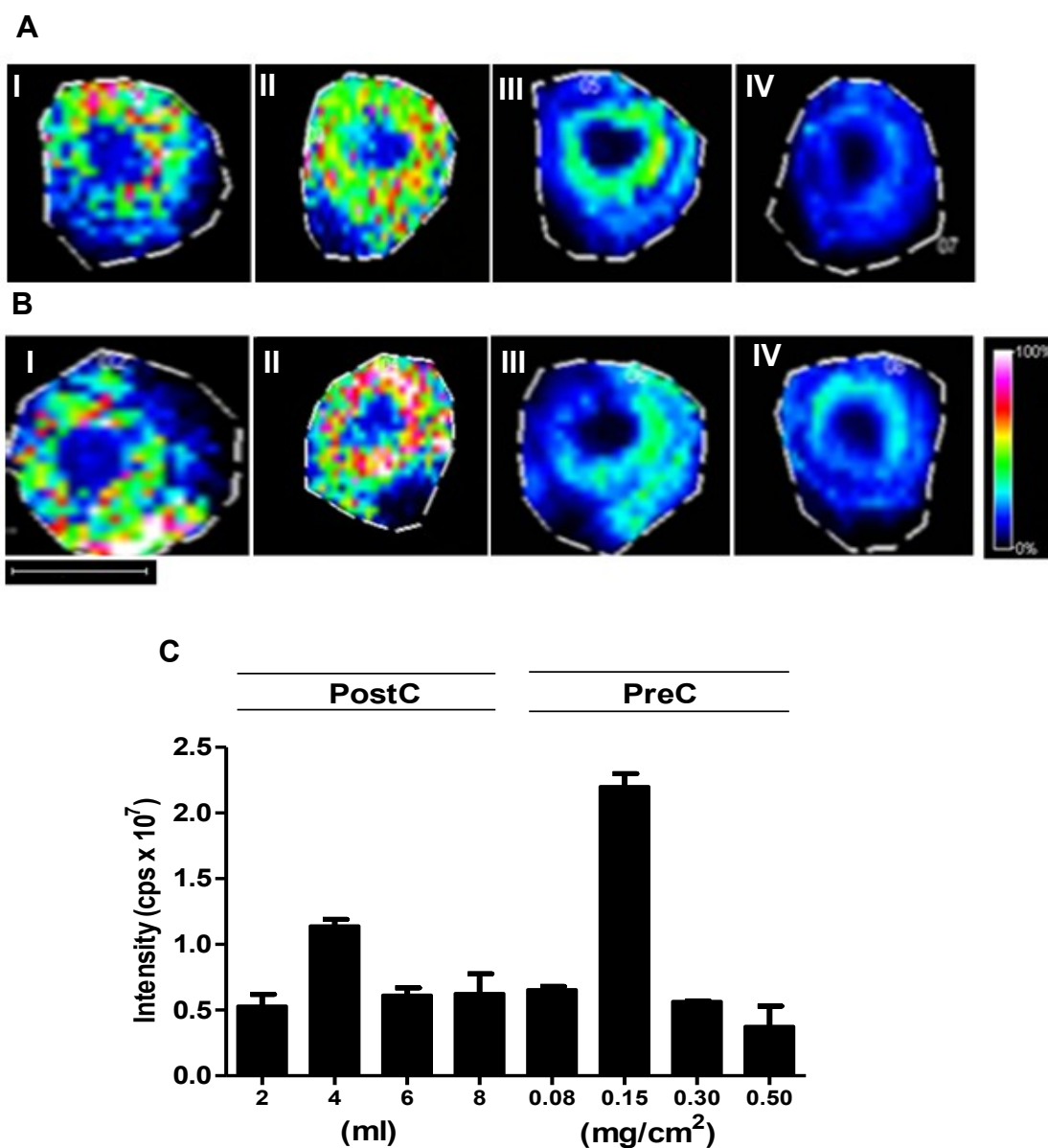


**Figure 3.19:** Optimisation of derivatisation reagent application for MALDI-FTICRMS of corticosteroids Girard T (GirT) hydrazones in adrenal gland tissue sections. Greatest intensities of signal were achieved by pre-coating with 0.15 mg/cm<sup>2</sup> of GirT, without a significant analyte delocalisation being obvious. Higher concentrations of GirT in pre-coating deposition led to significant ion suppression. Gradient distribution of corticosterone GirT derivative detected at [M]<sup>+</sup> *m/z* 460.317 Da. After (a) Post-coating with **I** 2 mL, **II** 4 mL, **III** 6 mL, **IV** 8 mL of 5 mg/mL GirT solution. Pre-coating (b) with **I** 0.08 mg/cm<sup>2</sup>, **II** 0.15 mg/cm<sup>2</sup>, **III**: 0.30 mg/cm<sup>2</sup>, **IV**: 0.50 mg/cm<sup>2</sup>. Lateral resolution was set at 150 μm. Signal intensity is depicted by colour as per the scale shown. Scale bar (2mm). (c) Relative intensity of the GirT-corticosterone at [M]<sup>+</sup> *m/z* 460.317 Da using pre-and post-coating experiments. Data are mean ± SEM (n=3/per solvent condition). cps: count per second. **PostC**: Post-coated, **PreC**= Pre-coated.

### 3.3.5.8.2. *Pre-coating of slides*

In order to control the undesired effects during derivatisation reagent application, pre-coated slides were evaluated. ITO-slides were coated with different amounts of GirT and tissues were thaw-mounted and incubated them for derivatisation. Post coating (4 mL of GirT (5 mg/mL solution in methanol + 0.2 %v/v TFA) was used as control condition and the spatial distribution of GirT-CORT was used to assess the delocalisation . Using pre-coated slides, the greatest signal intensity of GirT-CORT was achieved using 0.15 mg/cm<sup>2</sup> of GirT reagent (**Figure 3.19**). Moreover, pre-coating yielded higher intensity signals than those detected with post-coating approaches. Overall analyte diffusion was not different during pre-coating at 0.15 mg/cm<sup>2</sup> compared with all post-coated conditions. However pre-coating slides with higher amounts (**Figure 3.19 A III, VI**) was associated with substantial ion suppression across the adrenal gland tissue section.

### 3.3.5.9. *Application of matrix by sublimation*

In order to further control the analyte delocalisation during matrix application, sublimation was evaluated as deposition technique. Sublimation of matrix such as CHCA onto tissue slices was achieved using a glass sublimator as shown in **Figure 3.21**



**Figure 3.21:** Glass sublimator used for MALDI matrix deposition.

The finely dispersed coating of the organic MALDI matrices that result from sublimation was visually evident on the glass slides. An example of this is shown in **Figure 3.22** where CHCA was applied by spraying or sublimation onto a sample section of rat adrenal gland. A close-up view of matrix deposited onto a glass cover slip is shown in **Figure 3.22 B, D**. As is shown in **Figures 3.22 C,D**, sublimation led to a smaller crystal size (sub- $\mu\text{m}$ ) compared with a standard spray-coating that can achieve crystal size around 10-20  $\mu\text{m}$  (**Figure 3.22 B**). The matrix sublimed under reduced pressure (0.05 Torr) at temperatures between 120  $^{\circ}\text{C}$  and 140  $^{\circ}\text{C}$  without decomposition. The recommended coating of 0.18  $\text{mg}/\text{cm}^2$  of matrix was thick enough to yield abundant ions upon laser irradiation. However, under these conditions, signal intensity of GirT-CORT was not enough to generate a MSI image of its distribution (**Figure 3.23 B**). This observation was supported by the fact that the signal in the area of the mass spectrum aligned with the mass of GirT-hydrazones was substantially suppressed in comparison with that obtained with spray-coating (**Figure 3.23 DI**).

As sublimation is a very dry technique, recrystallisation was performed to increase the analyte extraction from the tissue. However, as is shown in **Figure 3.23 C**, the signal

was still too low to produce a suitable MS image. Representative mass spectra are shown in **Figure 3.23 DII**. Therefore this approach was not pursued further.

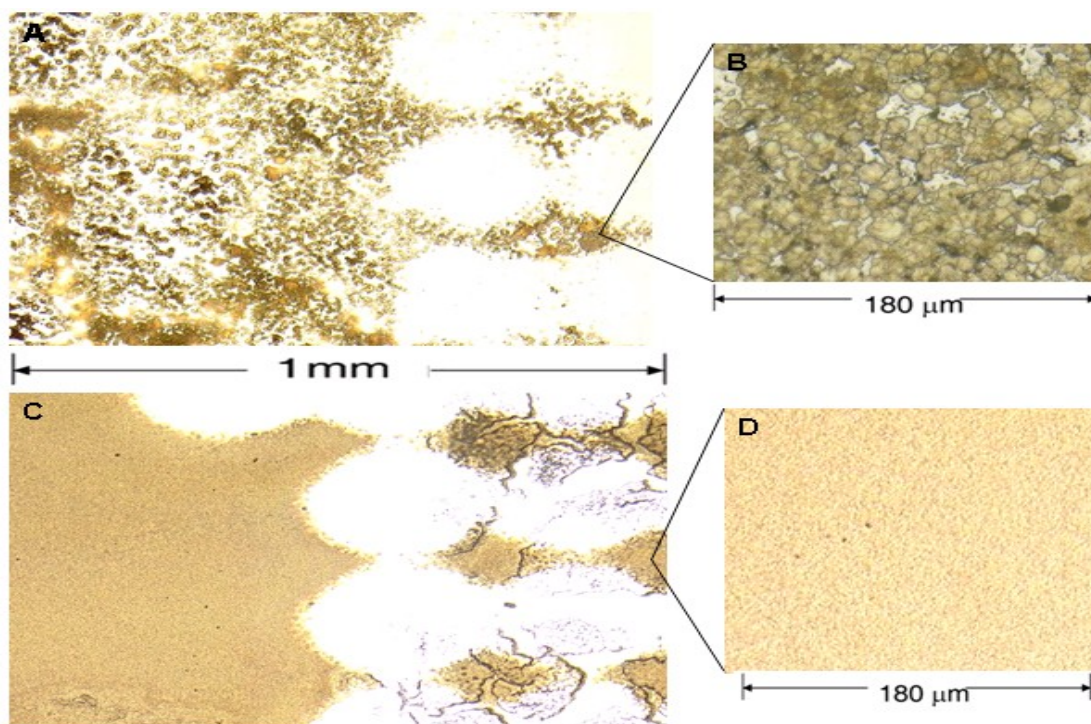


**Figure 3.22:** Comparison of TLC and sublimation as matrix application techniques. **(a)** Photograph (25 x magnifications) of a rat adrenal gland tissue mounted on an ITO-MALDI glass slide and coated with CHCA matrix (4 mL) of 10 mg/mL of CHCA by a pneumatic TLC sprayer. **(b)** Optical microscope image of CHCA crystals (40 x magnifications). **(c)** Photograph (25 x magnifications) of an adrenal gland tissue on an ITO-MALDI glass slide and coated with CHCA matrix (2.74 mg/slide) by sublimation. **(d)** Optical image (40 x magnifications) of crystals formed following sublimation.

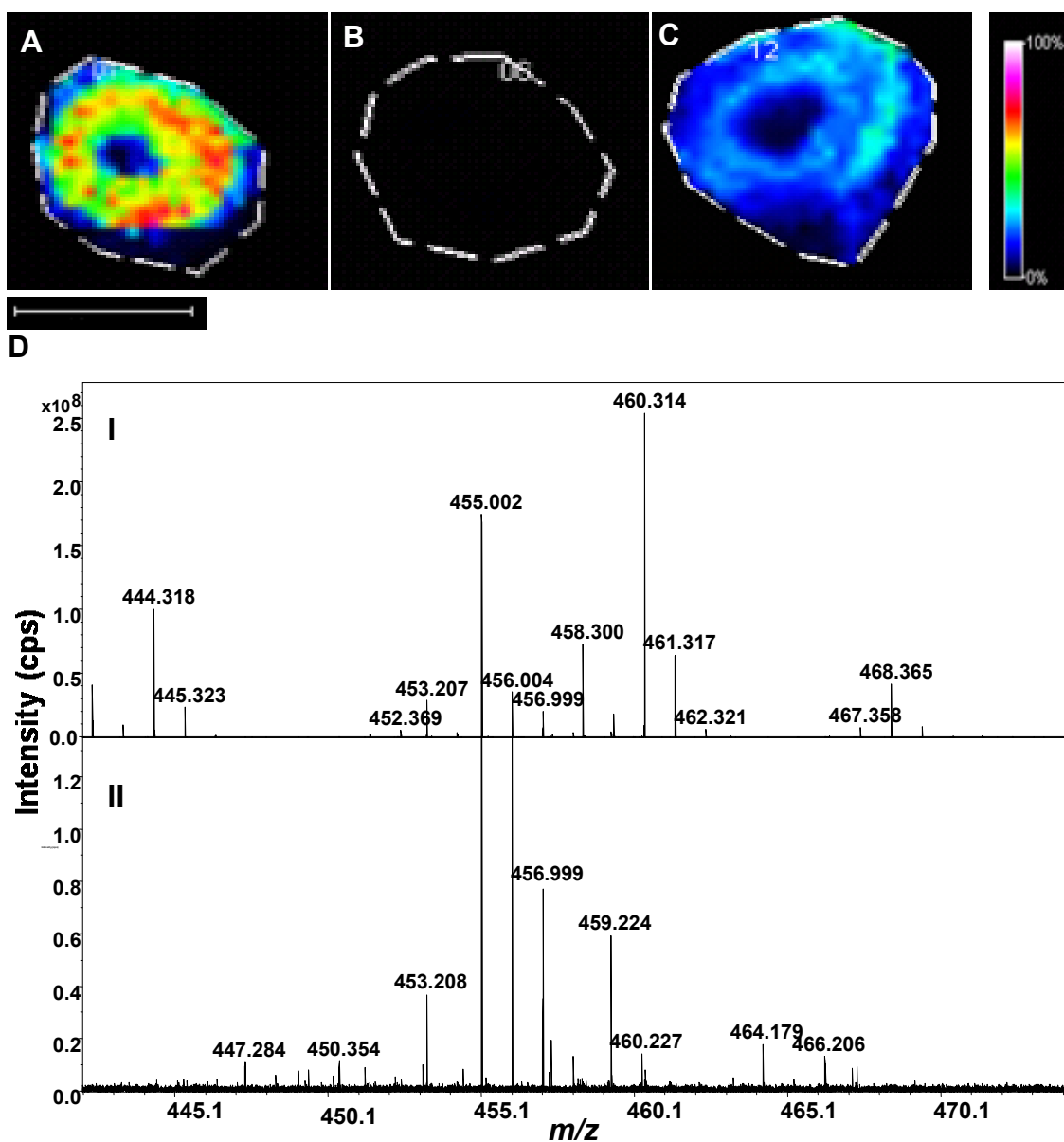


**Figure 3.23:** Sublimation of CHCA matrix for MALDI-FTICRMS analysis of corticosteroids GirT hydrazones in rat adrenal gland tissue. Signal of Girard T corticosterone (GirT-CORT) was completely suppressed by either sublimation or sublimation followed recrystallisation in comparison with a spray-coated tissue section by TLC-sprayer. Gradient distribution of corticosterone GirT derivative detected at  $[M]^+$   $m/z$  460.3170Da (a) TLC-sprayer coated (Control). (b) Sublimation ( $0.18 \text{ mg/cm}^2$ ). (c) Sublimation/recrystallisation from methanol: water 50:50 +1 %v/v formic acid 95 sec,  $90^\circ\text{C}$ ). ( $n=3/\text{condition}$ ). Signal intensity is depicted by colour as per the scale shown. Scale bar (2 mm). (d): Representative MALDI-FTICRMS of Girard T (GirT)-derivatives during the sublimation studies. The signal of GirT-CORT at  $m/z$  460.314 Da was substantially suppressed in sublimed tissue sections. (dI) Spray coated tissue section (dII) Tissue coated by sublimation followed recrystallisation. cps: count per second.

### 3.3.5.10. Tissue washing to limit ion suppression

A tissue washing procedure was evaluated using ammonium formate and acetate as washing solutions to ameliorate ion suppression caused by inorganic salts and soluble proteins across the tissue surface. As shown in **Figure 3.24**, not only was the tissue morphology adversely affected by washing (**Figure 3.24 A II, III**), but also the signal intensity of GirT-CORT was substantially reduced (**Figure 3.24 B II, III**) in comparison with a control tissue (**Figure 3.24 A I**); therefore this approach was not pursued further.

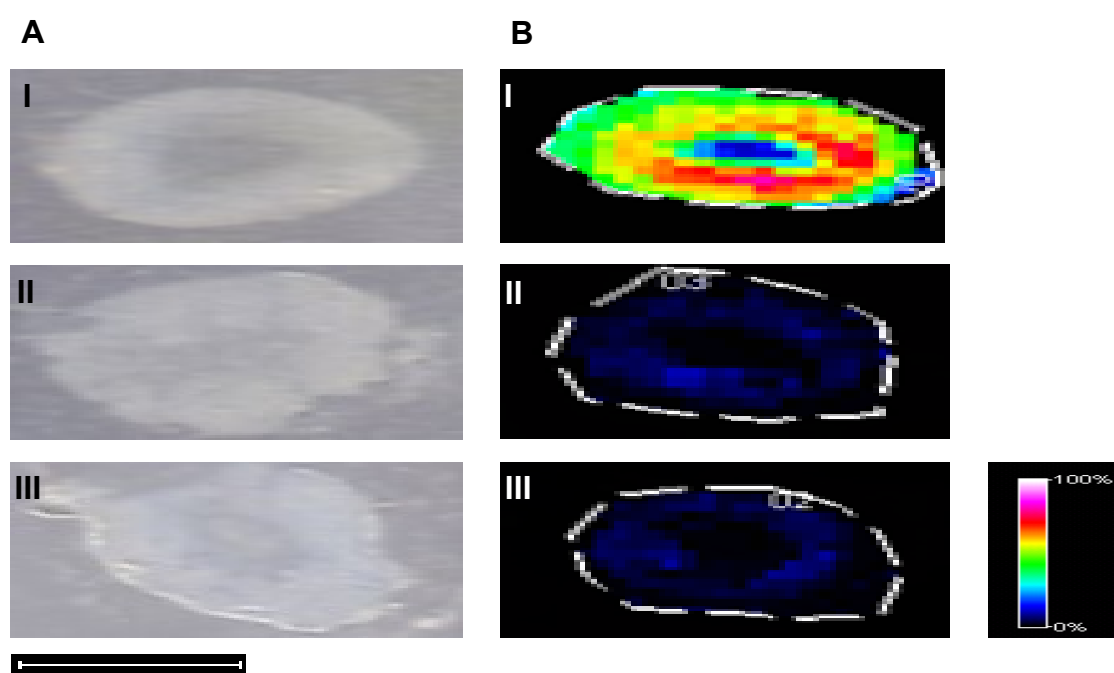


**Figure 3.24:** The effect of washing the tissue surface prior to MALDI-FTICRMS of corticosteroids as Girard T (GirT) hydrazones in rat adrenal gland sections. Results show that tissue washing caused alteration of tissue morphology and suppression of the signal intensity of endogenous corticosteroids imaged as GirT derivatives. (a) Representative optical images of washed tissue sections at 1200 dot per inch (dpi) resolution. **I:** Ammonium acetate washing (AmAc) pH=7 (n=3). **II** Ammonium formate washing (AmFor) pH=4 (n=2). **III** Un-washed control tissue sections (n=3). (b) Representative gradient distribution of GirT derivative of corticosterone detected at  $[M]^+$ ;  $m/z$  460.317 Da. **I:** AmAc washing (n=3). **II** AmFor washing (n=3), **III** Un-washed controls (n=3). Lateral resolution was set at 150  $\mu$ m. Signal intensity is depicted by colour as per the scale shown. Scale bar = 2 mm.

### 3.4. Discussion

The main focus of this chapter was the development and optimisation of a derivatisation technique for use to assess the spatial distribution of corticosterone and its 11-hydroxy metabolite in a biological tissue (adrenal gland) by MSI using a MALDI-FTICRMS platform. Either off and on tissue using pure standards, native corticosteroids were difficult to ionise in the MALDI process giving only low abundance  $[M+H]^+$  ions. The signal could not be improved by use of several novel MALDI matrices. Best ionisation yields were achieved by using the standard MALDI matrix,  $\alpha$ -cyano-cinnamic acid (CHCA). Good sensitivity was also observed by using 2, 5-dihydroxybenzoic acid (DHB), which is a favoured matrix for small molecule analysis, but the main drawback of this approach was the large crystal size, unsuitable for high spatial resolution imaging (Goodwin, 2012). 4-Chloro- $\alpha$ -cyano-cinnamic acid (Cl-CCA) was synthesised in-house, rationally-designed by (Jaskolla *et al.*, 2008) to have a lower proton affinity (PA) and same wavelength absorption (very important for a successful matrix/analyte energy transfer and desorption) than its analogue. Cl-CCA showed suitable ionisation/desorption yields with a much cleaner total ion current (TIC) spectra in the mass range and can be used as a back-up MALDI matrix. However it was inferior to CHCA.

It is hypothesized that PA is crucial for analyte incorporation into the matrix crystal lattice via ion-pair formation with positively charged functional groups. The final ion yield is the result of a complex interplay of analyte incorporation into the matrix crystals, ionisation and ion stability. The lower PA of Cl-CCA can be rationalised as follows: for both CHCA and Cl-CCA, the proton will be located either at the

carboxylic or at the cyano group. In both cases, the positive charge of  $[\text{CHCA}+\text{H}]^+$  can be delocalised over the whole conjugated  $\Pi$ -electron system promoted by the electron-donating effect of the 4-OH group. This stabilisation of the protonated matrix molecule results in a larger PA. The charge delocalization is much less pronounced in the case of a 4-Cl functional group. This is substantiated by density functional theory (DFT) electron-density calculations which exhibit a loss of net positive charge in the para position for Cl-CCA because of the strong electron-withdrawing chloro substituent. However, further decrease the PA of the matrix by more or stronger electron-withdrawing substituents, such as  $\text{CF}_3$  will fail because of the induced hypochromic shifts and the reduction of neodymium-doped yttrium aluminium garnet (Nd:YAG) laser absorption wavelength at 337 nm, used for MALDI analysis.

The attempt to generate the molecular distribution map of neutral steroids in a rat adrenal gland failed, mainly because of the poor ionisation efficiency in MALDI due to the lack of either hydrogen donor or acceptor moieties in the molecular structure. After a screening of several derivatisation reagents, steroids were derivatised using a positive charged hydrazine (Girard-T reagent) as it showed the best results in terms of signal intensity. The OTCD reaction conditions were optimised to achieve the best sensitivity and reproducibility. Hydrazone formation by Girard reagents is a two-step reaction that involves condensation, which is normally achieved by using protic solvent in a weak acid media as catalyst. Derivatisation using methanol/TFA led to the highest yield after one hour incubation at 37 °C in a moisturising environment. Due to the fact that TFA is a strong organic acid that can promote the backward reaction by hydrolysis, stability testing of GirT derivatives was performed and reassuringly degradation was not observed in the typical sample preparation period which is around 20 minutes.



Regarding matrix deposition techniques, both spray and dry coating techniques were evaluated. Spray coating using a pneumatic TLC sprayer accomplished the best analyte extraction from tissue sections. However, the main drawback of this technique is the diffusion effect caused by the matrix solvent and compounded here by the derivatisation process. The analyte delocalisation was controlled by the standardisation of all possible variables, such as nitrogen flow, distance from the MALDI target, time in between passes and solvent volume during manual-based deposition. This issue can also be solved by using automatic matrix deposition devices. Sublimation was evaluated as a dry-deposition technique which allow direct solid to gas phase transition in a reduced pressure environment. During sublimation, a substance, in this case, the MALDI matrix is recrystallised from its molecular gaseous state onto the cold MALDI glass target. The evenness of the coating on the condenser surface reflects the random Brownian motion of the released gaseous matrix molecules. Sublimation has previously been reported as a method matrix application of MSI by Hankin (Hankin *et al.*, 2007). The finely dispersed coating of the organic MALDI matrices that result from sublimation was visually evident in comparison with spray-coating leading to sub-micron crystal sizes which are suitable for high resolution MSI. However, unfortunately signal intensity of GirT steroids was completely suppressed. Sublimation is a solvent-free technique and this may lead to poor analyte extraction from the tissue section. Sublimation followed by recrystallisation was also evaluated in order to increase the extraction from the tissue section without any success. Sublimation has been used for the analysis of non-polar compounds such as lipids in tissue section, but it has not yet been applied for the analysis of polar compounds by MSI. Upon derivatisation, the non-polar neutral steroids were converted to polar quaternary

hydrazones in which desorption/ionisation process is driven by the positive charged quaternary amine. Thus, sublimation may not be an adequate matrix deposition technique for very polar compounds when the matrix solvent plays a key role in compound extraction from tissue sections. In conclusion, spray-coated based techniques, has shown to be the most suitable deposition methodology for MSI of GirT steroids in the studied tissue sections. The fact that spray-based deposition techniques using CHCA as matrix led to crystal size in the sub 10  $\mu\text{m}$  range, MSI can only be performed at  $> 10 \mu\text{m}$  spatial resolution.

The quality of MSI results depends heavily on the choice and execution of sample preparation methods. Specific molecular classes often require different sample preparation treatments, such as optimised washing steps (Goodwin, 2012). Several washing methods have been tested using different buffers systems at different pH by pipette application of the solution onto the sample and subsequent removal by pipette. However, such washing led to undesired morphological changes, as the tissue was severely damaged. Moreover, a considerable loss of sensitivity was observed, so, the washing step was ruled out as part of the sample preparation procedure.

In this chapter, an OTCD-MALDI-FITCRMS MSI platform was successfully developed and optimised to detect endogenous corticosteroids in a biological tissue section (rat adrenal gland). With MSI spatial distribution maps of endogenous steroids were generated adding molecular information at histology level that is impossible to achieve by using the standard tissue homogenisation approach. Having failed to generate molecular maps of native corticosteroids due to the lack of sensitivity, the signal was boosted (up to  $10^4$ -fold) by using tissue derivatisation. Sample preparation

conditions and MALDI-FTICRMS parameters were optimised to achieve the best possible sensitivity. Moreover, analyte diffusion was also controlled by using pre-coated GirT slides to minimise analyte delocalisation. GirT hydrazone derivatives were confirmed by using an orthogonal MS platform (LESA) validating the MSI platform specificity.

### **3.5. Conclusion**

A MSI platform using a MALDI-FTICRMS was developed and optimised for spatial distribution analysis of endogenous and exogenous  $\alpha$ - $\beta$  unsaturated- keto steroids as Girard T hydrazones derivatives in biological tissue sections. In subsequent Chapters, this approach will be applied to answer questions about the distribution and turnover of glucocorticoids in metabolic tissues and brain and applied to alternative analytes.

## Chapter 4

# Application of the MALDI-FTICR-MSI for the assessment of the spatial distribution of endogenous steroids in biological tissues

### 4.1. Introduction

In chapter three a derivatisation reaction was established which allowed detection of glucocorticoids in a rat adrenal tissue where they are highly abundant. In principle this derivative should enable detection of GCs in multiple tissue types but also open up opportunities to detect other  $\alpha$ - $\beta$  unsaturated steroids and oxysterols.

#### 4.1.1. Androgens

Sex steroids such as androgens play a key role in the stimulation and control of the development and maintenance of male characteristics in vertebrates acting by binding with androgen receptors (Labrie, 2004). In terms of the chemistry, most of the androgens contain a ketone group in the molecular structure. This allows the neutral androgens to be derivatised by Girard T reagents leading to the corresponding hydrazones derivatives. A general biosynthetic pathway of the principal androgens is displayed in **Figure 4.1**.

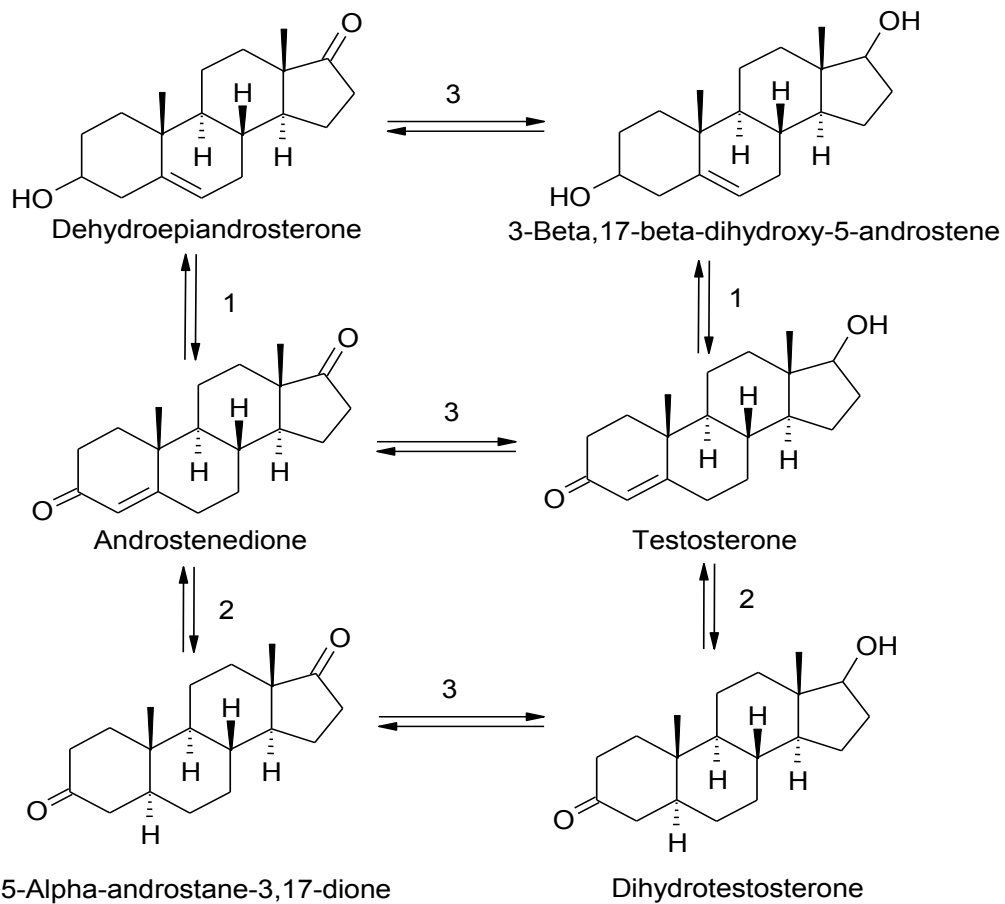


**Figure 4.1** Biosynthetic pathways and interconversion of the major androgens. The numbers refer to the enzymes involved in the reactions: 1=3 $\beta$ -hydroxy  $\Delta$ 5- steroid isomerase, 2 = 5 $\alpha$ -reductases, and 3 = 17 $\beta$ -hydroxy steroid dehydrogenase. Adapted from (Longcope, 2003).

In prostate tissue, direct determination of androgen levels provides a perspective on the organ that is not available via androgen serum levels. The principle prostatic androgens, primarily dihydrotestosterone (DHT) and secondarily testosterone, can be readily assayed in quick-frozen prostate biopsy cores or surgical specimens. Such assays have proved important in establishing (Bartsch *et al.*, 2002) that DHT is a permissive factor in Benign Prostatic Hypertrophy (BPH) pathogenesis, a mechanism for the treatment of BPH, (Carson *et al.*, 2003) an understanding of prostate cancer

chemoprevention, an explanation for the ‘escape’ of prostate cancer from castration therapy, prostate safety of testosterone replacement therapy, and insights into the cause of racial differences of prostate cancer (Schitz-Drager *et al.*, 2007). However, compared with studies of circulating androgens, few studies of prostate tissue androgens are available. This is a major knowledge gap, because circulating androgen levels might not reflect the androgenic activity within the prostate gland and tissue homogenate does not provide distribution information within a specific cell population, ignoring the distinct compartments and functions within tissues or organs. Therefore, spatial distribution determination of prostate tissue androgens would be a valuable tool in androgen research and potentially in clinical diagnosis.

#### **4.1.2. Oxysterols**

Going upstream in the steroid metabolic pathway, oxygenated derivatives of cholesterol (oxysterols) present a remarkably diverse profile of biological activities, including effects on sphingolipid metabolism, platelet aggregation, apoptosis, and protein prenylation (Brown *et al.*, 2009). The most notable oxysterol activities centre on the regulation of cholesterol homeostasis, which appears to be controlled in part by a complex series of interactions of oxysterol ligands with various receptors, such as the oxysterol binding protein, the cellular nucleic acid binding protein, the sterol regulatory element binding protein, the LXR nuclear receptors, and the low-density lipoprotein receptor (Brown *et al.*, 1999; Massey, 2006).

In contrast to glucocorticoids, most of the oxysterols have the alcohol as the main functionality in the molecular structure. However, some physiological relevant oxysterols (IV, VII and IX) have the hydrazine reactive ketone moiety, so application

of the OTCD-MSI would be feasible (**Figure 4.2**). Identification of the endogenous oxysterols and elucidation of their enzymatic origins are topics of active investigation. Currently, endogenous oxysterols are being analysed by LC/MS using tissue homogenate, losing the histological information at molecular level. This is particularly important in tissues such as brain where oxysterols play different roles in different cell compartments in several CNS diseases, e.g. Alzheimer's disease (van Reyk *et al.*, 2006). Therefore, spatial distributions of oxysterols would be beneficial in understanding the underlying biological mechanism. A representative formation pathway is shown in **Figure 4.2**.

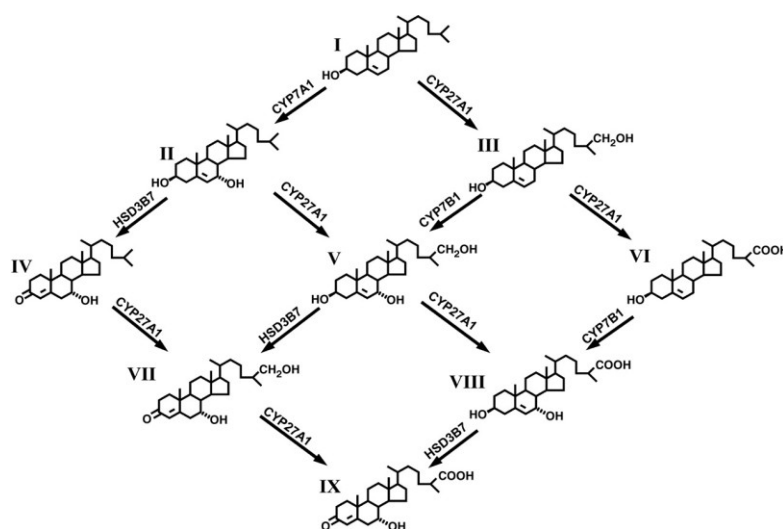


**Figure 4.2:** Metabolism of cholesterol (I) and 27-hydroxycholesterol (III) into 7 $\alpha$ -hydroxy-3-oxo-4-cholestenoic acid (7 $\alpha$ -OH-4-CA) (IX). Based on previously described pathways in other tissues, the formation of 7 $\alpha$ -OH-4-CA (IX) may proceed via an initial formation of 7 $\alpha$ -hydroxycholesterol (II), 7 $\alpha$ -hydroxy-4-cholesten-3-one (IV), and 7 $\alpha$ ,27-dihydroxy-4-cholesten-3-one (VII) or via the formation of 27-hydroxycholesterol (27-OHC) (III), cholestenoic acid (VI), and 7 $\alpha$ -hydroxy-cholestenoic acid (VIII). There is considerable potential for crossover between the different pathways. CYP7A1, cholesterol 7 $\alpha$ -hydroxylase; CYP7B1, oxysterol 7 $\alpha$ -hydroxylase; CYP27A1, sterol 27-hydroxylase; HSD3B7, 3 $\beta$ -hydroxy-C27-steroid dehydrogenase/isomerase; 27-OHC, 27-hydroxycholesterol. Adapted from (Meaney *et al.*, 2007).



In this chapter, the OTCD-MALDI-MSI platform will be explored:

- 1) to identify and quantify glucocorticoids in tissues other than adrenal gland and also tissues derived from humans.
- 2) to identify and quantify different classes of steroids and sterols in relevant biological tissues sections.

## **4.2. Methods**

### **4.2.1. Screening of tissues for suitability to detect glucocorticoids**

Brain and liver tissues were obtained from C57BL/6j mice (6-7 weeks, male). Animals were from Harlan Olac Ltd (Bicester, UK) and killed as per **section 2.2**. Human term placenta from uncomplicated pregnancies was obtained and collected within 15–20 min of vaginal delivery or Caesarean section. Tissues were taken in compliance with the Human Tissue Act 2004 (HTA) under ethical approval. Tissue sectioning was carried out as described in **section 2.3** and histological staining was performed as per **section 2.4**. On-tissue chemical derivatisation was carried out as described in **section 2.5** and matrix was applied as per **section 2.6**. MALDI-FTICR-MSI analysis performed as described in **section 2.8.1** and the ions monitored of GirT-CORT and GirT-11DHC as detailed in **Table 2.1**

### **4.2.2. Detection of androgens**

#### **4.2.2.1. Standards on-tissue**

Standards of both TESTO and DHT (10 µg, 1 µg/µL) of each steroid were mixed with CHCA solution (10 µL, 10 mg/mL in 50:50 (acetonitrile: water) + 0.2 % v/v TFA) using the standard dried droplet method as described in **section 3.2.2.1**. Then, 1 µL of the (steroid: matrix) solution was spotted onto a rat prostate section (n=3) and analysed by MALDI-FTICRMS as described in **section 2.8.2**. Ions monitored of GirT-TESTO and GirT-DHT were detailed in **Table 2.1**.

#### **4.2.2.2.            *Imaging of androgens on prostate tissue sections***

Prostate tissues were obtained from Sprague Dawley male rats (5-7 weeks, ~175-200 g). Animals were from Harlan Olac Ltd (Bicester, UK) and killed as per **section 2.2** and processed as **4.2.1**. Ions of GirT-TESTO and GirT-DHT were monitored as detailed in **Table 2.1**. d<sub>8</sub>CORT was used as ISTD and a normalisation marker for heat map generation.

#### **4.2.3.            *Detection of keto-oxysterols***

##### **4.2.3.1            *Standards on-tissue***

Standards of both 7 $\alpha$ -hydroxy-4-cholesten-3-one (IV) and 7 $\alpha$ ,27-dihydroxy-4-cholesten-3-one (VII) (10 $\mu$ g, 1 $\mu$ g/ $\mu$ L) were mixed with CHCA solution (10  $\mu$ L, 10 mg/ml in 50:50 (acetonitrile: water) + 0.2 % v/v TFA) using the standard dried droplet method as described in **section 3.2.2.1**. Then, 1  $\mu$ L of the (steroid: matrix) solution was spotted onto a rat brain section (n=3) and analysed by MALDI-FTICRMS as described in **section 2.8.2**. Ions monitored of GirT-IV and GirT-VII were as detailed in **Table 2.1**.

#### 4.2.4.2. *Imaging of keto-oxysterols on rat brain tissue sections*

Brain tissues were obtained from Sprague Dawley male rats (5-7 weeks, ~175-200 g). Animals were from Harlan Olac Ltd (Bicester, UK) and killed as per **section 2.2**. Tissues were processed as per **section 4.2.1**. Ions of GirT-IV and GirT-VII were monitored as detailed in **Table 2.1**. d<sub>8</sub>CORT was used as ISTD and a normalisation marker for heat map generation.

### 4.3. Results

#### 4.3.1. MSI of glucocorticoids

##### 4.3.1.1. *Murine liver*

**Figure 4.3** shows the distribution of glucocorticoids in liver section as determined by MSI, with an unstructured pattern. Both CORT and 11DHC were detected as their hydrozone derivatives with high signal to noise ratios ( $S/N > 200$ ) and good mass accuracy ( $<10$  ppm). The signal intensity of GirT-CORT was considerably higher than its inactive metabolite, as liver is rich in  $11\beta$ -HSD1. Histological information could not be interpreted from an MS image, generated at  $150\ \mu\text{m}$  lateral resolution as the spatial resolution was not enough to differentiate cell types.

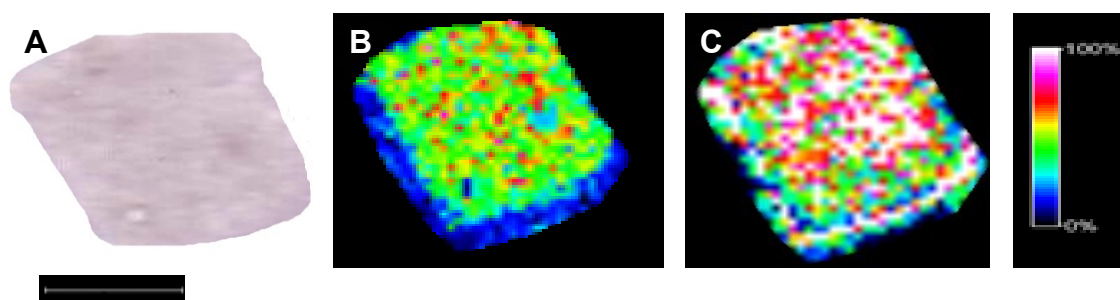


**Figure 4.3:** Molecular imaging by MALDI-FTICR-MSI of corticosteroid hydrazones in representative murine liver sections. Molecular regional distribution maps showed corticosterone (GirT-CORT) and 11-dehydrocorticosterone (GirT-11DHC) derivatives distributed across the section. Histological information could not be interpreted, as the spatial resolution was not enough to distinguish different cellular populations (a) Histological image of a cryosection of murine liver section stained with haematoxylin and eosin. Heat map of (b): GirT-11DHC at  $m/z$  458.301 Da, (c): GirT-CORT at  $m/z$  460.317 Da collated by MALDI-FTICRMS. Signal intensity is depicted by color on the scale shown. Scale bar (2 mm). Lateral resolution was set to  $150\ \mu\text{m}$ .

#### 4.3.1.2. *Murine brain*

The OTCD MSI platform was applied to a murine brain section to generate regional distribution maps of corticosteroids. The analysis was focused on CORT and 11DHC, a product and substrate of the 11 $\beta$ -HSD1 enzyme, respectively. Both steroids were detected as their hydrazone derivatives with good mass accuracy ( $\pm 5$  ppm) against the corresponding monoisotopic molecular weights (**Figure 4.4.E**). Moreover, the S/N ratios for both corticosteroids derivatives were above 10, allowing reliable heat maps to be generated. Signals for corticosteroids were found with greatest intensity across the hippocampus, cortex and amygdala (**Figure 4.4 C, D**) in agreement with the localisation of the mRNA of 11 $\beta$ -HSD1 (**Figure 4.4 B**).

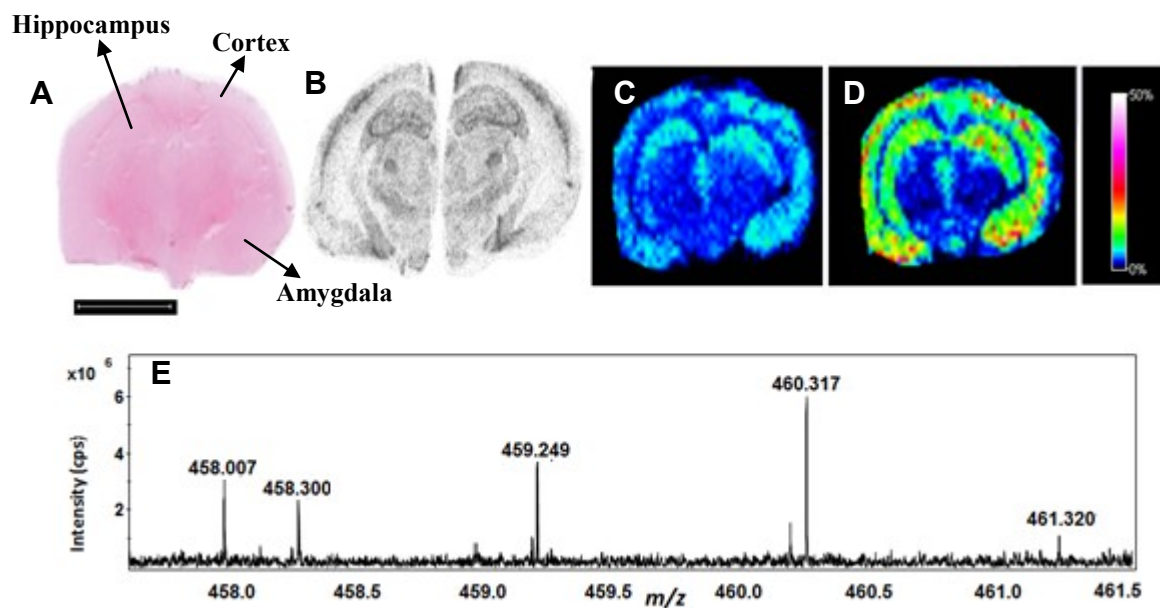


**Figure 4.4:** Molecular regional distribution maps showed corticosterone (GirT-CORT) and 11 dehydrocorticosterone (GirT-11DHC) derivatives primarily distributed in cortex, hippocampus and amygdala, co-localised with 11 $\beta$ -HSD1 mRNA. (a) Histological image of a cryosection of murine brain section stained with haematoxylin and eosin. (b) *In-situ* hybridization (ISH) of 11 $\beta$ -HSD1 mRNA (Imaged gifted by Joyce Yau, University of Edinburgh). Heat map of (c) GirT-11DHC at  $m/z$  458.300 Da, (d) GirT-CORT at  $m/z$  460.317 Da collated by MALDI-FTICR-MS. Signal intensity is depicted by color on the scale shown. Scale bar (2 mm) for imaging, histology and *ISH*. (e) Representative MALDI-FTICRMS spectrum of GirT-11DHC and GirT-CORT in murine brain section. **cps** = counts per second.

#### 4.3.1.3. *Human placenta*

After successful generation of molecular maps of corticosteroids in murine tissues, a feasibility study was conducted on human tissues for potential translational applications. Human placenta was studied, as an 11 $\beta$ -HSD2 rich tissue. Cortisol (GirT-F) and cortisone (GirT-E) hydrazones were detected at  $m/z$  476.312 and  $m/z$  474.296 respectively, with good mass accuracy ( $< 5$  ppm) (Figure 4.5 E). It can be extrapolated from data in section 3.3.51, that a relative response factor of  $\sim 1$  may be assumed for all

keto-steroids derivatives that contain one hydrazine tag. Thus, as shown in **Figure 4.5**, E (product) level (**Figure 4.5 B**) was higher than F (substrate) (**Figure 4.5 C**), each with a different distribution pattern.

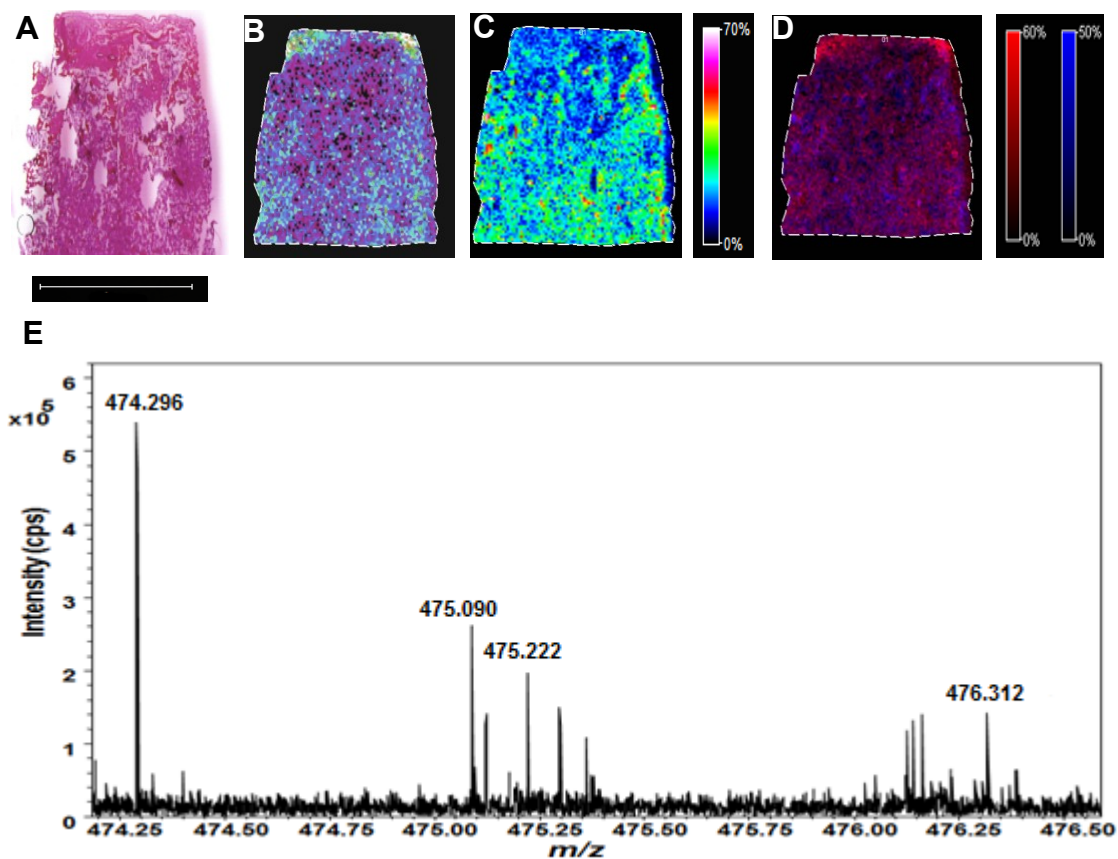


**Figure 4.5:** Molecular imaging by MALDI-FTICR-MSI of corticosteroid hydrazones in a representative human placenta section. (a) Histological image of a cryosection of human placenta sample stained with haematoxylin and eosin. Heat map of Girard T (GirT) derivatives of: (b) cortisol (GirT-F) at  $m/z$  476.312 Da (c) cortisone (GirT-E) at  $m/z$  474.303 Da collated by MALDI-FTICRMS. Signal intensity is depicted by color on the scales shown. Scale bar (2 mm). Lateral resolution was set to 100  $\mu\text{m}$  (e) Representative MALDI-FTICRMS spectrum of both GirT hydrazones in human placenta sample. cps = counts per second.



## 4.3.2. Imaging of androgens

### 4.3.2.1. Standards

The feasibility of derivatising androgens was tested by spotting experiments using testosterone (TESTO) and androstenedione (A4) as androgen standards. The predicted reaction of both androgens with GirT reagent is shown in **Figure 4.6** and both derivatives were detected as hydrazone derivatives at  $m/z$  402.312 Da for TESTO and  $m/z$  400.302 Da for A4 with good mass accuracy (<10 ppm) against their corresponding theoretical monoisotopic mass (**Figure 4.7**).

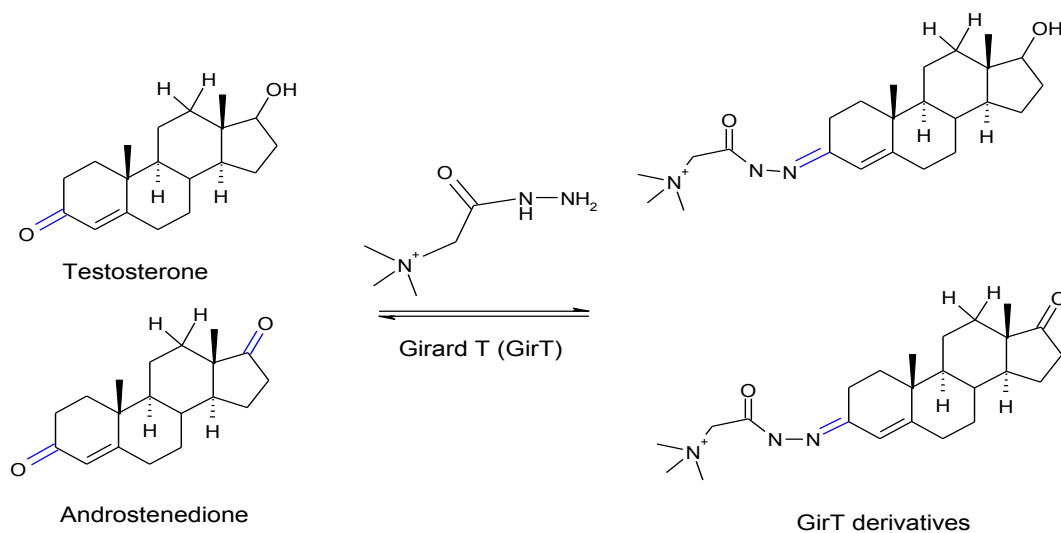


**Figure 4.6:** Androgens GirT derivatisation reaction scheme. Ketone reactive-moiety (blue)

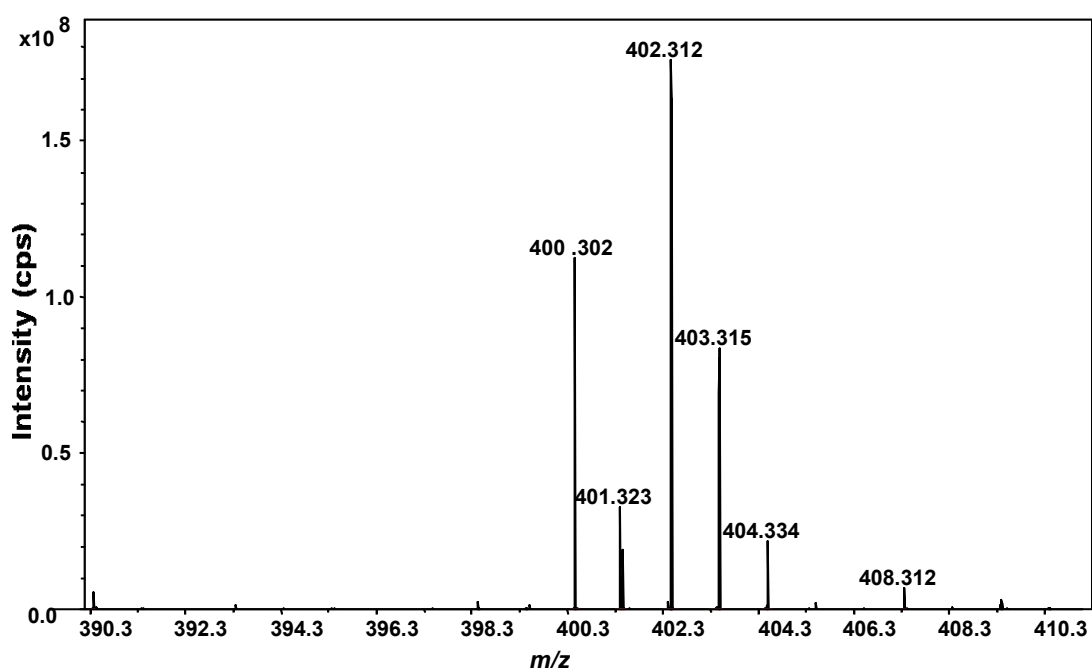


**Figure 4.7:** Representative MALDI-FTICRMS of Girard T (GirT)-derivatives of androgens standards (5 ng). Observed quasimolecular ion at  $m/z$  402.312 (GirT-testosterone) and at  $m/z$  400.302 (GirT-androstenedione). **cps:** count per second.

#### 4.3.2.2. *Imaging androgens in prostate*

The MSI platform was applied to a rat prostate tissue (an androgen-rich tissue) in order to establish if the technique was able to generate molecular maps of androgens in a biologically relevant setting. **Figure 4.8** shown the distribution of testosterone (**Figure 4.8 B**) and androstenedione (**Figure 4.8 C**) detected as GirT-hydrazone derivatives. On the contrary, dihydrotestosterone (5DHT) could not be detected. In line with glucocorticoids, androgens FTICR spectra were well-defined showing an excellent mass accuracy against the theoretical monoisotopic spectra (**Figure 4.8 E**).

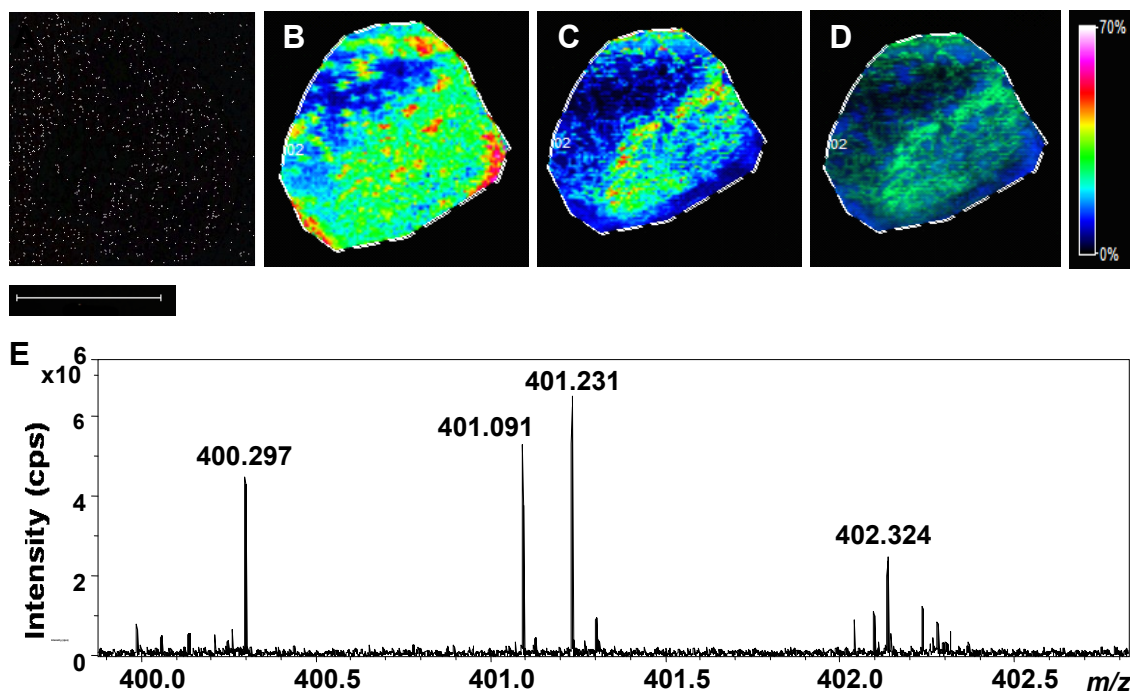


**Figure 4.8:** Molecular imaging by MALDI-FTICR-MSI of androgens as hydrazones derivatives in a rat prostate tissue section. (a) Optical image of a prostate cryosection. Heat map of GirT derivatives of: (b) Testosterone (GirT-TESTO) at  $m/z$  402.324 Da, (c): Androstenedione (GirT-A4) at  $m/z$  400.297 Da collated by MALDI-FTICRMS. (d): Heat map superimposition of GirT-A4 (green) and GirT-TESTO (blue). Signal intensity is depicted by color on the scale shown. Scale bar (2 mm). Lateral resolution was set to 100  $\mu\text{m}$ . (e) Representative MALDI-FTICRMS spectrum of androgen derivatives in rat prostate. cps = counts per second.

#### 4.3.2.3. *Androgens and Glucocorticoids*

As GirT reacts with all activated and non-activated ketone groups, an extended FTICRM spectra was generated to see the multiplex capabilities of the GirT derivatisation (**Figure 4.9**).

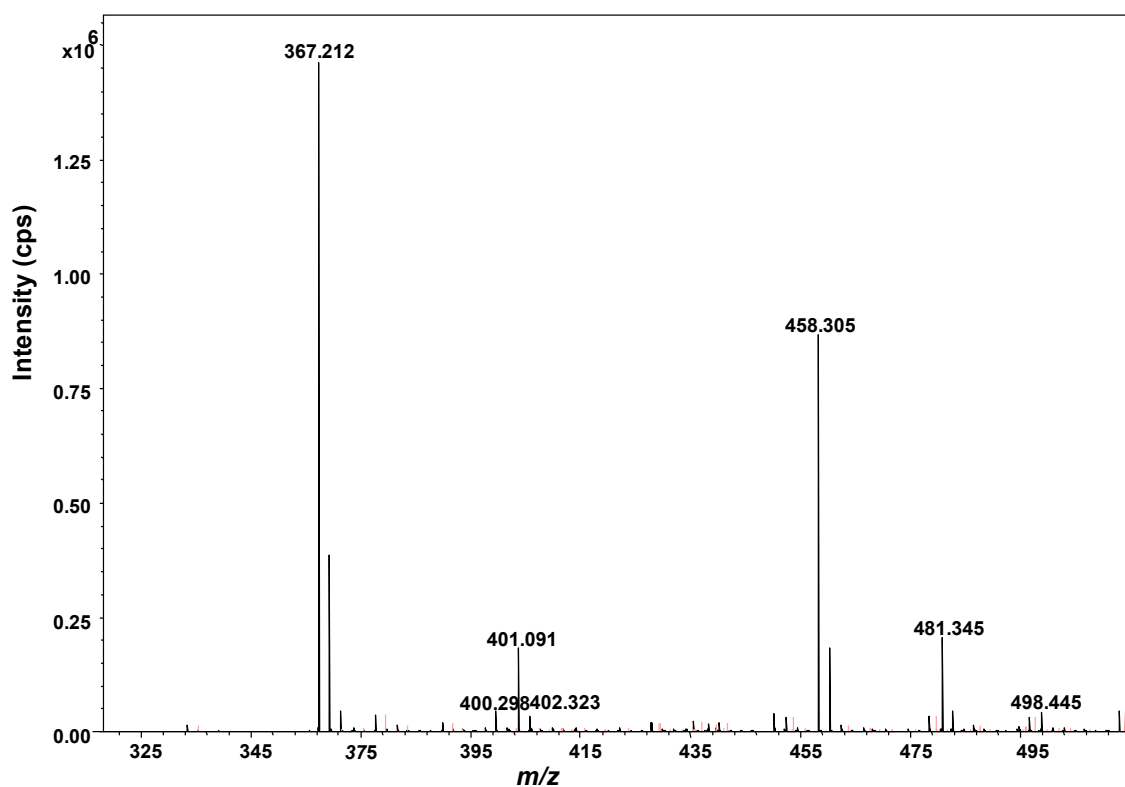


**Figure 4.9:** Representative extended MALDI-FTICRMS spectrum of androgens and glucocorticoids derivatives in rat prostate. Testosterone (GirT-TESTO) at  $m/z$  402.323 Da, Androstenedione (GirT-A4) at  $m/z$  400.298 Da and 11-dehydrocorticosterone (GirT-11DHC) at 458.305 Da. **cps** = counts per second.

### 4.3.3. Imaging of oxysterols

#### 4.3.3.1. Standards

Oxysterol standards,  $7\alpha$ -hydroxy-4-cholesten-3-one (IV) and  $7\alpha,27$ -dihydroxy-4-cholesten-3-one (VII) (**Figure 4.2**) were selected for a feasibility study to image oxysterols. These oxysterols shared the same ketone-reactive moiety as glucocorticoids, so, derivatisation reaction with GirT-hydrazine could be possible (**Figure 4.9**). Standard were derivatised as per in **section 2.6.4** and analysed as described in **section 2.9.2**. As is shown in **Figure 4.10** the selected oxysterols were

detected as GirT derivatives with good mass accuracy (<10 ppm against their corresponding theoretical monoisotopic mass).

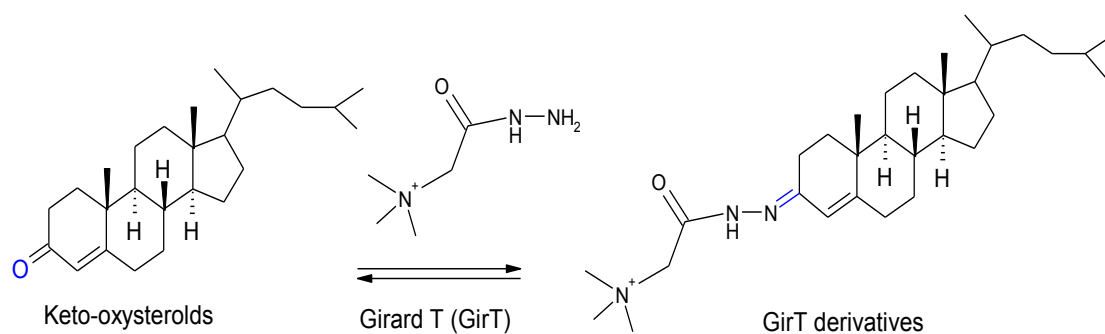


**Figure 4.10:** Proposed reaction scheme for derivatisation of keto-oxysterols with Girard T (GirT) reagent. Ketone reactive-moiety (blue)

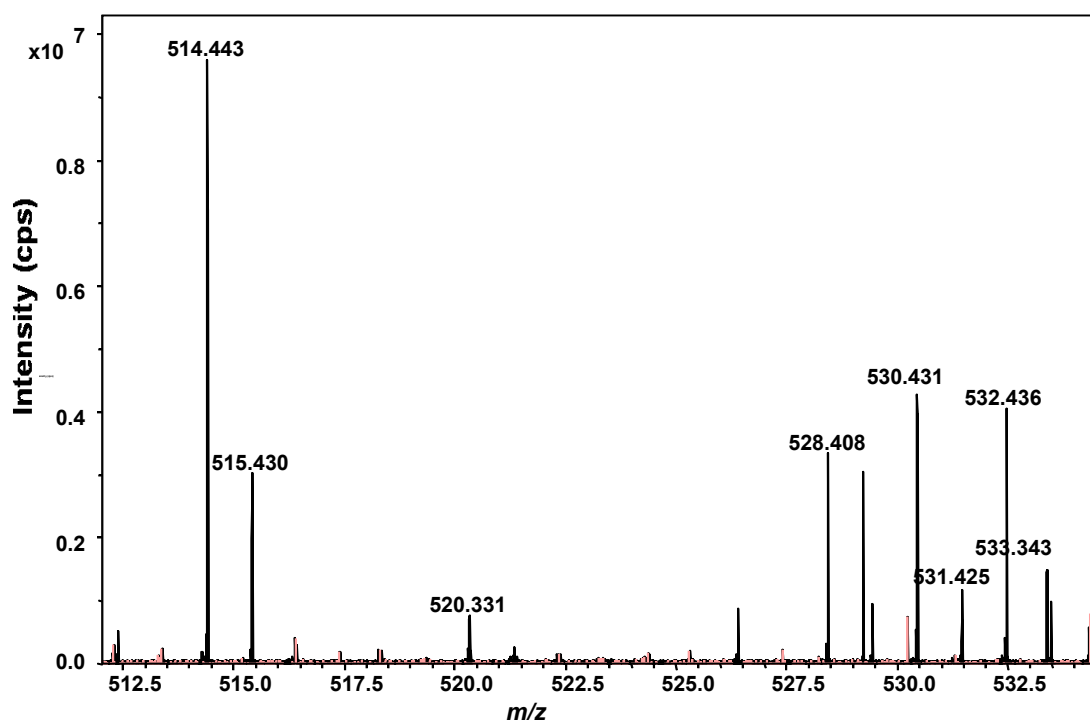


**Figure 4.11:** Representative MALDI-FTICRMS of Girard T (GirT)-derivatives of keto-oxysterols standards (5 ng). Observed protonated masses at  $m/z$  514.443 (GirT-IV) and at  $m/z$  530.431 (GirT-VII). Good mass accuracy was observed ( $\Delta < 10$  ppm on both derivatives). **cps**: count per second.

#### 4.3.3.2. *Imaging Oxysterols in Rat Brain*

It was proposed that the regional distribution of sterols with the hydrazine reactive motif may be measured in tissue by the OTCD-MSI platform (**Section 4.3.3.1**). In this example, molecular distribution maps of cholesterol metabolites (oxysterols) were successfully generated in a rat brain tissue section.

Both oxysterols measured,  $7\alpha$ -hydroxy-4-cholesten-3-one (GirT-IV) and  $7\alpha$ , 27-dihydroxy-4-cholesten-3-one (GirT-VII), were detected with an excellent mass accuracy of  $\pm 2.5$  ppm against their corresponding theoretical monoisotopic masses (**Figure 4.141E**). However, oxysterol IX could not be detected and MSI images were not generated.

The two detected oxysterols shared the same pattern and were widely distributed across the striatum, hippocampus, cortex and cerebellum (**Figure 4.11**). The relative abundance of the keto-oxysterol identified as (GirT-IV) at  $m/z$  514.444 was higher (**Figure 4.11 B**) than its hydroxyl metabolite (GirT-VII) at  $m/z$  530.532 (**Figure 4.11 C**).

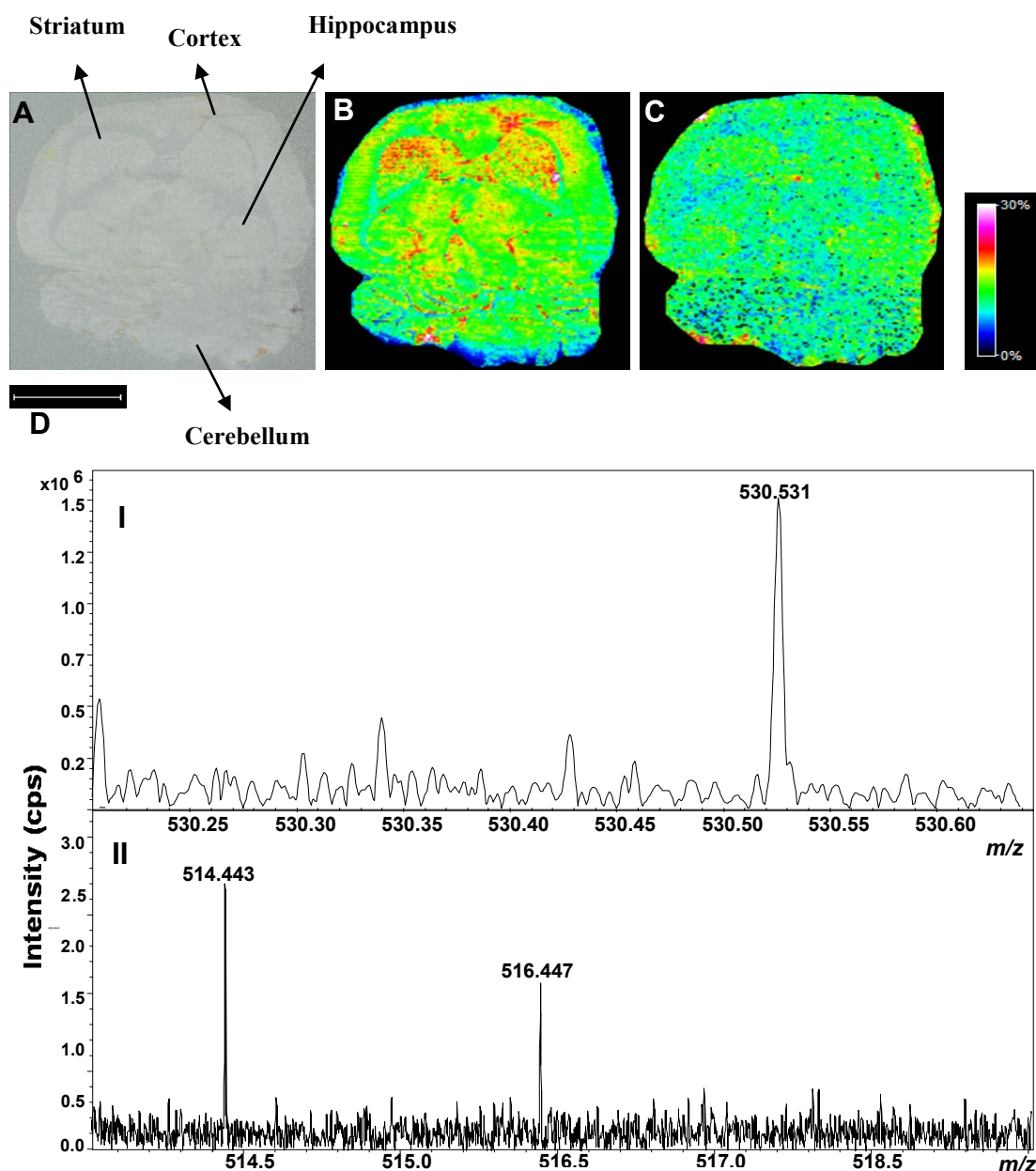


**Figure 4.12** : Molecular imaging by MALDI-FTICR-MSI of oxysterols detected as Girard T (GirT) hydrazone derivatives in a rat brain section. Oxysterols were distributed with high abundance in the striatum, hippocampus, cortex and cerebellum. (a) Optical image of a cryosection of rat brain section. Heat map of oxysterols derivatives of: (b)  $7\alpha$ -hydroxy-4-cholesten-3-one (GirT-IV) at  $m/z$   $514.443 \pm 0.025\text{Da}$ , (c)  $7\alpha,27$ -dihydroxy-4-cholesten-3-one (GirT-VII) at  $m/z$   $530.531 \pm 0.025\text{Da}$  by MALDI-FTICRMS. Signal intensity is depicted by color on the scale shown. Scale bar (10mm). Lateral resolution was set to  $150\ \mu\text{m}$ . (d) Representative MALDI-FTICRMS spectrum of (i) GirT-IV and (ii) GirT-VII in a rat brain section. **cps** = counts per second.

#### **4.4. Discussion**

In this chapter the application of the OTCD MSI platform to other physiological relevant keto-steroids was demonstrated in several tissue types. Girard reagents have been used to derivatise ketone-containing compounds such as (quinones, natural product, drug-like molecules and steroids) to form the corresponding hydrazone analogues. Upon derivatisation, neutral molecules are converted to positive-charged derivatives enhancing the detection during MS analysis. As it shown in **Ch 3**, the intensity of signal from neutral glucocorticoids was considerable enhanced upon derivatisation with GirT. In this chapter the application OTCD MSI platform was extended to other physiological relevant rodent and human tissues including human biopsies. Furthermore, molecular images were also generated for other keto-containing sterols such as androgens and oxysterols.

The main advantage of using MSI over conventional tissue-homogenate analysis is the generation of molecular distribution maps across the tissue section of both targeted exogenous and endogenous compounds. Tissue-homogenate analysis involves averaging of the composition across the tissue section and in most cases the tissue is not homogenous, with many different histological features due to diverse cell populations. However in some cases, homogeneity can be assumed when the spatial resolution of an image is not enough to distinguish different cell types. At the spatial resolution used in this study (200-100  $\mu\text{m}$ ), ten to twenty times the size of an average mammalian cell (10  $\mu\text{m}$ ), and histological evaluation would be possible in tissue such as brain, adrenal gland and kidney. For example in brain, the cortex can be



differentiated from the hippocampus and in the kidney, distinction of the medulla and cortex can also be possible.

Having generated the successful molecular maps of CORT and 11DHC in the adrenal gland, a number of tissues were evaluated as matrices for imaging glucocorticoids. In liver the steroids could be detected but this tissue appeared homogenous and therefore no particular advantage was gained by imaging. The size of the hepatocytes are much smaller than the laser spot size (50  $\mu\text{m}$ ) (Vind *et al.*, 1992), using MSI approaches at low spatial resolution mode. In the liver, steroid distribution may be studied at cell or sub-cellular resolution using high resolution MALDI (spot size  $\sim 5 \mu\text{m}$ ) or SIMS. However, increasing the spatial resolution dramatically decreases the sensitivity. Nonetheless relative abundance of glucocorticoids could be gleaned from this method, in a manner that avoids the losses and extensive processing required to handle tissue homogenate with subsequent LC-MS/MS.

Imaging of adipose, another metabolic tissue was not successful. Adipocytes are small and again the tissue may appear homogenous with low resolution imaging, Adipose also had another disadvantage as during on-tissue derivatisation the tissue is exposed to a wet environment leading to a substantial tissue disruption and analyte delocalisation making MSI of derivatised steroids practically impossible. This may be due to its high lipid content.

The method was applied to imaging these glucocorticoids in murine brain, where the levels of corticosteroid are lower than in the adrenal gland. The highest abundance in cortex, hippocampus and amygdala may reflect the higher expression of corticosteroid-

binding receptors as well as of 11 $\beta$ -HSD1 in these brain regions (Moisan *et al.*, 1990a).

This approach is pursued further in **Ch 5**.

The MALDI-MSI platform was also applied to human placenta tissue to evaluate the capability of the methodology of measuring human-counterpart corticosteroids, active cortisol and inactive cortisone. In the human placenta, the mRNA and protein for both 11 $\beta$ -HSD-1 and -2 are primarily expressed in the syncytiotrophoblast (Benediktsson *et al.*, 1997). It was demonstrated that the mRNA and protein levels of 11 $\beta$ -HSD2 increases with advancing gestation promoting the inactivation of cortisol (Blum *et al.*, 1995). A sample of human placenta tissue biopsy collected at term showed higher E levels than the active F. This finding was in agreement with the current understanding of the physiology of the placenta as the pattern of placental cortisol-cortisone metabolism changes from preferential reduction (formation of cortisol from cortisone) early in pregnancy to oxidation assisted by oestrogens (conversion of cortisol to cortisone) near term.

To further evaluate the advantage of MSI as a multiplex platform, the analysis was extended to androgens. In a rat prostate tissue section, testosterone and A4 were detected as hydrazone derivatives and the corresponding molecular maps were generated. These preliminary data open new avenues to study androgen metabolism and biomarkers at tissue-specific level in some important research areas such as testis development and prostate cancer. In particular prostate cancer, circulating levels of diagnostic biomarkers may not reflect the tissue microenvironment, therefore evaluation of tissue-specific biomarkers would be beneficial (Corrie *et al.*, 1985).

To further expand the applicability of the MSI platform to study sterol biology, molecular distribution maps of oxysterols were generated in a rat brain tissue section. Oxysterols  $7\alpha$ -hydroxy-4-cholesten-3-one (IV) and  $7\alpha, 27$ -dihydroxy-4-cholesten-3-one (VII) were selected with chemical motifs allowing them to react with GirT. These oxysterols are the substrate and product of the sterol 27-hydroxylase (CYP27A1), allowing inferences to be drawn about the enzyme activity. This enzyme is located in the energy-producing centres of cells (mitochondria), where it is involved in the pathway that breaks down cholesterol to form acids used to digest fats (bile acids) (Li *et al.*, 2007). Sterol 27-hydroxylase plays a key role in maintaining normal cholesterol levels in the body. Accumulation of some oxysterols throughout the body, particularly in the brain and tendons has been proposed to lead to the signs and symptoms of cerebrotendinous xanthomatosis and cognitive impairment (Pannu *et al.*, 2013). So knowing the molecular distribution could be valuable to understanding the underlying mechanism. However, as only detection was achieved, further development and validation must be carried out before using this method to study oxysterol biology.

#### **4.5. Conclusion**

In this chapter the potential for the application of MALDI-MSI with OTCD using Girard-T reagent to study diverse steroid and sterol biology has been demonstrated. Molecular maps have been generated of glucocorticoids, androgens and oxysterols in several rodent tissue sections, where analytes were selected with the appropriate chemical groups to react with Girard T. Indeed this could be expanded to include progesterone-type molecules as well. Furthermore, beyond murine and rat tissues, human samples have been successfully analysed showing good selectivity and sensitivity in detecting human steroid counterparts. MALDI-MSI is a powerfully multiplexed platform to study tissue molecular histology. Indeed, its ability to uncover biomolecular intratumour heterogeneity may grow to provide a valuable tool for addressing one of the key challenges facing adrenal oncology research.

## Chapter 5

# Monitoring effects of 11 $\beta$ -hydroxysteroid dehydrogenase-1 deficiency or inhibition on region-specific corticosteroid concentrations in brain by MALDI/LESA-FTICRMS-MSI

### 5.1. Introduction

Measurement of plasma concentrations of steroid hormones has shown the intricate control of their secretion from endocrine glands. Recently, it has been recognised that steroid concentrations within tissues are also modulated locally by steroid-generating and inactivating enzymes. This has been confirmed in spontaneous human enzyme deficiency syndromes, recapitulated by genetic disruption in mice and using pharmacological inhibitors (Simpson *et al.*, 1994). Dysregulation of steroid-metabolizing enzyme expression is thought important in the pathophysiology of steroid-dependent disease, including breast cancer, prostate disease and obesity. Moreover, inhibitors of these enzymes have proved the reduction of steroid action in these disorders. A key limitation in the field of 'steroid intracrinology', however, is the inability to study steroid concentrations at tissue level, particularly in organs with region-specific expression of key-role enzymes, such as the brain. Up to now, the

inferences of the consequences of enzyme manipulation for local steroid concentrations therefore remain qualitative rather than quantitative.

This chapter will focus on the role of 11 $\beta$ -HSD1, which is highly expressed in metabolically active tissues such as the liver, adipose, kidney, and brain and mainly converts inactive into active glucocorticoids (Chapman *et al.*, 1997). The potential for therapeutic intervention has been demonstrated in rodent models where selective 11 $\beta$ -HSD1 inhibitors lower plasma glucose, improve insulin sensitivity and in some studies reduce body weight in mice (Bujalska *et al.*, 2008; Hughes *et al.*, 2008; Webster *et al.*, 2007). In the brain, 11 $\beta$ -HSD1 mRNA expression and activity is mainly observed in the cerebellum, hippocampus and cortex (Moisan *et al.*, 1990a). Higher levels are found in Purkinje cells in the cerebellum, CA3 pyramidal cells in the hippocampus and layer V neurons in the neocortex. Inhibition of 11 $\beta$ -HSD1 in brain is associated with improved memory (Sooy *et al.*, 2010) but the consequences for local steroid regeneration in the brain sub-regions where 11 $\beta$ -HSD1 is expressed are uncertain. Furthermore, 11 $\beta$ -HSD1 can interconvert other keto substrates, including 7-keto and 7 $\alpha$ -hydroxycholesterol (Mitic *et al.*, 2013), but it has been difficult to establish the equilibrium of these reactions *in vivo*. In this chapter, OTCD, in combination with MSI was applied, for the first time to quantify and validate the detection of CORT and 11DHC and alternative substrates within sub-regions of murine brain, following manipulation of 11 $\beta$ -HSD1. The aim of this chapter is to monitor the effects of 11 $\beta$ -hydroxysteroid dehydrogenase-1 (11 $\beta$ -HSD1) deficiency or inhibition on region-specific corticosteroids concentration in brain.

## **5.2. Methods**

### **5.2.1. Biomatrix**

The effect of deficiency of the 11 $\beta$ -HSD1 enzyme was studied in the following models:

- C57BL/6j 11 $\beta$ -HSD1<sup>-/-</sup> mice (KO) and their wild-type (WT) littermates (male, 2-3 months) were bred in-house. The genetically modified animals were genotyped using protocols described by (Morton *et al.*, 2001) and obtained from in-house breeding colony
- C57BL/6j mice (6-7 weeks, male) were from Harlan Olac Ltd (Bicester, UK) and studied after pharmacological inhibition of 11 $\beta$ -HSD1 (n=6/group, killed 1h, 4hs and 6hs after receiving UE2316 (25 mg/kg oral, in DMSO: PEG-400: saline (0.9 %w/v) (2:38:60)) or vehicle).

In all studies, animals were killed by decapitation at 09:00 h, Plasma was prepared from trunk blood, collected in EDTA. Tissues were snap frozen in liquid nitrogen and stored (-80 °C).

### **5.2.2. MSI**

#### **5.2.2.1. Steroids**

Tissues were harvested as per **section 2.2** and MSI performed as described in **section 2.8.1**. The identities of ions of the steroid-GirT hydrazones were confirmed on-tissue by CID using LESA as described in **section 2.9**. The average spectral intensities of steroid derivatives in ROIs across the cortex, hippocampus and amygdala were

recorded using MSI, presented as ratios of CORT/11DHC and compared with those generated by LESA and LC-MS/MS.

#### **5.2.2.2. *UE2316***

Tissues were harvested as per **section 2.2**, matrix was applied as described in **section 2.6**, analysed by MALDI-FTICR-MS as per **section 2.8.1** and MS images generated using the quasimolecular ion of UE 2316 as per **Table 2.1**.

#### **5.2.3. Approaches to validate quantitation**

##### **5.2.3.1. *Extraction of steroids from whole brain***

Analysis was adapted from (Griffiths *et al.*, 2011). In brief, murine brain (~300mg) was homogenised in methanol–acetic acid (100:1 v/v, 10 mL) using a mechanical homogeniser and assisted by ultrasonication. The supernatant was retained and the pellet formed followed centrifugation (5000 × g, 10 min, 4 °C), further extracted with methanol–acetic acid (100:1 v/v, 10 mL). The supernatants were combined and stored at -80 °C. The extract was reduced to dryness and re-dissolved (3 mL, methanol/dichloromethane/water (7:2:1, v/v)) and enriched with internal standard. d<sub>8</sub>CORT (5 ng). The sample, prepared in methanol/dichloromethane/water (7:2:1, v/v), was passed through a diethylaminohydroxypropyl Sephadex LH-20 (GE Healthcare, Sweden) anion-exchange column in its acetate form (7 × 0.4 cm). The column was washed with 2 mL of the same solvent, followed by 1 mL of methanol/dichloromethane/water (2:2:1, v/v), and the “flow-through” and “wash” combined, dried and re-dissolved in methanol–acetic acid (2 mL, 100:1 v/v) with the final addition of water (2 mL). The solution was passed through a Bond-elut (HLB, 2 g,



Waters, Manchester, UK) cartridge. After washing with water (2 mL), methanol–water (1:1, 3 mL) and hexane–ethyl acetate (5:1, 2 mL), the steroids were eluted with ethyl acetate (2 mL). The residue was evaporated, re-dissolved in 50:50 (methanol: H<sub>2</sub>O with 0.1% of formic acid (FA)) and subjected to LC-MS/MS analysis as per **section 5.2.3.3**. Calibration curve was prepared as described in **section 5.2.3.3**

#### **5.2.3.2.        *Extraction of steroids from plasma***

Analysis was adapted from Hughes (Hughes *et al.*, 2010). The method consisted of the following: 500 µL (for HPLC), 50 µL (for MALDI) of plasma was transferred to 10 mL glass tube; ISTD was then added (50 ng) to each sample followed the extraction with CHCl<sub>3</sub> (3 x5 mL), the solutions were shaken (15min, centrifuged (3500 g, 50 min, 4°C)), the organic extracts were combined, retained and the plasma removed. The organic layers were dried under oxygen free nitrogen (OFN) at RT, submitted to LC-MS/MS analysis as described in **section 5.2.3.3**.

#### **5.2.3.3.        *Quantitative analysis of steroids by LC-MS/MS***

Solutions (0.1 mg/mL in methanol) of CORT and 11DHC were serially diluted with water (as simulated media) to prepare calibration standards (0.1-50 ng each steroid) with the addition of d<sub>8</sub>CORT (5 ng), and processed as tissue (**section 5.2.2.2**) and plasma (**section 5.2.2.3**). The final extracts were dissolved in (50:50) methanol: formic acid 0.1% v/v. Separation was achieved on an Inerstil ODS-3 100 x 2.1 mm, 3 µm (GL Sciences, Torrance, USA) column. Mobile phases, consisting of 0.1% v/v FA in H<sub>2</sub>O (A) and 0.1 % v/v formic acid in 90:10 (acetonitrile: methanol) (B), were used at a flow rate of 0.3 mL/min, with an initial hold of 3 min at 35 % B followed by a linear

gradient to 90 % B in 8 min and re-equilibration at initial conditions (2 min). Column and autosampler temperatures were 45 °C and 10 °C respectively. Electrospray ionisation was performed with an ion source voltage of 4500V, medium collision gas and source temperature 450°C. Data were acquired by multiple reaction monitoring at the following transitions (collision energy, declustering potential, cell exit potential): CORT  $m/z$  347→121 (31,148,12 V); 11DHC  $m/z$  345→121 (30,155,15 V); and  $d_8$ CORT  $m/z$  355→125 (32, 119,12 V). Peaks area ratios were calculated and interpolated onto a standard curve (peak area ratio vs amount) derived from data generated by corresponding calibration samples.

#### **5.2.4. Extraction of UE2316 from whole brain**

Brain tissue (~150 mg) was homogenized in 5 mL of buffer (50:45:5 Hepes: Tris (0.1 M): sodium lauryl sulphate (0.5%), pH 9.5 adjusted with sodium hydroxide (NaOH) containing 100 µg/mL of Protein K enzyme. UE2346 ([4-(4-chlorophenyl-4-fluoro-1-piperidinyl) [5-(1H-pyrazol-4-yl)-3-thienyl]-methanone) was added (ITSD 100 ng) and homogenates were incubated in a rotating water bath (37°C, 60 min). Samples were allowed to cool to RT and subjected to centrifugation (3500 g, 15 min, 4°C). Supernatants were filtered through a 0.45 µm nylon (Millipore, Chesire, UK) filters and extracted with 3 x 5 mL of ethyl acetate. Organic layers were reduced to dryness under gentle stream of nitrogen at RT and residues were reconstituted in (acetonitrile: water 50:50 containing 0.1 % formic acid) (100 µL) and samples were then submitted to LC-MS/MS analysis as described in **section 5.2.4.1**.

#### **5.2.4.1.            *Quantitative LC-MS/MS UE2316 analysis***

Stock solutions of 1 mg/mL of UE 2316 and UE 2346 (ISTD) were obtained by dissolving 1.0 mg of corresponding analytes in 1 mL of methanol. Working standards of 5, 25, 100, 250, and 500 ng were prepared by serial dilution of the stock solution in methanol and were stored in vials at  $-20^{\circ}\text{C}$  protected from light. Standard curves were prepared using water as a simulated media and ion suppression was evaluated by standard addition experiments at 25 and 250 ng respectively using brain tissue from an untreated mouse. The final extract was dissolved in mobile phase (50:50) acetonitrile: formic acid 0.1% v/v. Separation was achieved on a Kinetex PFP column 100 x3 mm, 2.6  $\mu\text{m}$  (Phenomenex, Macclesfield, UK,). Mobile phases, consisting of 0.1% v/v FA in  $\text{H}_2\text{O}$  (A) and 0.1% v/v formic acid in acetonitrile (B), were used at a flow rate of 0.35 mL/min, with an initial hold of 2 min at 20% B followed by a linear gradient to 100% B in 10 min and re-equilibration at initial conditions (2 min). Column and autosampler temperatures were  $40^{\circ}\text{C}$  and  $10^{\circ}\text{C}$  respectively. Electrospray ionisation was performed with an ion source voltage of 5000V, medium collision gas and source temperature  $450^{\circ}\text{C}$ . Data were acquired by multiple reaction monitoring of the following transitions (collision energy, declustering potential, cell exit potential): UE2316  $m/z$  391 $\rightarrow$ 177 (31,148,12V) and UE2346  $m/z$  482 $\rightarrow$ 194 (35, 115,10V). Peaks area ratios were calculated and interpolated onto a standard curve (peak area ratio vs amount) derived from data generated by corresponding calibration samples.

#### **5.2.5.            *Data analysis***

Data are expressed as mean  $\pm$  SEM and differences were analyzed using two-way ANOVA with Bonferroni's post-hoc test (MSI and LESA) and Student's t-test (LC-

MS/MS) as appropriate. Statistical significance was accepted at  $p < 0.05$ . A statistical trend is defined as  $0.05 < p < 0.1$ . For correlation analysis between MSI, LESA and LC-MS/MS, Bland-Altman plots with 95% confidence intervals were used. Analysis was performed according to **section 2.10**.

### **5.3. Results**

#### **5.3.1. Studies of genetic manipulation of 11 $\beta$ -HSD1**

Endogenous CORT (**Figure 1B, 1D**) and 11DHC (**Figure 1C, 1E**) were successfully detected as GirT hydrazones by MSI in sections of murine brain from both wild-type (WT) and 11 $\beta$ -HSD1<sup>-/-</sup> mice. Corticosteroid derivatives were detected in highest abundance in the cortex, hippocampus and amygdala as demonstrated in **Ch4**. In 11 $\beta$ -HSD1<sup>-/-</sup> mice, the CORT/11DHC ratio was reduced in these regions of interest (**Figure 5.1F**). Absolute ratios (and magnitude of difference between 11 $\beta$ -HSD1<sup>-/-</sup> and WT mice) obtained by LC-MS/MS and LESA were similar to those determined by MSI (**Figure 5.1F**). Absolute measurements (**Figure 5.1G**) suggested the change in pattern between genotypes was driven by both increased amounts of 11DHC and reduced amounts of CORT, although only the former was statistically significant.

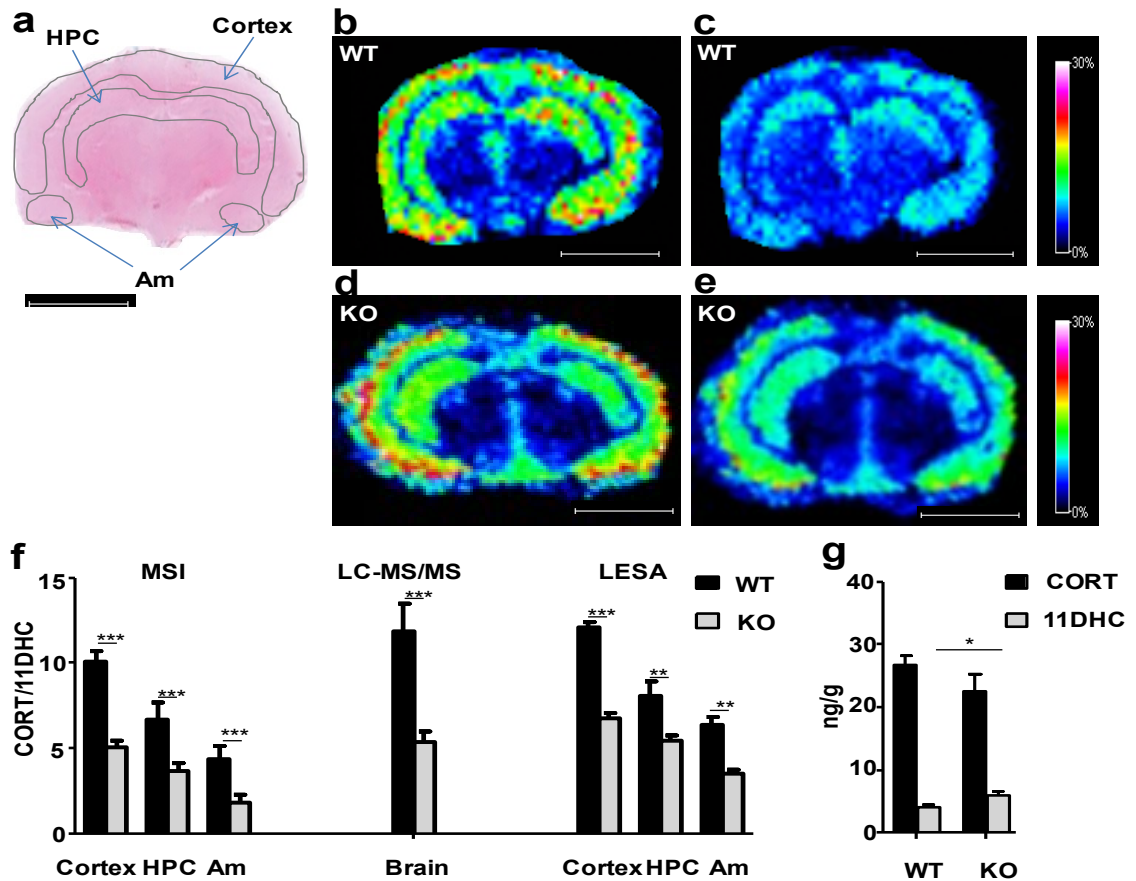


**Figure 5.1:** Effect of 11 $\beta$ -hydroxysteroid dehydrogenase type 1 deficiency on proportions of active and inactive glucocorticoids in regions of murine brain. Girard T (GirT) corticosteroid hydrazones (corticosterone (CORT) and 11-dehydrocorticosterone (11DHC)) were most abundant in the cortex, hippocampus and amygdala with lower CORT/11DHC ratios observed upon disruption of the enzyme primarily caused by an accumulation of 11DHC. (a) Histological image of cryosection of murine brain stained with haematoxylin and eosin with the outline of the MSI regions of interest (ROIs) (cortex; hippocampus, HPC; and amygdala, Am). (b, d) Heat map distribution by MALDI-FTICR-MSI of GirT-CORT derivative at  $m/z$  460.317 Da in wild type (WT) (b) and 11 $\beta$ -HSD1 $^{-/-}$  (KO) (d) mice. (c, e) Heat map distribution by MALDI-FTICR-MSI of GirT-11DHC derivative at  $m/z$  458.301 Da in WT (c) KO (e) mice. Signal intensity is depicted by color on the scale shown. Scale bar (2mm). cps = count per second. (f) CORT/11DHC ratios measured by MALDI-FTICR-MSI (MSI), LC-MS/MS and LESA in regions of interest in murine brain were lower in KO mice than WT ( $p < 0.001$  overall between genotypes). (g) Differences between genotypes in CORT/11DHC ratios were caused by an increase of 11DHC and a trend ( $0.05 < p < 0.1$ ) to a similar magnitude of reduction in CORT in 11 $\beta$ -HSD1 $^{-/-}$  mice, measured in whole brain by LC-MS/MS. Statistical analysis was by two-way ANOVA for LESA and MSI and Student's  $t$ -test for LC-MS/MS and absolute measurements ( $n=12$ ). Data are mean  $\pm$  SEM. \* $P < 0.05$ , \*\*  $P < 0.01$  and \*\*\*  $P < 0.001$ .

### 5.3.1.1. *CORT and 11DHC quantitation in plasma and brain by LC/MS*

Upon enzyme depletion, an average decline in the absolute level of CORT (~16 %) with a simultaneous increase (~50 %) with 11DHC level was observed in brain homogenate. However, no differences were observed in plasma levels as both WT and KO shown the same profile (**Figure 5.2**).

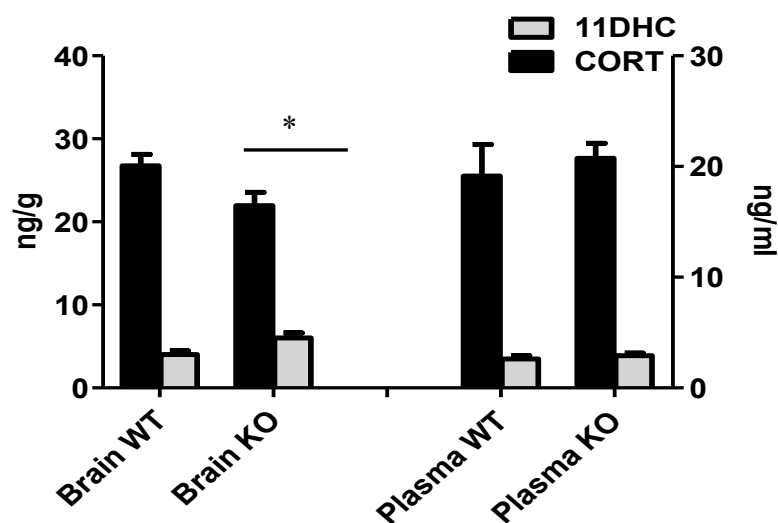


**Figure 5.2:** Absolute quantitation of corticosterone (CORT) and 11-dehydrocorticosterone (11DHC) measured by LC-MS/MS of plasma and brain homogenate in 11 $\beta$ -HSD1<sup>-/-</sup> (KO) and WT mice. A decline in CORT and an increase of 11DHC levels were observed in KO mice brains homogenate. On the contrary, no difference were observed in plasma levels. Statistical analysis was by Student's *t*-test (n=12). Data are mean  $\pm$  SEM. \*P<0.05.

### 5.3.2. *Studies of pharmacological inhibition of 11 $\beta$ -HSD1*

The small molecule 11 $\beta$ -HSD1 inhibitor UE2316 (**Figure 5.3**) was used to attenuate regeneration of active CORT in mice. MSI was initially used to establish which tissue had been exposed to drug, with specific reference to brain. MSI analysis of small drug-like molecules has been described elsewhere (Caprioli, 2007). As for most MS-based

techniques the molecule must contain a readily ionisable moiety to be suitable for analysis. In this case, the murine 11 $\beta$ -HSD1 inhibitor (UE2316) studied has piperidinyl moiety which promotes the proton adduct formation leading to an efficient ionisation in MALDI. In contrast to steroids, derivatisation was not needed, as the sensitivity was enough to generate a suitable molecular map. MS images were successfully generated for UE2316 in murine brain section after time-dependent dosing study and the relative abundance obtained was validated using the standard tissue-homogenate LC-MS/MS platform described in section 5.2.3.1.

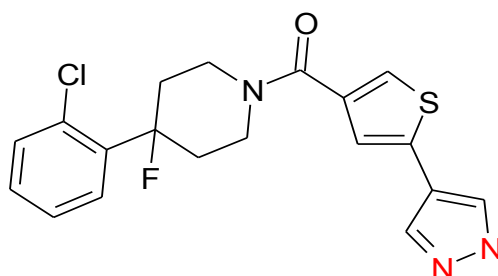


**Figure 5.3:** Molecular structure of UE 2316. Piperidinyl moiety in red

Following a single oral dose of UE2316, levels of the drug detected by MSI reached a maximum in brain one hour post-dose (**Figure 5.43B**, vehicle, **Figure 5.4C-E**, UE2316); the MSI data were confirmed by LC-MS/MS of drug in whole brain (**Figure 5.4F**). Therefore this time point was selected for subsequent analysis of changes in steroid levels. The regional distribution of glucocorticoids was similar in brains of vehicle and UE2316 treated mice (**Figure 5.4H,J** (CORT), **5.4I,K** (11DHC)). Treatment with UE2316 reduced CORT/11DHC ratios measured by MSI in the cortex, hippocampus and amygdala (**Figure 5.4L**). Quantitative analysis by LC-MS/MS confirmed these findings (**Figure 5.4M**).

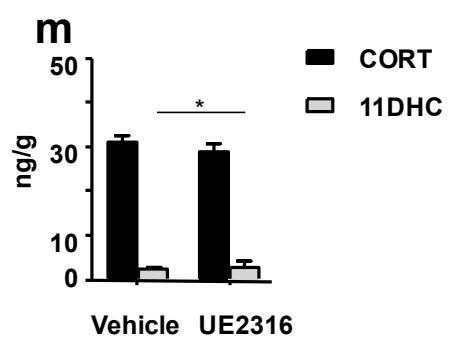
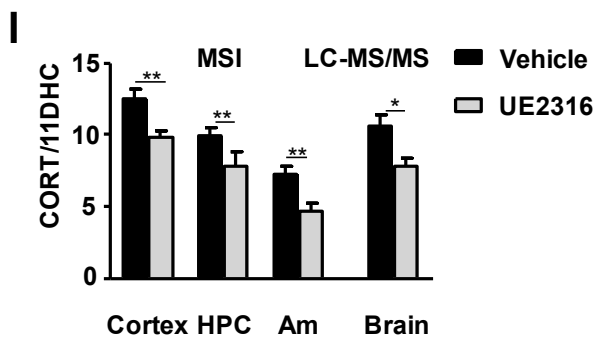
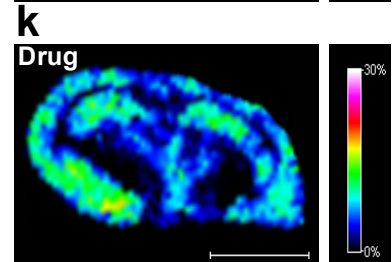
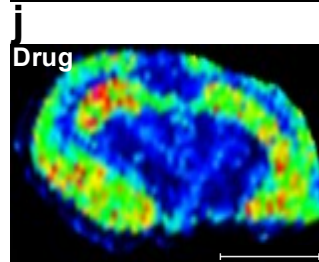
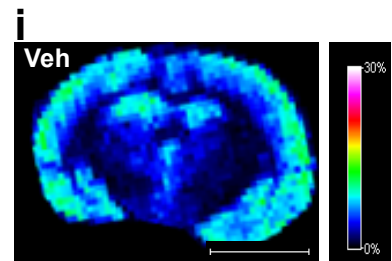
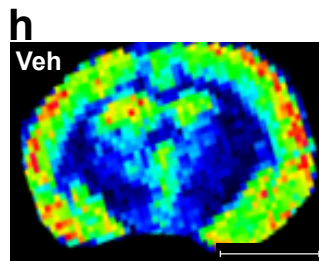
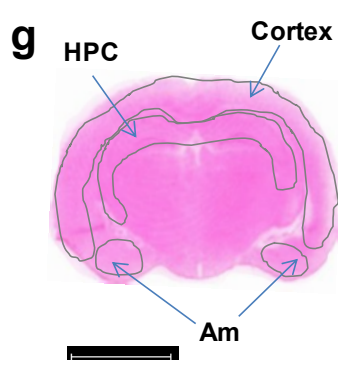
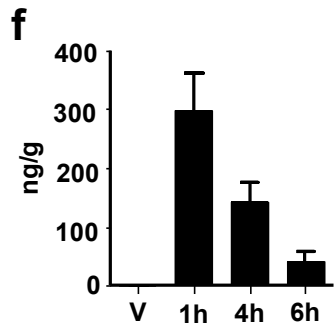
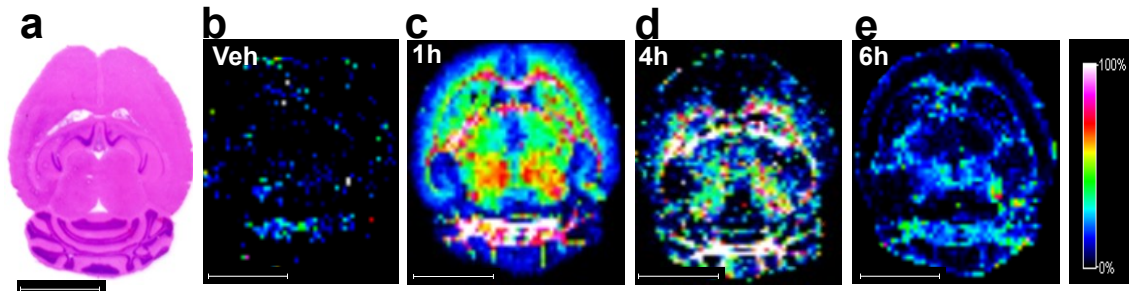




**Figure 5.4:** Effect of pharmacological inhibition of 11 $\beta$ -hydroxysteroid dehydrogenase type 1 (11 $\beta$ -HSD1) with UE2316 in C57BL/6 mice. Girard T (GirT) derivatives (corticosterone (CORT) and 11-dehydrocorticosterone (11DHC)) were mostly distributed across the cortex, hippocampus and amygdala, before and after enzyme inhibition, CORT/11DHC ratios showed a significant decline as a result of an increased 11DHC metabolite. **(a)** Histological image of horizontal cryosection of murine brain stained with haematoxylin and eosin. **(b-e)** MSI heat map distribution of  $m/z$  390.084 Da representing UE2316 in brain over a 1-6 h time course in mice receiving Vehicle (V) or UE2316 (D). **(f)** Amounts of UE2316 in whole brain measured by LC-MS/MS demonstrated the same temporal pattern as those determined by MSI. **(g)** Histological image of coronal cryosection of murine brain stained with haematoxylin and eosin with the outline of the MSI regions of interest (ROIs) (cortex; hippocampus, HPC; and amygdala, Am). **(h, j)** MSI heat map of GirT-CORT at  $m/z$  460.317 Da brain from mice receiving Vehicle **(h)** or UE2316 (1h post dose) **(j)**. **(i, k)** GirT-11DHC at  $m/z$  458.301 Da in brain from mice receiving Vehicle **(i)** or UE2316 **(k)**. Signal intensity is depicted by color on the scale shown. Scale bar (2mm). **cps** = count per second. **(l)** A significant decline ( $p < 0.01$ , overall between groups) in CORT/11DHC ratios was observed across the ROIs by MSI in the brain after administration of UE2316, showing good agreement with data generated by LC-MS/MS in whole brain. **(m)** Absolute quantification of corticosteroids in brain tissue by LC-MS/MS showed that the differences in CORT/11DHC ratios were associated with an increase of 11DHC and a trend to a decrease in CORT in UE2316-treated mice. Statistical analysis was performed using two-way ANOVA for MSI and Student's t-test for LC-MS/MS and absolute measurements ( $n=12$ ). Data are mean  $\pm$  SEM. \* $P < 0.05$ , \*\* and  $P < 0.01$ .

### 5.3.3. *Agreement between methods of quantitative analysis*

Good agreement was observed between MSI and LC-MS/MS (**Figure 5.5A**) and between MSI and LESA (**Figure 5.5B**), in measuring the (CORT/11DHC) ratios across the range of values, although MSI-LESA demonstrated a negative bias using Bland-Altman analysis.

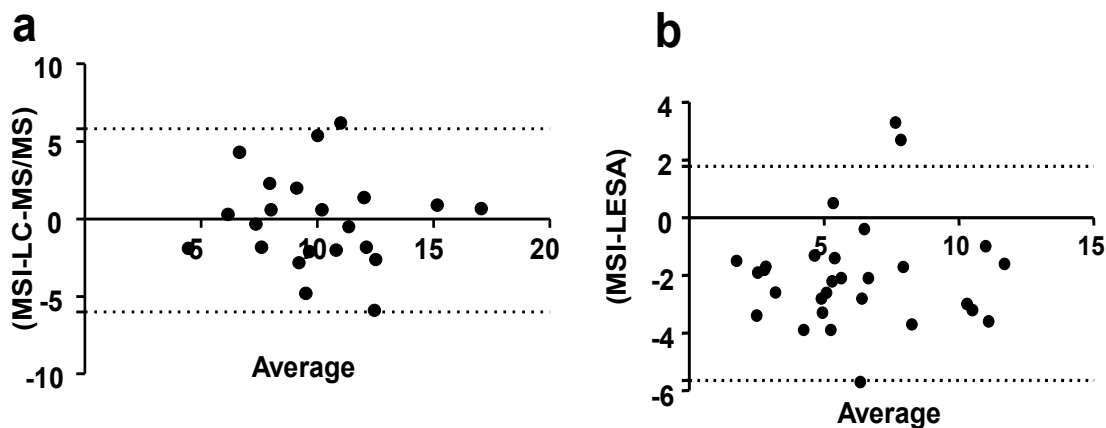


**Figure 5.5:** Agreement between MSI and alternative methods for measuring corticosteroids. Bland-Altman plots with 95% confidence intervals for agreement for ratios of corticosterone to 11-dehydrocorticosterone (CORT/11DHC) measured in wild type murine brain by: (a) MSI and LC-MS/MS; (b) MSI and LESA.

#### 5.3.4. *Quantitation of alternative substrates of 11-HSD1*

The GirT derivative of 7-ketocholesterol was detected by MSI in brain sections (**Figure 5.6**) and its abundance increased in mice with disruption (**Figure 5.6B-D**) or inhibition (**Figure 5.65E-G**) of 11 $\beta$ -HSD1.

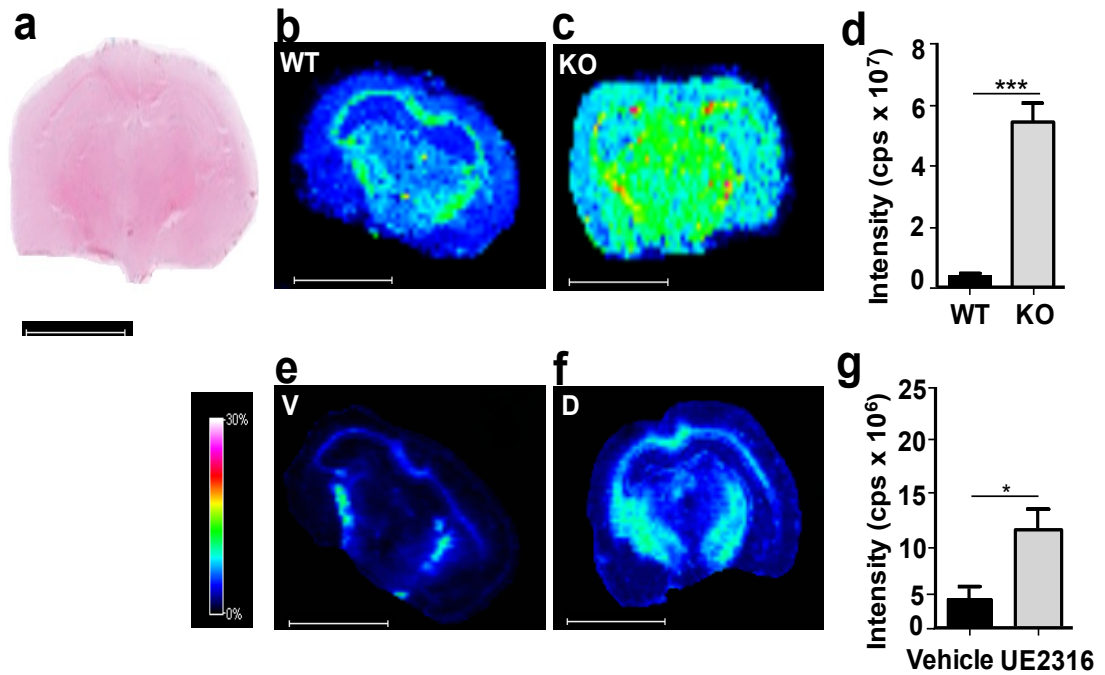


**Figure 5.6:** MSI detection of 7-ketocholesterol, an alternative substrate for 11 $\beta$ -HSD1. A significant increase in Girard T 7-ketocholesterol (GirT-7KC) intensity was observed across the whole brain in mice after disruption of 11 $\beta$ -HSD1 (KO) and after administration of UE2316 (1 h post-dose). (a) Histological image of coronal cryosection of murine brain stained with haematoxylin and eosin. MSI heat map of GirT-KC at *m/z* 514.437 in (b) wild type (WT), (c) KO and brain from mice receiving (e) Vehicle (V) or (f) UE2316 (D). Quantification of MSI signal intensity for GirT-7KC across the whole brain for (d) wild type versus 11 $\beta$ -HSD1<sup>-/-</sup> mice and for (g) mice treated with vehicle or UE2316. Signal intensity is depicted by color on the scale shown. Scale bar (2 mm). **cps** = counts per second. Statistical analysis was performed using two way ANOVA (n=12). Data are mean  $\pm$  SEM. \*P<0.05 and \*\*\* P<0.001.

## 5.4. Discussion

Neutral steroids were converted to positively charged hydrazone derivatives using Girard reagents T (GirT), enabling detection and quantitation by MALDI and LESA with FTICR-MSI. Validation was performed with LC-MS/MS. MSI demonstrated alterations in amounts of brain glucocorticoids (and 7-ketocholesterol, an alternative substrate) in mice with 11 $\beta$ -HSD1 deficiency, and allowed simultaneous pharmacokinetic/pharmacodynamic studies with an 11 $\beta$ -HSD1 inhibitor. A potent, selective and orally bioavailable piperidiny-pyrazol inhibitor of 11 $\beta$ -HSD1 (UE2316) was used; UE2316 crosses the blood-brain barrier and displays potency across species (K<sub>i</sub>: mouse, 162 nM,; rat, 80 nM)

This novel application of OTCD coupled with MSI permits detection of poorly ionisable endogenous corticosteroid hormones within tissues, by generating permanently charged derivatives which yield intense signals upon MALDI-FTICR analysis. The spatial distribution of the substrate and product of 11 $\beta$ -HSD1, 11DHC and CORT, in murine brain had been visualized in **Ch4**. Here quantitation of these analytes in brains from 11 $\beta$ -HSD1 deficient mice allowed quantitative assessment of the consequences of regional activity of 11 $\beta$ -HSD1 for local steroid levels, and the approach also allowed pharmacodynamic and pharmacokinetic assessment of an 11 $\beta$ -HSD1 inhibitor within the brain. This technique has the potential to be applied to other steroids and sterols to investigate steroid intracrinology in multiple organs and in solid tumors.

OTCD coupled with MALDI-FTICR-MSI was successfully applied in murine brain, where discriminating abundance of glucocorticoids in sub-regions was possible. As shown in **Ch4**, wild-type mice on a C57BL/6 background, the highest abundance of the glucocorticoids tested was again in cortex, hippocampus and amygdala and may reflect the higher expression of corticosteroid-binding receptors as well as of 11 $\beta$ -HSD1 in these brain regions. To evaluate use of the technique to interpret biological variations in tissue steroid levels, proof-of-principle experiments were performed using brains of mice with 11 $\beta$ -HSD1 deficiency or receiving pharmacological 11 $\beta$ -HSD1 inhibitors. Changes in enzyme activity were quantified by CORT/11DHC ratios, which is appropriate since derivatives of both steroids possess similar ionisation yields and signal intensities, as previously demonstrated in **section 3.3.5.1**, when compared using post-processing vector normalization (RMS). An alternative approach would have been to incorporate a labeled steroid (e.g. d<sub>8</sub>CORT) in the matrix, allowing signal intensity to be normalised; this approach also offers the advantage of a further read-out of uniformity of matrix application but was not employed here. Disrupting or inhibiting 11 $\beta$ -HSD1 was anticipated to increase the CORT/11DHC ratio, as previously reported in homogenates of brain from 11 $\beta$ -HSD1 deficient mice (Yau *et al.*, 2007). This was indeed detected, and quantified in brain sub-regions, with an increase of the signal intensity of GirT-11DHC and a smaller decline in GirT-CORT levels across the cortex, hippocampus and amygdala with 11 $\beta$ -HSD1 deficiency or inhibition. These brain regions have high abundance of 11 $\beta$ -HSD1 mRNA, which when translated in protein, may regulate active and inert glucocorticoid levels (Moisan *et al.*, 1990a).

CORT in the brain is derived both from the circulation and from local 11 $\beta$ -HSD1 activity. The proportionate contribution of each source, however, is unknown. To date, this has been inferred for some tissues, imprecisely, from studies using arteriovenous sampling in combination with stable isotope tracers, by sampling interstitial fluid by microdialysis, or by quantifying steroid concentrations in whole tissue homogenates *ex vivo* (**section 1.24**). The MSI data here provides the novel insight into the role of the enzyme in tissues. In mice with 11 $\beta$ -HSD1 deficiency, the CORT/11DHC ratio was unaltered in plasma but within specific regions of tissues, the local ratio of active and inactive steroid was altered. A ~16 % decline in active CORT with 11 $\beta$ -HSD1 deficiency in regions of the brain where 11 $\beta$ -HSD1 is normally most highly expressed; suggesting the contribution of 11 $\beta$ -HSD1 to the intracellular pool of CORT in these experimental conditions is relatively modest and the circulation contributes considerably to steroid availability.

Lastly using MSI, it was possible to image alternative substrates of 11 $\beta$ -HSD1, in this case 7-ketocholesterol. Previously it has been difficult to establish whether 11 $\beta$ -HSD1 predominantly reduces 7-ketocholesterol to 7 $\beta$ -hydroxycholesterol or if oxidation dominates (Mitic *et al.*, 2013). Indeed, changes in the balance of circulating oxysterols are modest in 11 $\beta$ -HSD1<sup>-/-</sup> mice. By demonstrating accumulation of 7-ketocholesterol with 11 $\beta$ -HSD1 deficiency, data obtained using MSI may suggest that reduction of oxysterols by 11 $\beta$ -HSD1 predominates.

## **5.5. Conclusions**

MSI with on-tissue derivatisation is a powerful new tool to study the regional variation in abundance of steroids in brain tissue sections. This is the first technique capable of detecting and quantifying corticosteroids to  $<200\ \mu\text{m}$  resolution, and at physiological concentrations, allowing application within region-specific areas of murine brain. We have demonstrated its utility for measuring pharmacodynamic effects of small molecule inhibitors of  $11\beta\text{-HSD1}$ ; in combination with pharmacokinetic imaging, this will facilitate screening of the disposition of such drugs being developed to treat Alzheimer's disease. This offers the prospect of many novel insights into tissue-specific steroid and sterol biology.

# Chapter 6

## Measuring 11 $\beta$ -hydroxysteroid dehydrogenase-1 turn-over using MSI with stable isotope tracer infusion

### 6.1. Introduction

11 $\beta$ -HSD1 is widely expressed, including in the liver and adipose and brain (Seckl *et al.*, 2001). Its main function is believed to be catalysing the regeneration of active glucocorticoids, cortisol (F) in humans and corticosterone (CORT) in rodents, from inactive cortisone (E) and 11-dehydrocorticosterone (11DHC) respectively, therefore, amplifying glucocorticoid receptor activation independently of the circulating level of active glucocorticoids. Its importance as a tissue-specific regulator of metabolism has been demonstrated using animal models (Masuzaki *et al.*, 2003; Masuzaki *et al.*, 2001). Tissue-specific dysregulation of 11 $\beta$ -HSD1 has been inferred in human obesity from indirect measurements (Rask *et al.*, 2001; Tomlinson *et al.*, 2002), therefore, 11 $\beta$ -HSD1 has become an attractive target for ameliorating metabolic syndrome. Selective and potent 11 $\beta$ -HSD1 inhibitors have been developed with some evidence of success (Webster *et al.*, 2007). However, key questions remain about the role of 11 $\beta$ -HSD1 in aetiology of metabolic disease and CNS in humans. It has been proved that inhibition of 11 $\beta$ -HSD1 in brain is associated with improved memory (Sooy *et al.*, 2010) but the



consequences for local steroid regeneration in the brain sub-regions where 11 $\beta$ -HSD1 is expressed are not known. Of pressing importance is understanding the magnitude of regeneration of cortisol within individual tissues; until this can be assessed, consequences and sites of dysregulation or enzyme inhibition remain uncertain. An idea persists that 11 $\beta$ -HSD1 may catalyse the dehydrogenase conversion of active to inactive under some circumstances (Bujalska *et al.*, 2002; Hughes *et al.*, 2012); thus, *in vitro* enzyme expression or activity driven by co-factor and substrate cannot be extrapolated *in vivo*. Studies measuring endogenous F and E (Kannisto *et al.*, 2004) or dilution of stable isotope F tracer (Basu *et al.*, 2004) in the hepatic vein suggest that there is substantial splanchnic F regeneration but this methodology does not distinguish activity in the liver from the contribution of visceral adipose tissue, which *in vitro* studies suggest is considerable (Katz *et al.*, 1999b). Venous sampling has demonstrated local F regeneration in subcutaneous adipose tissue, but the errors associated with this method is wide (Basu *et al.*, 2004).

As the MSI platform was successfully applied to measure endogenous concentrations as ratios in mouse brain, in this chapter, we aimed to apply the OTCD-MSI platform to measure the contribution of tissue-specific cortisol regeneration primarily in the brain using a stable isotope tracer, 9,11,12,12[<sup>2</sup>H]<sub>4</sub>-cortisol (d<sub>4</sub>F). D<sub>4</sub>F is converted to 9,12,12[<sup>2</sup>H]<sub>3</sub>-cortisone (d<sub>3</sub>E) by 11 $\beta$ -HSD2 in the kidney and d<sub>3</sub>E is converted to 9,12,12[<sup>2</sup>H]<sub>3</sub>-cortisol (d<sub>3</sub>F) by 11 $\beta$ -HSD1 (Andrew *et al.*, 2002) (**Figure 6.1**). Unlike cortisol or d<sub>3</sub>F, d<sub>4</sub>F cannot be regenerated by 11 $\beta$ -HSD1. Using this approach the rate of cortisol turnover in the brain may be compared with that in adipose and liver alongside plasma. Furthermore, the effects of 11 $\beta$ -HSD1 deficiency on the region-specific cortisol regeneration in metabolic tissues can be evaluated using genetically

modified mice and a selective inhibitor. In contrast with tissue homogenate approaches, with MSI it is possible to evaluate the regional turn-over within different compartment in brain tissues, where the consequences for local steroid regeneration in different sub-regions are still not known.

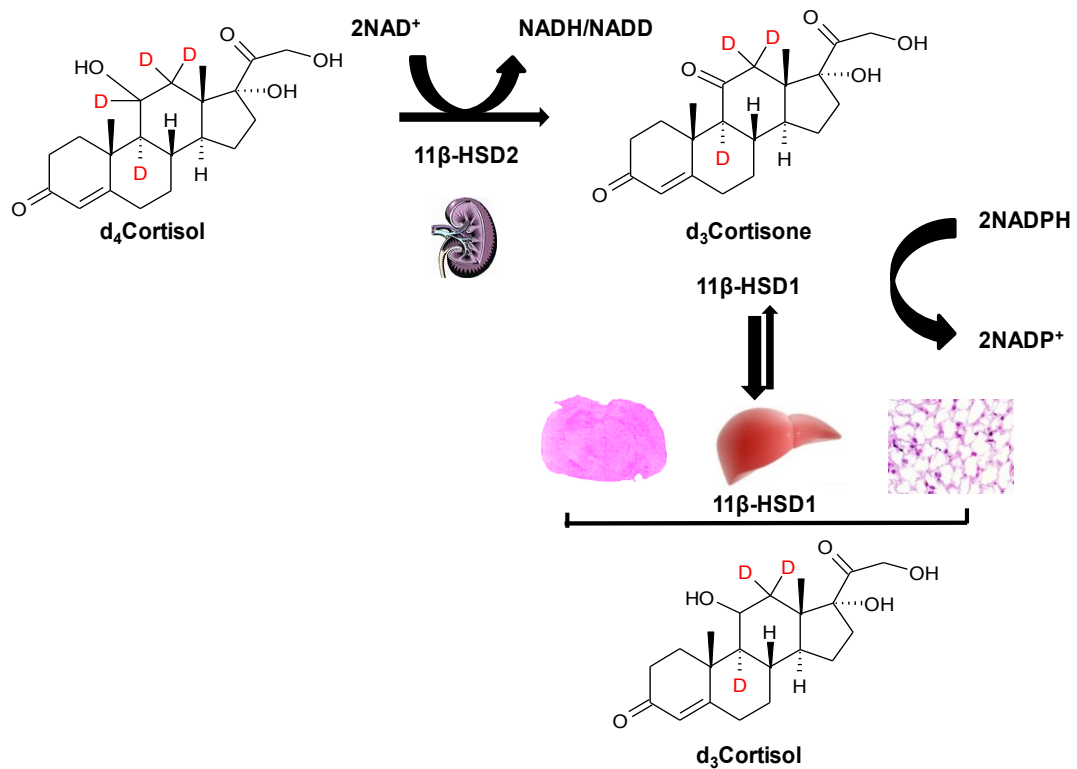


**Figure 6.1:** Cortisol turnover at the tissue level using stable isotope tracers. 9,11,12,12- $^2\text{H}_4$ -cortisol ( $d_4$ F) is converted to d3-9,12,12- $^2\text{H}_3$ -cortisone ( $d_3$ E) by 11 $\beta$ -HSD2 in the kidney and  $d_3$ E is converted to 9,12,12- $^2\text{H}_3$ -cortisol ( $d_3$ F) by 11 $\beta$ -HSD1.

## 6.2. Methods

### 6.2.1. Biomatrices

The effect of the 11 $\beta$ -HSD1 activity enzyme on the cortisol turn-over was studied in the following models. Four groups of mice (n=3/group) were studied:

- **Group 1:** C57Bl/6j from Harlan Olac Ltd (Bicester, UK) (male, 12 weeks), infused with d<sub>4</sub>F 1.75 mg/day for 6, 24 and 48 h termed “controls”.
- **Group 2:** C57Bl/6 mice from Harlan Olac Ltd (male, 12 weeks) infused with vehicle (dimethylsulfoxide (DMSO): propylenglycol (PG) (50:50) termed “vehicle”.
- **Group 3:** C57Bl/6j 11 $\beta$ -HSD1<sup>-/-</sup> mice (male, 2-3 months) bred in-house and genotyped using protocols described by Morton (Morton *et al.*, 2001), infused with 1.75 mg/day of d<sub>4</sub>F for 48 h, termed KO.
- **Group 4:** C57Bl/6 mice (12 weeks, male) from Harlan Olac Ltd infused with 1.75 mg/day of d<sub>4</sub>F for 48 h and studied 1, 2, 4 h hours post-dose (HPD) of UE2316 (11 $\beta$ -HSD1 inhibitor; 25 mg/kg oral gavage) or vehicle (DMSO: PG) (50:50), termed 1 h (1HDP), 2 h (2HPD) and 4 h (4HPD) post-dose, respectively

The d<sub>4</sub>F solution was administered at a rate of 1.03  $\mu$ L/hr by subcutaneous surgical implantation of mini-osmotic pumps (ALZET model 1003 with a reservoir volume 100 $\mu$ L, Cupertino, CA, USA). Pumps were primed overnight in saline solution prior to insertion. Animals were killed by decapitation and plasma was prepared from trunk blood, collected in ethylenediamine tetraacetic acid (EDTA) coated tubes. Tissues were

snap frozen in liquid nitrogen and stored (-80°C) at cull as per **section 2.2** and **2.3**, respectively.

### **6.2.2. FTICRMS spectral characterisation of deuterated glucocorticoids (standard on tissue)**

On-tissue spectral characterisation of the tracers was performed using a control tissue section (murine brain) sectioned as per **section 2.3** with spots (5 ng, 10 µg/mL; methanol: water (1:1)) of d<sub>4</sub>F and d<sub>3</sub>F applied to the surface manually (n=3). Spots were allowed to dry, then GirT (1µL; 5 mg/mL) in methanol: water (80:20) was deposited on top. The MALDI glass slide was placed in the reaction chamber and derivatised according to **section 2.5**. After derivatisation, matrix CHCA was applied as per **section 2.6** and allowed to dry (RT) and stored in a dessicator until MALDI-FTICRMS analysis. MSI was performed in full mass (230-1500 Da) (broadband mode) as described in **section 2.8.2**. Ions of GirT-d<sub>4</sub>F and GirT-d<sub>3</sub>F were monitored as detailed in **Table 2.1**. Ion intensities were recorded and response factors were calculated.

### **6.2.3. Detection of d<sub>4</sub>F and d<sub>3</sub>F in an infused murine brain (control) section**

Brain tissues were obtained from **Group 1** as per **section 6.2.1** (48 h time point). Tissue sectioning was carried out as described in **section 2.3**. OTCD was carried out as described in **section 2.5** and matrix was applied as per **section 2.6**. MALDI-FTICR-MSI analysis was performed as described in **section 2.8.1** acquired in both broadband mode and constant accumulation of selected ions (CASI™) using an isolation window at 470±25Da in profiling mode. Ions of GirT-d<sub>4</sub>F and GirT-d<sub>3</sub>F were monitored as

detailed in **Table 2.1**. d<sub>8</sub>CORT was also monitored as ISTD for window normalisation marker as explained in **section 2.8.1**.

#### **6.2.4. Structural confirmation of d<sub>4</sub>F and d<sub>3</sub>F in brain (control) sections from a mouse infused with d<sub>4</sub>F analysed by CID experiments using LESA-nanoESI-FTIRMS.**

Brain tissues were obtained from **Group 1** as per **section 6.2.1** (48 h time point). Tissue sectioning was carried out as described in **section 2.3**. OTCD was carried out as described in **section 2.5** and tissues were analysed immediately using LESA-nanoESI-FTICRMS as described in **section 2.9**. Ions were isolated at  $m/z$  470.3±20Da for 30 s yielding a 2 Mword time-domain transient. CID fragmentation was carried out at 28 eV and CID spectra recorded and fragments proposed.

#### **6.2.5. Time-dependent cortisol turn-over using stable isotope tracers in metabolic tissues**

##### **6.2.5.1. Plasma analysis**

Plasma analysis was performed as previously described by Stimson et al (Stimson *et al.*, 2009). Plasma cortisol, d<sub>3</sub>F, d<sub>4</sub>F, CORT, and d<sub>3</sub>E were measured by LC/MS-MS. Epi-cortisol (500 ng) was added to 1.5 mL plasma and extracted using 15 mL chloroform. Samples were evaporated and then reconstituted in mobile phase (60% methanol and 40% 5 mmol/L ammonium acetate) before injection into a Thermo Finnigan LC-MS/MS, consisting of a TSQ Quantum Discovery Mass Spectrometer and a Surveyor Liquid Chromatogram using an Allure biphenyl column (50 mm × 4.6 mm × 5 μm; Thames Restek), with column temperature 25°C and mobile phase flow rate

0.5 mL/min. Ionization was achieved by positive electrospray. The precursor and product  $m/z$  and the collision energy used were as follows: EpiF (363→121),(35eV), d<sub>3</sub>F (366→121), (47eV), d<sub>4</sub>F (367→121), (39eV), CORT (346→121), (41eV), and d<sub>3</sub>E (364→164), (42eV). Compounds were quantified by the ratio of area under peak of interest to area under peak of internal standard against a standard curve.

#### **6.2.5.2.        *Extraction of steroids from liver tissue***

The method was adapted from McInnes et al. (McInnes *et al.*, 2004). Murine liver tissue (~300 mg) was homogenised in methanol–acetic acid (100:1 v/v, 10 mL) using a mechanical homogeniser and assisted by ultrasonication and enriched with internal standard, d<sub>8</sub>CORT (ISTD) (5 ng). The supernatant was retained and the pellet formed followed centrifugation (5000 × g, 10 min, 4 °C), further extracted with methanol–acetic acid (100:1 v/v, 10 mL) and the supernatants combined and dried under oxygen free nitrogen (OFN) at RT, submitted for derivatisation as per **section 2.5** and analysed by MALDI-FTICRMS as per procedure in **section 2.8.2.**, using an isolation window of 470.3±50 Da.

#### **6.2.5.3.        *Whole brain analysis***

Extraction was performed as described in **section 5.2.3.1** and analysis carried out as per **section 2.8.2.**, using an isolation window of 470.3±50 Da.

#### **6.2.5.4.        *Extraction of steroids from adipose tissue***

The method was adapted from (Hughes *et al.*, 2010). Adipose samples (250 mg) were mechanically homogenised in ethyl acetate (1 mL), enriched with internal standard

(d<sub>8</sub>CORT, 5 ng), dripped onto chilled ethanol: glacial acetic acid: water (95:3:2 v/v) (10 mL) and stored at -80 °C overnight. Samples attained 4 °C, before being sonicated (8 x 15 s bursts) and centrifuged (3000x g, 30 min, 4 °C). The supernatant was reduced to dryness under (OFN, 60°C), methanol (10 mL) added and stored at -80 °C overnight. To remove lipids, tissue extracts attained room temperature then hexane (10 mL) was added and mixed. The hexane layer was discarded and the remaining methanol removed by evaporation. Water (400 µL) and ethyl acetate (4 mL) were added to the dried steroidal extract, the organic layer removed, dried and the residue derivatised as per **section 2.5** and analysed by MALDI-FTICRMS as per procedure in **section 2.8.2.**, using an isolation window of 470.3±50 Da.

#### **6.2.5.5. *MSI of deuterium labelled cortisol metabolites in murine brain***

Tissues were harvested as per **section 2.2**, OTCD was carried out as per **section 2.5** and MSI performed as described in **section 2.8.1**. The ions of GirT-d<sub>4</sub>F, GirT-d<sub>3</sub>E and GirT-d<sub>3</sub>F and ISTD (d<sub>8</sub>CORT) were monitored according to **Table 2.1**. The average spectral intensities of GirT-d<sub>4</sub>F GirT-d<sub>3</sub>E and GirT-d<sub>3</sub>F in ROIs across the cortex, hippocampus and amygdala were recorded using MSI, presented as ratios of derivatised d<sub>4</sub>F/d<sub>3</sub>F and d<sub>3</sub>E/d<sub>8</sub>CORT (ISTD). An average value was calculated based on the weighted average.

For tissue homogenate analysis, the average spectral intensities of the corresponding GirT-d<sub>4</sub>F, GirT-d<sub>3</sub>E, GirT-d<sub>3</sub>F, CORT and GirT-d<sub>8</sub>CORT ions (**Table 2.1**) were recorded and presented as ratios tracer/tracee ratios (TTR) of d<sub>4</sub>F/d<sub>3</sub>F, d<sub>4</sub>F/d<sub>8</sub>CORT and d<sub>3</sub>E/d<sub>8</sub>CORT as hydrazone derivatives respectively. The amount of d<sub>8</sub>CORT was normalised (d<sub>8</sub>CORT /mg tissue) across different tissues to allow intra-tissue

comparison. The intensities of GirT derivatives of deuterated steroids were corrected for any potential background monoisotopic contribution.

## **6.2.6. PK/PD study of UE 2316 using stable isotope tracer**

### **6.2.6.1. *Extraction and analysis of plasma UE2316***

150  $\mu$ L of plasma was transferred to 10 mL glass tube; ISTD (UE 2346) was then added (50 ng) to each sample followed by extraction with ethyl acetate (3 x 5 mL), the solutions were shaken (15 min, centrifuged (3500 x g, 50 min, 4 °C)), the organic extracts were combined, retained and the plasma removed. The organic layers were dried under OFN at RT, submitted to LC-MS/MS analysis as described in **section 5.2.35.**

### **6.2.6.2. *Extraction and analysis of UE2316 in whole liver, adipose and brain***

Liver, adipose and brain (~150 mg) were homogenised in 5 mL of buffer (50:45:5 Hepes: Tris (0.1 M): sodium lauryl sulphate (SDS) (0.5 %)) pH 9.5 adjusted with NaOH containing 100  $\mu$ g/mL of Protein K enzyme. UE2346 was added (125 ng) and homogenates were incubated at 37 °C in a rotating water bath for 60 min. Samples were cooled down to RT and centrifuged (3500 x g, 15 min, 4°C), supernatants were filtered through a 0.45 $\mu$ m nylon filter and extracted with 3 x 5 mL of ethyl acetate. Organic layers were reduced to dryness under gentle stream of nitrogen at RT and residues were reconstituted in acetonitrile: water (50:50 containing 0.1% formic acid) (100  $\mu$ L) and samples were then submitted to LC-MS/MS analysis as per **section 5.2.5.**

The amount of ISTD (UE2346) was normalised to allow comparison of UE2316 levels in different tissues.



#### **6.2.6.3. *MSI of UE2316 in murine brain.***

Tissues were harvested as per section 2.2, matrix was applied as described in section 2.6, analysed by MALDI-FTICRMS as per section 2.8.1 in broadband mode and MS images generated using the protonated mass of UE2316 as per Table 2.1 and normalised using vector normalisation (RMS).

#### **6.2.6.4. *MSI of deuterium labelled cortisol metabolites in murine brain***

Analysis was performed as described in section 6.2.5.5.

#### **6.2.6.5 *MSI of UE2316 and its metabolites***

Tissues (Group 4 at 4HPD) were harvested as per section 2.2, matrix was applied as described in section 2.6, analysed by MALDI-FTICRMS as per section 2.8.1 in broadband mode and MS images generated using the protonated mass of UE2316 metabolites at  $m/z$  406.078681Da and  $m/z$  404.06303Da, respectively. Data were normalised using vector window normalisation using the quasimolecular ion of UE2316.

#### **6.2.7. *Data analysis***

Data are expressed as mean  $\pm$  SEM and differences were analysed using two-way ANOVA with Bonferroni's post-hoc test and Student's t-test as appropriate. Statistical significance was accepted at  $p < 0.05$ . A statistical trend is defined as  $0.05 < p < 0.1$ .

The rate of appearance (Ra) of  $d_3F$  was calculated using equation (1).

$$Ra\ d_3F = \frac{\text{Infusion rate of } d_4F}{TTR \left( \frac{d_4F}{d_3F} \right)} \quad (1)$$

**TTR:** Tracer/tracee ratio

The tissue  $d_3F$  regeneration corrected for changes in circulating contribution (plasma, P) ( $\Delta TTR_T$ ) was calculated using equation (2).

$$\Delta TTR (T) = TTR (P) \left( \frac{d_4F}{d_3F} \right) - TTR (T) \left( \frac{d_4F}{d_3F} \right) \quad (2)$$

**T:** Tissue, **P:** Plasma

## 6.3. Results

### 6.3.1. FTICR Spectra of deuterated glucocorticoids

#### 6.3.1.1. Spectral characterisation

Spectral characterisation was carried out by spotting experiments on a murine brain section using  $d_4F$  and  $d_3F$  ( $d_3E$  is not commercially available). As previously shown in **section 4.2.5** the human counterpart glucocorticoids reacted in the same way as the rodent counterpart with Gir-T. So, as expected, both labelled analogues formed the corresponding GirT-derivatives at  $m/z$  479.331 Da for  $d_3F$  and  $m/z$  480.337 Da for  $d_4F$  (**Figure 6.2**). Good mass accuracy ( $<10$  ppm against their corresponding theoretical monoisotopic mass,  $m/z$  479.331 Da for GirT- $d_3F$  and  $m/z$  480.331 Da for GirT-  $d_4F$  ) was observed for both derivatives (**Figure 6.2**). There was no need for correction of potential of M+D isotopomer contribution in  $d_4F$  from  $d_3F$  as both monoisotopic masses were well distinguished using HRMS (350.000 resolution power at 400Da)

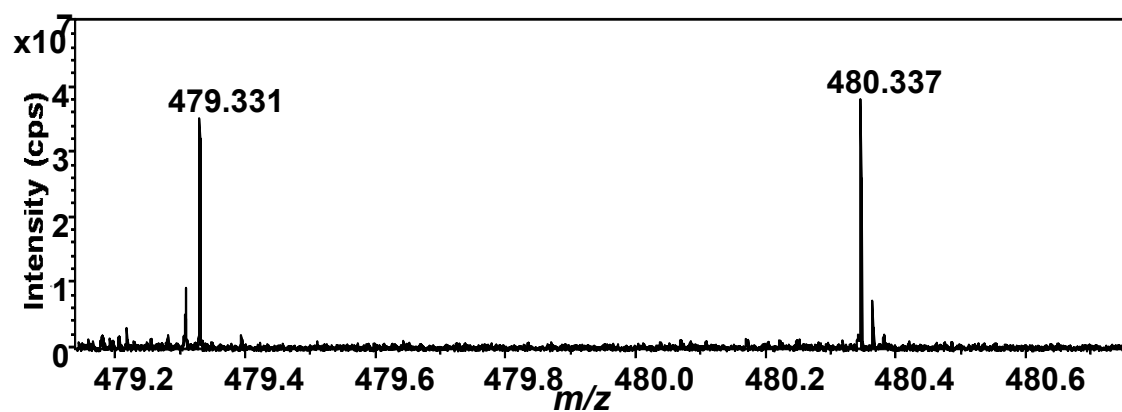


**Figure 6.2:** Representative MALDI-FTICRMS of Girard T (GirT)-derivatives of deuterium labelled glucocorticoid standards (5 ng). Observed ions at  $m/z$  479.33066Da for GirT- $d_3F$  and  $m/z$  480.33696Da for GirT-  $d_4F$ . cps: count per second.

### 6.3.1.2. Implementation of CASI™ for MSI

In order to increase the sensitivity of the MSI detection by separating target ions from the background noise, continuous accumulation of selected ions (CASI™) was invoked. A 48 h d<sub>4</sub>F infused brain tissue was analysed in full mass range and also with CASI™ (Figure 6.3). As shown in Table 6.1 (S/N) ratios were boosted using CASI™ by 50 times (d<sub>4</sub>F) and 10 times (d<sub>3</sub>F) allowing a better sensitivity than detection by full mass, with a better mass accuracy.

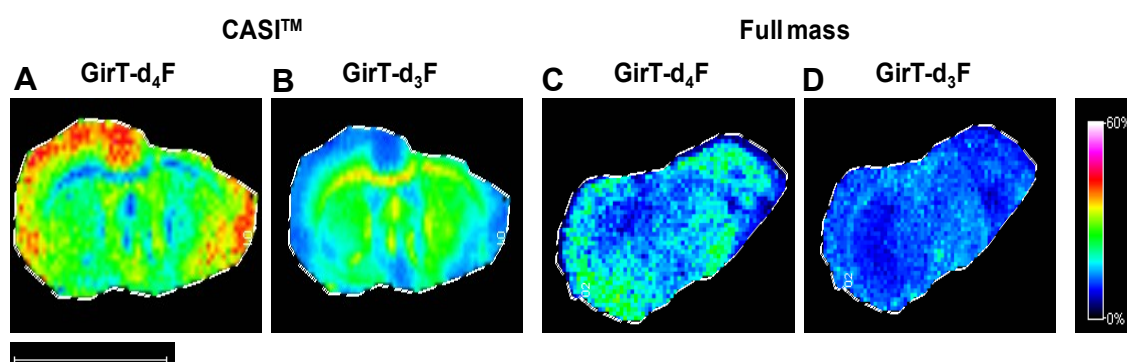


**Figure 6.3:** Molecular imaging by MALDI-FTICR-MSI of hydrazone derivatives of stable isotope tracer (d<sub>4</sub>F) and tracee (d<sub>3</sub>F) in representative murine brain sections. Molecular regional distribution maps show an increase in signal intensity by using continuous accumulation of selected ions (CASI™). Heat map using CASI™ of (a) GirT-d<sub>4</sub>F at  $m/z$  480.337 Da, (b) GirT-d<sub>3</sub>F at  $m/z$  479.331 Da. Heat map in full mass. (c) GirT-d<sub>4</sub>F at  $m/z$  480.337 Da, (d) GirT-d<sub>3</sub>F at  $m/z$  479.331 Da collated by MALDI-FTICRMS. Signal intensity is depicted by color on the scale shown. Scale bar (2 mm).

**Table 6.1: Full mass Vs. CASI™**

Tracer MSI	Mass Accuracy (ppm)		Signal/ Noise (S/N)	
	d <sub>4</sub> F	d <sub>3</sub> F	d <sub>4</sub> F	d <sub>3</sub> F
Fullmass	-2.4	-12.0	8.2	5.3
CASI™	-0.6	-3.1	400.5	50.8

S/N: Signal/Noise, ppm: part per million. Mass accuracy and S/N values (n=3/sections).

6.3.1.3. *Detection of d<sub>4</sub>F and d<sub>3</sub>F using CASI<sup>TM</sup> in a tissue section following in vivo administration of d<sub>4</sub>F*

After successfully detecting both deuterated cortisol analogues in a standard spotted tissue, the MSI platform was applied to murine brain section from a mouse treated with d<sub>4</sub>F in order to assess feasibility of generating molecular maps of both tracer and tracee in a biologically relevant setting. In line with unlabelled glucocorticoids, FTICR spectra of both steroids were well-defined showing an excellent mass accuracy (< 5 ppm) against the theoretical monoisotopic masses and good signal intensity (S/N above 50 for both steroids) (**Figure 6.4**).

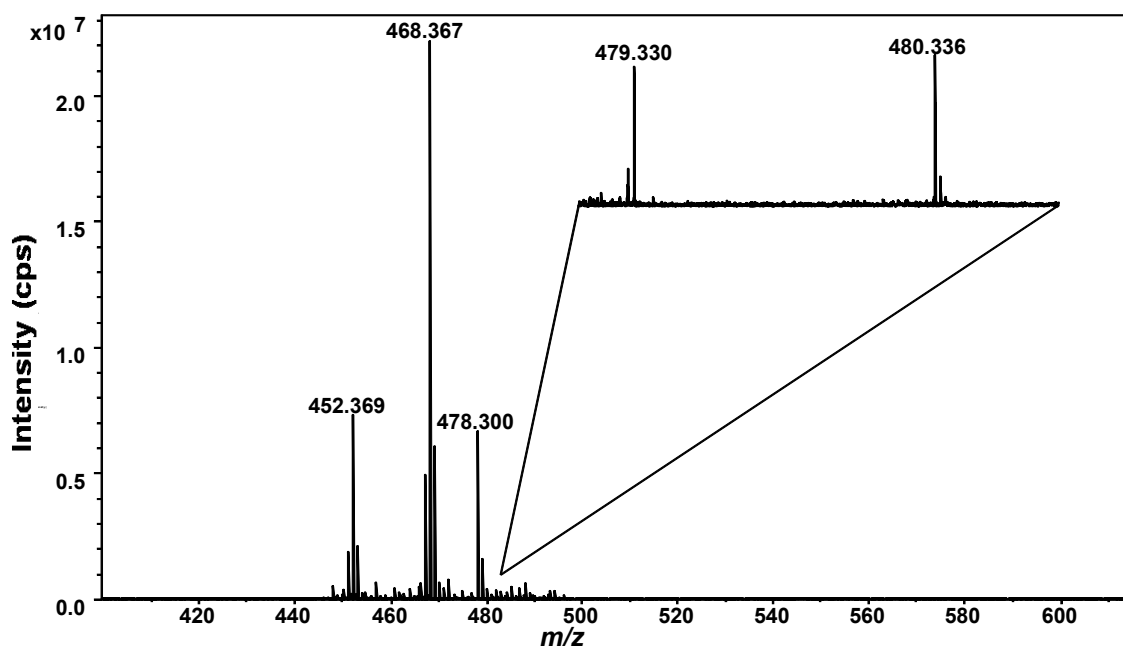


**Figure 6.4:** Representative CASI<sup>TM</sup>-MALDI-FTICRMS of Girard T (GirT)-derivatives of labelled glucocorticoids in brain from a mouse infused with d<sub>4</sub>F for 48h. Observed molecular ions at *m/z* 479.330 Da for GirT-d<sub>3</sub>F and *m/z* 480.336 Da for GirT-d<sub>4</sub>F were in agreement with the corresponding monoisotopic theoretical masses (*m/z* 479.331 Da for GirT- d<sub>3</sub>F and *m/z* 480.331 Da for GirT- d<sub>4</sub>F). **cps**: counts per second.

**6.3.1.4.        *Structural confirmation by CID experiments using LESA-nanoESI-FTICRMS***

Structural confirmation by fragmentation was achieved using LESA-nanoESI-FTICRMS, performed as described in **section 2.10**. This process provided fragmentation patterns typical of GirT hydrazones (**Figure 6.5**). These were concordant with the structures of steroid hydrazones, extrapolating from unlabelled rodent steroids, which shared the same five membered ring rearrangement as previously reported in **section 3.3.5.6**. CID of the GirT derivatives generated a series of fragment ions characteristic of the loss of the quaternary amine tag  $[M-59]^+$  and carbon monoxide  $[M-87]^+$  of the derivatised group at  $m/z$  421,  $m/z$  393 (GirT-d<sub>4</sub>F) and  $m/z$  420,  $m/z$  392 (GirT- d<sub>3</sub>F), respectively.

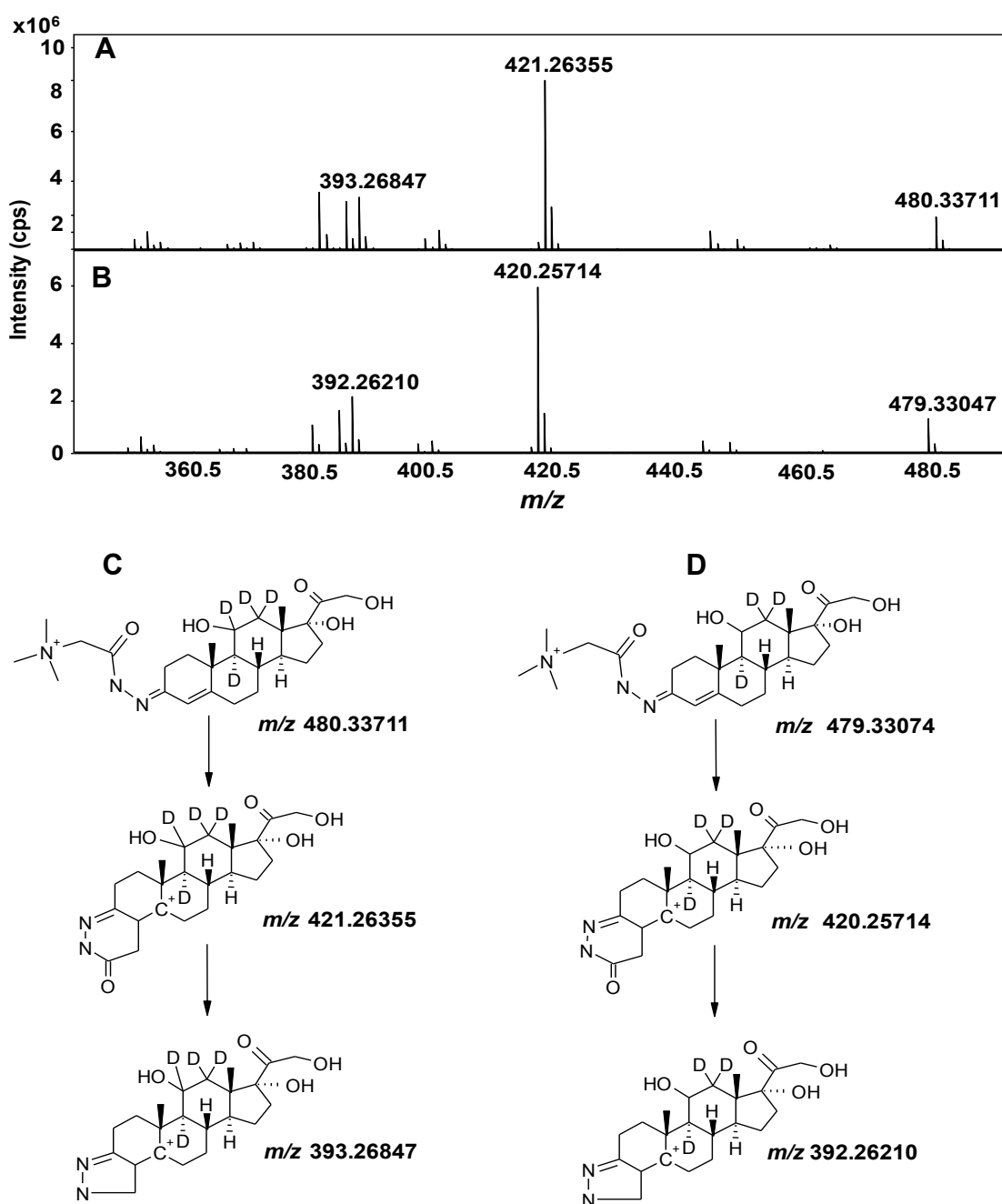


**Figure 6.5:** Mass spectra of Girard T (GirT) derivatives of deuterium labelled cortisol following liquid extraction surface analysis with nanoESI-FTICR collision induced dissociation (CID). CID mass spectra and proposed fragmentation patterns were in agreement with the literature. Precursors (**a**) at  $m/z$  480.33711Da (GirT- $d_4$ F) and (**b**) at  $m/z$  479.33074Da (GirT- $d_3$ F). Proposed fragmentation patterns (**c**): GirT- $d_4$ F (**d**): GirT- $d_3$ F. cps = counts per second. Cell isolation was 20 s and collision energy was set to 28 eV.

### **6.3.2. Cortisol turn-over using stable isotope tracers**

#### **6.3.2.1. *Tracer enrichment in plasma***

$d_4F$  was detected with very low signal intensity ( $S/N \sim 8$ ) after 6 h infusion of  $d_4F$  (**Figure 6.6A**). The dehydrogenation metabolite ( $d_3E$ ) was also very low at this time point ( $S/N \sim 6$ ) (**Figure 6.6B**) as was regenerated active  $d_3F$  ( $S/N \sim 4$ ) (**Figure 6.6C**). After 24 h of  $d_4F$  infusion, the signal intensity of  $d_4F$ ,  $d_3E$  and  $d_3F$  increased ( $S/N > 100$ ) allowing regeneration to active steroid to be detected. This process continued to equilibrate until 48h infusion, inferred from absolute concentration of  $d_4F$ ,  $d_3E$  and  $d_3F$  in **Figure 6.6A-C**. Tracers were not detected in mice infused with vehicle. Upon tracer infusion, endogenous levels of CORT declined after 6 h infusion and became undetectable (below LOD,  $S/N < 3$ ) after 24 and 48 h. **Figure 6.6D** shows the rate of appearance of  $d_3F$ , derived from the  $d_4F/d_3F$  ratios using equation 1, which showed a time-dependent increase **Figure 6.7E**.



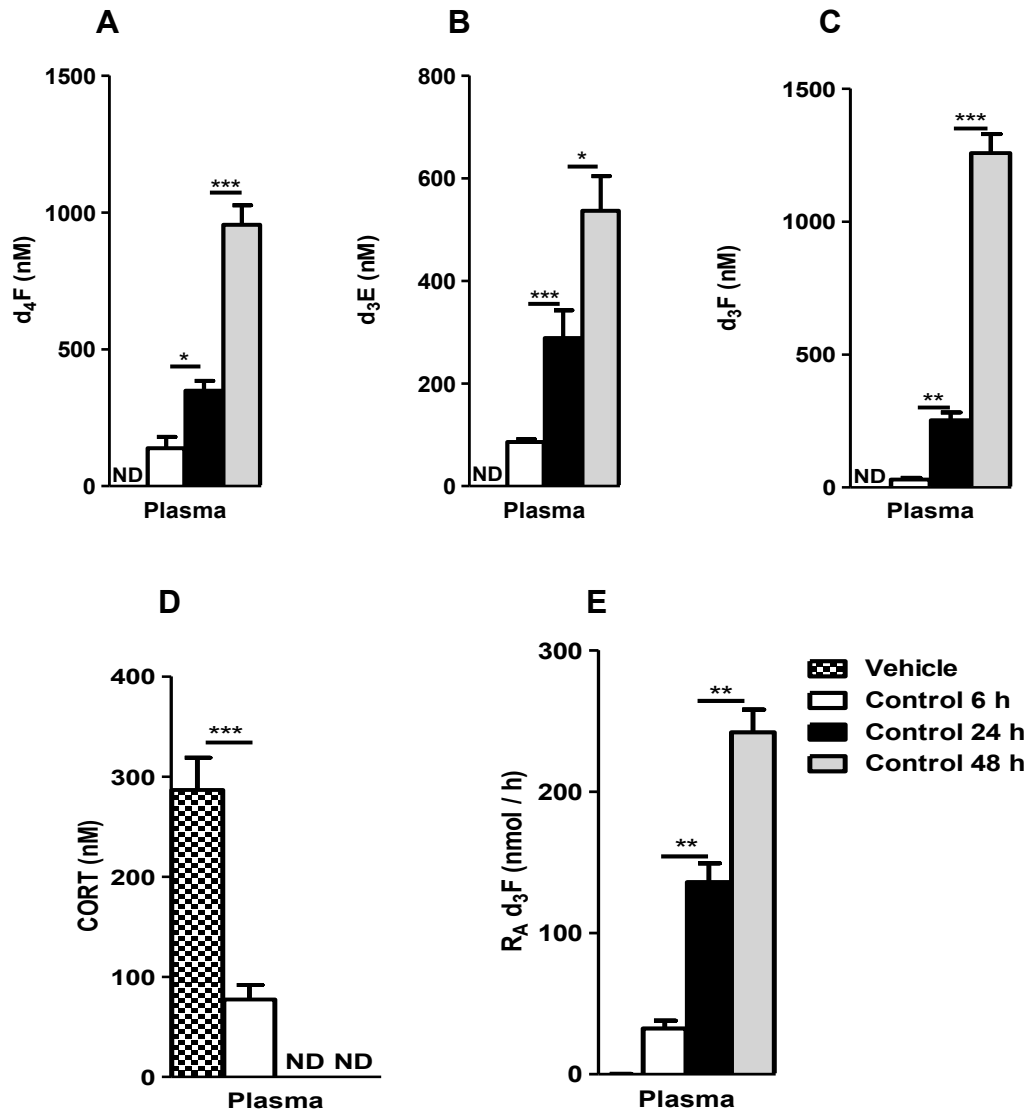


**Figure 6.6:** Concentration of circulating tracer and metabolites in plasma from wild-type mice. D<sub>4</sub>F and their metabolites d<sub>3</sub>E and d<sub>3</sub>F (tracee) continued to increase until 48 h d<sub>4</sub>F infusion and a considerable decline of CORT was observed after 6 h. **R<sub>A</sub>** shown a time-dependent increase. Absolute concentration (a) d<sub>4</sub>F. (b): d<sub>3</sub>E and (c) d<sub>3</sub>F. (d) CORT and (e) R<sub>A</sub> d<sub>3</sub>F. Statistical analysis was performed using two-way ANOVA with Bonferroni's post-hoc test. Data are mean ± SEM (n=3). \*\*\* P<0.001, \*\* P<0.01 and \* P<0.05. **R<sub>A</sub>**: Rate of appearance. **Control**: Wild-type mice without drug.

### 6.3.2.2. *Tracer enrichment in tissues*

To evaluate the tracer penetration into tissues (**Figure 6.7A**), total  $d_3E$  production (**Figure 6.7B**) and  $d_3F$  regeneration (**Figure 6.7C**) in tissues, analysis of liver, brain and adipose were conducted using tissue homogenate. For liver and adipose, performing MSI did not offer additional value as histological information cannot be obtained from these tissues in imaging mode at spatial resolution of 150  $\mu\text{m}$ . Penetration of  $d_4F$  in the liver and brain displayed a time-dependent increase reaching the highest levels at 48 h (**Figure 6.7A**) with a similar pattern observed for  $d_3E$  (**Figure 6.7B**). In adipose tissue both tracer and inert metabolite were only detected after 48 h and in lower abundances, with low S/N $\sim$ 7. Regarding  $d_3F$  generation, (**Figure 6.7C**) levels peaked at 48 h for liver and brain, which in the latter was only detectable after 24 h. In adipose,  $d_3F$  was only observed after 48 h with a low S/N ration ( $\sim$  4). As previously found in plasma, endogenous levels of CORT in the liver declined after 6 h infusion and became undetectable (below LOD, S/N $<$  3) after 24 and 48 h (**Figure 6.7D**). However, in the brain and adipose, the depletion of endogenous CORT was slower than plasma and liver as significant decline was only observed after 24 h and CORT was still detectable in adipose after 48 h (**Figure 6.7D**).

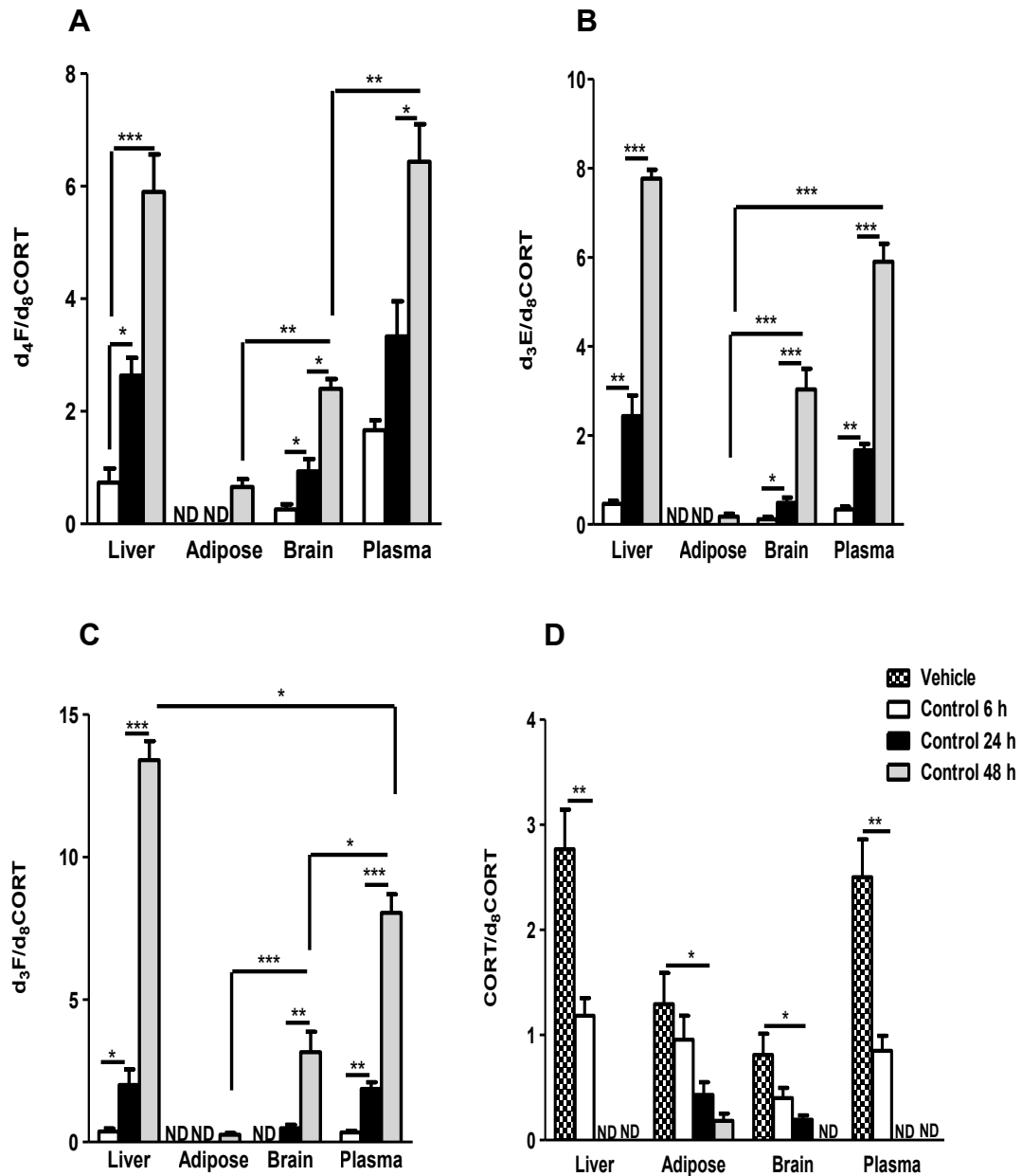


**Figure 6.7:** Estimation of (a)  $d_4F$ , (b)  $d_3E$ , (c)  $d_3F$  and (d) CORT normalised to ISTD ( $d_8CORT$ ) measured by MALDI-FTICRMS in tissues (liver, brain, adipose alongside plasma) from wild-type mice. A time-dependent increase in both tracer and metabolites amounts was observed for liver and brain after 48 h infusion of tracer. In contrast, in adipose tracer and inert metabolite were only observed at 48 h with low S/N (~5). In liver levels of CORT declined after 6 h and became non-detectable (S/N<3) after 24 h. However, in brain and adipose, levels declined after 24 h and were still detectable after 48 h in the adipose.  $d_8CORT$  intensity was normalized across tissues. Statistical analysis was performed using two-way ANOVA with Bonferroni's post-hoc test. Data are mean  $\pm$  SEM (n=3). \*\*\* P<0.001, \*\* P<0.01 and \* P<0.05. ND: non-detectable. **Control:** Wild-type mice without drug.

### 6.3.2.3. Tracer enrichment in murine brain assessed by MSI

In the brain,  $d_4F$  (**Figure 6.8A**) and the inactive metabolite  $d_3E$  (**Figure 6.8B**) were detected with very low signal intensity ( $S/N \sim 4$ ) after 6 h infusion of tracer. Regeneration to active  $d_3F$  could not be observed or was below the LOD at this time point (**Figure 6.8C**). After 24 h, the signal intensity of  $d_4F$ ,  $d_3E$  and  $d_3F$  increased ( $S/N > 50$ ) representing production of  $d_3E$  from plasma (**Figure 6.8B**) and allowing regeneration to active steroid to be detected (**Figure 6.8C**).

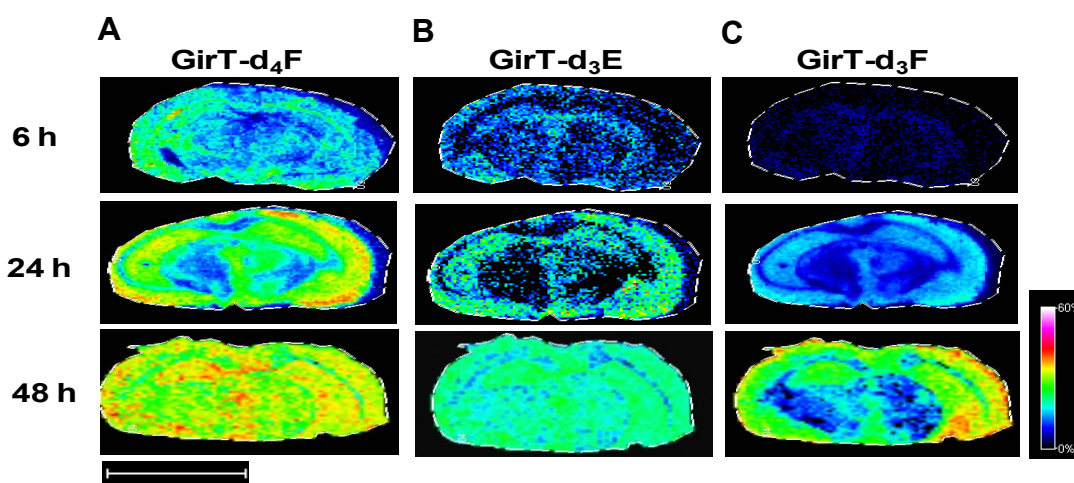


**Figure 6.8:** Cortisol turnover assessed in tissues by measuring the proportions of active and inactive deuterium labeled cortisol as GirT derivatives in regions of murine brain by MALDI-FTICR-MSI. GirT- $d_4F$  and the inactive metabolite GirT- $d_3E$  were effectively detected after 24 h. Regeneration of  $d_3F$  was detectable by 24 h, but more readily after 48 h of infusion. Signal for  $d_3F$  was most intense in the cortex, hippocampus and amygdala. Heat map distribution by MALDI-FTICR-MSI of (a) GirT- $d_4F$  at  $m/z$  480.331 Da (b) GirT- $d_3E$  at  $m/z$  477.293 Da (c) GirT- $d_3F$  at  $m/z$  479.331 Da. Signal intensity is depicted by color on the scale shown. Scale bar (2 mm).

As previously shown in **Ch4** with corticosterone,  $d_3F$  was detected in highest abundance in the cortex, hippocampus and amygdala (**Figure 6.9**). In all regions, the brain displayed the same pattern of a time-dependent increase for both tracer (**Figure**

6.9A), d<sub>3</sub>E (Figure 6.9B) and d<sub>3</sub>F (Figure 6.9C) with higher regeneration found in the hippocampus. Furthermore, as previously shown in tissue homogenate, CORT was depleted after 24 h in all brain regions (Figure 6.9D). Of note, tracers were detected in plasma and liver after 6 h of tracer infusion, earlier than in brain.

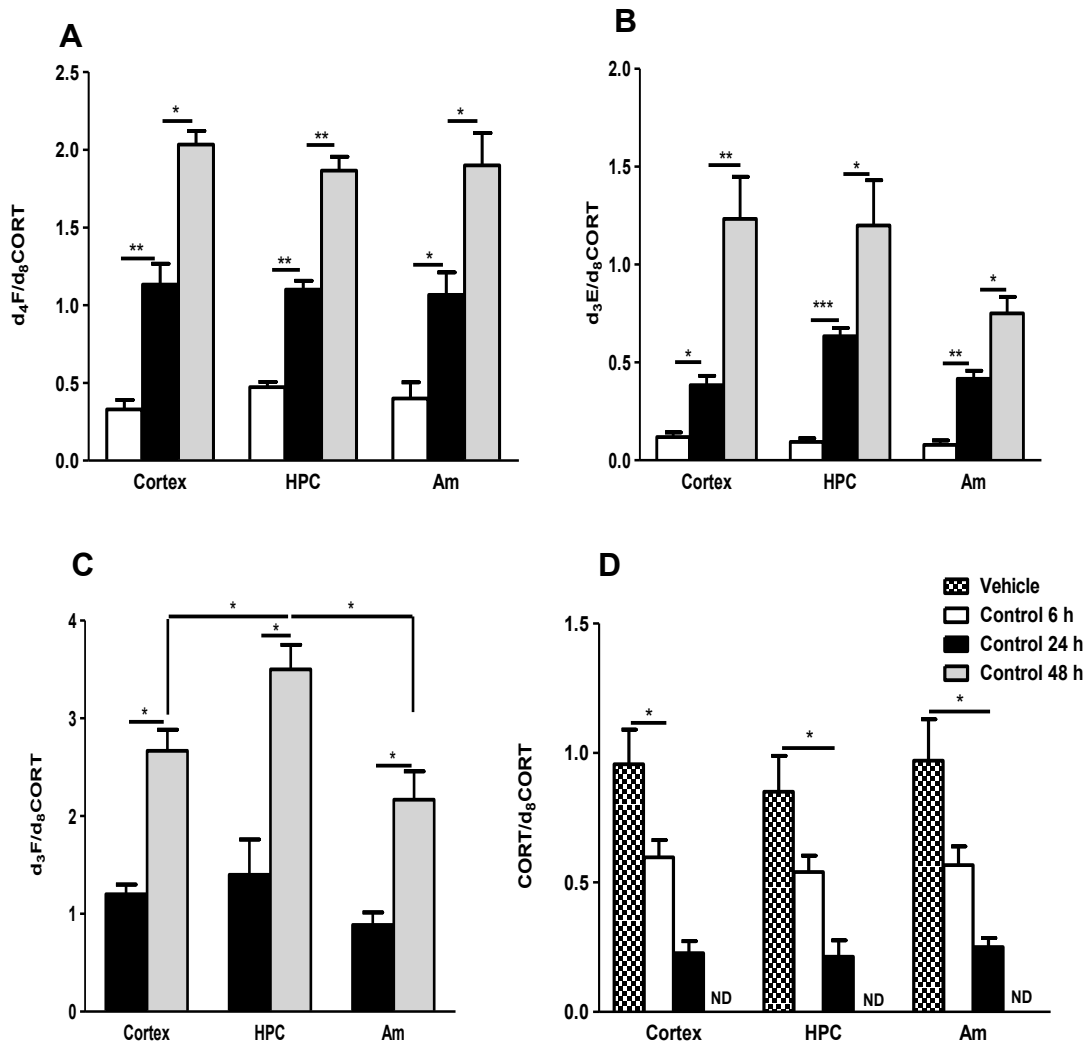


**Figure 6.9:** MALDI-FTICR-MSI in regions of interest in murine brain. (a) d<sub>4</sub>F/d<sub>8</sub>CORT (b) d<sub>3</sub>E/d<sub>8</sub>CORT (c) d<sub>3</sub>F/d<sub>8</sub>CORT (d) CORT/d<sub>8</sub>CORT. Synthesis of d<sub>3</sub>E increased with time as well as d<sub>3</sub>F generation with higher levels found in the hippocampus; CORT was depleted after 24 h infusion. Statistical analysis was performed using two-way ANOVA with Bonferroni's post-hoc test. D<sub>8</sub>CORT intensity was normalized across tissues. Data are mean ± SEM (n=3). \*\*\* P<0.001, \*\* P<0.01 and \* P<0.05. ND: non-detectable. **Control:** Wild-type mice without drug.

#### 6.3.2.4. *Cortisol regeneration in tissues*

Global  $d_3F$  regeneration was estimated as TTR ( $d_4F/d_3F$ ) ratios in plasma and tissue homogenates. Tissue-specific regeneration adjusted for the plasma contribution was calculated according to equation (2) and expressed as  $\Delta TTR_{(T)}$ . As shown in **Figure 6.10A**, TTR displayed a time-dependent reduction with lowest levels observed in the liver. In the brain, TTR displayed lower levels in the hippocampus at 48 h (**Figure 6.10B**). Levels of  $\Delta TTR_{(T)}$  in liver were higher than those found in the brain after 48 h (**Figure 6.10C**) and in both cases, a time-increase regeneration was found. In the brain higher regeneration was observed in the hippocampus. On the contrary, increment was not observed in adipose tissue (**Figure 6.10D**).

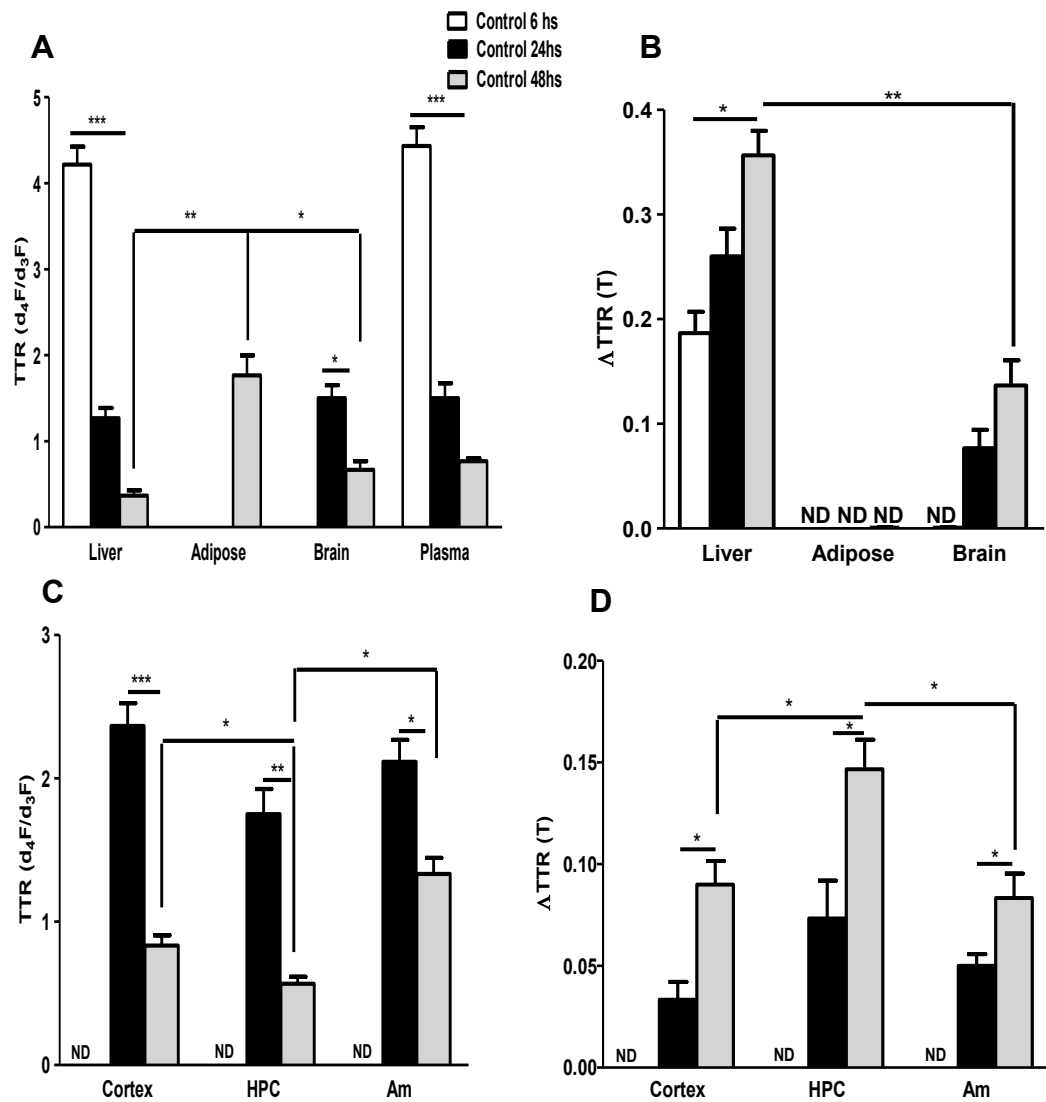


**Figure 6.10:** d<sub>3</sub>F regeneration measured as (a) TTR and (b)  $\Delta TTR_{(T)}$  in tissues and in different regions across the brain as TTR (c) and (d)  $\Delta TTR_{(T)}$  by MALDI-FTICRMS from wild-type mice. TTR (d<sub>4</sub>F/d<sub>3</sub>F) displayed a time-dependent decline pattern with lowest ratios found after 48 h. An increased of  $\Delta TTR_{(T)}$  was observed with time in liver and brain with higher regeneration found in Liver after 48h. In the brain, d<sub>3</sub>F regeneration was observed across the brain with higher levels found in the hippocampus. Statistical analysis was performed using two-way ANOVA with Bonferroni's post-hoc test. Data are mean  $\pm$  SEM (n=3). \*\*\* P<0.001, \*\* P<0.01 and \* P<0.05. ND: non-detectable. **Control:** Wild-type mice without drug.

### 6.3.2.5. *D<sub>3</sub>F* regeneration in mice with genetic disruption of 11 $\beta$ -HSD1

After 48 h infusion, similar d<sub>4</sub>F levels were found in plasma of both WT and KO mice (**Figure 6.11A**). Nevertheless, d<sub>3</sub>F could not be detected or it was below the LOD of the methodology in the plasma (S/N<3) (**Figure 6.11C**). However, absolute levels of d<sub>3</sub>E were significantly higher in the KO than control mice (**Figure 6.11B**) and endogenous CORT was not detectable (S/N<3) after 48 h infusion.

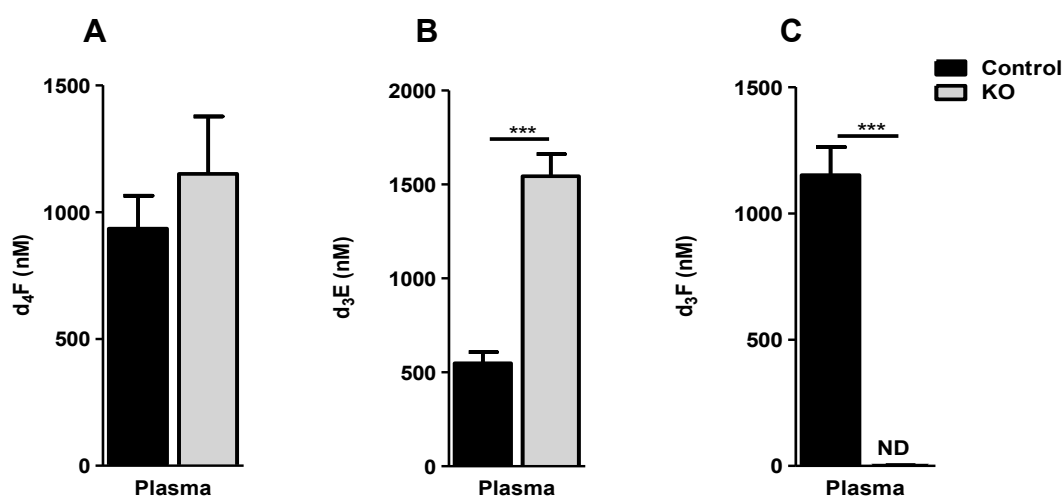


**Figure 6.11:** Concentrations of (a) d<sub>4</sub>F (b) d<sub>3</sub>E in plasma from mice with genetic disruption of 11 $\beta$ -HSD1 (KO), after 48h d<sub>4</sub>F infusion. After disrupting the enzyme, d<sub>3</sub>E displayed a significant accumulation in plasma against controls while levels of d<sub>4</sub>F remained unchanged. Statistical analysis was performed using two-way ANOVA with Bonferroni's post-hoc test. Data are mean  $\pm$  SEM (n=3). \*\*\* P<0.001. **Ra**=Rate of appearance. **ND**: No detectable. **Control**: Wild-type mice without drug

In all the tissue the levels of d<sub>4</sub>F remained unchanged upon enzyme disruption (**Figure 6.12A**). However, d<sub>3</sub>E accumulation was observed upon enzyme disruption in liver and brain, but not in adipose (**Figure 6.12B**). d<sub>3</sub>F regeneration was undetectable or below the LOD (S/N<3) in liver, brain and adipose tissues of the KO mice as  $\Delta$ TTR<sub>(T)</sub> was zero in all tissues (**Figure 6.12C**). MSI analysis further confirmed the results on the brain homogenate as d<sub>3</sub>F was also undetectable.



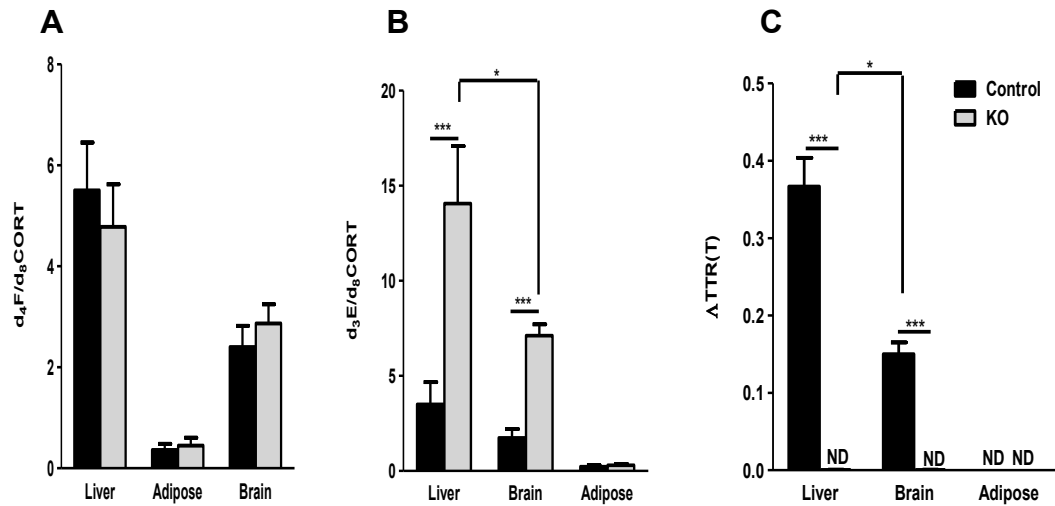


**Figure 6.12:** Estimation of levels of (a)  $d_4F$  and (b)  $d_3E$  normalized to internal standard ( $d_8CORT$ ) and (c)  $\Delta TTR(T)$  in liver, brain and adipose tissue of mice with genetic disruption of  $11\beta$ -HSD1 (KO) following 48 h  $d_4F$  infusion.  $D_4F$  levels were unchanged upon disruption of the enzyme.  $D_3E$  showed a significant accumulation in liver and brain in KO mice against controls with greater accumulation observed in the liver. However, changes were not observed in adipose tissue.  $D_3F$  regeneration was not observed as  $\Delta TTR(T)$  was undetectable, as  $D_8CORT$  intensity was normalized across tissues. Statistical analysis was performed using two-way ANOVA with Bonferroni's post-hoc test. Data are mean  $\pm$  SEM (n=3). \*\*\*  $P < 0.001$  and \*  $P < 0.05$ . **Control:** Wild-type mice without drug.

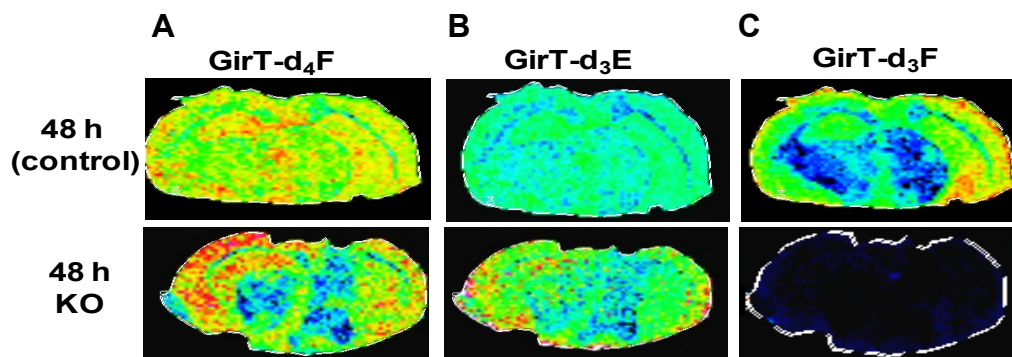


**Figure 6.13:** Cortisol turnover by measuring the proportions of active and inactive deuterium labeled cortisol and metabolites as GirT derivatives in regions of brain from mice with genetic disruption of  $11\beta$ -HSD1 (KO) following 48 h  $d_4F$  infusion. GirT- $d_3F$  could not be detected ( $S/N < 3$ ) after enzyme disruption in KO mice and accumulation of GirT- $d_3E$  was observed. Heat map distribution by MALDI-FTICR-MSI of (a) GirT- $d_4F$  at  $m/z$  480.331 Da (b) GirT- $d_3E$  at  $m/z$  477.293 Da (c) GirT- $d_3F$  at  $m/z$  479.331 Da. Signal intensity is depicted by color on the scale shown. Scale bar (2 mm).

### 6.3.3 PK/PD study of UE2316 using stable isotope tracers

#### 6.3.3.1 PK profile of UE2316

After achieving significant  $d_3F$  regeneration after 48 h, a time-dependent PK/PD study of the tissue specific effects of an  $11\beta$ -HSD1 inhibitor (UE2316) was conducted. UE2316 was administered and mice were killed 1, 2, 4 h post-dose (HPD). As shown in **Figure 6.14**, drug amounts in plasma peaked by 2HPD, declining by 4HPD.

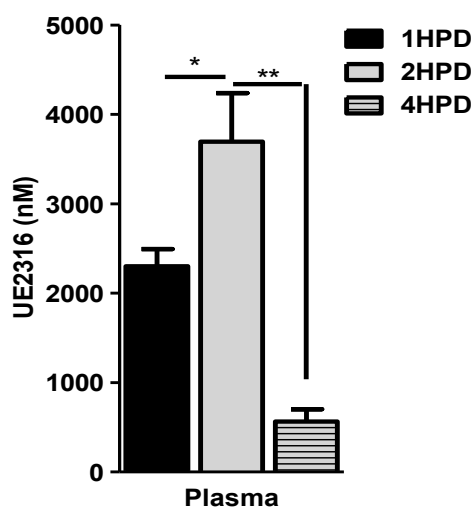


**Figure 6.14:** UE2316 levels in plasma during time dependent PK study. Plasma drug levels reached a peak at 2 hour post-dose (HPD) and were declining by 4 h. Statistical analysis was performed using two-way ANOVA with Bonferroni's post-hoc test. Data are mean  $\pm$  SEM (n=3). \*\*P<0.01 and \*P<0.05.

In other tissues tested, UE2316 amounts also reached a peak at 2HPD and declined at 4HPD. In the liver, drug levels were higher than in the brain at peak level (2HPD). UE2316 was not detected in adipose tissue or the signal was below the LOD (5 nmol/g) (**Figure 6.15**). MS distribution maps clearly confirmed the pattern of drug distribution in the brain (**Figure 6.16**), indicating the drug had crossed the blood brain barrier.

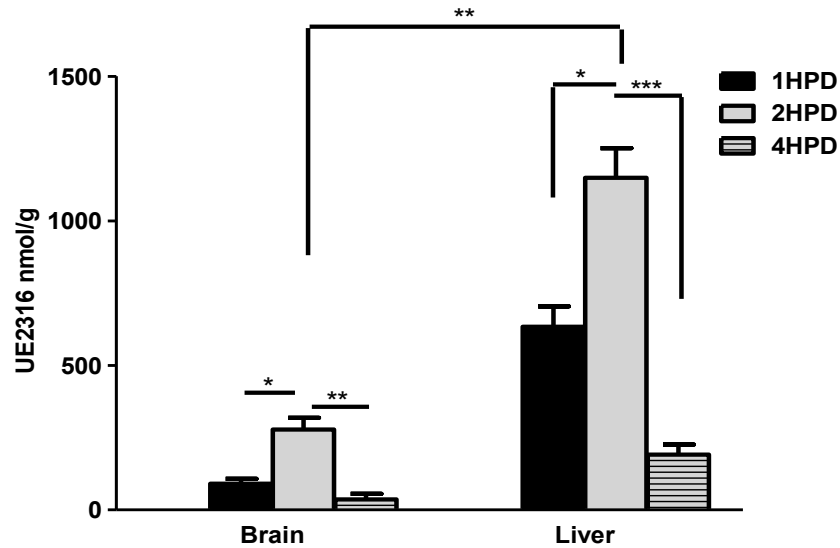


**Figure 6.15:** Levels of UE2316 in brain and liver tissues during d<sub>4</sub>F infusion. Drug (UE2316) levels peaked at 2 hour post-dose (HPD) and declined after 4 h. Absolute levels of drug in the liver were higher than brain at 2HPD. Statistical analysis was performed using two-way ANOVA with Bonferroni's post-hoc test. Data are mean ± SEM (n=3). \*\*\* P<0.001, \*\* P<0.01 and \* P<0.05.

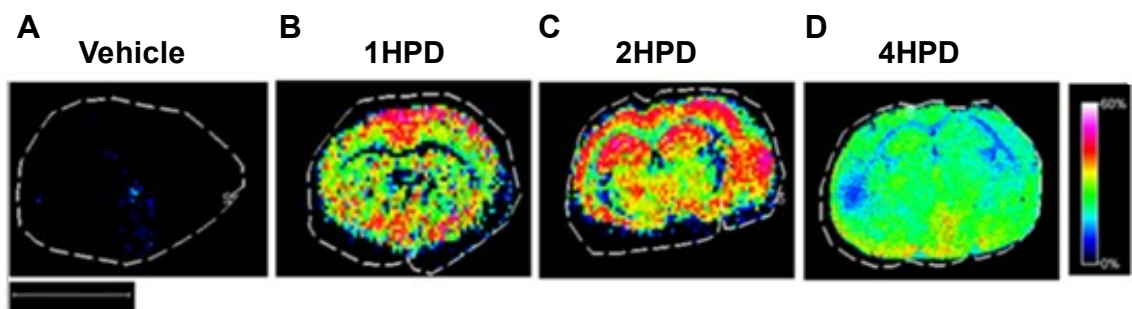


**Figure 6.16:** MS image distribution of UE2316 in murine brain after dosing. Drug levels peaked 2 hour post-dose (HPD) and decline at 4HPD. Heat map distribution by MALDI-FTICR-MSI of UE2316 at *m/z* 390.189 Da (a) Vehicle (b) 1HPD (c) 2HPD (d) 4HPD. Signal intensity is depicted by color on the scale shown. Scale bar (2 mm).

### 6.3.3.2 Plasma PD assessment of glucocorticoid regeneration after UE2316 treatment

After a time-dependent pharmacological inhibition using a selective  $11\beta$ -HSD1 inhibitor PD was assessed by measuring the  $d_4F/d_3F$  and rate of appearance ( $R_A$ ) of  $d_3F$ . In the plasma, tracer levels were unaffected during the study (Figure 6.17A) but an accumulation of the  $d_3E$  metabolite was observed at 2HPD (Figure 6.17B).  $D_3F$  concentration as well as the  $R_A$  of  $d_3F$  decreased after 2HPD (Figure 6.17C,D).

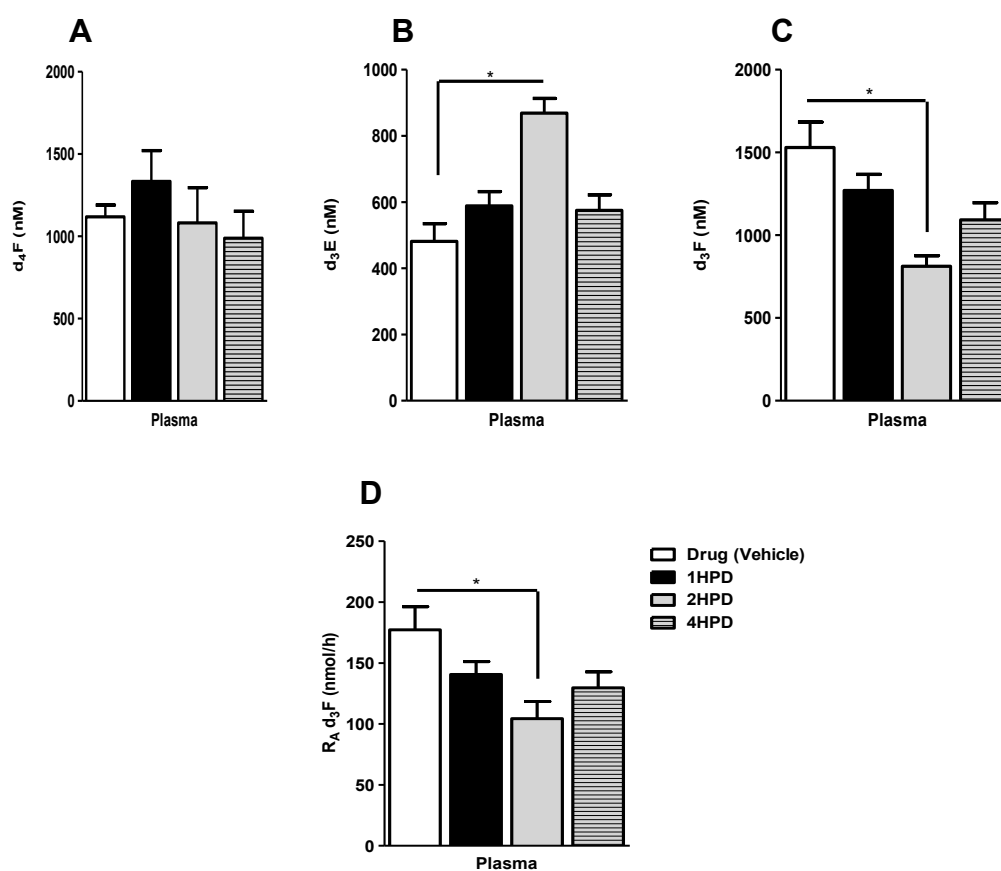


**Figure 6.17:** Plasma concentrations of (a)  $d_4F$  (b)  $d_3E$  (c)  $d_3F$  and (d) rate of appearance ( $R_A$ ) of  $d_3F$  in during timed inhibition of  $11\beta$ -hydroxysteroid dehydrogenase type 1 by UE2316. An accumulation of  $d_3E$  was found 2h post-dose (2HPD) while  $d_4F$  levels remained unchanged. Levels of  $d_3F$  and  $R_A$  decreased after 2HPD. Statistical analysis was performed using two-way ANOVA with Bonferroni's post-hoc test. Data are mean  $\pm$  SEM (n=3). \*P<0.05.

### 6.3.3.3. *Tissue PD assessment of glucocorticoid regeneration after UE2316 treatment*

PD was also evaluated in metabolic tissues and the brain. As is shown in **Figure 6.18A** no changes were observed in  $d_4F$  levels in any tissues during the study. A simultaneous accumulation of the inert metabolite ( $d_3E$ ) was found (**Figure 6.18B**) peaking at 2HPD in all tissue except in adipose and in brain, where levels remained unchanged after 4HPD. Tracee ( $d_3F$ ) level declined upon enzyme inhibition in all tissue except in the adipose, with lowest levels found at 2HPD.

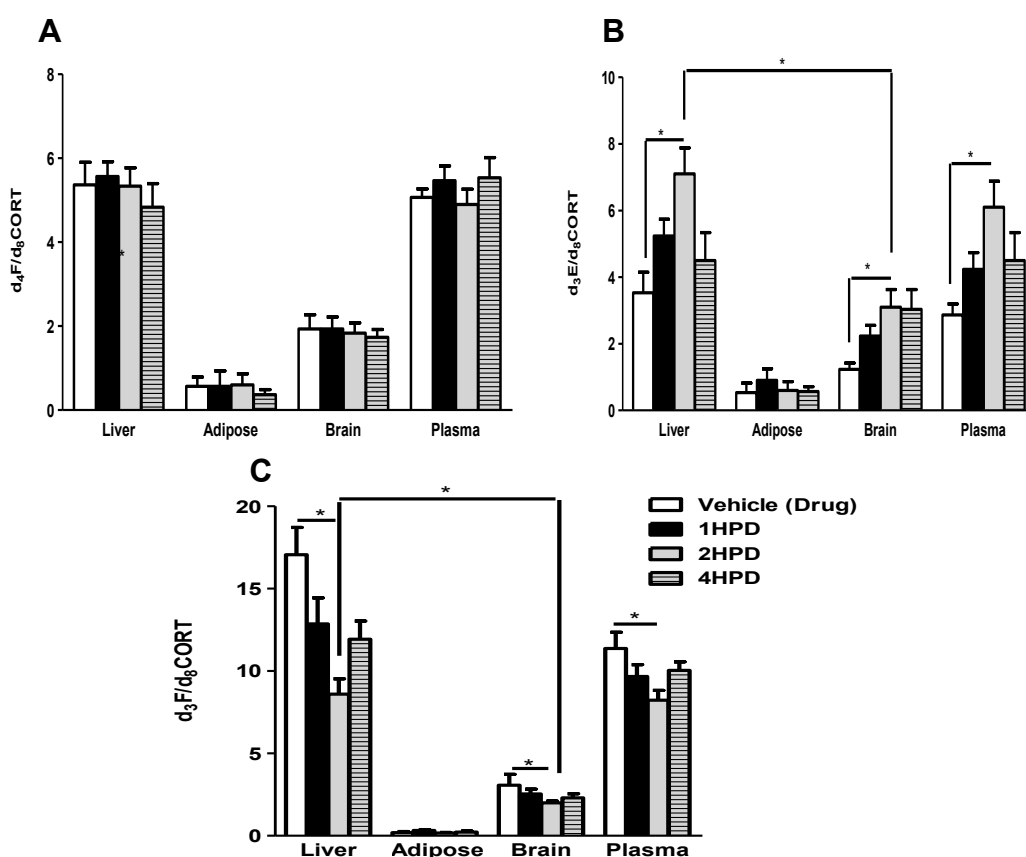


**Figure 6.18:** Estimation of (a)  $d_4F$  (b)  $d_3E$  and (c)  $d_3F$  levels normalized to internal standard ( $d_8CORT$ ) in liver, adipose, brain and plasma. tissue during UE2316 treatment.  $D_4F$  levels were unchanged while  $d_3E$  levels showed a significant accumulation in liver and brain 2HPD with a greater magnitude in the liver  $d_3E$  and  $d_3F$  displayed a time-dependent increased pattern upon pharmacological inhibition of the enzyme.  $D_8CORT$  was normalized for all tissues. Statistical analysis was performed using two-way ANOVA with Bonferroni's post-hoc test. Data are mean  $\pm$  SEM (n=3). \*P<0.05.

In the brain, molecular distribution maps (**Figure 6.19**) were generated and relative quantitation was conducted (**Figure 6.20**) for the tracer, tracee and the inert  $d_3E$  metabolite. As shown in **Figure 6.19C and 20C** a decline in signal intensity of  $d_3F$  was observed between 2 and 4 HPD primarily in the hippocampus and cortex in comparison with vehicle while the tracer levels were unchanged (**Figure 6.19A and 20A**). Furthermore, an accumulation of  $d_3E$  was observed at 2HPD in both cortex and hippocampus but interestingly not in the amygdala (**Figure 6.19B, 20B**).

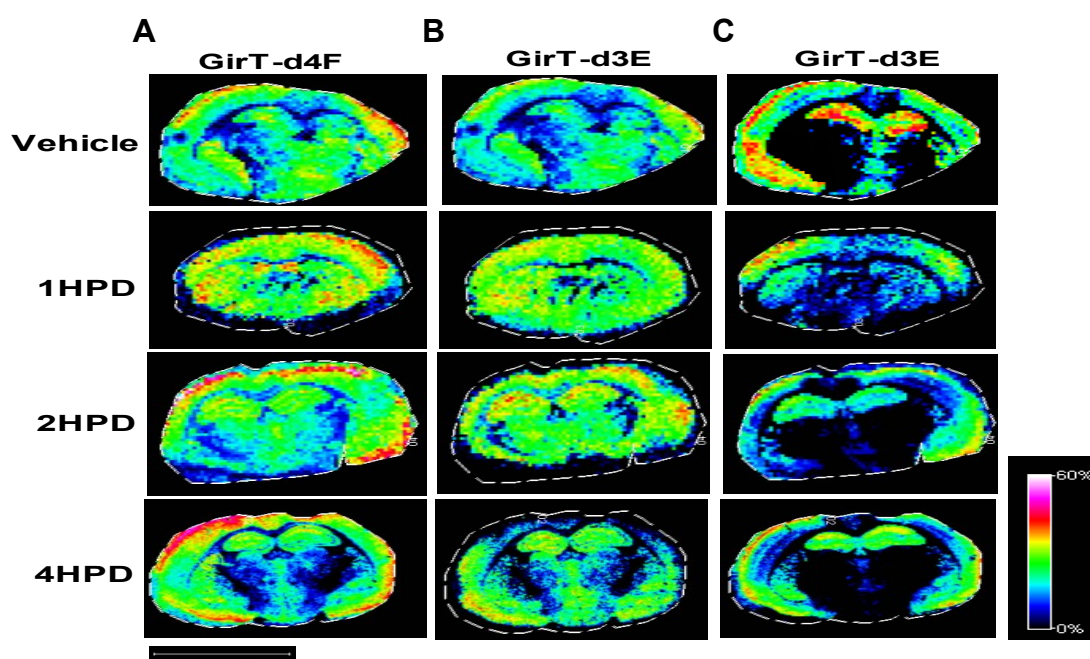


**Figure 6.19:** Evaluation of changes in  $d_4F$ ,  $d_3E$  and  $d_3F$  following inhibition of  $11\beta$ -hydroxysteroid dehydrogenase type 1 using UE2316 by MSI in murine brain. Signal intensity of GirT- $d_3F$  decline upon treatment with an accumulation of  $d_3E$  metabolite primarily at 2HPD. No differences were observed in  $d_4F$  levels during treatment. MS images of (a) GirT- $d_4F$  at  $m/z$  480.331 Da (b) GirT- $d_3E$  at  $m/z$  477.293 Da (c) GirT- $d_3F$  at  $m/z$  479.331 Da. Signal intensity is depicted by color on the scale shown. Scale bar (2 mm).

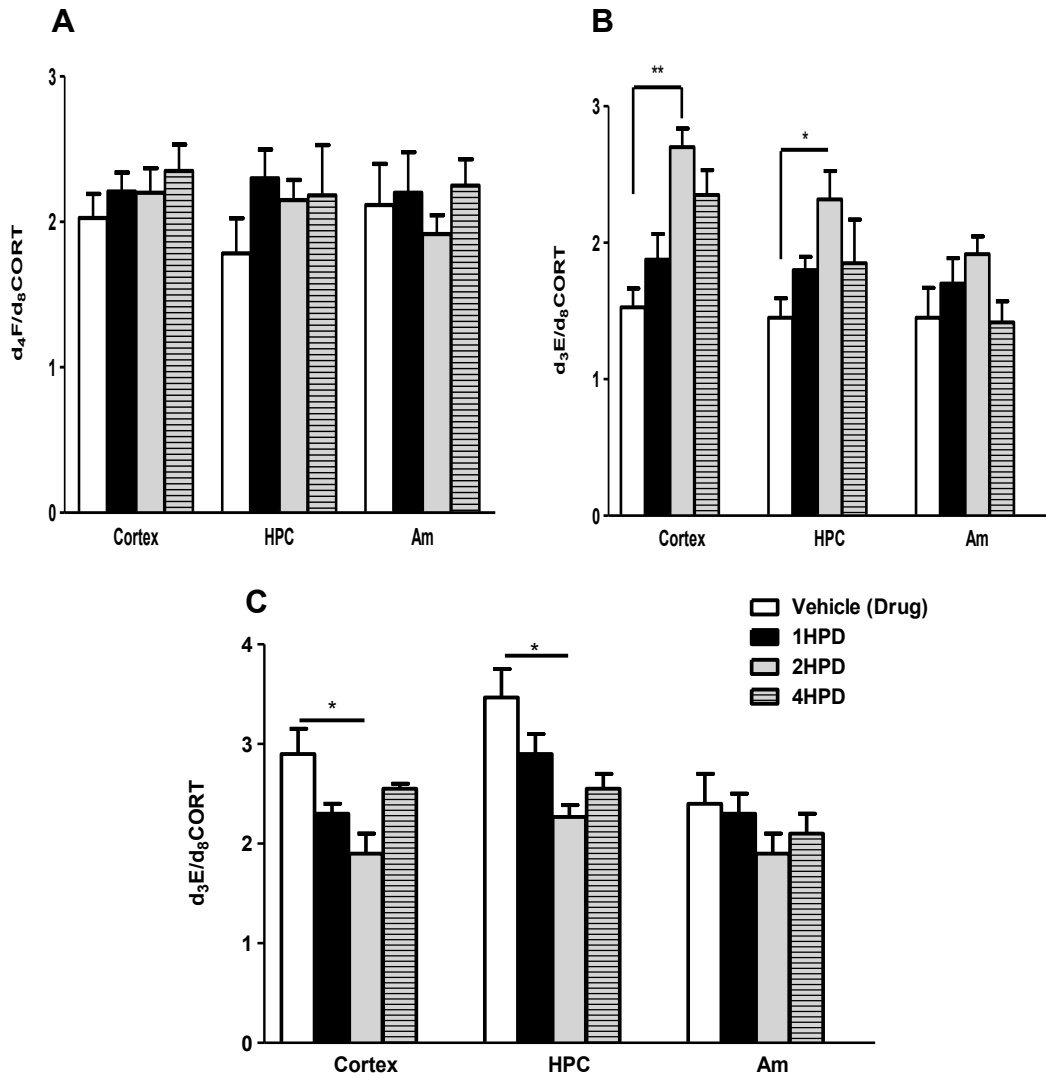


**Figure 6.20:** MALDI-FTICR-MSI in regions of interest (ROI) in murine brain. (a)  $d_4F/d_8CORT$  (b)  $d_3E/d_8CORT$  and (c)  $d_3F/d_8CORT$ . Levels of tracer were unchanged and removal of  $d_3E$  may have been impaired with time. On the contrary,  $d_3F$  generation was suppressed after 2HPD.  $D_8CORT$  intensity was normalized across tissues. Statistical analysis was performed using two-way ANOVA with Bonferroni's post-hoc test. Data are mean  $\pm$  SEM (n=3). \*\*  $P<0.01$  and \* $P<0.05$ .

#### **6.3.3.4. *Tissue-cortisol regeneration suppression in tissues upon pharmacological inhibition***

PD was assessed by calculation of the TTR ( $d_4F/d_3F$ ) ratios on plasma and tissues. Tissue-specific PD measured as tracee ( $d_3F$ ) suppression during the pharmacological inhibition was calculated according to equation (2) and expressed as  $\Delta TTR_{(T)}$ .

In plasma and in all tissues except in the adipose, TTR ( $d_4F/d_3F$ ) ratios were significantly increased 2HPD after administration of the pharmacological inhibitor, indicative of lower  $d_3F$  regeneration with the effect declined towards 4HPD as expected in the brain. (**Figure 6.21A**).  $\Delta TTR$  confirmed the pattern observed in the TTR as tissue-specific suppression of the  $d_3F$  synthesis was found after correction for plasma contribution upon enzyme inhibition (**Figure 6.21B**).

In the brain, region-specific PD was assessed by MSI. As shown in **Figure 6.21C** an increase was observed after 2 and 4 HPD in cortex and hippocampus, an indication of lower regeneration of  $d_3F$  by  $11\beta$ -HSD1. Interestingly, no significant changes were found in the amygdala (**Figure 6.21D**).



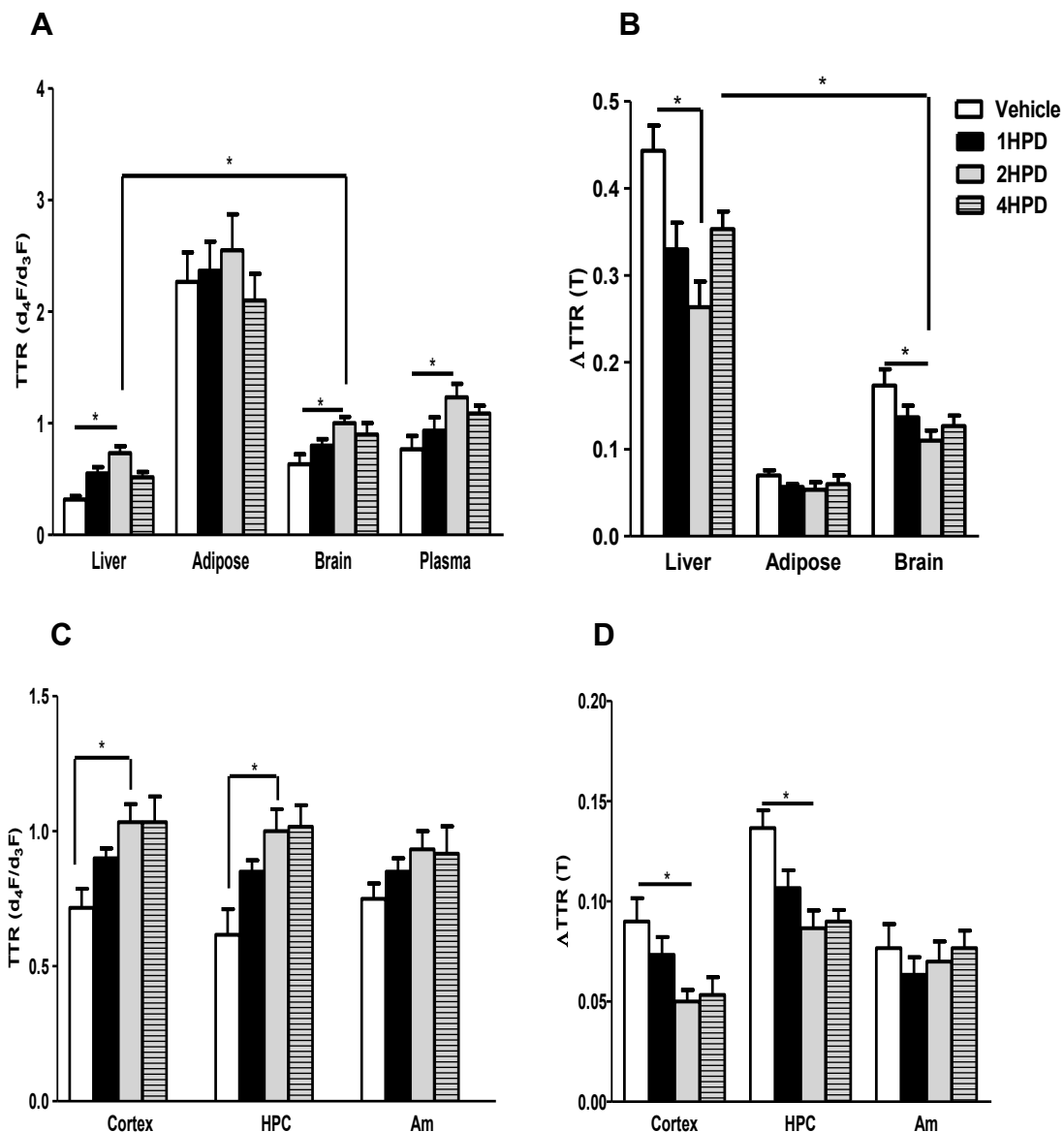


**Figure 6.21:** Suppression of d<sub>3</sub>F regeneration measured as (a) TTR and (b) ΔTTR (T) in tissues and in different regions across the brain as TTR (c) and (d) ΔTTR<sub>(T)</sub> by MALDI-FTICRMS upon enzyme inhibition by UE2316. TTR (d<sub>4</sub>F/d<sub>3</sub>F) displayed a time-dependent increased pattern with higher ratios found at 2HPD except for adipose tissue. A decline of ΔTTR<sub>(T)</sub> was observed with time in liver and brain with higher suppression found in the liver at 2HPD. In the brain, d<sub>3</sub>F synthesis suppression was observed across the brain with an exception of the amygdala with higher levels of ΔTTR<sub>(T)</sub> found in the hippocampus. Statistical analysis was performed using two-way ANOVA with Bonferroni's post-hoc test. Data are mean ± SEM (n=3). \*P<0.05.

### 6.3.3.5. UE2316 metabolism

To further exploit the advantage of multiplexed analysis of MSI, metabolite identification was carried out in the liver and brain from mice treated with UE2316 (4HPD). In the liver (using tissue homogenate), two potential phase II metabolites were observed at  $m/z$  565.132 Da proposed as a metabolite formed by N-glucuronidation (**Metabolite I**) and at  $m/z$  521.011 Da as a further phase I metabolite formed by decarboxylation (**Metabolite II**) (**Figure 6.22**).

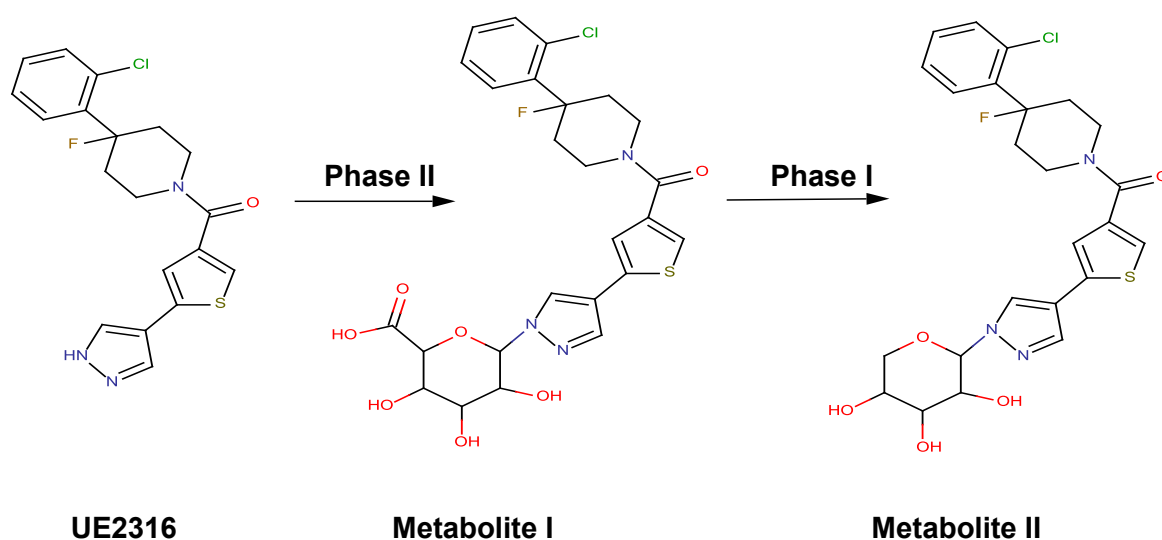


**Figure 6.22:** Proposed metabolic pathway for UE2316 in the liver

In the brain, two metabolites were potentially detected. From the molecular structure of UE2316, it is anticipated that the piperidine alpha hydrogens will be prompt to oxidise by phase I CYP450 enzymes leading to potential hydroxylation and further oxidised ketone products (**Figure 6.23**). Molecular distribution maps were generated for the theoretical monoisotopic masses of the proposed metabolites (**Figure 6.23**). A proposed hydroxylation product at  $m/z$  406.079 Da **Metabolite III**) (**Figure 6.24**) was

detected mainly distributed across the striatum and cortex. On the contrary, a further oxidised metabolite at  $m/z$  404.063 Da (**Metabolite IV**) (possible ketone formation) was mainly found in the hippocampus and amygdala. The distinct distribution of each metabolite is clearly shown in **Figure 6.24D**.

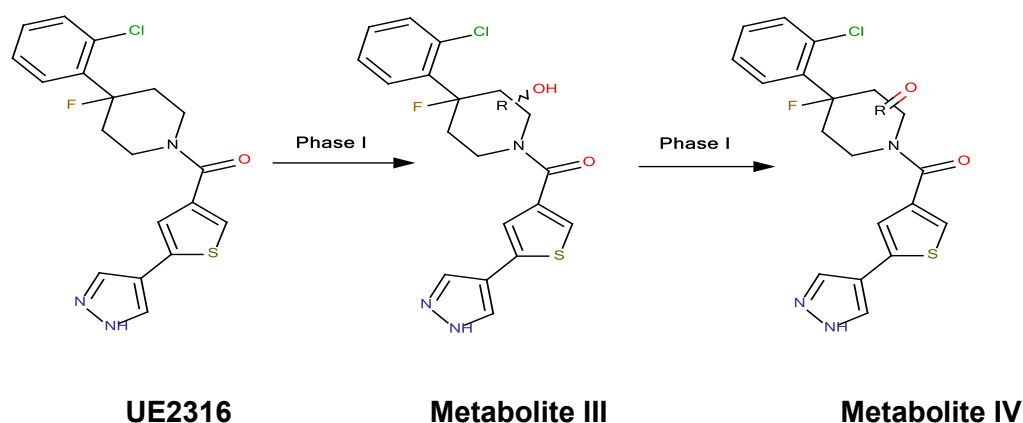


**Figure 6.23:** Proposed metabolic pathway for UE2316 in the brain

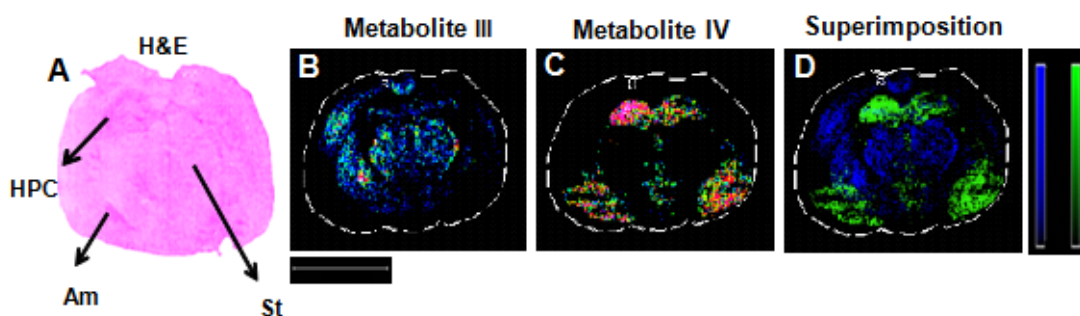


**Figure 6.24:** Metabolite identification MSI in mouse brain of UE2316 4 hours post-dose. Proposed Phase I metabolites had different distribution across brain, with metabolite I mainly distributed in the striatum and cortex and metabolite II found in the hippocampus and amygdala. (a): Haemotoxylin and eosin (H & E) histological staining. Molecular distribution maps of (b): Potential hydroxylation metabolite (Metabolite I) at 406.079 Da. (c): Ketonic metabolite at  $m/z$  404.063 Da (Metabolite II). (d): Molecular superimposition maps of Metabolite I (blue) and Metabolite II (green). Scale bar (2 mm). **HPC:** hippocampus, **Am:** amygdala, **St:** Striatum.

## 6.4 Discussion

The OTCD-MSI platform was successfully applied to measure the contribution of  $d_3F$  regeneration at tissue-specific level using stable isotope tracer ( $d_4F$ ). As previously demonstrated with unlabelled corticosteroids, neutral tracer and their corresponding metabolites were converted to positively charged hydrazone derivatives using (GirT), enabling detection and quantitation by MALDI-FTICRMSI and structures were further confirmed by LESA. In **Ch4**, measurement of endogenous steroids had been achieved but this did not allow assessment of rates of tissue-specific regeneration of active glucocorticoids. For this, a stable-isotope tracer was employed.

As previously performed for other steroids, the GirT derivatisation was evaluated for labelled cortisol ( $d_4F$ ) and ( $d_3F$ ) on-tissue spotted standards on a control brain with a successful outcome as both labelled derivatives were detected with an acceptable signal/noise ( $S/N > 200$ ) and good mass accuracy ( $< 5$  ppm). As the ionisation was driven by the GirT-tag, the response factor between  $d_4F$  and  $d_3F$  was 1.04, in concordance with what already had been found for unlabelled corticosteroids in **Ch5**. Therefore, the deuterium atoms did not have any effect on either the derivatisation reaction or the efficiency of ionisation. Furthermore, preliminary detection of endogenous labelled  $d_4F$  and  $d_3F$  in an infused brain ( $d_4F$ , 48 h) was achieved and structures confirmed by LESA shared the same fragmentation patterns as previously described for unlabelled analogues in **section 3.3.5.6**. Interestingly, the distribution of  $d_3F$  during CASI<sup>TM</sup> optimisation was primarily located in the striatum and corpus callosum in contrast to the tracer that it was primarily found across the cortex, hippocampus and amygdala.

After tracer infusion, the levels of d<sub>4</sub>F in the plasma reached around 349 ± 22 nM (24 h infusion) and 955 ± 54 nM after 48 h infusion, higher than endogenous levels of CORT (286 ± 29 nM) observed in vehicle-infused (DMSO:PG) mice. In humans, the normal physiological concentration of cortisol is ranging from (138-635nM, diurnal) and (83-441nM, afternoon) (Aldhahi *et al.*, 2004), therefore, during the study, physiological level of d<sub>4</sub>F was slightly exceeded. In a biochemistry context,  $K_M$  is the concentration of substrate at which half the active sites are filled. Thus,  $K_M$  can provide a measure of the substrate concentration required for significant catalysis to occur and also an approximation of substrate concentration in vivo. The measured substrate (d<sub>3</sub>E) concentration at 48 h infusion was 536 ± 39 nM thus, in the range of  $K_M$  values of 11β-HSD1 (0.1-0.3μM (reduction)). Furthermore the  $[S]/K_M$  ratio was between 1.5-2, close to normal values at physiological concentration typically between 0.01 and 1.0. After 6 h of d<sub>4</sub>F infusion, endogenous CORT was depleted in plasma from baseline levels 286 ± 29 nM (vehicle-infused) to 77±18 nM and ultimately not detected. This will have arisen through negative feedback suppression of ACTH by d<sub>4</sub>F and loss of stimulation of the adrenal cortex.

As this is the first study conducted in rodent using d<sub>4</sub>F as a tracer, cortisol regeneration was compared to that observed in human studies. Followed d<sub>4</sub>F infusion, levels peaked at 955± 54 nM (tracer), 536 ± 39 nM (d<sub>3</sub>E) and 1257 ± 45 nM (d<sub>3</sub>F) in 48 h with cortisol turn-over higher than in humans as whole-body rate of appearance of d<sub>3</sub>F at 48 h was lower (242 ± 25 nmol/h infused at 0.07 mg/h) than values found in human

studies at steady-state ( $\sim 1$  nmol/h infused at  $\sim 1$  mg/h, corrected for body weight) (Andrew *et al.*, 2005).

Followed  $d_4F$  infusion, the presence of tracer could be demonstrated after 6 h in plasma, liver and brain and after 48 h in adipose, these differences must reflect differences in access to tissues and indeed Hughes *et al.* (Hughes *et al.*, 2013) previously showed slow turnover of the adipose steroid pool in human adipose.  $D_3E$ , the substrate for  $11\beta$ -HSD1 reductase, followed the same pattern as observed in  $d_4F$  but with lower levels. The contribution of circulating substrate could not be subtracted, therefore levels of  $d_3E$  measured as  $d_3E/d_8CORT$  in tissues account for total  $d_3E$  in both tissues and circulating pools. Lastly  $d_3F$  was readily detected in plasma and liver at 6 h, but it took 24 h to appear in brain, where it was located primarily in cortex, hippocampus and amygdala, the hippocampus being the more active region. Again in adipose, it took 48 h for  $d_3F$  to be detected having a  $S/N \sim 7$  at this time point. Endogenous CORT was depleted (below LOD) from plasma and liver after 6 h. However, in the brain and adipose CORT levels were decreased after 24 h becoming undetectable (below LOD) in the brain after 48 h but not in the adipose as CORT was still detectable after 48 h infusion.

In the liver, which is an  $11\beta$ -HSD1-rich tissue, the turnover was higher as the  $d_4F/d_3F$  ratios were lowest at all time points and showed a similar pattern as in the plasma. The blood contribution to apparent cortisol regeneration in tissues was estimated by subtracting the plasma TTR ( $d_4F/d_3F$ ) ratios expressed as  $\Delta TTR_{(T)}$  (equation 2). In liver and brain local regeneration was observed, in contrast to adipose in which turn-over was not observed. In previous studies in humans it has been asserted that the measured

whole body rate of appearance reflects the splanchnic bed, of which liver 11 $\beta$ -HSD1 makes the greatest contribution (Andrew *et al.*, 2005). Interestingly, unlike in humans, the tracer had not reached steady state during the time interval tested. A reason of this observation could be due to the minipump taking time to reach maximum infusion rate.

Beyond plasma, target tissue availability of glucocorticoids is also regulated in blood by their plasma protein binding, largely to corticosteroid-binding globulin (CBG as well as albumin). CBG binds physiological glucocorticoids (F, CORT) with high affinity, but has low or minimal affinity for their inert 11-keto-forms (E, 11-DHC) (Breuner *et al.*, 2002). CBG may also act to deliver glucocorticoids to target cells. Binding to CBG and lower affinity proteins such as albumin ensures that only a small amount (2–5%) of physiological glucocorticoid is ‘free’ in the circulation (Rosner, 1990). Traditionally, steroid transport across the cell membrane was assumed to be a passive process following a concentration gradient. However, an increasing number of transporters of steroids have been identified, such as the organic anion transporter-3 in the adrenal (Atanasov *et al.*, 2008), the multidrug resistance P-glycoprotein in the central nervous system (Baker *et al.*, 1991), and the glucocorticoid importer in the liver (Lackner *et al.*, 1998). Particularly, in the brain, where d<sub>4</sub>F took 24 h to be detected, the Mdr/p-glycoprotein/ABCB1 transporter acts particularly at the blood–brain barrier (but also on other membranes) to partially exclude specific corticosteroids from brain (as in many peripheral organs), although such membrane ‘barriers’ are not absolute. Nonetheless p-glycoprotein minimises access of synthetic steroids like dexamethasone to the brain (Meijer *et al.*, 1998) and appears responsible for the preferential access of corticosterone rather than cortisol to human cerebrospinal fluid (Karssen *et al.*, 2001).

In the adipose some *in vivo* human studies (Lackner *et al.*, 1998; Stimson *et al.*, 2009) suggested that the slow rate of accumulation of d<sub>4</sub>F is determined by transport between plasma and intra-adipose steroid pools rather than by rapid enzymatic inactivation. This may reflect dissolution in triglyceride depots. This contrasts very markedly with the liver, in which d<sub>4</sub>F levels were detected after 6 h infusion with a considerable regeneration after 24 h. It is possible that in the adipose tissue the slow accumulation is a reflection of its relatively low blood flow ~3 ml/100 g adipose tissue/min (Katz *et al.*, 1999b) vs. ~400 ml/min in liver (Stimson *et al.*, 2009). Furthermore, another *in vivo* study reported that adipose uptake of [<sup>3</sup>H]<sub>2</sub>-cortisol was approximately five times slower than that of sex steroids due to solubility in the triglyceride pool (only 12.7% uptake at 3 h) (Bleau *et al.*, 1974).

In term of the PK, there is no evidence that d<sub>4</sub>F and cortisol have different PK profile due to a “primary isotope effect” (Andrew *et al.*, 2002), although their affinity for transporters has not been tested. The current data indicating slow turnover between plasma and tissue pools of cortisol are consistent with the intraadipose cortisol pool integrating the longer-term variations in circulating glucocorticoid concentrations. However, unless there are multiple pools of glucocorticoid within the adipose, with a cytosolic “free” pool that turns over more quickly than a triglyceride-bound pool, then it appears unlikely that intraadipose cortisol concentrations vary widely during acute changes in plasma cortisol. Thus, diurnal variation in intraadipose cortisol concentrations is likely to be small. This contrasts with other tissues, such as brain (Droste *et al.*, 2008) and liver (Stavreva *et al.*, 2009) where, at least in rodents, tissue concentrations vary even with ultradian (hourly) fluctuations in plasma glucocorticoids. It will be important to establish the rates of exchange between plasma and other



intracellular cortisol pools in other organs.

After genetic disruption of 11 $\beta$ -HSD1, d<sub>3</sub>F generation was not detected in plasma or any tissues, suggesting that 11 $\beta$ -HSD1 is the only enzyme carrying out this reaction. Furthermore, accumulation d<sub>3</sub>E was also observed upon enzyme depletion reinforcing the concept that 11 $\beta$ -HSD1 acts primarily as a reductase in the tissues tested here.

After a more modest intervention, pharmacological inhibition using an inhibitor selective for murine 11 $\beta$ -HSD1 (UE2316), a similar pattern was seen. The circulating concentrations of drug achieved a peak in tissues after 2 h and declined towards 4 h after a single bolus. The blood concentrations achieved during the study were greater (3-23 times) than UE2316 K<sub>i</sub> (162nM), predicting full enzyme blockage. The dose chosen was based on previous unpublished studies where *ex vivo* assessment of enzyme activity supported these magnitudes of enzyme inhibition in liver and brain, although this was not measured here. The absolute amounts in tissues were also above K<sub>i</sub> as levels found in the brain were 278  $\pm$  23 nmol/g and 1149  $\pm$  81 nmol/g in the liver. In adipose, UE2316 was not detected, suggesting the drug could not reach the adipose tissue during the time of the study, in agreement with previous *in vitro* studies carried out by Webster et al. (unpublished). Adipose is poorly perfused, and it takes more time for the drug to reach the tissue, perhaps explaining null or poor inhibitory effects. This fits with lack of accumulation of d<sub>3</sub>E and no change in TTR (d<sub>4</sub>F/d<sub>3</sub>F) in adipose in the time course studied.

As for most drug-like molecules like UE2316, the distribution is generally uneven because of differences in blood perfusion, tissue binding (e.g, because of lipid content),

regional pH, and permeability of cell membranes. Distribution equilibrium between blood and tissue is reached more rapidly in richly vascularised areas (e.g. liver), unless diffusion across cell membranes is the rate-limiting step. For interstitial fluids of most tissues, drug distribution rate is determined primarily by perfusion. For poorly perfused tissues (e.g. adipose), distribution was very slow, presumably due to moderate lipophilicity of UE2316 measured by its partition-coefficient (LogP) (3.8) (unpublished) which may lead to high drug/lipid affinity. Because fat is poorly perfused, equilibration time was long, especially in highly lipophilic drugs. Furthermore, the extent of drug distribution into tissues depends on the degree of plasma protein and tissue binding. In the bloodstream, UE2316 is mostly bound to plasma proteins (>80%) (unpublished) and only unbound drug is available for passive diffusion to extravascular or tissue sites where the pharmacologic effects of the drug occur. Therefore, the unbound drug concentration in systemic circulation typically determines drug concentration at the active site and thus efficacy. Like most hydrophobic drugs, UE2316 could reach the CNS via brain capillaries and cerebrospinal fluid (CSF). Although the brain receives about one sixth of cardiac output, drug penetration is restricted because of the brain's permeability characteristics. However, due to its moderate high LogP, UE2316 reached the brain readily 1h post-dose. The reason is the blood-brain barrier, which consists of the endothelium of brain capillaries and the astrocytic sheath. The endothelial cells of brain capillaries, which appear to be more tightly joined to one another than those of most capillaries, may slow the diffusion of water-soluble drugs. The astrocytic sheath consists of a layer of glial connective tissue cells (astrocytes) close to the basement membrane of the capillary endothelium (de Vries *et al.*, 1997). Also due to its LogP, UE2316 may enter the

ventricular CSF directly via the choroid plexus, and then passively diffuse into brain tissue from CSF.

Again in vehicle treated mice,  $1118 \pm 59$  nM of d<sub>4</sub>F was achieved in the circulation and rates of appearance of d<sub>3</sub>F were lowered in the whole body, following administration of the inhibitor. This could be seen as the TTR (d<sub>4</sub>F/d<sub>3</sub>F) ratios increasing in plasma. The time course of change mirrored those of the drug concentrations, with a small delay.

The most significant increase of TTR (d<sub>4</sub>F/ d<sub>3</sub>F) and  $\Delta$ TTR<sub>(T)</sub> ratios in brain and liver were observed 2-4 HDP, aligning with the peak in drug concentration at 2 h. Furthermore, tissue-specific suppression of d<sub>3</sub>F regeneration was also found after subtraction of the circulating pool contribution.

There was a considerable decline in drug levels after 4HPD. The ratio of active to inactive steroid in liver and plasma responded quickly to the declining drug, but the brain levels were still altered 4HPD, suggesting buffering of this pool or long dwell time on the enzyme. As no compensation is possible from the adrenal gland, one hypothesis could be that the circulating d<sub>3</sub>F can be further metabolised by other enzymes. In adipose, levels of tracee were not altered, presumably due to the slow turnover and poor drug penetration in adipose tissue. Further experiments such as influence of H6PDH enzyme on cortisol regeneration and effects of tissue specific KO (e.g. liver, brain) would be beneficial to further understand the regulation at tissue-specific level.

In regards to UE2316 metabolism, standard pharmacokinetic assessments are generally carried out after the peak of the drug concentration is reached, in this case after 2HPD.

In the liver (homogenate), phase II metabolites were identified as potential glucuronidation derivatives (metabolite III and IV) potentially catalysed by UDP-glucuronosyltransferase CYP enzymes. Based on the  $m/z$  Metabolite IV was proposed as a decarboxylation product of metabolite III potentially catalysed by cyp152 CYP 450 family enzymes. In a tissue collected 4HPD two further metabolites were identified in the brain with different spatial distribution. The metabolite I was proposed as a phase I CYP450 potentially catalysed by (CYP2A6) sub-families through hydroxylation at the acidic 3-5  $\alpha$ -halogenated position of the piperidine ring and further oxidise to metabolite II by a potential P450 reductase (CYPOR). It is well documented (Gonzalez, 1988) that the CYP 450 content in the brain is low (less than 1% found in the liver). However, several studies have shown that the levels of CYPs in specific neurons can be as high or higher than levels in hepatocytes (Miksys *et al.*, 2002). Although it is unlikely that brain CYPs contribute to overall clearance of xenobiotics, they are able to metabolise a variety of compounds, including many drugs that cross the blood–brain barrier to produce their pharmacological effects within the brain. Given their highly localised expression and extreme sensitivity to environmental inducers, they may contribute substantially to much of the observed inter individual variation in response to centrally acting drugs. They may also be responsible for some of the variation seen in side effects and toxicities of drugs that enter the CNS (Miksys *et al.*, 2002). Therefore, the different spatial distribution patterns observed in the MS images could be related with the enzymes' localisation across the brain, but further work need to be performed in order to confirm this hypothesis. However, in order to fully confirmed all proposed metabolites structures, further characterisation analysis such as MS fragmentation and NMR must be carried out.

## 6.5 Conclusion

In this Chapter, I confirmed that deuterated cortisol tracer with in combination OTCD-MALDI-FTICR-MSI can usefully be employed to measure, for the first time, the region-specific turnover in the  $11\beta$ -HSD pathway in mouse brain and to infer the regional activity of  $11\beta$ -HSD1 isozyme. In this study, the data obtained with this novel tool provides new insight into the physiology of glucocorticoid metabolism in brain and metabolic tissues in rodents. In agreement with other human studies, data show slow  $11\beta$ -HSD1 activity in adipose may be due to lack of access of  $d_3E$  leading to low  $d_3F$  generation.  $D_3F$  regeneration was observed in the liver and moderate regeneration in brain primarily in the hippocampus and cortex where  $11\beta$ -HSD1 expression is high. Furthermore, this work has also demonstrated that OTCD-MSI with deuterium cortisol labelling is a promising *ex vivo* high sensitivity, high resolution and multiple compounds detection label-free methodology that can potentially be used to assess the tissue-specific pharmacokinetic and pharmacodynamic profiles of novel  $11\beta$ -HSD1 inhibitors. This study has clearly shown the benefit of using MSI over conventional LC/MS on tissue homogenate in drug metabolism.

# Chapter 7

## Overall summary and future perspectives

### 7.1. Overall summary

In this thesis, a MSI platform using a MALDI-FTICRMS was developed and optimised for spatial distribution analysis of endogenous and exogenous  $\alpha$ - $\beta$  unsaturated- keto steroids as Girard T hydrazone derivatives in biological tissue sections. The application of MALDI-MSI with OTCD using Girard-T reagent to study diverse steroid and sterols biology has been demonstrated. Molecular maps have been generated of glucocorticoids, androgens and oxysterols in several rodent tissue sections, where analytes were selected with the appropriate chemical groups to react with Girard T. Furthermore, beyond murine and rat tissues, human samples have been successfully analysed. This platform was further validated using a biological proof of concept study in which detection and distribution of endogenous corticosteroids were achieved within sub-regions of murine brain, following manipulation of  $11\beta$ -HSD1 enzyme.

In this thesis it was also demonstrated that the MSI platform can usefully be used to measure the region-specific turnover in the  $11\beta$ -HSD pathway in a mouse brain and to infer the activity of  $11\beta$ -HSD1 isozyme using stable isotope tracers. The data obtained with these novel tools provide new insight into the physiology of glucocorticoid metabolism in brain and metabolic tissues in rodents. Furthermore, the methodology was used to assess the tissue-specific pharmacokinetic and pharmacodynamic profiles

of novel 11 $\beta$ -HSD1 inhibitors showing its benefit in the assessment of regional metabolite distribution in the mouse brain, impossible to achieve using the conventional LC/MS approaches in tissue homogenate.

## **7.2. Future perspectives**

MALDI-MSI is an emerging tool to enhance understanding of drugs, metabolites and endogenous compounds (lipids, proteins) directly in tissue sections. Its ability to co-localise drug or metabolite distribution with histological information has been transformational in biochemistry and can be achieved at meaningful levels of spatial resolution.

However, before MALDI-MSI is accepted as a quantitative tool a number of issues still need to be addressed, such as regional ion-suppression and reproducibility of sample preparation. In addition, industry and researchers will further develop and refine hardware and software to make the MSI approach more robust and easier to implement in a high-throughput capacity. Iterative technical improvements in ionisation and mass analysers will increase the sensitivity and speed of MSI experiments. Limitations of spatial resolution have to be addressed if cellular imaging is needed to allow specific assessment of steroid/drug trafficking across different organelles; techniques like SIMS or new developments in nanoSIMS may hold the key. Nano-structure initiator mass spectrometry (NIMS) (Yanes et al., 2009), laser ablation electrospray ionisation (LAESI) (Nemes & Vertes, 2010) and nano-DESI (Takats et al., 2004), amongst others, may also broaden the scope for application of the MSI in steroid biology. MSI can aid the refinement of clinical studies and an increasing use of in situ MSI for analysis of

clinical samples is predicted.

In terms of MSI of steroids, the platform can be expanded to study progesterone and estrogens, but more challenging on-tissue derivatisation approaches have to be carried out in order to be able to detect the low physiological levels. In particular for estrogens, to reach the pM physiological concentrations, the LOD needs to be improved up to 100 times of those achieved for glucocorticoids. The application of CASI<sup>TM</sup> may hold the key as shown very promising results on derivatised glucocorticoids and the fact that the ionisation is mostly driven by the GirT-tag other keto-steroids should follow the same desorption/ionisation mechanism.

In case high spatial resolution is desirable (molecular histology), MALDI (up to 5  $\mu\text{m}$ ) or SIMS (up to 50 nm) can be used, nevertheless, the sampling area decreases inversely proportional with spatial resolution leading to a loss of sensitivity.

As in MSI, achieving a better sensitivity can compromise spatial resolution, so the question to be answered (whole body/organ vs. profiling) is the determining factor in a successful MSI analysis. If spatial resolution is not needed, LESA can be used as it is one of most sensitive platforms, particularly, using FTICRMS as ions can be accumulated for a longer period of time than MALDI leading to better S/N ratios.

In this thesis, it has been demonstrated for the first time that the spatial distribution of low levels steroids in biological tissue section (primarily in the brain) can be studied by tissue derivatisation followed MALDI-FTICRMS analysis. This is the first technique capable of detecting and quantifying corticosteroids to  $<200 \mu\text{m}$  resolution, and at physiological concentrations, allowing application within region-specific areas of



murine brain. its utility for measuring pharmacodynamic effects of small molecule inhibitors of 11 $\beta$ -HSD1; in combination with pharmacokinetic imaging was also demonstrated. This offers the prospect of many novel insights into tissue-specific steroid and sterol biology

# Appendix I

- i.           Synthesis of 4-chloro- $\alpha$ -cyanocinnamic acid (Cl-CCA)**
- ii.           Introduction**

MALDI has become an enabling technology for the fields of proteomics and metabolomics. Despite its widespread use, for example, in small molecule identification, a comprehensive model for the generation of free gas-phase ions has not yet been developed. All matrices in use today, such as CHCA, have been found empirically and stem from the early days of MALDI. By systematic and targeted variation of the functional groups of the  $\alpha$ -cyanocinnamic acid core unit, 4-chloro- $\alpha$ -cyanocinnamic acid (Cl-CCA) was selected and synthesised as previously described by Jaskolla and co-workers (Jaskolla *et al.*, 2008). The key feature of the novel matrix is a lower proton affinity than its hydroxyl analogue which may enhance the proton transfer from a reactive protonated matrix species to the analytes of interest by increasing the ion formation via a chemical ionisation mechanism with proton. This increase in performance promises to have an impact on future analytical applications of MALDI, because current sensitivity limits are overcome and more comprehensive analyses come into reach.

### iii. Methods

### iv. Synthesis

The synthesis was carried out as previously described by Jaskolla (Jaskolla *et al.*, 2008). Cl-CCA was synthesized by standard Knoevenagel condensation using cyanoacetic acid and 4-chlorobenzaldehyde with ammonium acetate as a catalyst (**Figure APX1**). Cyanoacetic acid (1eq), 4-chlorobenzaldehyde (0.9 eq) and ammonium acetate (0.15 eq) were refluxed, with stirring, in toluene (60 mL). After separation of the reaction water by a Dean Stark trap (4 h), the reaction mixture was allowed to cool (40°C) and filtered. The crude product was washed with distilled water and purified by repeated recrystallization from methanol/water (1:1).

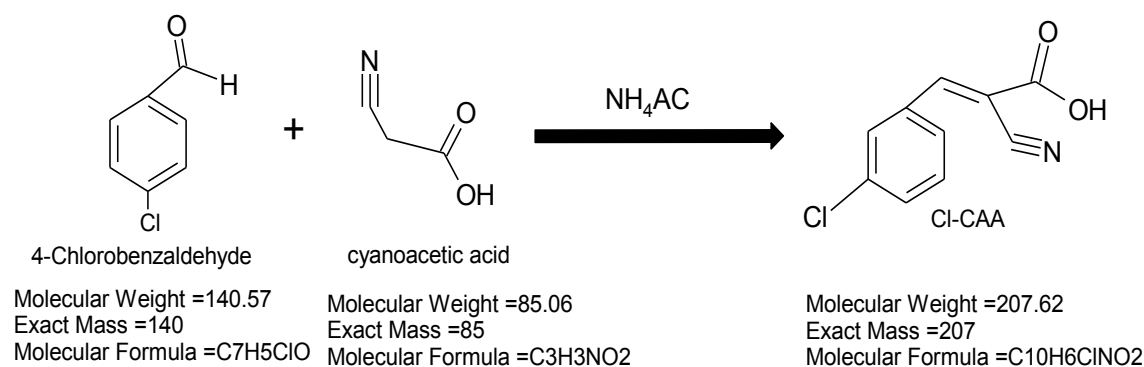


**Figure APX1:** 4-chloro- $\alpha$ -cyanocinnamic acid synthetic scheme. Cl-CCA: (4-chloro- $\alpha$ -cyanocinnamic acid), NH<sub>4</sub> AC: ammonium acetate.

**v. LC/MS (yield calculation)**

Separation was achieved on an Inerstil ODS-3 100 x 2.1 mm, 3  $\mu\text{m}$  (GL Sciences, Torrance, USA) column. Mobile phases, consisting of 0.1% v/v formic acid (FA) in  $\text{H}_2\text{O}$  (A) and 0.1% v/v FA in acetonitrile (B), were used at a flow rate of 0.3 mL/min, with an initial hold of 3 min at 5% B followed by a linear gradient to 95% B in 15 min and re-equilibration at initial conditions (3 min). ZMD single Quad with ESI source was used in negative ion mode. Data were acquired in broadband mode (50-500 Da). 10  $\mu\text{L}$  of a 0.1 mg/mL solution of the re-crystallised material was injected in the LC/MS system.

**vi. Accurate mass determination**

Accurate mass measurement was performed using a 12T SolariX MALDI-FTICR-MS in broadband mode, covering a mass range of (98-1500 Da). Analysis was performed at 2 Mword time-domain transient in broadband mode using negative ion mode at 500 laser shots using 5 scans/spot.

**vii. Nuclear magnetic resonance (NMR) characterisation**

5 mg of the final product was dissolved in 0.8 mL of deuterated dimethyl sulfoxide ( $\text{DMSO-d}_6$ ) and transfer to an NMR tube (Bruker Daltonics, Bremen, GmbH).  $^1\text{H}$  NMR and  $^{13}\text{C}$  NMR spectra of these samples were measured at 500.13 MHz  $^1\text{H}$  and  $^{13}\text{C}$  using a Bruker DRX-500 spectrometer (Bruker Daltonics, Bremen, GmbH).

## viii. Results

The overall yield of product, a colourless powder with needle shaped crystals, was ~60 % assessed after three consecutive re-crystallisations. Accurate mass analysis detected an ion at 206.00167Da (**Figure APX2**) with a mass accuracy of 4.2 ppm against the expected Cl-CCA deprotonated monoisotopic quasimolecular ion.

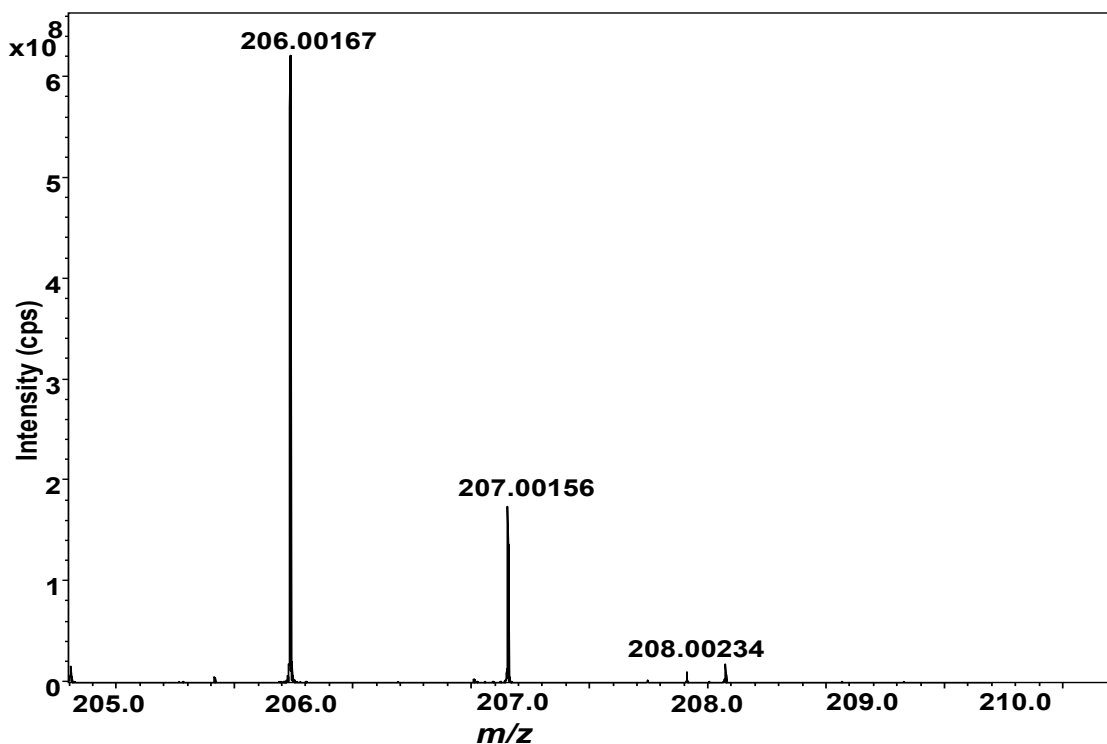


**Figure APX2:** MALDI-FTICR-MS of 4-chloro- $\alpha$ -cyanocinnamic acid (Cl-CCA) cps: count per seconds.

Proton  $^1\text{H}$ NMR and  $^{13}\text{C}$ NMR spectra were concordant with Cl-CCA structure with  $^1\text{H}$  NMR signals at (500 MHz, DMSO- $d_6$ , 25°C):  $\delta = 8.3$  (*s*, *COOH*),  $\delta = 8.0$ -7.8 (*d*, 2H,  $J = 9.6$  Hz Ar-H), 7.7 – 7.5 (*d*, 2H,  $J = 9.5$  Hz, Ar-H), 4.9 (*s*, 1H, CH conjugated Ar-H),

3.15 (s,  $H_2O$ ) ppm (**Figure APX3A**) and  $^{13}C$ NMR at  $\delta = 164.36, 152.65, 139.49, 131.11, 130.1, 128.89, 117.01,$  and  $105.58.22$  ppm (**Figure APX3B**)

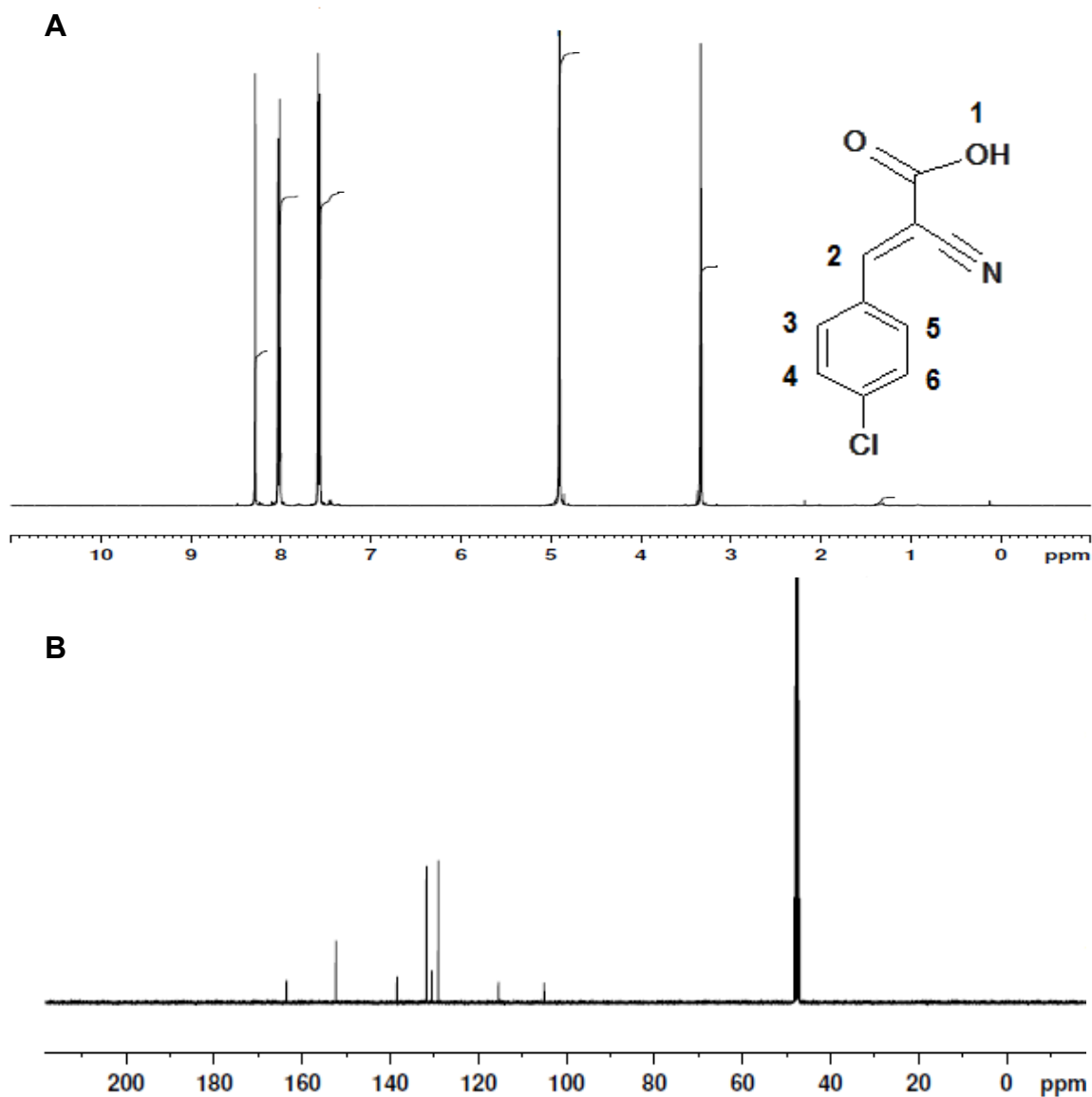


**Figure APX3** : (a):  $^1H$ NMR and (b):  $^{13}C$ NMR spectra of 4-chloro- $\alpha$ -cyanocinnamic acid (Cl-CCA)  
ppm: part per million.

## **ix. Conclusion**

The chlorine analogue of CCA, Cl-CCA, was successfully synthesised and characterised with a very good reaction yield according with the proposed synthetic scheme.

## 8. References

- Agarwal AK, Monder C, Eckstein B, White PC (1989). Cloning and expression of rat cDNA encoding corticosteroid 11 $\beta$ -dehydrogenase. *J.Biol.Chem.* **264**: 18939-18943.
- Agarwal AK, Tusie-Luna M-T, Monder C, White PC (1990). Expression of 11 $\beta$ -hydroxysteroid dehydrogenase using recombinant vaccinia virus. *Mol.Endocrinol.* **4**: 1827-1832.
- Albiston AL, Obeyesekere VR, Smith RE, Krozowski ZS (1994). Cloning and tissue distribution of the human 11 $\beta$ -hydroxysteroid dehydrogenase type 2 enzyme. *Mol.Cell.Endocrinol.* **105**: R11-R17.
- Aldhahi W, Mun E, Goldfine AB (2004). Portal and peripheral cortisol levels in obese humans. *Diabetologia* **47**(5): 833-836.
- Altelaar AF, Luxembourg SL, McDonnell LA, Piersma SR, Heeren RM (2007). Imaging mass spectrometry at cellular length scales. *Nature protocols* **2**(5): 1185-1196.
- Altelaar AF, van Minnen J, Jimenez CR, Heeren RM, Piersma SR (2005). Direct molecular imaging of *Lymnaea stagnalis* nervous tissue at subcellular spatial resolution by mass spectrometry. *Analytical chemistry* **77**(3): 735-741.
- Andrew R, Phillips DIW, Walker BR (1998). Obesity and gender influence cortisol secretion and metabolism in man. *Journal of Clinical Endocrinology & Metabolism* **83**: 1806-1809.
- Andrew R, Smith K, Jones GC, Walker BR (2002). Distinguishing the activities of 11 $\beta$ -hydroxysteroid dehydrogenases *in vivo* using isotopically labelled cortisol. *Journal of Clinical Endocrinology & Metabolism* **87**: 277-285.
- Andrew R, Westerbacka J, Wahren J, Yki-Jarvinen H, Walker BR (2005). The contribution of visceral adipose tissue to splanchnic cortisol production in healthy humans. *Diabetes* **54**: 1364-1370.
- Andrews RC, Walker BR (1999). Glucocorticoids and insulin resistance: old hormones, new targets. *Clinical Science* **96**: 513-523.
- Atanasov AG, Nashev LG, Gelman L, Legeza B, Sack R, Portmann R, *et al.* (2008). Direct protein-protein interaction of 11 $\beta$ -hydroxysteroid dehydrogenase type 1 and hexose-6-phosphate dehydrogenase in the endoplasmic reticulum lumen. *Biochem Biophys Acta* **1783**: 1536-1543.
- Baker ME, Fanestil DD (1991). Licorice, computer-based analyses of dehydrogenase sequences, and the regulation of steroid and prostaglandin action. *Mol.Cell.Endocrinol.* **78**: C99-C102.



Bartsch G, Rittmaster RS, Klocker H (2002). Dihydrotestosterone and the concept of 5alpha-reductase inhibition in human benign prostatic hyperplasia. *World J Urol* **19**(6): 413-425.

Basu R, Basu A, Grudzien M, Jung P (2009). Liver is the site of splanchnic cortisol production in obese nondiabetic humans. *Diabetes* **58**: 39-45.

Basu R, Edgerton DS, Singh RJ, A. C, Rizza RA (2006). Splanchnic cortisol production in dogs occurs primarily in the liver: Evidence for substantial hepatic specific 11beta hydroxysteroid dehydrogenase type 1 activity. *Diabetes* **55**: 3013-3019.

Basu R, Singh RJ, Basu A, Chittilapilly EG, Johnson CM, Toffolo G, *et al.* (2004). Splanchnic cortisol production in humans: evidence for conversion of cortisone via the 11beta-hydroxysteroid dehydrogenase (11betahsd) type 1 pathway. *Diabetes* **53**: 2051-2059.

Baxter JD (1976). Glucocorticoid hormone action. *Pharmac.Ther.* **2**: 605-659.

Beato M, Herrlich P, Shutz G (1995). Steroid hormone receptors: many actors in search of a plot. *Cell* **83**: 851-857.

Becker JS, Matusch A, Depboylu C, Dobrowolska J, Zoriy MV (2007). Quantitative imaging of selenium, copper, and zinc in thin sections of biological tissues (slugs-genus arion) measured by laser ablation inductively coupled plasma mass spectrometry. *Analytical chemistry* **79**(16): 6074-6080.

Benediktsson R, Calder AA, Edwards CRW, Seckl JR (1997). Placental 11 $\beta$ -hydroxysteroid dehydrogenase: a key regulator of fetal glucocorticoid exposure. *Clinical endocrinology* **46**: 161-166.

Benninghoven A, Sichtermann WK (1978). Detection, identification and structural investigation of biologically important compounds by secondary ion mass spectrometry. *Analytical chemistry* **50**(8): 1180-1184.

Best R, Walker BR (1997). Additional value of measurement of urinary cortisone and unconjugated cortisol metabolites in assessing the activity of 11 $\beta$ -hydroxysteroid dehydrogenase *in vivo*. *Clinical Endocrinology (Oxford)* **47**: 231-236.

Bland JM, Altman DG (1986). Statistical methods for assessing agreement between two methods of clinical measurement. *Lancet* **i**: 307-310.

Bleau G, Roberts KD, Chapdelaine A (1974). The *in vitro* and *in vivo* uptake and metabolism of steroids in human adipose tissue. *The Journal of clinical endocrinology and metabolism* **39**(2): 236-246.

- Blum S, Buhler H, Lichtenstein I, Siebe H (1995). Characterization of human placental 11 $\beta$ -hydroxysteroid dehydrogenase, a key enzyme of corticosteroid metabolism. *Cellular Physiology & Biochemistry* **5**(3): 167-175.
- Bocchi B, Kenouch S, Lamarre-Cliche M, Muffat-Joly M, Capron MH, Fiet J, *et al.* (2004). Impaired 11 $\beta$ -hydroxysteroid dehydrogenase type 2 activity in sweat gland ducts in human essential hypertension. *Hypertension* **43**(4): 803-808.
- Boonen E, Vervenne H, Meersseman P, Andrew R, Mortier L, Declercq PE, *et al.* (2013). Reduced Cortisol Metabolism during Critical Illness. *New England Journal of Medicine*.
- Bradshaw JAO, O.S.; Meyer, K.A.; Goering, D.E. (2009) Combined chemical and topographic imaging at atmospheric pressure via microprobe laser desorption/ionization mass spectrometry– atomic force microscopy. *Rapid Commun Mass Spectrom* **23** (3781-3786)
- Breuner CW, Orchinik M (2002). Plasma binding proteins as mediators of corticosteroid action in vertebrates. *The Journal of endocrinology* **175**(1): 99-112.
- Brodbelt-Lustig JS, Cooks RG (1989). Determination of relative gas-phase basicities by the proton-transfer equilibrium technique and the kinetic method in a quadrupole ion-trap. *Talanta* **36**(1-2): 255-260.
- Brown AJ, Jessup W (1999). Oxysterols and atherosclerosis. *Atherosclerosis* **142**: 1-28.
- Brown AJ, Jessup W (2009). Oxysterols: Sources, cellular storage and metabolism, and new insights into their roles in cholesterol homeostasis. *Molecular Aspects of Medicine* **30**: 111-122.
- Brown RW, Chapman KE, Edwards CRW, Seckl JR (1993). Human placental 11 $\beta$ -hydroxysteroid dehydrogenase: evidence for and partial purification of a distinct NAD-dependent isoform. *Endocrinology* **132**: 2614-2621.
- Brust AA, Ransohoff W, Reiser MF (1951). Blood pressure responses to ACTH and cortisone in normotensive and hypertensive subjects in the resting state and during autonomic blockade with tetra-ethyl ammonium chloride. *J.Clin.Invest.* **30**: 630.
- Buhrman DL, Price PI, Rudewiczcor PJ (1996). Quantitation of SR 27417 in human plasma using electrospray liquid chromatography-tandem mass spectrometry: A study of ion suppression. *Journal of the American Society for Mass Spectrometry* **7**(11): 1099-1105.
- Bujalska IJ, Draper N, Tomlinson JW, Stewart PM, Walker EA (2003). Hexose-6-phosphate dehydrogenase directs 11-hydroxysteroid dehydrogenase type 1 reductase activity in human adipose tissue. *Programme of the 85th Meeting of the Endocrine Society*: O36-35.

Bujalska IJ, Gathercole LL, Tomlinson JW, Darimont C, Ermolieff J, Fanjul AN, *et al.* (2008). A novel selective 11 $\beta$ -hydroxysteroid dehydrogenase type 1 inhibitor prevents human adipogenesis. *The Journal of endocrinology* **197**(2): 297-307.

Bujalska IJ, Kumar S, Stewart PM (1997). Does central obesity reflect 'Cushing's disease of the omentum'? *Lancet* **349**: 1210-1213.

Bujalska IJ, Walker EA, Hewison M, Stewart PM (2002). A switch in dehydrogenase to reductase activity of 11 $\beta$ -hydroxysteroid dehydrogenase type 1 upon differentiation of human omental adipose stromal cells. *Journal of Clinical Endocrinology and Metabolism* **87**(3): 1205-12

Caprioli R (2007). MALDI mass spectrometry for direct tissue analysis: a new tool for biomarker discovery. *Proteome Research* **4**(4): 1138-1142.

Caprioli RM, Farmer TB, Gile J (1997). Molecular imaging of biological samples: localization of peptides and proteins using MALDI-TOF MS. *Analytical chemistry* **69**(23): 4751-4760.

Carmichael J, Paterson IC, Diaz P, Crompton GK, Kay AB, Grant IWB (1981). Corticosteroid resistance in chronic asthma. *Brit.Med.J.* **282**: 1419-1422.

Carson-Jurica MA, Schrader WT, O'Malley BW (1990). Steroid receptor family: structure and functions. *Endocrine reviews* **11**(2): 201-220.

Carson C, III, Rittmaster R (2003). The role of dihydrotestosterone in benign prostatic hyperplasia. *Urology* **61**(4 Suppl 1): 2-7.

Castellino S, Groseclose MR, Wagner D (2011). MALDI imaging mass spectrometry: bridging biology and chemistry in drug development. *Bioanalysis* **3**(21): 2427-2441.

Chacon A, Zagol-Ikapitte I, Amarnath V, Reyzer ML, Oates JA, Caprioli RM, *et al.* (2011). On-tissue chemical derivatization of 3-methoxysalicylamine for MALDI-imaging mass spectrometry. *Journal of mass spectrometry : JMS* **46**(8): 840-846.

Chandra S, Lorey ID, Smith DR (2002). Quantitative subcellular secondary ion mass spectrometry (SIMS) imaging of boron-10 and boron-11 isotopes in the same cell delivered by two combined BNCT drugs: in vitro studies on human glioblastoma T98G cells. *Radiation research* **157**(6): 700-710.

Chapman KE, Kotelevtsev YV, Jamieson PM, Williams LJS, Mullins JJ, Seckl JR (1997). Tissue-specific modulation of glucocorticoid action by the 11 $\beta$ -hydroxysteroid dehydrogenases. In: *Biochemical Society Transactions* Vol. 25, pp 583-587.

Chaurand P, Schwartz SA, Billheimer D, Xu BJ, Crecelius A, Caprioli RM (2004a). Integrating histology and imaging mass spectrometry. *Analytical chemistry* **76**(4): 1145-1155.

- Chaurand P, Schwartz SA, Capriolo RM (2004b). Profiling and imaging proteins in tissue sections by MS. *Analytical chemistry* **76**(5): 87A-93A.
- Chernushevich IV, Loboda AV, Thomson BA (2001). An introduction to quadrupole-time-of-flight mass spectrometry. *Journal of mass spectrometry : JMS* **36**(8): 849-865.
- Connell JMC, Whitworth JA, Davies DL, Lever AF, Richards AM, Fraser R (1987). Effects of ACTH and cortisol administration on blood pressure, electrolyte metabolism, atrial natriuretic peptide and renal function in normal man. *J.Hypertens.* **5**: 425-433.
- Corrie JET, Edwards CRW, Budd PS (1985). A radioimmunoassay for 18-hydroxycortisol in plasma and urine. *Clin.Chem.* **31**: 849-852.
- Costanzo LS (2006). *Physiology*. 3rd edn. Saunders Elsevier: Philadelphia, PA.
- de Vries HE, Kuiper J, de Boer AG, Van Berkel TJ, Breimer DD (1997). The blood-brain barrier in neuroinflammatory diseases. *Pharmacological reviews* **49**(2): 143-155.
- Dill AL, Ifa DR, Manicke NE, Costa AB, Ramos-Vara JA, Knapp DW, *et al.* (2009). Lipid profiles of canine invasive transitional cell carcinoma of the urinary bladder and adjacent normal tissue by desorption electrospray ionization imaging mass spectrometry. *Analytical chemistry* **81**(21): 8758-8764.
- Draper N, Walker EA, Bujalska IJ, Tomlinson JW, Chalder SM, Arlt W, *et al.* (2003). Mutations in the genes encoding 11 $\beta$ -hydroxysteroid dehydrogenase type 1 and hexose-6-phosphate dehydrogenase interact to cause cortisone reductase deficiency. *Nature Genetics* **34**(4): 434-439.
- Dreisewerd K (2003). The desorption process in MALDI. *Chemical reviews* **103**(2): 395-426.
- Droste SK, de Groote L, Atkinson HC, Lightman SL, Reul JM, Linthorst AC (2008). Corticosterone levels in the brain show a distinct ultradian rhythm but a delayed response to forced swim stress. *Endocrinology* **149**(7): 3244-3253.
- Eikel D, Vavrek M, Smith S, Bason C, Yeh S, Korfmacher WA, *et al.* (2011). Liquid extraction surface analysis mass spectrometry (LESA-MS) as a novel profiling tool for drug distribution and metabolism analysis: the terfenadine example. *Rapid communications in mass spectrometry : RCM* **25**(23): 3587-3596.
- Falth M, Skold K, Norrman M, Svensson M, Fenyo D, Andren PE (2006). SwePep, a database designed for endogenous peptides and mass spectrometry. *Molecular & cellular proteomics : MCP* **5**(6): 998-1005.
- Fletcher JS, Vickerman JC, Winograd N (2011). Label free biochemical 2D and 3D imaging using secondary ion mass spectrometry. *Current opinion in chemical biology* **15**(5): 733-740.

- Franck J, Arafah K, Barnes A, Wisztorski M, Salzet M, Fournier I (2009). Improving tissue preparation for matrix-assisted laser desorption ionization mass spectrometry imaging. Part 1: using microspotting. *Analytical chemistry* **81**(19): 8193-8202.
- Fraser R, Ingram MC, Anderson NH, Morrison C, Davies E, Connell JMC (1999). Cortisol effects on body mass, blood pressure, and cholesterol in the general population. *Hypertension* **33**: 1364-1368.
- Fuchs B, Schober C, Richter G, Suss R, Schiller J (2007). MALDI-TOF MS of phosphatidylethanolamines: different adducts cause different post source decay (PSD) fragment ion spectra. *Journal of biochemical and biophysical methods* **70**(4): 689-692.
- Funder JW (1993). Mineralocorticoids, glucocorticoids, receptors and response elements. *Science* **259**: 1132-1133.
- Gambineri A, Tomassoni F, Munarini A, Stimson RH, Mioni R, Pagotto U, *et al.* (2011). A combination of polymorphisms in HSD11B1 associates with in vivo 11 $\beta$ -HSD1 activity and metabolic syndrome in women with and without polycystic ovary syndrome. *European journal of endocrinology / European Federation of Endocrine Societies* **165**(2): 283-292.
- Gonzalez FJ (1988). The molecular biology of cytochrome P450s. *Pharmacological reviews* **40**(4): 243-288.
- Goodwin RJ (2012). Sample preparation for mass spectrometry imaging: small mistakes can lead to big consequences. *Journal of proteomics* **75**(16): 4893-4911.
- Goodwin RJ, Pennington SR, Pitt AR (2008). Protein and peptides in pictures: imaging with MALDI mass spectrometry. *Proteomics* **8**(18): 3785-3800.
- Goodwin RJ, Pitt AR (2010). Mass spectrometry imaging of pharmacological compounds in tissue sections. *Bioanalysis* **2**(2): 279-293.
- Goodwin RJ, Pitt AR, Harrison D, Weidt SK, Langridge-Smith PR, Barrett MP, *et al.* (2011). Matrix-free mass spectrometric imaging using laser desorption ionisation Fourier transform ion cyclotron resonance mass spectrometry. *Rapid communications in mass spectrometry : RCM* **25**(7): 969-972.
- Griffiths WJ, Wang Y (2011). Analysis of oxysterol metabolomes. *Biochimica et biophysica acta* **1811**(11): 784-799.
- Groseclose MR, Massion PP, Chaurand P, Caprioli RM (2008). High-throughput proteomic analysis of formalin-fixed paraffin-embedded tissue microarrays using MALDI imaging mass spectrometry. *Proteomics* **8**(18): 3715-3724.
- Guan S, Marshall AG, Wahl MC (1994). MS/MS with high detection efficiency and mass resolving power for product ions in Fourier transform ion cyclotron resonance mass spectrometry. *Analytical chemistry* **66**(8): 1363-1367.

- Hamm G, Bonnel D, Legouffe R, Pamelard F, Delbos JM, Bouzom F, *et al.* (2012). Quantitative mass spectrometry imaging of propranolol and olanzapine using tissue extinction calculation as normalization factor. *Journal of proteomics* **75**(16): 4952-4961.
- Hankin JA, Barkley RM, Murphy RC (2007). Sublimation as a method of matrix application for mass spectrometric imaging. *Journal of the American Society for Mass Spectrometry* **18**(9): 1646-1652.
- Hanukoglu I (1992a). Current research on steroid metabolism: transition from biochemistry to molecular-cell biology. *The Journal of steroid biochemistry and molecular biology* **43**(8): 745-749.
- Hanukoglu I (1992b). Steroidogenic enzymes: structure, function, and role in regulation of steroid hormone biosynthesis. *The Journal of steroid biochemistry and molecular biology* **43**(8): 779-804.
- Heeren RM, Chughtai K (2010). Mass Spectrometric Imaging for Biomedical Tissue Analysis. *Chemical reviews* **110**: 3237-3277.
- Heirholzer G, Koch F, Rehn J (1966). [Hypophlogisty as a special form of allophlogisty according to Heilmeyer]. *Klinische Wochenschrift* **44**(10): 590-591.
- Hellman L, Nakada F, Zumoff B, Fukushima D, Bradlow HL, Gallacher TF (1971). Renal capture and oxidation of cortisol in man. *J.Clin.Endocrinol.* **33**: 52-62.
- Hendrickson CL, Drader JJ, Laude DA, Jr., Guan S, Marshall AG (1996). Fourier transform ion cyclotron resonance mass spectrometry in a 20 T resistive magnet. *Rapid communications in mass spectrometry : RCM* **10**(14): 1829-1832.
- Higashi T, Nishio T, Hayashi N, Shimada K (2007). Alternative procedure for charged derivatization to enhance detection responses of steroids in electrospray ionization-MS. *Chemical & pharmaceutical bulletin* **55**(4): 662-665.
- Higashi T, Shimada K (2004). Derivatization of neutral steroids to enhance their detection characteristics in liquid chromatography-mass spectrometry. *Analytical and bioanalytical chemistry* **378**(4): 875-882.
- Hoffmann Ed, Stroobant V (2001). *Mass spectrometry : principles and applications*. 2nd edn. Wiley: Chichester ; New York.
- Holle A, Haase A, Kayser M, Hohndorf J (2006). Optimizing UV laser focus profiles for improved MALDI performance. *Journal of mass spectrometry : JMS* **41**(6): 705-716.

Holmes MC, Abrahamsen CT, K.L. F, Paterson JM, Mullins JJ, Seckl JR (2006). The mother or the fetus? 11 $\beta$ -Hydroxysteroid dehydrogenase type 2 null mice provide evidence for direct fetal programming of behavior by endogenous glucocorticoids. *Journal of Neuroscience* **26**(14): 3840-3844.

Hughes KA, Manolopoulos KN, Iqbal J, Cruden NL, Stimson RH, Reynolds RM, *et al.* (2012). Recycling between cortisol and cortisone in human splanchnic, subcutaneous adipose and skeletal muscle tissues *in vivo*. *Diabetes* **61**: 1357-1364.

Hughes KA, Reynolds RM, Andrew R, Critchley HO, Walker BR (2010). Glucocorticoids turn over slowly in human adipose tissue *in vivo*. *The Journal of clinical endocrinology and metabolism* **95**(10): 4696-4702.

Hughes KA, Reynolds RM, Critchley HO, Andrew R, Walker BR (2013). Glucocorticoids turn over slowly in human adipose tissue. *Journal of Clinical Endocrinology & Metabolism* **95**: 4696-4702.

Hughes KA, Webster SP, Walker BR (2008). 11-Beta-hydroxysteroid dehydrogenase type 1 (11 $\beta$ -HSD1) inhibitors in type 2 diabetes mellitus and obesity. *Expert Opinion in Investigative Drugs* **17**(4): 481-496.

Ifa DR, Gumaelius LM, Eberlin LS, Manicke NE, Cooks RG (2007). Forensic analysis of inks by imaging desorption electrospray ionization (DESI) mass spectrometry. *The Analyst* **132**(5): 461-467.

James VHT (1992). *The adrenal gland*. 2nd edn. Raven Press: New York.

Jamieson PM, Walker BR, Chapman KE, Rossiter S, Seckl JR (2000). 11 $\beta$ -Hydroxysteroid dehydrogenase type 1 is a predominant 11 $\beta$ -reductase in intact perfused rat liver. *J.Endocrinol.* **165**: 685-692.

Jaskolla TW, Lehmann WD, Karas M (2008). 4-Chloro-alpha-cyanocinnamic acid is an advanced, rationally designed MALDI matrix. *Proceedings of the National Academy of Sciences of the United States of America* **105**(34): 12200-12205.

Joels M, Baram TZ (2009a). The neuro-symphony of stress. *Nature reviews. Neuroscience* **10**(6): 459-466.

Joels M, Krugers HJ, Lucassen PJ, Karst H (2009b). Corticosteroid effects on cellular physiology of limbic cells. *Brain research* **1293**: 91-100.

Jones EA, Lockyer NP, Kordys J, Vickerman JC (2007). Suppression and enhancement of secondary ion formation due to the chemical environment in static-secondary ion mass spectrometry. *Journal of the American Society for Mass Spectrometry* **18**(8): 1559-1567.

- Jurchen J, Rubakhin S, Sweedler J (2005) MALDI-MS imaging of features smaller than the size of the laser beam. *Journal of the American Society for Mass Spectrometry* **16** (10):1654-1659. doi:10.1016/j.jasms.2005.06.006
- Kaletas BK, van der Wiel IM, Stauber J, Lennard JD, Guzel C, Kros JM (2009). Sample preparation issues for tissue imaging by imaging MS. *Proteomics* **9**(10): 2622-2633.
- Kallback P, Shariatgorji M, Nilsson A, Andren PE (2012). Novel mass spectrometry imaging software assisting labeled normalization and quantitation of drugs and neuropeptides directly in tissue sections. *Journal of proteomics* **75**(16): 4941-4951.
- Kannisto K, Pietilainen KH, Ehrenborg E, Rissanen A, Kaprio J, Hamsten A (2004). Overexpression of 11beta-hydroxysteroid dehydrogenase-1 in adipose tissue is associated with acquired obesity and features of insulin resistance: studies in young adult monozygotic twins. *The Journal of clinical endocrinology and metabolism* **89**(9): 4414-
- Karas M, Hillenkamp F (1988). Laser desorption ionization of proteins with molecular masses exceeding 10,000 daltons. *Analytical chemistry* **60**(20): 2299-2301.
- Karas M, Kruger R (2003). Ion formation in MALDI: the cluster ionization mechanism. *Chemical reviews* **103**(2): 427-440.
- Karssen AM, Meijer OC, van der Sandt IC, Lucassen PJ, de Lange EC, de Boer AG, *et al.* (2001). Multidrug resistance P-glycoprotein hampers the access of cortisol but not of corticosterone to mouse and human brain. *Endocrinology* **142**(6): 2686-2694.
- Katz JR, Mohamed-Ali V, Wood PJ, Yudkin JS, Coppack SW (1999a). An in vivo study of the cortisol-cortisone shuttle in subcutaneous abdominal adipose tissue. *Clinical endocrinology* **50**(1): 63-68.
- Katz JR, Mohamed-Ali V, Wood PJ, Yudkin JS, Coppack SW (1999b). An in vivo study of the cortisol-cortisone shuttle in subcutaneous abdominal adipose tissue. *Clin.Endocrinol.* **50**: 63-68.
- Kelly JJ, Martin A, Whitworth JA (2000). Role of erythropoietin in cortisol-induced hypertension. *Journal of human hypertension* **14**(3): 195-198.
- Kertesz V, Van Berkel GJ (2010). Fully automated liquid extraction-based surface sampling and ionization using a chip-based robotic nanoelectrospray platform. *Journal of mass spectrometry : JMS* **45**(3): 252-260.
- Kipari T, Hadoke PWF, Iqbal J, Man TY, Miller E, Coutinho AE, *et al.* (2013). 11 $\beta$ -hydroxysteroid dehydrogenase type 1 deficiency reduces atherosclerosis and plaque inflammation independent of risk factors: key role of the lesional environment. *FASEB J.*



- Klemcke HG, Christenson RK (1996). Porcine placental 11 $\beta$ -hydroxysteroid dehydrogenase activity. *Biology of Reproduction* **55**(1): 217-223.
- Klinkert I, McDonnell LA, Luxembourg SL, Altelaar AF, Amstalden ER, Piersma SR (2007). Tools and strategies for visualization of large image data sets in high-resolution imaging mass spectrometry. *The Review of scientific instruments* **78**(5): 053716.
- Knochenmuss R (2014). MALDI mechanisms: wavelength and matrix dependence of the coupled photophysical and chemical dynamics model. *The Analyst* **139**(1): 147-156.
- Koeniger SL, Talaty N, Luo Y, Ready D, Voorbach M, Seifert T (2011). A quantitation method for mass spectrometry imaging. *Rapid communications in mass spectrometry : RCM* **25**(4): 503-510.
- Kotelevtsev YV, Brown RW, Fleming S, Edwards CRW, Seckl JR, Mullins JJ (1999). Hypertension in mice caused by inactivation of 11 $\beta$ -hydroxysteroid dehydrogenase type 2. *Journal of Clinical Investigation* **103**: 683-689.
- Kotelevtsev YV, Holmes MC, Burchell A, Houston PM, Scholl D, Jamieson PM (1997). 11 $\beta$ -Hydroxysteroid dehydrogenase type 1 knockout mice show attenuated glucocorticoid inducible responses and resist hyperglycaemia on obesity and stress. *Proceedings of the National Academy of Sciences USA* **94**: 14924-14929.
- Krozowski Z, Maguire JA, Stein-Oakley AN, Dowling J, Smith RE, Andrews RK (1995). Immunohistochemical localization of the 11 $\beta$ -hydroxysteroid dehydrogenase type II enzyme in human kidney and placenta. *Journal of Clinical Endocrinology & Metabolism* **80**(7): 2203-2209.
- Labrie F (2004). Adrenal androgens and intracrinology. *Seminars in reproductive medicine* **22**(4): 299-309.
- Labrie F (1991). Intracrinology. *Molecular and cellular endocrinology* **78**(3): C113-118.
- Labrie F, Dupont A, Simard J, Luu-The V, Belanger A (1993). Intracrinology: the basis for the rational design of endocrine therapy at all stages of prostate cancer. *European urology* **24 Suppl 2**: 94-105.
- Labrie F, Veilleux R, Fournier A (1988). Glucocorticoids stimulate the growth of mouse mammary carcinoma Shionogi cells in culture. *Molecular and cellular endocrinology* **58**(2-3): 207-211
- Lackner C, Daufeldt S, Wildt L, Allera A (1998). Glucocorticoid-recognizing and -effector sites in rat liver plasma membrane. Kinetics of corticosterone uptake by isolated membrane vesicles. III. Specificity and stereospecificity. *The Journal of steroid biochemistry and molecular biology* **64**(1-2): 69-82.

- Lakshmi V, Sakai RR, McEwen BS, Monder C (1991). Regional distribution of 11 beta-hydroxysteroid dehydrogenase in rat brain. *Endocrinology* **128**(4): 1741-1748.
- Lavery GG, Walker EA, Draper N, Jeyasuria P, Marcos J, Shackleton CHL (2006). Hexose-6-phosphate dehydrogenase knock-out mice lack 11 $\beta$ -hydroxysteroid dehydrogenase type 1-mediated glucocorticoid generation. *Journal of Biological Chemistry* **281**: 6546-6551.
- Leake RE, Freshney RI, Munir I (1987). Steroid response in vivo and in vitro. In: Green B, Leake RE (ed)(eds). *Steroid hormones; a practical approach*, edn. Oxford: IRL Press. p^pp 205-208.
- Lednicer D (2011). *Steroid chemistry at a glance*. edn. Wiley: Hoboken.
- Leloup-Hatey J (1976). [A method to measure the rate of metabolic clearance and secretion of cortisol in the eel (*Anguilla anguilla* L.)]. *Canadian journal of physiology and pharmacology* **54**(3): 262-276.
- Lemaire R, Stauber J, Wisztorski M, Van Camp C, Desmons A, Deschamps M (2007). Tag-mass: specific molecular imaging of transcriptome and proteome by mass spectrometry based on photocleavable tag. *Journal of proteome research* **6**(6): 2057-2067.
- Li T, Chan W, Chiang JYL (2007). PXR induces CYP27A1 and regulates cholesterol metabolism in the intestine. *Journal of Lipid Reseach* **48**(2): 373-384.
- Lindsay RS, Lindsay RM, Waddell BJ, Seckl JR (1996). Prenatal glucocorticoid exposure leads to offspring hyperglycaemia in the rat: studies with the 11 $\beta$ -hydroxysteroid dehydrogenase inhibitor carbenoxolone. *Diabetologia* **39**: 1299-1305.
- Livingstone DE, Barat P, Di Rollo EM, Rees GA, Weldin BA, Rog-Zielinska EA, *et al.* (2014). 5alpha-Reductase type 1 deficiency or inhibition predisposes to insulin resistance, hepatic steatosis and liver fibrosis in rodents. *Diabetes*.
- Livingstone DEW, Jones GC, Smith K, Andrew R, Kenyon CJ, Walker BR (2000). Understanding the role of glucocorticoids in obesity: tissue-specific alterations of corticosterone metabolism in obese Zucker rats. *Endocrinology* **141**(2): 560-563.
- Longcope C (2003). Androgens, estrogens, and mammary epithelial proliferation. *Menopause* **10**(4): 274-276.
- Lorence MC, Murry BA, Trant JM, Mason JI (1990). Human 3 beta-hydroxysteroid dehydrogenase/delta 5-4isomerase from placenta: expression in nonsteroidogenic cells of a protein that catalyzes the dehydrogenation/isomerization of C21 and C19 steroids. *Endocrinology* **126**(5): 249

Luxembourg SLM, T.H.; McDonnell, L.A.; Heeren, R.M.A. (2004) High-Spatial Resolution Mass Spectrometric Imaging of Peptide and Protein Distributions on a Surface. *Anal Chem* **76**:5339- 53443-2498.

Maclullich AMJ, Deary IJ, Starr JM, Ferguson KJ, Wardlaw JM, Seckl JR (2005). Plasma cortisol levels, brain volumes and cognition in healthy elderly men. *Psychoneuroendocrinology* **30**(5): 505-515.

Makarov A. (2000). "Electrostatic axially harmonic orbital trapping: A high-performance technique of mass analysis". *Analytical Chemistry* : AC **72** (6): 1156–62.

Malmberg H, Nygren P, Sjövall LaJ, L (2013). Subcellular localisation of cholesterol and phosphocholine with pattern-recognition-imaging-TOF-SIMS. *Spectroscopy* **18**: 503-511.

Mange A, Chaurand P, Perrochia H, Roger P, Caprioli RM, Solassol J (2009). Liquid chromatography-tandem and MALDI imaging mass spectrometry analyses of RCL2/CS100-fixed, paraffin-embedded tissues: proteomics evaluation of an alternate fixative for biomarker discovery. *Journal of proteome research* **8**(12): 5619-5628.

Manier ML, Reyzer ML, Goh A, Dartois V, Via LE, Barry CE, 3rd (2011). Reagent precoated targets for rapid in-tissue derivatization of the anti-tuberculosis drug isoniazid followed by MALDI imaging mass spectrometry. *Journal of the American Society for Mass Spectrometry* **22**(8): 1409-1419.

Marshall AG, Hendrickson CL, Jackson GS (1998). Fourier transform ion cyclotron resonance mass spectrometry: a primer. *Mass spectrometry reviews* **17**(1): 1-35.

Marto JA, Marshall AG, May MA, Limbach PA (1995). Ion trajectories in an electrostatic ion guide for external ion source fourier transform ion cyclotron resonance mass spectrometry. *Journal of the American Society for Mass Spectrometry* **6**(10): 936-946.

Massey JB (2006). Membrane and protein interactions of oxysterols. *Current Opinion in Lipidology* **17**(3): 296-301.

Masuzaki H, Kenyon CJ, Elmquist JK, Morton NM, Paterson JM, Shinyama H, *et al.* (2003). Transgenic amplification of glucocorticoid action in adipose tissue causes high blood pressure in mice. *Journal of Clinical Investigation* **112**: 83-90.

Masuzaki H, Paterson JM, Shinyama H, Morton NM, Mullins JJ, Seckl JR, *et al.* (2001). A transgenic model of visceral obesity and the Metabolic Syndrome. *Science* **294**: 2166-2170.

Mattson C, Reynolds RM, Simonyte K, Olsson T, Walker BR (2009). Combined Receptor Antagonist Stimulation of the Hypothalamic-Pituitary-Adrenal Axis test identifies impaired negative feedback sensitivity to cortisol in obese men. *Journal of Clinical Endocrinology & Metabolism* **94**: 1347-1352.

- McConnell JD (1995). Prostatic growth: new insights into hormonal regulation. *Br J Urol* **76 Suppl 1**: 5-10.
- McInnes KJ, Kenyon CJ, Chapman KE, Livingstone DEW, Macdonald LJ, Walker BR (2004). 5 $\alpha$ -Reduced glucocorticoid metabolites, novel endogenous activators of glucocorticoid receptors (GR). *Journal of Biological Chemistry* **279**(22): 22908-22912.
- Meaney S, Heverin M, Panzenboeck U, Ekstrom L, Axelsson M, Andersson U (2007). Novel route for elimination of brain oxysterols across the blood-brain barrier: conversion into 7 $\alpha$ -hydroxy-3-oxo-4-cholestenoic acid. *Journal of lipid research* **48**(4): 944-951.
- Meijer OC, de Lange ECM, Breimer DD, Bohr AG, Workel JO, de Kloet ER (1998). Penetration of dexamethasone into brain glucocorticoid targets is enhanced in *mdr1A* P-glycoprotein knockout mice. *Endocrinology* **139**: 1789-1793.
- Michalski A, Damoc E, Hauschild JP, Lange O, Wieghaus A, Makarov A, *et al.* (2011). Mass spectrometry-based proteomics using Q Exactive, a high-performance benchtop quadrupole Orbitrap mass spectrometer. *Molecular & cellular proteomics : MCP* **10**(9): M111 011015.
- Miksys SL, Tyndale RF (2002). Drug-metabolizing cytochrome P450s in the brain. *Journal of psychiatry & neuroscience : JPN* **27**(6): 406-415.
- Miller WL, Auchus RJ (2011). The molecular biology, biochemistry, and physiology of human steroidogenesis and its disorders. *Endocrine reviews* **32**(1): 81-151.
- Mitchell DR, Lyles KW (1990). Glucocorticoid-induced osteoporosis: mechanisms for bone loss; evaluation of strategies for prevention. *Journal of gerontology* **45**(5): M153-158.
- Mitic T, R A, Walker BR, Hadoke PWF (2013). Inter-conversion of 7-ketocholesterol and 7 $\alpha$ -hydroxycholesterol by 11 $\beta$ -HSD1 in the mouse aortic wall: implications for vascular function
- Moghrabi N, Andersson S (1998). 17 $\beta$ -hydroxysteroid dehydrogenases: physiological roles in health and disease. *Trends in endocrinology and metabolism: TEM* **9**(7): 265-270.
- Moisan M-P, Seckl JR, Edwards CRW (1990a). 11 $\beta$ -Hydroxysteroid dehydrogenase bioactivity and messenger RNA expression in rat forebrain: localization in hypothalamus, hippocampus and cortex. *Endocrinology* **127**: 1450-1455.
- Moisan M-P, Seckl JR, Monder C, Agarwal AK, White PC, Edwards CRW (1990b). 11 $\beta$ -Hydroxysteroid dehydrogenase mRNA expression, bioactivity and immunoreactivity in rat cerebellum. *Neuroendocrinology* **2**: 853-858.

Moore CCD, Mellon SH, Murai J, Siiteri PK, Miller WL (1993). Structure and function of the hepatic form of 11 $\beta$ -hydroxysteroid dehydrogenase in the squirrel monkey, an animal model of glucocorticoid resistance. *Endocrinology* **133**: 368-375.

Morton NM (2010). Obesity and corticosteroids: 11 $\beta$ -Hydroxysteroid type 1 as a cause and therapeutic target in metabolic disease. *Molecular and cellular endocrinology* **316**(2): 154-164.

Morton NM, Holmes MC, Fievet C, Staels B, Tailleux A, Mullins JJ (2001). Improved lipid and lipoprotein profile, hepatic insulin sensitivity and glucose tolerance in 11 $\beta$ -hydroxysteroid dehydrogenase 1 knockout mice. *Journal of Biological Chemistry* **276**: 41293-41300.

Nilsson A, Fehniger TE, Gustavsson L, Andersson M, Kenne K, Marko-Varga G (2010). Fine mapping the spatial distribution and concentration of unlabeled drugs within tissue micro-compartments using imaging mass spectrometry. *PloS one* **5**(7): e11411.

Nygren H, Hagenhoff B, Malmberg P, Nilsson M, Richter K (2007). Bioimaging TOF-SIMS: High resolution 3D imaging of single cells. *Microscopy research and technique* **70**(11): 969-974.

Olson RE (1998). Discovery of the lipoproteins, their role in fat transport and their significance as risk factors. *The Journal of nutrition* **128**(2 Suppl): 439S-443S.

Pannu PS, Allahverdian S, Francis GA (2013). Oxysterol generation and liver X receptor-dependent reverse cholesterol transport: not all roads lead to Rome. *Molecular and cellular endocrinology* **368**(1-2): 99-107.

Parvin L, Galicia MC, Gauntt JM, Carney LM, Nguyen AB, Park E (2005). Electrospray diagnostics by Fourier analysis of current oscillations and fast imaging. *Analytical chemistry* **77**(13): 3908-3915.

Patti GJ, Woo HK, Yanes O, Shriver L, Thomas D, Uritboonthai W (2010). Detection of carbohydrates and steroids by cation-enhanced nanostructure-initiator mass spectrometry (NIMS) for biofluid analysis and tissue imaging. *Anal. Chem.* **82**(1): 121-128.

Praveen EP, Sahoo JP, Kulshreshtha B, Khurana ML, Gupta N, Dwivedi SN (2011). Morning cortisol is lower in obese individuals with normal glucose tolerance. *Diabetes, metabolic syndrome and obesity : targets and therapy* **4**: 347-352.

Puia G, Santi MR, Vicini S, Pritchett DB, Purdy RH, Paul SM (1990). Neurosteroids act on recombinant human GABAA receptors. *Neuron* **4**(5): 759-765.

- Rask E, Olsson T, Söderberg S, Andrew R, Livingstone DEW, Johnson O (2001). Tissue-specific dysregulation of cortisol metabolism in human obesity. *Journal of Clinical Endocrinology & Metabolism* **86**: 1418-1421.
- Rask E, Walker BR, Söderberg S, Livingstone DEW, Eliasson M, Johnson O (2002). Tissue-specific changes in peripheral cortisol metabolism in obese women: increased adipose 11 $\beta$ -hydroxysteroid dehydrogenase type 1 activity. *Journal of Clinical Endocrinology and Metabolism* **87**: 3330-3336.
- Reyzer ML, Hsieh Y, Ng K, Korfmacher WA, Caprioli RM (2003). Direct analysis of drug candidates in tissue by matrix-assisted laser desorption/ionization mass spectrometry. *Journal of mass spectrometry : JMS* **38**(10): 1081-1092.
- Rosmond R, Dallman MF, Bjorntorp P (1998). Stress-related cortisol secretion in men: relationships with abdominal obesity and endocrine, metabolic and haemodynamic abnormalities. *Journal of Clinical Endocrinology and Metabolism* **83**: 1853-1859.
- Rosner W (1990). The functions of corticosteroid-binding globulin and sex hormone-binding globulin: recent advances. *Endocrine reviews* **11**(1): 80-91.
- Ruh H, Salonikios T, Fuchser J, Schwartz M, Sticht C, Hochheim C (2013). MALDI imaging MS reveals candidate lipid markers of polycystic kidney disease. *Journal of lipid research* **54**(10): 2785-2794.
- Rusvai E, Naray-Fejes-Toth A (1993). A new isoform of 11 $\beta$ -hydroxysteroid dehydrogenase in aldosterone target cells. *J.Biol.Chem.* **268**: 10717-10720.
- Sandeep TC, Andrew R, Homer NZM, Andrews RC, Smith K, Walker BR (2005). Increased *in vivo* regeneration of cortisol in adipose tissue in human obesity and effects of the 11 $\beta$ -hydroxysteroid dehydrogenase type 1 inhibitor carbenoxolone. *Diabetes* **54**: 872-879.
- Sapolsky RM, Krey LC, McEwen BS (1986). The neuroendocrinology of stress and ageing. The glucocorticoid cascade hypothesis. *Endocr.Rev.* **7**: 284-301.
- Schitz-Drager BJ, Fischer C, Bismarck E, Dorsam HJ, Lummen G (2007). The Prostate Cancer Prevention Trial (PCPT). Relevance for clinical practice. *Urologe A* **46**: 1366-1368.
- Schwartz SA, Reyzer ML, Caprioli RM (2003). Direct tissue analysis using matrix-assisted laser desorption/ionization mass spectrometry: practical aspects of sample preparation. *Journal of mass spectrometry : JMS* **38**(7): 699-708.
- Seckl JR, Morton NM, Chapman KE, Walker BR (2004a). Glucocorticoids and 11beta-hydroxysteroid dehydrogenase in adipose tissue. *Recent progress in hormone research* **59**: 359-393.

Seckl JR, Walker BR (2001). 11 $\beta$ -Hydroxysteroid dehydrogenase 1 - a tissue specific amplifier of glucocorticoid action. *Endocrinology* **142**: 1371-1376.

Seckl JR, Walker BR (2004b). 11beta-hydroxysteroid dehydrogenase type 1 as a modulator of glucocorticoid action: from metabolism to memory. *Trends in endocrinology and metabolism: TEM* **15**(9): 418-424.

Shariatgorji M, Nilsson A, Goodwin RJ, Svenningsson P, Schintu N, Banka Z (2012). Deuterated matrix-assisted laser desorption ionization matrix uncovers masked mass spectrometry imaging signals of small molecules. *Analytical chemistry* **84**(16): 7152-7157.

Sheraz, S; Razo, IB; Kohn, PT;Lockyer, NP and Vickerman, JC. Enhancing Ion Yields in TOF-SIMS - A Comparative Study of Argon and Water Cluster Primary Beams *Analytical Chemistry* 87 (2015) 2367–2374

Sigurjonsdottir HA, Andrew R, Stimson RH, Johannsson G, Walker BR (2009). Lack of regulation of 11beta-hydroxysteroid dehydrogenase type 1 during short-term manipulation of GH in patients with hypopituitarism. *European journal of endocrinology / European Federation of Endocrine Societies* **161**(3): 375-380.

Simpson ER, Mahendroo MS, Means GD, Kilgore MW, Hinshelwood MM, Graham-Lorence S (1994). Aromatase Ctochrome P450, the enzyme responsible for estrogen biosynthesis. *Endocrine reviews* **15**(3): 342-355.

Singh G GA, Xu K,Blair IA. (2000). Liquid chromatography/electron capture atmospheric pressure chemical ionization/mass spectrometry: analysis of pentafluorobenzyl derivatives of biomolecules and drugs in the attomole range. *Analytical chemistry* **72**: 3007-3013.

Sooy K, Webster SP, Noble J, Binnie M, Walker BR, Seckl JR (2010). Partial deficiency or short-term inhibition of 11beta-hydroxysteroid dehydrogenase type 1 improves cognitive function in aging mice. *The Journal of Neuroscience* **30**(41): 13867-13872.

Spengler B, Hubert M (2002) Scanning microprobe matrix-assisted laser desorption ionization (SMALDI) mass spectrometry: instrumentation for sub-micrometer resolved LDI and MALDI surface analysis. *Journal of the American Society for Mass Spectrometry* **13** (6):735-748.

Stafford G, Jr. (2002). Ion trap mass spectrometry: a personal perspective. *Journal of the American Society for Mass Spectrometry* **13**(6): 589-596.

Stavreva DA, Wiench M, John S, Conway-Campbell BL, McKenna MA, Pooley JR, *et al.* (2009). Ultradian hormone stimulation induces glucocorticoid receptor-mediated pulses of gene transcription. *Nature cell biology* **11**(9): 1093-1102.

Steen H, Kuster B, Mann M (2001). Quadrupole time-of-flight versus triple-quadrupole mass spectrometry for the determination of phosphopeptides by precursor ion scanning. *Journal of mass spectrometry : JMS* **36**(7): 782-790.

Stewart PM (1988). *11 $\beta$ -hydroxysteroid dehydrogenase and hypertension*. edn. M.D. Thesis: University of Edinburgh.

Stewart PM, Boulton A, Kumar S, Clark PMS, Shackleton CHL (1999). Cortisol metabolism in human obesity: impaired cortisone - cortisol conversion in subjects with central adiposity. *Journal of Clinical Endocrinology & Metabolism* **84**: 1022-1027.

Stewart PM, Corrie JET, Shackleton CHL, Edwards CRW (1988). Syndrome of apparent mineralocorticoid excess: a defect in the cortisol-cortisone shuttle. *J.Clin.Invest.* **82**: 340-349.

Stewart PM, Wallace AM, Atherden SM, Shearing CH, Edwards CRW (1990). Mineralocorticoid activity of carbenoxolone: contrasting effects of carbenoxolone and liquorice on 11 $\beta$ -hydroxysteroid dehydrogenase activity in man. *Clin.Sci.* **78**: 49-54.

Stimson RH, Andersson J, Andrew R, Redhead DN, Karpe F, Hayes PC (2009). Cortisol release from adipose tissue by 11 $\beta$ -hydroxysteroid dehydrogenase type 1 in humans. *Diabetes* **58**: 46-53.

Stimson RH, Andrew R, McAvoy NC, Tripathi D, Hayes PC, Walker BR (2011). Increased whole-body and sustained liver cortisol regeneration by 11 $\beta$ -hydroxysteroid dehydrogenase type 1 in obese men with type 2 diabetes provides a target for enzyme inhibition. *Diabetes* **60**(3): 720-725.

Stimson RH, Johnstone AM, Homer NZM, Wake DJ, Morton NM, R. A (2007). Dietary macronutrient content alters cortisol metabolism independently of changes in body weight in obese men. *Journal of Clinical Endocrinology & Metabolism* **92**: 4480-4484.

Stimson RH, Mohd-Shukri NA, Bolton JL, Andrew R, Reynolds RM, Walker BR (2014). The postprandial rise in plasma cortisol in men is mediated by macronutrient-specific stimulation of adrenal and extra-adrenal cortisol production. *The Journal of clinical endocrinology and metabolism* **99**(1): 160-168.

Stocco DM, Clark BJ (1996). Role of the steroidogenic acute regulatory protein (StAR) in steroidogenesis. *Biochemical pharmacology* **51**(3): 197-205.

Stoeckli M, Staab D, Schweitzer A, Gardiner J, Seebach D (2007). Imaging of a beta-peptide distribution in whole-body mice sections by MALDI mass spectrometry. *Journal of the American Society for Mass Spectrometry* **18**(11): 1921-1924.

Strain GW, Zumoff B, Strain JJ (1980). Cortisol production in obesity. *Metabolism: Clinical & Experimental* **29**(10): 980-985.



Takats Z, Wiseman JM, Gologan B, Cooks RG (2004). Mass spectrometry sampling under ambient conditions with desorption electrospray ionization. *Science* **306**(5695): 471-473.

Tannin GM, Agarwal AK, Monder C, New MI, White PC (1991). The human gene for 11 $\beta$ -hydroxysteroid dehydrogenase. *J.Biol.Chem.* **266**: 16653-16658.

Todd PJ, Schaaff TG, Chaurand P, Caprioli RM (2001). Organic ion imaging of biological tissue with secondary ion mass spectrometry and matrix-assisted laser desorption/ionization. *Journal of mass spectrometry : JMS* **36**(4): 355-369.

Tomlinson JW, Sinha B, Bujalska I, Hewison M, Stewart PM (2002). Expression of 11 $\beta$ -hydroxysteroid dehydrogenase type 1 in adipose tissue is not increased in human obesity. *Journal of Clinical Endocrinology & Metabolism* **87**(12): 5630-5635.

van Reyk DM, Brown AJ, Hult'en LM, Dean RT, Jessup W (2006). Oxysterols in biological systems: sources, metabolism and pathophysiological relevance. *Redox Report* **11**(6): 255-262.

Vestal ML, Campbell JM (2005). Tandem time-of-flight mass spectrometry. *Methods in enzymology* **402**: 79-108.

Vickerman, J and Briggs, D. ToF-SIMS: Materials Analysis by Mass Spectrometry. IM Publications LLP; 2nd edition edition (31 July 2013)

Vind C, Dich J, Grunnet N (1992). Regulation by growth hormone and glucocorticoid of testosterone metabolism in long-term cultures of hepatocytes from male and female rats. *Biochemical pharmacology* **44**(8): 1523-1528.

Wake DJ, Homer NZM, Andrew R, Walker BR (2006). Acute regulation of 11 $\alpha$ -hydroxysteroid dehydrogenase type 1 activity by insulin and Intralipid infusions in humans. *Journal of Clinical Endocrinology & Metabolism* **91**: 4682-4688.

Wake DJ, Rask E, Livingstone DEW, Soderberg S, Olsson T, Walker BR (2003). Local and systemic impact of transcriptional upregulation of 11 $\beta$ -hydroxysteroid dehydrogenase type 1 in human adipose tissues in obesity. *Journal of Clinical Endocrinology & Metabolism* **88**: 3983-3988.

Wake DJ, Stimson RH, Tan GD, R. A, Homer NZM, Karpe F (2007). Influence of peroxisome proliferator-activated receptor (PPAR)  $\alpha$  and agonists on 11 $\alpha$ -hydroxysteroid dehydrogenase type 1 *in vivo* in humans. *Journal of Clinical Endocrinology & Metabolism* **92**: 1848-1856.

Walker BR (2007). Glucocorticoids and cardiovascular disease. *European journal of endocrinology / European Federation of Endocrine Societies* **157**(5): 545-559.

Walker BR, Campbell JC, Fraser R, Stewart PM, Edwards CRW (1992a). Mineralocorticoid excess and inhibition of 11 $\beta$ -hydroxysteroid dehydrogenase in patients with ectopic ACTH syndrome. *Clin.Endocrinol.(Oxf)* **27**: 483-492.

Walker BR, Connacher AA, Webb DJ, Edwards CRW (1992b). Glucocorticoids and blood pressure: a role for the cortisol/cortisone shuttle in the control of vascular tone in man. *Clin.Sci.* **83**: 171-178.

Walker BR, Edwards CRW (1992c). Cushing's syndrome. In: James VHT (ed)^(eds). *The adrenal gland*, 2 edn. New York: Raven Press. p^pp 289-318.

Walker BR, Seckl JR, Phillips DIW (1995). Increased sensitivity to glucocorticoids in adult males with the metabolic syndrome.

Walker BR, Stewart PM, Shackleton CHL, Padfield PL, Edwards CRW (1993). Deficient inactivation of cortisol by 11 $\beta$ -hydroxysteroid dehydrogenase in essential hypertension. *Clinical Endocrinology (Oxford)* **39**: 221-227.

Walker EA, Clark AM, Hewison M, Ride JP, Stewart PM (2001). Functional expression, characterization, and purification of the catalytic domain of human 11-beta-hydroxysteroid dehydrogenase type 1. *The Journal of biological chemistry* **276**(24): 21343-21350.

Walsh PC, Madden JD, Harrod MJ, Goldstein JL, MacDonald PC, Wilson JD (1974). Familial incomplete male pseudohermaphroditism, type 2. Decreased dihydrotestosterone formation in pseudovaginal perineoscrotal hypospadias. *New England Journal of Medicine* **291**(18): 944-949.

Webster JI, Carlstedt-Duke J (2002). Involvement of multidrug resistance proteins (MDR) in the modulation of glucocorticoid response. *The Journal of steroid biochemistry and molecular biology* **82**(4-5): 277-288.

Webster SP, Pallin TD (2007). 11beta-hydroxysteroid dehydrogenase type 1 inhibitors as therapeutic agents. *Expert opinion on therapeutic patents* **17**: 1407-1422.

Wei L, MacDonald TM, Walker BR (2004). Taking glucocorticoids by prescription is associated with subsequent cardiovascular disease. *Annals of Internal Medicine* **141**: 764-770.

White PC, Mune T, Agarwal AK (1997). 11 beta-Hydroxysteroid dehydrogenase and the syndrome of apparent mineralocorticoid excess. *Endocrine reviews* **18**(1): 135-156.

White RE, Manitpisitkul P (2001). Pharmacokinetic theory of cassette dosing in drug discovery screening. *Drug metabolism and disposition: the biological fate of chemicals* **29**(7): 957-966.

- Wiley WC (1956). Bendix Time-of-Flight Mass Spectrometer. *Science* **124**(3226): 817-820.
- Winograd N, Garrison BJ (2010). Biological cluster mass spectrometry. *Annu.Rev.Phys.Chem.* **61**: 305-322.
- Wiseman JM, Ifa DR, Song Q, Cooks RG (2006). Tissue imaging at atmospheric pressure using desorption electrospray ionization (DESI) mass spectrometry. *Angewandte Chemie* **45**(43): 7188-7192.
- Yang CA, Nixon M, Kenyon CJ, Livingstone DEW, Duffin R, Rossi AG (2011). 5 $\alpha$ -Reduced glucocorticoids exhibit dissociated anti-inflammatory and metabolic effects. *British Journal of Pharmacology* **164**(6): 1611-1671.
- Yau JL, McNair KM, Noble J, Brownstein D, Hibberd C, Morton N (2007). Enhanced hippocampal long-term potentiation and spatial learning in aged 11beta-hydroxysteroid dehydrogenase type 1 knock-out mice. *J Neurosci* **27**(39): 10487-10496.
- Yin WW, Wang M, Marshall AG, Ledford EB (1992). Experimental evaluation of a hyperbolic ion trap for fourier transform ion cyclotron resonance mass spectrometry. *Journal of the American Society for Mass Spectrometry* **3**(3): 188-197.
- Zhou A, Wei Z, Read RJ, Carrell RW (2006). Structural mechanism for the carriage and release of thyroxine in the blood. *Proceedings of the National Academy of Sciences of the United States of America* **103**(36): 13321-13326.
- Zimmerman TA, Monroe EB, Tucker KR, Rubakhin SS, Sweedler JV (2008). Chapter 13: Imaging of cells and tissues with mass spectrometry: adding chemical information to imaging. *Methods in cell biology* **89**: 361-390.
- Zubarev RA, Makarov A (2013). Orbitrap mass spectrometry. *Analytical chemistry* **85**(11): 5288-5296.

## **Appendix II**

### **Published Articles**

## Mass Spectrometry Imaging for Dissecting Steroid Intracrinology within Target Tissues

Diego F. Cobice,<sup>†</sup> C. Logan Mackay,<sup>‡</sup> Richard J. A. Goodwin,<sup>§</sup> Andrew McBride,<sup>†</sup> Patrick R. Langridge-Smith,<sup>‡</sup> Scott P. Webster,<sup>†</sup> Brian R. Walker,<sup>†</sup> and Ruth Andrew<sup>\*,†</sup>

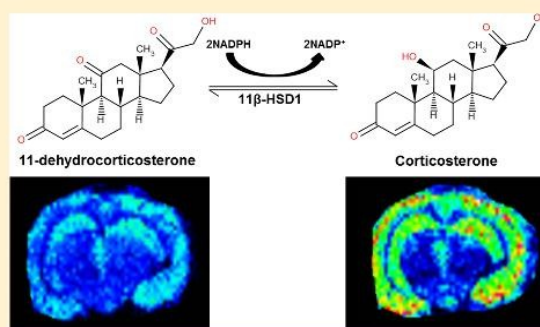
<sup>†</sup>University/British Heart Foundation Centre for Cardiovascular Science, Queen's Medical Research Institute, University of Edinburgh, 47 Little France Crescent, Edinburgh, EH16 4TJ, United Kingdom

<sup>‡</sup>SIRCAMS, School of Chemistry, Joseph Black Building, The King's Buildings, University of Edinburgh, West Mains Road, Edinburgh, EH9 3JJ, United Kingdom

<sup>§</sup>AstraZeneca R&D, Alderley Park, Macclesfield, Cheshire SK10 4TF, United Kingdom

### Supporting Information

**ABSTRACT:** Steroid concentrations within tissues are modulated by intracellular enzymes. Such "steroid intracrinology" influences hormone-dependent cancers and obesity and provides targets for pharmacological inhibition. However, no high resolution methods exist to quantify steroids within target tissues. We developed mass spectrometry imaging (MSI), combining matrix assisted laser desorption ionization with on-tissue derivatization with Girard T and Fourier transform ion cyclotron resonance mass spectrometry, to quantify substrate and product (11-dehydrocorticosterone and corticosterone) of the glucocorticoid-amplifying enzyme 11 $\beta$ -HSD1. Regional steroid distribution was imaged at 150–200  $\mu$ m resolution in rat adrenal gland and mouse brain sections and confirmed with collision induced dissociation/liquid extraction surface analysis. In brains of mice with 11 $\beta$ -HSD1 deficiency or inhibition, MSI quantified changes in subregional corticosterone/11-dehydrocorticosterone ratio, distribution of inhibitor, and accumulation of the alternative 11 $\beta$ -HSD1 substrate, 7-ketocholesterol. MSI data correlated well with LC-MS/MS in whole brain homogenates. MSI with derivatization is a powerful new tool to investigate steroid biology within tissues.



Measurement of steroid hormone concentrations in plasma over more than 50 years has revealed the intricate control of their secretion from endocrine glands. In recent decades, it has been recognized that steroid concentrations within tissues are also modulated, independently of circulating steroid concentrations, by local steroid-generating and inactivating enzymes. This has been confirmed in spontaneous human enzyme deficiency syndromes, recapitulated by genetic deletion in mice and using pharmacological inhibitors; examples include amplification of estrogen action by aromatase,<sup>1</sup> androgen action by 5 $\alpha$ -reductase type 2,<sup>2</sup> and glucocorticoid action by 11 $\beta$ -HSDs.<sup>3</sup> Dysregulation of steroid-metabolizing enzyme expression is thought to be important in the pathophysiology of steroid-dependent disease, including breast cancer, prostate disease, and obesity. Moreover, inhibitors of these enzymes have proved useful to reduce steroid action in these disorders. A key limitation in this established field of "steroid intracrinology", however, is the inability to study steroid concentrations within tissues, particularly in organs with region-specific expression of relevant enzymes, such as the brain, or within heterogeneous samples, such as from cancers. Inferences of the consequences of enzyme (dys)regulation and inhibition for local steroid

concentrations therefore remain qualitative rather than quantitative.

Mass spectrometry is widely regarded as the gold standard for steroid quantification in plasma. Mass spectrometry imaging (MSI) and liquid extraction surface analysis (LESA) have recently been developed to map spatial distribution of molecules in tissues allowing localization, detection, identification, and quantitation of compounds in complex biological matrices.<sup>4</sup> The distribution of cholesterol, chemically similar to steroids, has been imaged in brain<sup>5,6</sup> and in liver<sup>7</sup> while corticosteroids and androgens have been detected in a nonbiological matrix by cation-enhanced nanostructure-initiator mass spectrometry.<sup>8</sup> However, localization of endogenous neutral steroids in biological tissues by MSI is challenging, not only because of their relatively low abundance but also because of their lack of either hydrogen donor or acceptor moieties, resulting in poor ionization yields during matrix assisted laser desorption (MALDI). Furthermore, steroids are

Received: September 11, 2013

Accepted: October 17, 2013

Published: October 17, 2013

susceptible to ion suppression by more abundant molecules, such as lipids and proteins. Although steroids can be ionized by conventional electrospray or APCI, detection in the low subpg range in tissues is largely out of reach, and these quantitative approaches do not offer two-dimensional imaging. For electrospray ionization (ESI), derivatization<sup>10,11</sup> enhances the ionization efficiency of neutral corticosteroids, for example, using Girard reagents.<sup>12</sup> Similar approaches have allowed Girard P (GirP) derivatives of oxysterols to be detected with fmole sensitivity in rat brain homogenates using MALDI<sup>13</sup> and have enhanced sensitivity for cholesterol analysis using *N*-alkylpyridinium isotope quaternization in analysis of human hair homogenate by MALDI-FTICR.<sup>14</sup> The recent innovation of on-tissue chemical derivatization (OTCD)<sup>15,16</sup> has paved the way for application of derivatization techniques to MSI for investigation of tissue steroids.

We aimed to develop MSI initially for analyzing corticosteroids. The major glucocorticoid in rodents, corticosterone (CORT), is relatively abundant and, in addition to its secretion from the zona fasciculata of the adrenal cortex, is also generated within target tissues from the inert precursor 11-dehydrocorticosterone (11DHC) by the enzyme 11 $\beta$ -HSD1.<sup>3</sup> Inhibition of 11 $\beta$ -HSD1 in brain is associated with improved memory,<sup>17,18</sup> but the consequences for local steroid concentrations in the brain subregions where 11 $\beta$ -HSD1 is expressed are uncertain. Moreover, 11 $\beta$ -HSD1 can interconvert other keto and hydroxy substrates,<sup>19–22</sup> including 7-keto and 7 $\beta$ -hydroxycholesterol, but it has been difficult to establish the equilibrium of these reactions in vivo. We have applied OTCD, in combination with MSI, for the first time to quantify and validate the detection of CORT and 11DHC and alternative substrates within subregions of murine brain. Neutral steroids were converted to positively charged hydrazones derivatives using Girard reagents T (GirT), enabling detection and quantitation by MALDI and LESA with Fourier transform ion cyclotron MSI (MALDI-FTICR-MSI). Validation was performed with LC-MS/MS. MSI demonstrated alterations in brain glucocorticoids (and 7-ketocholesterol, an alternative substrate) in mice with 11 $\beta$ -HSD1 deficiency and allowed simultaneous pharmacokinetic/pharmacodynamic studies with an 11 $\beta$ -HSD1 inhibitor. A potent, selective, and orally bioavailable piperidinyl-pyrazol inhibitor of 11 $\beta$ -HSD1 (UE 2316) was used; UE 2316 crosses the blood–brain barrier and displays potency across species (IC50: mouse, 162 nM; rat 80nM).<sup>23</sup>

## MATERIALS AND METHODS

**Chemicals and Reagents.** Internal standard (ISTD) corticosterone-2,2,4,6,6,7 $\alpha$ ,21,21 ( $d_8$ CORT) (purity 95–97%) was from Cambridge Isotopes (MA, USA); 11-dehydrocorticosterone (11DHC) was from Steraloids Inc. (PA, USA); UE2316, [4-(2-chlorophenyl)-4-fluoro-1-piperidinyl][5-(1H-pyrazol-4-yl)-3-thienyl]-methanone, and UE2346 were synthesized by High Force Ltd., UK.<sup>23</sup> Solvents were glass-distilled HPLC grade (Fisher Scientific, Loughborough, UK). 4-Chloro- $\alpha$ -cyanocinnamic acid (Cl-CCA) was synthesized in-house.<sup>24</sup> All other chemicals were purchased from Sigma-Aldrich (Dorset, UK) unless otherwise stated.

**Animals and Biomatrix Collection.** Licensed procedures were performed under the UK Animals (Scientific Procedures) Act, 1986. Sprague–Dawley male rats (5–7 weeks, ~175–200 g, source of adrenal glands) and C57BL/6 mice (6–7 weeks, male) were from Harlan Olac Ltd. (Bicester, UK). 11 $\beta$ -HSD1<sup>-/-</sup> mice (KO) and their wild type (WT) littermates

(male, 2–3 months) were bred in-house.<sup>25</sup> The genetically modified animals were obtained from an in house breeding colony and were slightly older than commercial stock; however, age-matched controls were used in each experiment. In all studies, animals were killed by decapitation at 09:00 h; plasma was prepared from trunk blood, collected in EDTA. Tissues were snap frozen in liquid nitrogen and stored (–80 °C).

**Tissue Sectioning and Mounting.** The cryostat (Leica Microsystems Inc., Bannockburn, IL, USA) was cleaned and tissue embedded in gelatin solution 10% w/v. Coronal/horizontal brain and adrenal cryosections (10  $\mu$ m) were cut and frozen (–80 °C), adapted from Koeniger.<sup>26</sup> Briefly: (1) fifteen tissue sections (50  $\mu$ m thick) were collected for confirmatory quantitation; (2) two adjacent sections were thaw mounted onto glass slides (Superfrost, Thermo Scientific, Braunschweig, Germany) and retained for histological examination; (3) four adjacent sections for MSI/LESA (10  $\mu$ m) were thaw mounted onto conductive indium tin-oxide (ITO)-coated glass slides (Bruker Daltonics, Bremen, GmbH) precoated with GirT-reagent (0.15 mg/cm<sup>2</sup>), and further sections for histology ( $\times 2$ ) and confirmatory quantitation ( $\times 15$ ) were harvested as above. Tissue sections for confirmatory quantitation were combined, weighed at room temperature (RT), and stored at –80 °C until LC-MS/MS analysis. Tissue sections for MSI were stored in a vacuum desiccator (RT, 1h) and then at –80 °C.

**Instrumentation.** MSI was performed using a 12T Solarix MALDI-FTICR-MS (Bruker Daltonics, MA, US) employing a Smartbeam 1 kHz laser, with instrument control using Solarix control v1.5.0 (build 42.8), Hystar 3.4 (build 8), and FlexImaging version 3.0 (build 42). On-tissue collision induced dissociation was carried out by liquid extraction surface analysis (LESA)-nanoESI-FTICR-MS using Triversa nanomate (Ad-View, NY, USA). Confirmatory liquid chromatography-tandem MS (LC-MS/MS) analysis was performed using a triple-quadrupole linear ion trap mass spectrometer (QTRAP 5500, AB Sciex, Cheshire, UK) coupled with an ACQUITY ultra high pressure liquid chromatography (UPLC; Waters, Manchester, UK).

**MALDI-FTICR-MSI Analysis.** Optical images were taken using a flatbed scanner (Cannon LiDE-20, Cannon, UK). MSI analysis was performed using 250 laser shots, with a laser spot diameter of ~50  $\mu$ m, and laser power was optimized for consistent ion production. Ions were detected between  $m/z$  250 and 1500, yielding a 1 Mword time-domain transient, and with a laser spot raster spacing of 100–300  $\mu$ m unless otherwise stated. MSI data were subject to the vector normalization method (RMS) at 0.995 as ICR noise reduction threshold. Mass precision was typically  $\pm 0.025$  Da. Average abundances were determined by defining specific regions of interest (ROI). A measure of the average abundance was then assigned from the summed spectra. Neutral steroids were analyzed (without application of derivatization reagent) in positive and negative ion modes at +ve  $m/z$  345.20604, –ve  $m/z$  343.19148 for 11DHC and +ve  $m/z$  347.22169, –ve  $m/z$  345.20604 for CORT. Ions formed by the derivatives were monitored in positive mode, with +ve  $m/z$  458.30133 (GirT-11DHC) and +ve  $m/z$  460.31698 (GirT-CORT) and +ve  $m/z$  468.36718 (GirT- $d_8$ CORT). UE2316 was monitored at +ve  $m/z$  390.08377 and GirT-7 ketocholesterol (GirT-7KC) was monitored at +ve  $m/z$  514.43670.  $\alpha$ -Cyano-4-hydroxycinnamic acid (CHCA) matrix ion at +ve  $m/z$  417.04834 was also

monitored to assess matrix application uniformity and perform an internal calibration.

**On-Tissue Chemical Derivatization (OTCD).** From  $-80^{\circ}\text{C}$ , tissues were allowed to dry in a vacuum desiccator (20 min). The GirT precoated glass slide ( $0.15\text{ mg/cm}^2$ ) was sprayed with 2 mL of methanol containing 0.2% v/v of TFA; then, it was placed in a sealed Petri dish (or similar container) containing moist tissue paper to create a moisturizing reaction environment. Two ml of distilled water was enough to produce a suitable reaction media; more water may cause analyte delocalization due to derivatization reagent diffusion. A moist kim-wipe tissue was placed around the inner walls of the container without touching the glass slide. The tissue was incubated (60 min,  $40^{\circ}\text{C}$ ) in an oven or water bath and then allowed to cool and dry in a vacuum desiccator (RT, 15 min) to remove the condensed water prior to matrix deposition as above. Other derivatization reagents were evaluated such as isonicotinoyl and sulfonyl chlorides among other hydrazine reagents. Details of optimization and derivatization screening are in Supporting Information, Table S1.

**Matrix Application.** Matrix (CHCA; 10 mg/mL) in acetonitrile (80% + 0.2% v/v TFA) was applied by a pneumatic TLC sprayer (20 mL per slide with a nitrogen flow of 7.5 L/min at a distance of 20 cm from the MALDI target). Each manual pass took approximately 1 s, and the process was repeated with 5–10 s between passes until a uniform matrix coating was achieved on the tissue section. The tissue section was then allowed to dry (RT) and stored in a desiccator until analysis.

**Detection of Endogenous Steroids in Murine Tissue Using Derivatization.** Steroids were imaged in adrenal glands from Sprague–Dawley rats and brains from C57Bl/6 mice ( $n = 6/\text{tissue}$ ). Tissues were prepared, derivatized as described, and matrix applied. Steroid derivatives were imaged by MALDI-FTICR-MS.

**Histological Staining.** Cryosections were stained using hematoxylin and eosin.<sup>27</sup> After fixation in cold acetone, tissue sections were examined using an optical microscope (40 $\times$ , Leica Microsystems Inc., Bannockburn, IL, USA) with CCD camera (Hitachi model 3969, Japan).

**Liquid Extraction Surface Analysis (LESA)-ESI-FTICR-MS.** This was performed in both adrenal and brain sections. Steroids within tissue sections were derivatized as previously described and analyzed immediately using LESA-nanoESI-FTICR-MS as follows: solvent, methanol/water (50:50 with 0.1% v/v of formic acid); pick-up volume, 1.5  $\mu\text{L}$ ; dispense volume, 1.2  $\mu\text{L}$  at 0.2 mm away from surface; droplet rest time (delay), 5 s; aspiration volume, 1.4  $\mu\text{L}$  at 0.0 mm away from surface. ESI-FTICR-MS was performed using the 12T SolariX dual source (ESI-MALDI) with SolariX control v1.5.0 (build 42.8). Ions were detected between  $m/z$  250 and 1500, yielding a 2 Mword time-domain transient. Ions of GirT-hydrazones (as for MALDI analysis above) were isolated for 30 s prior to isolation ( $m/z$   $460.3 \pm 5$  Da) and CID experiments. CID was carried out using 28 eV as collision energy.

**Confirmatory Analysis by LC-MS/MS.** Analyses of corticosteroids (adapted from Wang)<sup>13</sup> and UE2316 in murine brain were performed using LC-MS/MS in multiple reaction monitoring mode (MRM), for method details see Supporting Information.

**Influence of 11 $\beta$ -HSD1 on Amounts of Active and Inactive Glucocorticoids in Brain Tissue.** The effect of deficiency of the 11 $\beta$ -HSD1 enzyme was studied using 11 $\beta$ -

HSD1<sup>-/-</sup> (knockout, KO) mice and their wild type littermates ( $n = 6/\text{group}$ ) and after pharmacological inhibition of 11 $\beta$ -HSD1 in C57BL/6 mice ( $n = 6/\text{group}$ , killed 1, 4, and 6 h after receiving UE2316 (20 mg/kg oral, in DMSO/PEG-400/saline (0.9% w/v) (2:38:60)) or vehicle).

Tissues were harvested at cull, and MSI was performed as described. The identities of ions of the steroid-GirT hydrazones were confirmed on-tissue by CID using LESA. The average spectral intensities of steroid derivatives in ROIs across the cortex, hippocampus, and amygdala were recorded using MSI, presented as ratios of CORT/11DHC and compared with those generated by LESA and LC-MS/MS.

**Statistical Analysis.** Data are expressed as mean  $\pm$  SEM, and differences were analyzed using two-way ANOVA with Fisher's posthoc test (MSI and LESA) and Student's *t* test (LC-MS/MS). Statistical significance was accepted at  $p < 0.05$ . Statistical calculations were performed using Statistica version 8.0, StatSoft, Inc. Tulsa, OK, USA. Data generated by different analytical methods were compared by Bland-Altman plots.

**Structure Drawing.** Molecular structure drawing was performed using MarvinSketch 5.4.0.1, Chemaxon Ltd., Budapest, Hungary.

## RESULTS

### OTCD-MALDI-FTICR-MSI Method Development and Optimization.

To detect corticosterone (CORT) and 11-dehydrocorticosterone (11DHC), standards were analyzed by MALDI mass spectrometry.  $[\text{M} + \text{H}]^+$  pseudomolecular ions were the most abundant ions detected when standards of corticosterone (CORT) and 11-dehydrocorticosterone (11DHC) were analyzed, with masses at  $m/z$  347.22101 and  $m/z$  345.20632, in close agreement with the theoretical masses  $m/z$  347.22169 and  $m/z$  345.20604, respectively (Figure S1a,b, Supporting Information); ions due to dehydration were not observed. Initial imaging attempts in adrenal tissue, monitoring only the  $[\text{M} + \text{H}]^+$  ion of the glucocorticoids of interest, yielded ions with mass accuracy of  $-3.2$  ppm (CORT) and  $-18.3$  ppm (11DHC) (Figure S1c,e,f,h,i, Supporting Information) but with low signal-to-noise ratio. Limits of detection (LODs) of CORT and 11DHC were  $\sim 30$  ng (off-tissue) and 1  $\mu\text{g}$  (on-tissue).

To improve images of neutral steroids in tissues, a number of approaches were pursued to enhance their low intensity signal. Initially, matrix screening was performed using both standard and novel matrices, to identify reagents which may enhance energy transfer. Substantial differences were observed between matrices; the maximum signal intensity and desorption yield was achieved using CHCA (Figure S2a, Supporting Information). Interestingly, the novel 4-chloro- $\alpha$ -cyanocinnamic acid (Cl-CCA), which possesses a lower proton affinity than its hydroxyl analogue and increased the signal of poorly ionizable peptides,<sup>24</sup> demonstrated lower intensity signals in combination with steroids than CHCA, although the background signal was noticeably lower in the low mass range (200–400 Da). Despite using CHCA, the LOD did not reach the required subpg levels of endogenous corticosteroids in tissue.

Derivatization was explored by introducing readily ionizable or permanently charged groups, an approach effective in enhancing signal intensity with LC-MS/MS.<sup>11–13</sup> Poor desorption or ionization by MALDI analysis was found using derivatives targeting the primary (C21) alcohol moiety with acyl and sulfonyl chlorides. Screening derivatization reactions, targeting the  $\alpha$ - $\beta$  unsaturated ketone at C3 in the steroid A-ring (Table S1, Supporting Information), improved signal

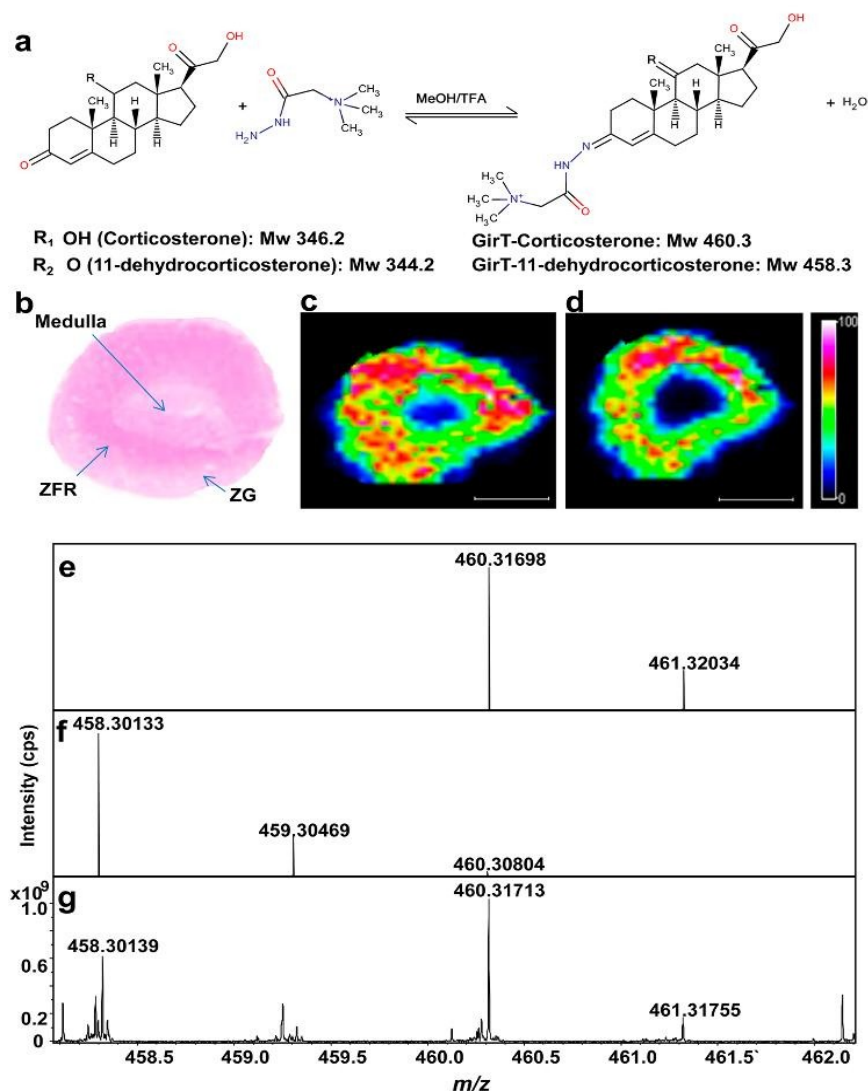


**Figure 1.** Molecular imaging by MALDI-FTICR-MSI of corticosteroid derivatives prepared with Girard T reagent (GirT) in representative rat adrenal gland sections. Molecular regional distribution maps showed GirT-CORT ( $m/z$  460.31713) and GirT-11DHC ( $m/z$  458.30139) in high abundance in the zona fasciculata/reticularis (site of glucocorticoids synthesis) with mass accuracy of  $\pm 5$  ppm from their theoretical monoisotopic masses and (S/N) signal-to-noise ratios above 100. (a) Derivatization of corticosterone and 11-dehydrocorticosterone with GirT. (b) Histological image of a cryosection of rat adrenal gland stained with hematoxylin and eosin (ZG = zona glomerulosa; ZFR = zona fasciculata reticularis). Heat map of GirT derivatives of: (c) corticosterone (GirT-CORT) at  $m/z$  460.31698  $\pm$  0.025 Da and (d) 11-dehydrocorticosterone (GirT-11DHC) at  $m/z$  458.30133  $\pm$  0.025 Da, collated by MALDI-FTICR-MS. Signal intensity is depicted by color on the scale shown. Simulated theoretical isotopic distribution pattern of: (e) GirT-CORT and (f) GirT-11DHC. (g) Representative FTICR-MS spectrum of corticosteroid hydrazones in rat adrenal gland, showing excellent agreement with theoretical mass. TFA = Trifluoroacetic acid. MeOH = Methanol.  $M_w$  = molecular weight (Da). cps = counts per second. Scale bar (2 mm).

intensity in positive mode when the corticosteroids were converted to derivatives either permanently charged or easily protonated. In particular, formation of a quaternary ammonium derivative, by a hydrazine type condensation reaction of the ketone at both C3 and C20 to form the water-soluble hydrazones group, greatly enhanced response (Table S1, Supporting Information).

The highest sensitivity was achieved with derivatives formed using GirT reagent. Derivatives of CORT and 11DHC

generated ions of similar intensities, with LODs of 0.01–0.03 pg (off-tissue) and 1–0.1 pg (on-tissue), and signals of the endogenous CORT and 11DHC in tissues were considerably enhanced (Figure 1c,d). GirT condensation is generally carried out using protic solvents in a weak acid media at room temperature with reaction times around 10–18 h achieving 60–80% of conversion to hydrazones.<sup>28</sup> Recent studies have shown that the reaction can be carried out in 30 min at 70 °C.<sup>29,30</sup> However, such a high temperature may cause



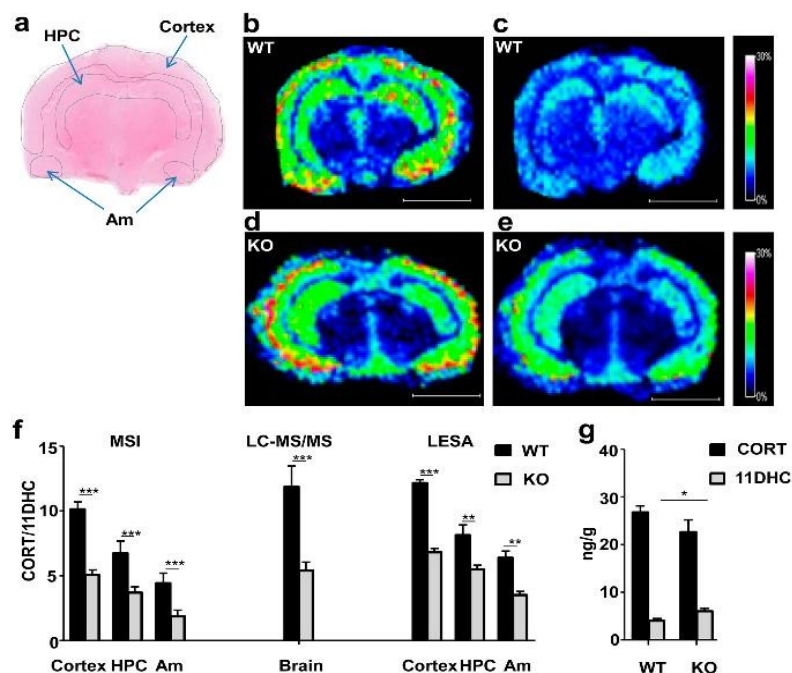


**Figure 2.** Effect of  $11\beta$ -hydroxysteroid dehydrogenase type 1 ( $11\beta$ -HSD1) deficiency on proportions of active and inactive glucocorticoids in regions of murine brain. Girard T (GirT) corticosteroid hydrazones (corticosterone (CORT) and 11-dehydrocorticosterone (11DHC)) were most abundant in the cortex, hippocampus, and amygdala with significant lower CORT/11DHC ratios observed upon transgenic disruption of the enzyme primarily caused by a significant accumulation of 11DHC. (a) Histological image of cryosection of murine brain stained with hematoxylin and eosin with the outline of the MSI-LESA regions of interest (ROIs) (cortex; hippocampus, HPC; and amygdala, Am). (b, d) Heat map distribution by MALDI-FTICR-MSI of GirT-CORT derivative at  $m/z$  460.31698  $\pm$  0.025 Da in wild type (b) and  $11\beta$ -HSD1 $^{-/-}$  (d) mice. (c, e) Heat map distribution by MALDI-FTICR-MSI of GirT-11DHC derivative at  $m/z$  458.30133  $\pm$  0.025 Da in wild type (c) and  $11\beta$ -HSD1 $^{-/-}$  (e) mice. Signal intensity is depicted by color on the scale shown. Scale bar (2 mm). (f) CORT/11DHC ratios measured by MALDI-FTICR-MSI (MSI), LC-MS/MS, and LESA in regions of interest in murine brain were significantly lower in  $11\beta$ -HSD1 $^{-/-}$  mice (KO) than wild type (WT) ( $p < 0.001$  overall between genotypes). (g) Differences between genotypes in CORT/11DHC ratios were caused by a statistically significant increase of 11DHC and a trend to a similar magnitude of reduction in CORT in  $11\beta$ -HSD1 $^{-/-}$  mice, measured in whole brain by LC-MS/MS. Statistical analysis was by two-way ANOVA for LESA and MSI and Student's *t* test for LC-MS/MS and absolute measurements ( $n = 12$ ). Data are mean  $\pm$  SEM. \* $P < 0.05$ , \*\* $P < 0.01$ , and \*\*\* $P < 0.001$ .

disruption of tissue morphology due to an increase of water vapor in the reaction chamber and can also lead to diffusion of the water-soluble GirT derivatives and ion suppression effects due to protein cleavage and tissue component degradation. The best yield, on-tissue, was achieved in 1 h at 40 °C, in a moisturizing environment using methanol/TFA as a solvent/catalyst system (Figure S2b, Supporting Information). The trifluoroacetate ion may facilitate the derivatization reagent incorporation due its tissue-penetration properties. Greatest signal intensity was achieved using 4 mL of 5 mg/mL solution for postcoating and 0.15 mg/cm<sup>2</sup> for precoating. In the ultimate protocol, slides were precoated with defined amounts of reagents, offering the additional benefit of limiting analyte diffusion. The reaction was quenched by dehydration to avoid subsequent hydrolysis. When GirT is used in MS analysis coupled with chromatography, the excess of derivatization reagent is diverted to waste to avoid ion-suppression in the MS ion source.<sup>29</sup> In OTCD, this is not practical, so the amount of derivatization reagent was limited to ensure maximum conversion and minimum ion-suppression.

Matrix was deposited using as a spray, and analyte diffusion as well as surface topology and crystal homogeneity were controlled by standardization of all possible variables, such as

nitrogen flow, distance from the MALDI target, time between passes, and solvent volume. Crystal homogeneity was inspected using light microscopy showing a uniform cocrystallization pattern. An image of the matrix ion was also recorded with each tissue to ensure even application. "Solvent-free" approaches to apply matrix, such as sublimation and sublimation/recrystallization, were evaluated but, in combination with GirT steroids, demonstrated poor signal-to-noise ratios. As previously reported,<sup>31</sup> proteolysis and tissue degradation during sample preparation may cause ion-suppression. With the optimized protocol in place, stability was evaluated temporally by assessing the intensity of signal from GirT-CORT applied on and off tissue sections; only 13% reduction in signal suppression/degradation was observed after 20 min at RT, within the necessary limit of tissue handling times (Figure S2c, Supporting Information).

GirT derivatives yielded spectra dominated by the molecular ion (Figure S3, Supporting Information), and high resolution MS was used to overcome the challenge of selecting specific analytes of interest from the many high abundance isobaric ions in the low mass range. Structural confirmation by fragmentation, using LESA-ESI-FTICR-MS followed by CID, allowed isolation of the precursor ions in the ICR cell, increasing both

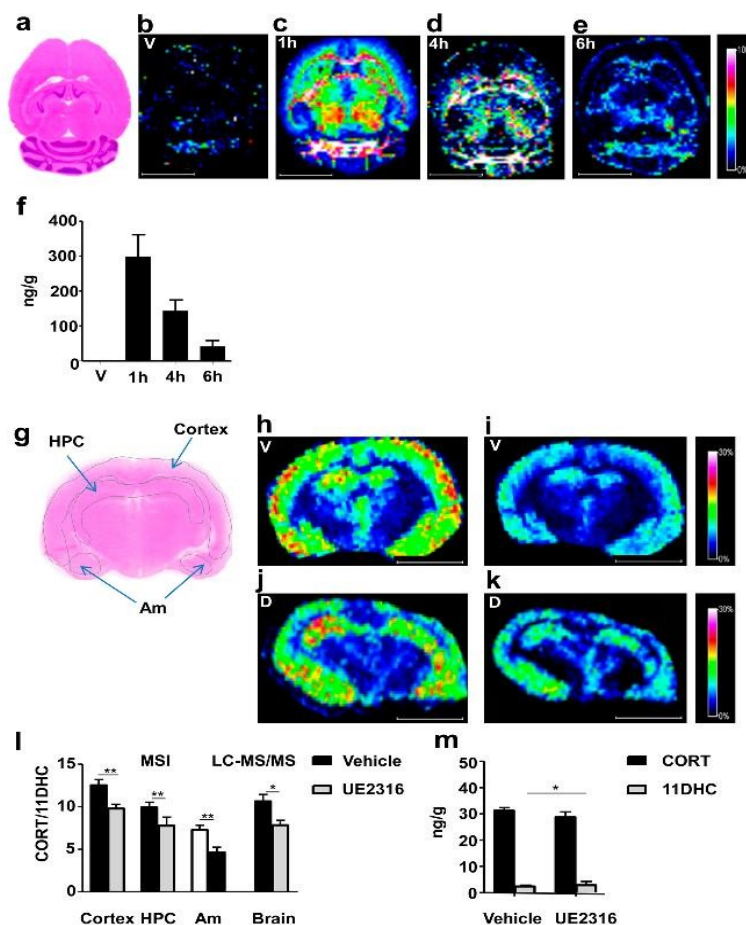


**Figure 3.** Effect of pharmacological inhibition of  $11\beta$ -hydroxysteroid dehydrogenase type 1 ( $11\beta$ -HSD1) with UE2316 in C57BL/6 mice. Girard T (GirT) derivatives (corticosterone (CORT) and 11-dehydrocorticosterone (11DHC)) were mostly distributed across the cortex, hippocampus, and amygdala; after enzyme inhibition, CORT/11DHC ratios showed a significant decline as a result of an increased 11DHC metabolite. (a) Histological image of horizontal cryosection of murine brain stained with hematoxylin and eosin. (b–e) MSI heat map distribution of  $m/z$  390.08377  $\pm$  0.025 Da representing UE2316 in brain over a 6 h time course in mice receiving Vehicle (V) or UE2316 (D). (f) Amounts of UE2316 in whole brain measured by LC-MS/MS demonstrated the same temporal pattern as those determined by MSI. (g) Histological image of coronal cryosection of murine brain stained with hematoxylin and eosin with the outline of the MSI regions of interest (ROIs) (cortex; hippocampus, HPC; and amygdala, Am). (h, j) MSI heat map of GirT-CORT at  $m/z$  460.31698  $\pm$  0.005 Da brain from mice receiving Vehicle (h) or UE2316 (1h post dose) (j). (i, k) GirT-11DHC at  $m/z$  458.30133  $\pm$  0.025 Da in brain from mice receiving Vehicle (i) or UE2316 (k). Signal intensity is depicted by color on the scale shown. Scale bar (2 mm). (l) A significant decline ( $p < 0.01$ , overall between groups) in CORT/11DHC ratios was observed across the ROIs by MSI in the brain after administration of UE2316, showing good agreement with data generated by LC-MS/MS in whole brain. (m) Absolute quantification of corticosteroids in brain tissue by LC-MS/MS showed that the differences in CORT/11DHC ratios were associated with a statistically significant increase of 11DHC and a trend to a decrease in CORT in UE2316-treated mice. Statistical analysis was performed using two-way ANOVA for MSI and Student's  $t$  test for LC-MS/MS and absolute measurements ( $n = 12$ ). Data are mean  $\pm$  SEM. \* $P < 0.05$  and \*\* $P < 0.01$ .

sensitivity and selectivity. This process provided fragmentation patterns typical of GirT hydrazones (Figure S4, Supporting Information), concordant with the structures of steroid hydrazones, extrapolating from GirP analogues, which may form a stable five member ring as previously reported.<sup>13</sup> CID of the GirT derivatives generated a series of fragment ions characteristic of the loss of the quaternary amine tag  $[M-59]^+$  and carbon monoxide  $[M-87]^+$  of the derivatized group at  $m/z$  399,  $m/z$  371 (GirT-11DHC) and  $m/z$  401,  $m/z$  373 (GirT-CORT), respectively. Also, a GirT-CORT selective fragment

was observed at  $m/z$  383 corresponding to the neutral loss of water at C11 of the  $m/z$  401 GirT-CORT fragment ion.

In rat adrenal gland, molecular distribution maps showed GirT-CORT ( $m/z$  460.31713) and GirT-11DHC ( $m/z$  458.30139) in high abundance in the zona fasciculata/reticularis (Figure 1c,d), with mass accuracy of  $\pm 5$  ppm from their theoretical monoisotopic masses (Figure 1e–g) and signal-to-noise ratios  $>100$ .

**Studies of Manipulation of  $11\beta$ -HSD1.** Endogenous CORT (Figure 2b,d) and 11DHC (Figure 2c,e) were successfully detected as GirT hydrazones by MSI in sections

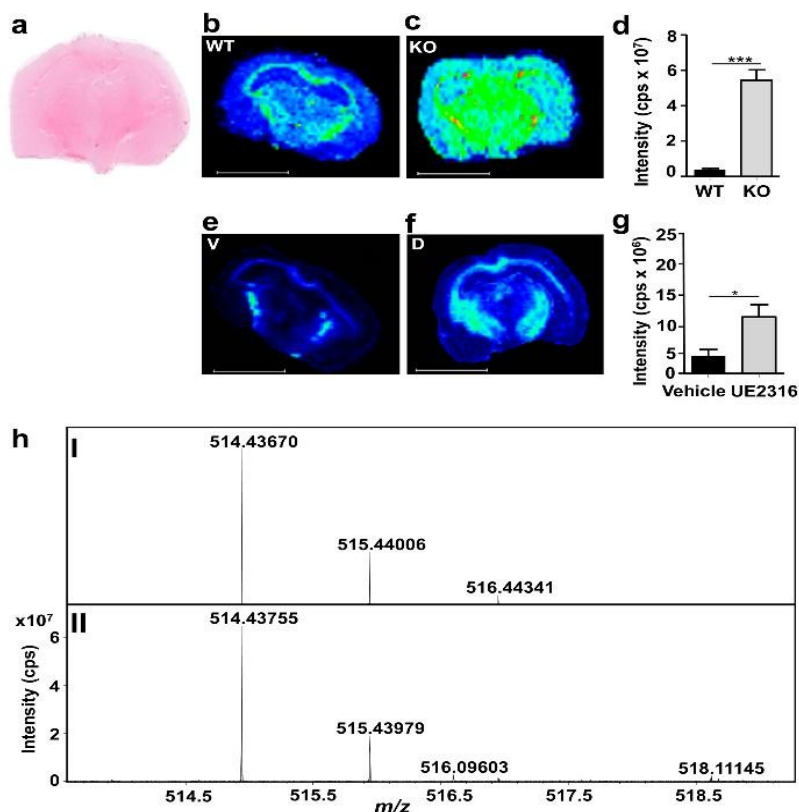


**Figure 4.** MSI detection of 7-ketocholesterol, an alternative substrate for  $11\beta$ -HSD1. A significant increase in Girard T 7-ketocholesterol (GirT-7KC) intensity was observed across the whole brain in mice after transgenic disruption of  $11\beta$ -HSD1 $^{-/-}$  (KO) and after administration of UE2316 (1 h postdose). (a) Histological image of coronal cryosection of murine brain stained with hematoxylin and eosin. MSI heat map of GirT-KC at  $m/z$  514.43670  $\pm$  0.025 Da in (b) wild type (WT), (c)  $11\beta$ -HSD1 $^{-/-}$ , and brain from mice receiving (e) Vehicle (V) or (f) UE2316 (D). Quantification of MSI signal intensity for GirT-7KC across the whole brain for (d) wild type versus  $11\beta$ -HSD1 $^{-/-}$  mice and for (g) mice treated with vehicle of UE2316. (h) (I) Theoretical monoisotopic distribution of GirT-7KC and (II) GirT-KC in mouse brain. GirT-7KC was detected in murine brain, and its levels increased in  $11\beta$ -HSD1 $^{-/-}$  mice (c) and following inhibition of the enzyme using UE2316 (f). Signal intensity is depicted by the scale shown. Scale bar (2 mm). cps = counts per second. Statistical analysis was performed using two way ANOVA ( $n = 12$ ). Data are mean  $\pm$  SEM. \* $P < 0.05$  and \*\*\* $P < 0.001$ .

of murine brain from both wild type (WT) and  $11\beta$ -HSD1 $^{-/-}$  mice. Corticosteroid derivatives were detected in highest abundance in the cortex, hippocampus, and amygdala. In  $11\beta$ -HSD1 $^{-/-}$  mice, the CORT/11DHC ratio was reduced in these regions of interest (Figure 2f). Absolute ratios (and magnitude of difference between  $11\beta$ -HSD1 $^{-/-}$  and WT mice) obtained by LC-MS/MS and LESA were similar to those determined by MSI (Figure 2f). Absolute measurements (Figure 2g) suggested the change in pattern between genotypes was driven by increased amounts of 11DHC and reduced amounts of CORT, although only the former was statistically significant.

Following a single oral dose of UE2316, an inhibitor of murine  $11\beta$ -HSD1, levels of the drug detected by MSI peaked in brain 1 h postdose (Figure 3b, vehicle, Figure 3c–e, UE2316); the MSI data were confirmed by LC-MS/MS of drug in whole brain (Figure 3f). The regional distribution of glucocorticoids was similar in brains of vehicle and UE2316 treated mice (Figure 3h,j (CORT), 3i,k (11DHC)) with UE2316 reducing CORT/11DHC ratios measured by MSI in the cortex, hippocampus, and amygdala (Figure 3l). Quantita-

tive analysis by LC-MS/MS confirmed these findings (Figure 3m).

**Correlation between Methods of Quantitation.** Good agreement was observed between MSI and LC-MS/MS (Figure S5a, Supporting Information) and between MSI and LESA (Figure S5b, Supporting Information), across the range of values, although MSI-LESA demonstrated a negative bias using Bland-Altman analysis.

**Quantitation of Alternative Substrates of  $11\beta$ -HSD1.** The GirT derivative of 7-ketocholesterol was detected by MSI in brain sections (Figure 4), and its abundance increased in mice with disruption (Figure 4b–d) or inhibition (Figure 4e–g) of  $11\beta$ -HSD1.

## DISCUSSION

This novel application of OTCD coupled with MSI permits detection of poorly ionizable endogenous corticosteroid hormones within tissues, by generating permanently charged derivatives which yield intense signals upon MALDI-FTICR analysis. The spatial distribution of the substrate and product of

11 $\beta$ -HSD1, 11DHC, and CORT in rat adrenal glands and murine brain was visualized. Quantitation in 11 $\beta$ -HSD1 deficient mice allowed assessment of the consequences of regional activity of 11 $\beta$ -HSD1 for local steroid levels, and the approach also allowed pharmacodynamic and pharmacokinetic assessment of an 11 $\beta$ -HSD1 inhibitor within the brain. This technique has the potential to be applied to other steroids and sterols to investigate steroid intracrinology in multiple organs and in solid tumors.

The novel use of GirT reagent permitted low LODs. Similar derivatives have been used to enhance analysis of sterols and steroids by LC-MS/MS (ESI),<sup>10–14,29,30</sup> but there has been limited application of derivatization for tissue imaging, with only two previous examples for nonsteroidal small molecules.<sup>15,16</sup> The reaction reported here favored the  $\alpha$ - $\beta$  unsaturated-keto moiety at C3 as the  $\pi$  electrons are delocalized across the conjugated system leaving the carbonyl susceptible to a nucleophilic attack. Indeed, monitoring the reaction products for up to 3 h did not reveal formation of multiple charged derivatives, indicative of reactions taking place at other positions. The efficiency of OTCD reaction was clearly demonstrated, as the signal intensity was considerably enhanced after conversion of native corticosteroids to their corresponding GirT hydrazones. The transformation of neutral steroid to their corresponding water-soluble and charged derivatives was achieved in a short period of time using a simple customized reaction chamber. The moisturizing environment was controlled by the amount of water and reaction temperature allowing little analyte diffusion. The derivatization allowed one to map the low levels of endogenous steroids on both adrenal gland and brain tissue sections. The concept of charge-tagging may be extrapolated to other neutral keto-steroids for the generation of molecular profiles in target tissues and, indeed here, was also used successfully to image 7-ketocholesterol.

Rat adrenal glands were selected as a model tissue for method development, and subsequently as a positive control, due to the anticipated high abundance of corticosteroids. Glucocorticoids were visualized and most abundant in the zona fasciculata, the major source of glucocorticoid synthesis, with lower signal in the outer zona glomerulosa, where corticosterone is further metabolized to aldosterone. This confirmed that unwanted diffusion of analytes was constrained by the tissue processing method. Spatial resolution of the laser is adjustable, but increasing the spatial resolution decreases sensitivity as the spot size sampled is smaller. In the adrenal, collecting data at 200  $\mu$ m resolution generated sufficient spatial information with adequate signal (signal/noise >100, compared with signal/noise  $\sim$ 20 at 50  $\mu$ m spatial resolution). In future use of the technique, the spatial resolution may be increased according to the region and tissue of interest but must be balanced against robustness of signal. Implementation of continuous accumulation of selected ions "CASI" may facilitate these advances.

OTCD coupled with MALDI-FTICR-MSI was successfully applied in murine brain, where discriminating abundance of glucocorticoids in subregions was possible. The highest abundance in cortex, hippocampus, and amygdala may reflect the higher expression of corticosteroid-binding receptors as well as of 11 $\beta$ -HSD1 in these brain regions.<sup>32</sup> To evaluate use of the technique to interpret biological variations in tissue steroid levels, proof-of-principle experiments were performed using brains of mice with 11 $\beta$ -HSD1 deficiency or receiving

pharmacological 11 $\beta$ -HSD1 inhibitors. Changes in enzyme activity were quantified by CORT/11DHC ratios, which is appropriate since derivatives of both steroids possess similar ionization yields and signal intensities when compared using postprocessing vector normalization (RMS). An alternative approach would have been to incorporate a labeled steroid (e.g., d<sub>6</sub>CORT) in the matrix, allowing signal intensity to be normalized; this approach also offers the advantage of a further read-out of uniformity of matrix application but was not employed here. Disrupting or inhibiting 11 $\beta$ -HSD1 was anticipated to increase the CORT/11DHC ratio, as previously reported in homogenates of brain from 11 $\beta$ -HSD1 deficient mice.<sup>33</sup> This was detected and quantified in brain subregions, with an increase of the signal intensity of GirT-11DHC and a smaller decline in GirT-CORT levels across the cortex, hippocampus, and amygdala with 11 $\beta$ -HSD1 deficiency or inhibition. These brain regions have high abundance of 11 $\beta$ -HSD1 mRNA.<sup>32</sup>

CORT in the brain is derived both from the circulation and from local 11 $\beta$ -HSD1 activity. The proportionate contribution of each source, however, is unknown. To date, this has been inferred for some tissues, imprecisely, from studies using arteriovenous sampling in combination with stable isotope tracers,<sup>34</sup> by sampling interstitial fluid by microdialysis<sup>35</sup> or by quantifying steroid concentrations in whole tissue homogenates *ex vivo*.<sup>36</sup> The MSI data here provides the novel insight that there is a small decline of only 16% in active CORT with 11 $\beta$ -HSD1 deficiency in regions of the brain where 11 $\beta$ -HSD1 is normally most highly expressed, suggesting the contribution of 11 $\beta$ -HSD1 to the intracellular pool of corticosterone in these experimental conditions is relatively modest.

Lastly using MSI, it was possible to image alternative substrates of 11 $\beta$ -HSD1, in this case 7-ketocholesterol. Previously, it has been difficult to establish whether 11 $\beta$ -HSD1 predominantly reduces 7-ketocholesterol to 7 $\beta$ -hydroxycholesterol or if oxidation dominates.<sup>22</sup> Indeed, changes in the balance of circulating oxysterols are modest in 11 $\beta$ -HSD1<sup>-/-</sup> mice. By demonstrating accumulation of 7-ketocholesterol with 11 $\beta$ -HSD1 deficiency, MSI has provided clear novel evidence that reduction of oxysterols by 11 $\beta$ -HSD1 predominates.

## CONCLUSIONS

MSI with on-tissue derivatization is a powerful new tool to study the regional variation in abundance of steroids within tissues. This is the first technique capable of detecting and quantifying corticosteroids to <200  $\mu$ m resolution and at physiological concentrations, allowing application within region-specific areas of murine brain. We have demonstrated its utility for measuring pharmacodynamic effects of small molecule inhibitors of 11 $\beta$ -HSD1; in combination with pharmacokinetic imaging, this will facilitate screening of the disposition of such drugs being developed to treat Alzheimer's disease. Importantly, this technique opens the door for expanding the range of steroids that can be studied by MALDI-MSI by adapting existing chemical derivatization methods. In the first instance, this may encompass other  $\alpha$ - $\beta$  unsaturated keto steroids, such as testosterone and progesterone, as well as keto-sterols, and may be applied in other tissues such as prostate gland and breast tissue. This offers the prospect of many novel insights into tissue-specific steroid and sterol biology.

## ■ ASSOCIATED CONTENT

## ■ Supporting Information

Additional information as noted in text. This material is available free of charge via the Internet at <http://pubs.acs.org>.

## ■ AUTHOR INFORMATION

## Corresponding Author

\*E-mail: [Ruth.Andrew@ed.ac.uk](mailto:Ruth.Andrew@ed.ac.uk). Tel: +44 (0) 131 242 6763. Fax: +44(0) 131 242 6779.

## Notes

The authors declare the following competing financial interest(s): D.F.C., C.L.M., R.J.A.G., A.M., P.R.L.S., and R.A. do not have any conflict of interest. B.R.W. and S.P.W. are inventors on patents owned by the University of Edinburgh relating to 11 $\beta$ -HSD1 inhibitors.

## ■ ACKNOWLEDGMENTS

We are grateful to the British Heart Foundation (D.F.C., R.A., B.R.W.) and the Wellcome Trust (A.M., B.R.W., S.P.W.) for funding this work. We thank SIRCAMS and the Mass Spectrometry Core of the Wellcome Trust Clinical Research Facility for technical support. We also thank Dr. Gregorio Naredo Gonzalez (Mass Spectrometry Core) for his help in the synthetic chemistry.

## ■ REFERENCES

- (1) Simpson, E. R.; Mahendroo, M. S.; Means, G. D.; Kilgore, M. W.; Hinshelwood, M. M.; Graham-Lorence, S.; Amareh, B.; Ito, Y.; Fisher, C. R.; Michael, M. D.; Mendelson, C. R.; Bulun, S. E. *Endocr. Rev.* **1994**, *15*, 342–355.
- (2) Russell, D. W.; Wilson, J. D. *Annu. Rev. Biochem.* **1994**, *63*, 25–61.
- (3) Seckl, J. R.; Walker, B. R. *TEM* **2004**, *15*, 418–424.
- (4) Heeren, R. M.; Chughtai, K. *Chem. Rev.* **2010**, *110*, 3237–3277.
- (5) Malmberg, H.; Nygren, P.; Sjövall, L. A. J. L. *Spectroscopy* **2013**, *18*, 503–511.
- (6) Dufresne, M.; Thomas, A.; Breault-Turcot, J.; Masson, J.-F.; Chaurand, P. *Anal. Chem.* **2013**, *85*, 3318–3324.
- (7) Winograd, N.; Garrison, B. J. *Annu. Rev. Phys. Chem.* **2010**, *61*, 305–322.
- (8) Patti, G. J.; Woo, H. K.; Yanes, O.; Shriver, L.; Thomas, D.; Uritboonthai, W.; Apon, J. V.; Steenwyk, R.; Manchester, M.; Siuzdak, G. *Anal. Chem.* **2010**, *82*, 121–128.
- (9) Singh, G.; Gutierrez, A.; Xu, K.; Blair, I. A. *Anal. Chem.* **2000**, *72*, 3007–3013.
- (10) Quirke, J. M.; Van Berkel, G. J. *J. Mass Spectrom.* **2001**, *36*, 1294–1300.
- (11) Higashi, T.; Yamauchi, A.; Shimada, K. *J. Chromatogr., B: Anal. Technol. Biomed. Life Sci.* **2005**, *825*, 214–222.
- (12) Shackleton, C. *J. Steroid Biochem. Mol. Biol.* **2010**, *121*, 481–490.
- (13) Wang, Y.; Hornshaw, M.; Alvelius, G.; Bodin, K.; Liu, S.; Sjövall, J.; Griffiths, W. J. *Anal. Chem.* **2010**, *78*, 164–173.
- (14) Wang, H.; Wang, H.; Zhang, L.; Zhang, J.; Guo, Y. *Anal. Chim. Acta* **2011**, *690*, 1–9.
- (15) Chacon, A.; Zagol-Ikapitte, I.; Amarnath, V.; Reyzer, M. L.; Oates, J. A.; Caprioli, R. M.; Boutaud, O. *J. Mass Spectrom.* **2011**, *46*, 840–846.
- (16) Manier, M. L.; Reyzer, M. L.; Goh, A.; Dartois, V.; Via, L. E.; Barry, C. E., III; Caprioli, R. M. *J. Am. Soc. Mass Spectrom.* **2011**, *22*, 1409–1419.
- (17) de Kloet, E. R.; Joels, M.; Holsboer, F. *Nat. Rev. Neurosci.* **2005**, *6*, 463–475.
- (18) Yau, J. L.; Noble, J.; Seckl, J. R. *J. Neurosci.* **2011**, *31*, 4188–4193.
- (19) Kotelevtsev, Y. V.; Brown, R. W.; Fleming, S.; Edwards, C. R. W.; Seckl, J. R.; Mullins, J. J. *J. Clin. Invest.* **1999**, *103*, 683–689.
- (20) Wamil, M.; Andrew, R.; Chapman, K. E.; Street, J.; Morton, N. M.; Seckl, J. R. *Endocrinology* **2008**, *149*, 5909–5918.
- (21) Hult, M.; Elleby, B.; Shafqat, N.; Svensson, S.; Rane, A.; Jornvall, H.; Abrahamson, L.; Oppermann, U. *Cell. Mol. Life Sci.* **2004**, *61*, 992–999.
- (22) Mitic, T.; Shave, S.; Semjonous, N.; McNae, I.; Cobice, D. F.; Lavery, G. G.; Webster, S. P.; Hadoke, P. W.; Walker, B. R.; Andrew, R. *Biochem. Pharmacol.* **2013**, *86*, 146–153.
- (23) Webster, S. P.; Seckl, J. R.; Walker, B. R.; Ward, P.; Pallin, T. D.; Dyke, H. J.; Perrior, T. R. PCT Intl. WO2011/033255, 2011.
- (24) Jaskolla, T. W.; Lehmann, W. D.; Karas, M. *Proc. Natl. Acad. Sci. U. S. A.* **2008**, *105*, 12200–12205.
- (25) Kotelevtsev, Y. V.; Holmes, M. C.; Burchell, A.; Houston, P. M.; Scholl, D.; Jamieson, P. M.; Best, R.; Brown, R. W.; Edwards, C. R. W.; Seckl, J. R.; Mullins, J. J. *Proc. Natl. Acad. Sci. U.S.A.* **1997**, *94*, 14924–14929.
- (26) Koeniger, S. L.; Talaty, N.; Luo, Y.; Ready, D.; Voorbach, M.; Seifert, T.; Cepa, S.; Fagerland, J. A.; Bouska, J.; Buck, W.; Johnson, R. W.; Spanton, S. *Rapid Commun. Mass Spectrom.* **2011**, *25*, 503–510.
- (27) Heap, B. J.; Kiernan, J. A. *J. Anat.* **1973**, *115*, 315–325.
- (28) Wheeler, O. *Chem. Rev.* **1962**, *62*, 205–221.
- (29) Khan, A. K.; Wang, Y.; Heidelberger, S.; Avelius, G.; Liu, S.; Sjövall, J.; Griffiths, W. J. *Steroids* **2006**, *71*, 42–53.
- (30) Griffiths, W. J.; Liu, S.; Avelius, G.; Sjövall, J. *Rapid Commun. Mass Spectrom.* **2003**, *17*, 924–935.
- (31) Goodwin, R. J.; Iverson, S. L.; Andren, P. E. *Rapid Commun. Mass Spectrom.* **2012**, *26*, 494–498.
- (32) Moisan, M.-P.; Seckl, J. R.; Monder, C.; Agarwal, A. K.; White, P. C.; Edwards, C. R. W. *Neuroendocrinology* **1990**, *2*, 853–858.
- (33) Sooy, K.; Webster, S. P.; Noble, J.; Binnie, M.; Walker, B. R.; Seckl, J. R.; Yau, J. L. W. *J. Neurosci.* **2010**, *30*, 13867–13872.
- (34) Hughes, K. A.; Manolopoulos, K. N.; Iqbal, J.; Cruden, N. L.; Stimson, R. H.; Reynolds, R. M.; Newby, D. E.; Andrew, R.; Karpe, F.; Walker, B. R. *Diabetes* **2012**, *61*, 1357–1364.
- (35) Wake, D. J.; Homer, N. Z. M.; Andrew, R.; Walker, B. R. *J. Clin. Endocrinol. Metab.* **2006**, *91*, 4682–4688.
- (36) Hughes, K. A.; Reynolds, R. M.; Critchley, H. O.; Andrew, R.; Walker, B. R. *J. Clin. Endocrinol. Metab.* **2013**, *95*, 4696–4702.

## Mass Spectrometry Imaging of Cassette-Dosed Drugs for Higher Throughput Pharmacokinetic and Biodistribution Analysis

John G. Swales,<sup>\*,†,‡,⊥</sup> James W. Tucker,<sup>†</sup> Nicole Strittmatter,<sup>||</sup> Anna Nilsson,<sup>§</sup> Diego Cobice,<sup>||</sup> Malcolm R. Clench,<sup>⊥</sup> C. Logan Mackay,<sup>||</sup> Per E. Andren,<sup>§</sup> Zoltán Takáts,<sup>||</sup> Peter J. H. Webborn,<sup>†</sup> and Richard J. A. Goodwin<sup>†</sup>

<sup>†</sup>Drug Safety and Metabolism, Innovative Medicines, AstraZeneca R&D, Alderley Park, Macclesfield, Cheshire SK10 4TG, U.K.

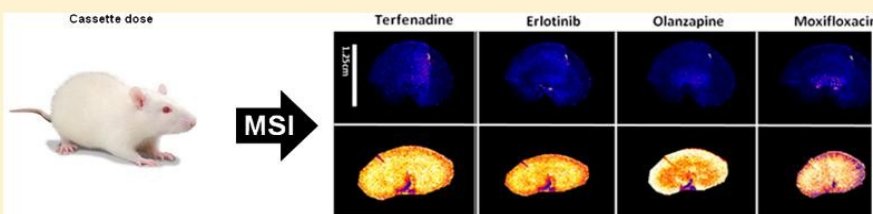
<sup>‡</sup>SIRCAMS, School of Chemistry, University of Edinburgh, Edinburgh EH8 9YL, U.K.

<sup>§</sup>Biomolecular Imaging and Proteomics, National Center for Mass Spectrometry Imaging, Department of Pharmaceutical Biosciences, Uppsala University, Uppsala 751 05, Sweden

<sup>||</sup>Department of Surgery and Cancer, Sir Alexander Fleming Building, Imperial College, London SW7 2AZ, U.K.

<sup>⊥</sup>Biomedical Research Centre, Sheffield Hallam University, Howard Street, Sheffield S1 1WB, U.K.

### Supporting Information



**ABSTRACT:** Cassette dosing of compounds for preclinical drug plasma pharmacokinetic analysis has been shown to be a powerful strategy within the pharmaceutical industry for increasing throughput while decreasing the number of animals used. Presented here for the first time is data on the application of a cassette dosing strategy for label-free tissue distribution studies. The aim of the study was to image the spatial distribution of eight nonproprietary drugs (haloperidol, bufuralol, midazolam, clozapine, terfenadine, erlotinib, olanzapine, and moxifloxacin) in multiple tissues after oral and intravenous cassette dosing (four compounds per dose route). An array of mass spectrometry imaging technologies, including matrix-assisted laser desorption/ionization mass spectrometry imaging (MALDI MSI), liquid extraction surface analysis tandem mass spectrometry (LESA-MS/MS), and desorption electrospray ionization mass spectrometry (DESI-MS) was used. Tissue analysis following intravenous and oral administration of discretely and cassette-dosed compounds demonstrated similar relative abundances across a range of tissues indicating that a cassette dosing approach was applicable. MALDI MSI was unsuccessful in detecting all of the target compounds; therefore, DESI MSI, a complementary mass spectrometry imaging technique, was used to detect additional target compounds. In addition, by adapting technology used for tissue profiling (LESA-MS/MS) low spatial resolution mass spectrometry imaging (~1 mm) was possible for all targets across all tissues. This study exemplifies the power of multiplatform MSI analysis within a pharmaceutical research and development (R&D) environment. Furthermore, we have illustrated that the cassette dosing approach can be readily applied to provide combined, label-free pharmacokinetic and drug distribution data at an early stage of the drug discovery/development process while minimizing animal usage.

The development of mass spectrometric analytical technologies has enabled pharmaceutical research and development to employ an increasingly wide array of high-throughput screening modalities. Compound optimization with early, parallel elucidation of the physicochemical and pharmacokinetic properties enables a broader choice of compound leads from which candidate drugs can be selected and has also been shown to reduce compound attrition in development.<sup>1</sup> The simultaneous dosing of drugs during *in vivo* research is typically termed cassette dosing (though also referred to as *N*-in-one dosing). Cassette dosing was first employed by pharmaceutical companies toward the end of the 1990s, when

simultaneous measurements of five compounds were made during the development of potential therapeutics for the treatment of benign prostatic hyperplasia.<sup>2</sup> Cassette dosing and analysis has been shown to be applicable for both orally<sup>3</sup> and intravenously<sup>4</sup> administered drugs. Factors that need to be considered when devising a cassette dosing experiment include mass spectrometry instrumentation and liquid chromatography (LC) requirements (positive or negative mode ionization),

Received: June 17, 2014

Accepted: August 1, 2014

Published: August 1, 2014

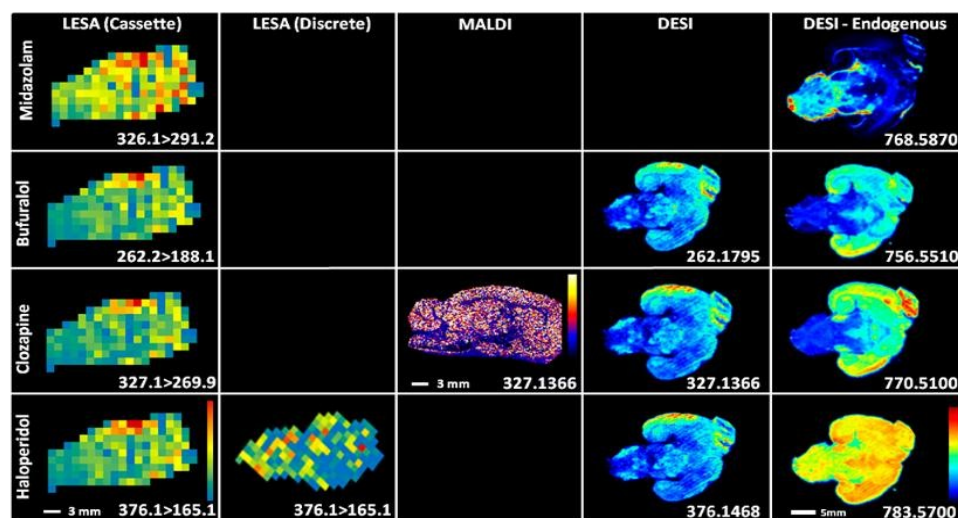


**Figure 1.** Images of intravenously dosed compounds detected using LESA-MS/MS, MALDI-MS, and DESI-MS after cassette dosing or discrete dosing (haloperidol), highlighting the value of using orthogonal analytical techniques to cover a wider chemical space than that covered by MALDI-MS alone.

whether drugs or their metabolites are likely to have common structures or fragmentation patterns, whether compounds require specific formulation (solubility at specific pH), and careful attention should be given to the dose levels selected. While such factors can be mitigated for by the selection of appropriate combinations of compounds to be analyzed, there remains a risk of drug–drug interactions during *in vivo* administration. This topic is extensively discussed in several reviews on cassette dosing.<sup>5–7</sup> Interactions mainly arise around competition at clearance pathways. Other reported interactions including heteroactivation of clearance pathways, which is the activation of a metabolic enzyme by a second drug acting through an allosteric mechanism (acting on a site other than the active site). There is also the chance of pharmacological and toxicological effects on organ blood flows and clearances.<sup>7</sup> However, during early drug discovery, the advantage of parallel preliminary experiments means that the risk of erroneous results from drug–drug interactions is outweighed by the saving in reduced time and cost, as noncassette experiments will always be performed on compounds that are to be progressed later in the discovery pipeline.

Traditionally discovery phase pharmacokinetic analysis has been performed using sensitive triple quadrupole mass spectrometers, usually in combination with rapid chromatography systems and operated with automated or semiautomated optimization software.<sup>8</sup> This generic approach enables rapid quantification of chemically diverse compounds from biofluids or tissue homogenates. While these methods are ideally suited for deriving pharmacokinetic parameters from homogeneous biofluids, they are less suitable to analysis of heterogeneous tissue samples. Furthermore, any tissue information from homogenates can be misleading due to factors such as residual blood concentration or dilution. Compound biodistribution information is usually collected at a later stage in a compound's life cycle using techniques like quantitative whole body autoradiography (qWBA).<sup>9</sup> Such analysis retains distribution information lost during homogenization but has major limitations such as the need for a radiolabeled compound,

rendering the technique impractical for discovery use. Label-based techniques are also limited in their inability to distinguish a parent compound from any metabolites that still contain the label, hence producing an ambiguous representation of a compound's distribution.

Mass spectrometry imaging (MSI),<sup>10,11</sup> regarded as collection of multiple mass spectra by rastering across a tissue section in two dimensions, and mass spectrometry profiling (MSP),<sup>12–15</sup> generally regarded as collection of mass spectra at discrete points on a tissue section, have recently emerged as technologies that have the capability to obtain label-free compound biodistribution, relative abundance, and quantitation data by analyzing tissue sections directly.

Such methods enable the simultaneous analysis of drugs, metabolites, endogenous small molecules, lipids, and peptides directly from tissue sections. Several comprehensive reviews describe methodologies<sup>16–18</sup> utilizing a range of sample ionization methods. Matrix-assisted laser desorption ionization (MALDI) is arguably the most effective for pharmaceutical research and is most commonly employed for MSI. However, alternative ionization methods such as desorption electrospray ionization (DESI) are amenable for use in MSI.<sup>25</sup> Techniques like liquid extraction surface analysis (LESA) can be used to increase the sensitivity of tissue analysis when target compounds cannot be detected by other MSI ionization methods, but their use to date has been restricted to low spatial tissue profiling at only a few sampling positions across a tissue section.<sup>13</sup> While the origins of LESA and DESI can both be traced back to electrospray ionization, they exhibit different but complementary strengths and weaknesses. LESA can have high sensitivity when used in selected reaction monitoring mode on a triple quadrupole MS but lacks the high spatial resolution that DESI is capable of providing. DESI, in contrast, can supply structure-rich mass spectrometry (MS) images (Figure 1, DESI endogenous masses, showing multiplex analysis within the cassette-dosed sections) at high spatial resolution ( $\sim 50 \mu\text{m}$ )<sup>25</sup> but has less apparent sensitivity due to the decrease in sampling area.

The utility of MSI is determined by the ability to detect the target compound at the level present in the sample and is determined by a number of factors such as the ionization efficiency and localized suppression caused by salts and endogenous compounds within the tissues. There is also a risk that the mass of the target compound is masked in the mass spectrum by endogenous compounds or MALDI matrix adduct signal. Therefore, "up-front" MSI ionization assessments are routinely performed to detect target compound in tissue samples before undertaking extensive studies. The risk of failing to detect a target in a sample can be further mitigated by using the orthogonal MSI techniques previously alluded to, such as LESA and DESI, which are becoming increasingly popular as imaging tools. These ionization techniques are essentially based on generic nanoelectrospray ionization and can be used to cover a much wider chemical space than MALDI which is limited by MALDI matrix selection. These ambient ionization techniques are often combined with triple quadrupole, ion trap, or time-of-flight mass spectrometers offering increased sensitivity at the cost of lower spatial resolution.

In a pharmacokinetic study multiple biofluid samples can be taken at required time points post dose; however, samples for MSI require the termination of the subject animal and the dissection and sectioning of a target organ. This means that a greater number of animals are required to generate corresponding time course MSI data. Effective cassette-dosed MSI experiments would be advantageous with a reduction in both the analytical turnaround time but also the animal handling and husbandry costs. Any significant reduction in the number of animals is advantageous, above and beyond cost savings and analysis time, as it is in keeping with industry-wide aims to reduce, reuse, and refine experimental animal numbers, the so-called "3-Rs".

The research presented here outlines a novel strategy of mass spectrometry tissue imaging and profiling in routine intravenous and orally cassette-dosed pharmacokinetic studies. MSI analysis was not adversely affected by cassette dosing, and the tissue distribution data corresponds with the plasma pharmacokinetic (PK) analysis and highlights the advantage of gaining important pharmacokinetic and distribution data from the same animals at an early phase of drug discovery. Demonstrated for the first time is enhanced tissue profiling technology (LESA) for low spatial resolution imaging. Furthermore, such analysis is combined with near cellular resolution MSI ( $\sim 20 \mu\text{m}$ ) and demonstrates that a suite of instrumentation enables detection of all target compounds, and therefore, a multiplatform MSI strategy is required for effective pharmaceutical research and development (R&D).

## MATERIALS AND METHODS

**Materials and Reagents.** Analytical grade acetonitrile, methanol, and formic acid were obtained from Fisher Scientific (Loughborough, Leicestershire, U.K.). 2-Methylbutane was obtained from Sigma-Aldrich (Poole, Dorset, U.K.). Test compounds were obtained in house from AstraZeneca compound management group (Macclesfield, Cheshire, U.K.) with the exception of moxifloxacin which was purchased from Sigma-Aldrich (Poole, Dorset, U.K.). MALDI-MS grade  $\alpha$ -cyano-4-hydroxycinnamic acid (CHCA) and 2,5-dihydroxybenzoic acid (DHB) were purchased from Sigma-Aldrich (Poole, Dorset, U.K.).

**Animals.** Adult male Hans Wistar rats (approximate weight 260 g) were obtained from Charles River Laboratories

(Margate, Kent, U.K.) and were acclimatized on site for a minimum of 3 days prior to dosing. Compounds administered by oral gavage and intravenous bolus injection (via the tail vein) were formulated in 5% dimethyl sulfoxide/95% (30% w/v Captisol in water). Control animals were dosed with vehicle via the same administration route in each arm of the study.

**Dosing and Scheduling.** An initial pilot study using intravenous administration consisted of the following: one animal was dosed with vehicle, one animal was dosed discretely with haloperidol (2 mg/kg), and two animals were cassette-dosed (2 mg/kg/compound, haloperidol, bufuralol, midazolam, and clozapine). All intravenously dosed animals were euthanized at 15 min post dose.

A more extensive study using oral administration consisted of the following: one animal was dosed with vehicle, two animals were dosed discretely with moxifloxacin (25 mg/kg), two animals were dosed discretely with olanzapine (10 mg/kg), and three animals were cassette-dosed (moxifloxacin, olanzapine, erlotinib, and terfenadine at 25, 10, 10, and 25 mg/kg, respectively). Blood samples were taken at 0.5, 1, 2, 3, 4, and 5 h post dose via the tail vein (0.2 mL) and 6 h via cardiac puncture (0.5 mL); the blood was spun at 4500g for 2 min to yield plasma (approximately 0.1 mL) which was subsequently stored at  $-20^\circ\text{C}$  prior to analysis. Animals were euthanized at either 2 or 6 h post dose.

All tissue dissection was performed by trained AstraZeneca staff (project license 40/3484, procedure number 10). Tissues (brain, kidneys, lungs, and liver) were snap-frozen in 2-methylbutane on dry ice, subsequent transfer of tissues was done on dry ice, and samples were stored at  $-80^\circ\text{C}$  until tissue processing.

**Tissue Processing.** Tissue sections were cut at a thickness of  $14 \mu\text{m}$  and thaw-mounted onto indium tin oxide (ITO)-coated MALDI target slides (Bruker Daltonics, Bremen, Germany) or standard glass microscope slides (VWR, Leicestershire, U.K.). Sections were taken at approximately equal depth from all organs to allow visualization of similar structures between samples. Organ tissue sections from cassette-dosed, discrete-dosed, and vehicle control animals were mounted adjacent on the same slides to minimize variability caused through variations in matrix application or when analyzing separate MALDI targets. Tissue sections were analyzed randomly and nonsequentially to limit the risk of any observed variation in relative abundance being as a result in loss of analyzer sensitivity during the course of the analysis. Mounted tissue sections were stored at  $-80^\circ\text{C}$  until required.

**MALDI Matrix Application.** Thaw-mounted tissue sections were dried in a stream of nitrogen when removed from  $-80^\circ\text{C}$  storage. Optical images were taken using a standard flat bed scanner (Seiko Epson, Negano, Japan) prior to MALDI matrix application. Matrix coating was applied as previously described for the analysis of small molecules using a pneumatic TLC sprayer (Sigma-Aldrich).<sup>19</sup> Either 15 mL of CHCA (10 mg/mL, 50/50 v/v acetonitrile/water, 0.1% TFA) or DHB (70 mg/mL, 50/50 v/v acetonitrile/water, 0.1% TFA) was applied. Following matrix application all subsequent transportation was performed with samples sealed in container to limit effects of light and humidity on sample and matrix. For high spatial resolution, tissue sections were transferred from  $-80^\circ\text{C}$  to a desiccator and dried for about 30 min prior to matrix coating. An optical image of the slide was acquired using a flatbed scanner (Epson perfection V500). The tissue was coated with DHB at a lower concentration of 35 mg/mL (50/50 v/v



methanol/water, 0.2% TFA) to reflect the more direct application of matrix and to prevent system blockages when using the TM-Sprayer tissue MALDI sample preparation system (HTX Technologies, LCC, Carrboro, NC, U.S.A.). A flow rate of 80  $\mu\text{L}/\text{min}$ , nitrogen pressure 8 psi, and a spray nozzle temperature of 95  $^{\circ}\text{C}$  were used for two passes and 90  $^{\circ}\text{C}$  for a subsequent four passes of the tissue.

**MALDI Mass Spectrometry Imaging.** MALDI MSI was initially performed using a MALDI q-TOF MS (MALDI SYNAPT G2 HDMS, Waters Corporation, U.K.). The region of interest selected for imaging was defined using HDI Imaging software (version 1.2, Waters Corporation, U.K.), where the spatial resolution was also set (100  $\mu\text{m}$ ). Positive ion data was acquired with the mass spectrometer set to sensitivity mode over the range of  $m/z$  100–1200 with 300 laser shots per raster position using a 1 kHz laser. Optimization of the mass spectrometer was achieved by tuning acquisition settings while collecting data from a manually deposited control spot of the target compounds (0.5  $\mu\text{L}$  of drug standard solution at approximately 2  $\mu\text{M}$  manually spotted onto the ITO target with equal volume of matrix in solution). Raw data was converted to image files via processing through Mass Lynx (version 4.1, Waters Corporation, U.K.), then viewed in HDI Imaging software (version 1.2, Waters Corporation, U.K.). Data was normalized by total ion current, and subsequent image analysis was performed. Mass filter windows were selected with a precision of  $\pm 0.04$  Da.

High mass resolution data were acquired on a 12 T Solarix FTICR (Bruker Daltonics, Billerica, MA) running Solarix control v1.5.0 build 103. Ions were excited (frequency chirp 48–500 kHz at 100 steps of 25  $\mu\text{s}$ ) for 0.8 s to yield broadband 2 Mword time-domain data. Each mass analysis was the sum of 400 random laser sample positions across tissue. Fast Fourier transforms and subsequent analyses were performed using DataAnalysis v 4.1 build 362.7 and FlexImaging v4.0 build 32 (Bruker Daltonics, Billerica, MA).

High spatial resolution MSI experiments were carried out in positive reflectron mode over a mass range of  $m/z$  150–900 using the UltrafleXtreme MALDI-TOF/TOF MS (Bruker Daltonics) equipped with a 2 kHz, smartbeam-II Nd:YAG laser. Data was collected at a spatial resolution of 15  $\mu\text{m}$ , summing up 500 laser shots/raster position. FlexImaging 3.0 (Bruker Daltonics) was used for data analysis, normalization, and molecular image extraction typically using mass selection window of  $\pm 0.05$  Da.

**DESI Mass Spectrometry Imaging.** DESI MSI analysis was performed using an Exactive mass spectrometer (Thermo Fisher Scientific Inc., Bremen, Germany) operated in positive ion mode. The mass spectrometer was equipped with a custom-built automated DESI ion source. The mass resolution used for all measurements was set to 100 000. Mass spectra were collected in the mass range of  $m/z$  = 150–1300. Methanol/water (95:5 v/v) was used as the electrospray solvent at a flow rate of 2.5  $\mu\text{L}/\text{min}$ . Nebulizing nitrogen was used as gas at a pressure of 10 bar. The height distance between the DESI sprayer and the sample surface was set to 2 mm with the distance between the sprayer and the inlet capillary set to 14 mm. The distance between the sample surface and the inlet capillary of the mass spectrometer was <1 mm. The angle between the sprayer tip and the sample surface was set at 80 $^{\circ}$ . For line scan experiments, the parameters described above were used with a scan speed of 150  $\mu\text{m}/\text{s}$ . Imaging experiments were conducted using 150  $\mu\text{m}$  spatial resolution. Image analysis

consisted of individual horizontal line scans combined into imzML format using the imzML converter V.1.1.4.5 ([www.maldi-msi.org](http://www.maldi-msi.org)). All images were created using 0.01 Da bin size and were normalized to the total ion count (TIC) to compensate for signal instabilities.

**LESA Mass Spectrometry Imaging.** LESA MSI was performed using LESA-MS/MS on a Triversa Nanomate chip-based electrospray ionization system (Advion, Ithaca, NY, U.S.A.) coupled to a QTRAP 5500 (AB Sciex, Framingham, MA, U.S.A.) mass spectrometer that was operated in positive ion multiple reaction monitoring (MRM) mode. The LESA sampling method consisted of aspiration of a 0.9  $\mu\text{L}$  volume of extraction solution (acetonitrile/water/formic acid 60/40/0.1 v/v/v). An amount of 0.5  $\mu\text{L}$  of the solution was then dispensed at a height of 0.4 mm above the tissue with a 1 s postdispense delay time; a liquid microjunction between the pipette tip and the sample was maintained throughout the procedure. An amount of 1.1  $\mu\text{L}$  of sample was reaspirated into the pipet tip prior to infusion via the Nanomate chip for tandem mass spectrometry (MS/MS) analysis. Relative abundance was determined between samples by comparison of MRM transition intensity at  $m/z$  326 > 291.2, 262.2 > 188.1, 327.1 > 269.9, and 376.1 > 165.1 for midazolam, bufuralol, clozapine, and haloperidol (intravenously dosed cassette), respectively, and 402.1 > 261.1, 313.1 > 256.1, 394.1 > 278.0, and 472.2 > 436.2 for moxifloxacin, olanzapine, erlotinib, and terfenadine (orally dosed cassette). LESA-MS/MS data was processed using a purpose-built software package capable of extracting relative abundance values from Analyst 6.1 (ABSciex, Framingham, MA, U.S.A.).

LESA-MS/MS images were created using in-house-developed software capable of color grading ion intensities acquired from each individual LESA spot in a heat map configuration.

**PK Bioanalysis.** Details of the preparation of bioanalytical stock solutions and the bioanalytical method used can be found in the Supporting Information.

## RESULTS AND DISCUSSION

Obtaining knowledge of the abundance and spatial distribution of compounds in target tissue can be extremely valuable in drug discovery or during a toxicological investigation. An understanding of the distribution profile of candidate drugs can be fed back into project design/make/test cycles, allowing researchers to refine the properties of chemical series early in the drug discovery process. In order to use such distribution information effectively the analysis techniques need to be high throughput while not compromising data quality. This study explores cassette dosing as a viable method of increasing throughput and decreasing the numbers of animals used in distribution studies using mass spectrometry imaging. Data quality was validated by comparing compounds dosed using the cassette approach with compounds that are dosed orally and intravenously as discrete formulations.

Technical replicates were not performed due to instrument time constraints, number of samples involved, and the cost of LESA consumables (specifically nanoESI emitters). However, reproducibility of MSI strategies have previously been reported and therefore were not considered to be required for these experiments where relative abundances were measured. If absolute quantitation was performed we would recommend technical replicate analysis to be performed.

**Test Substance Selection.** Four compounds were selected for a pilot intravenous cassette dosing experiment. Haloperidol,

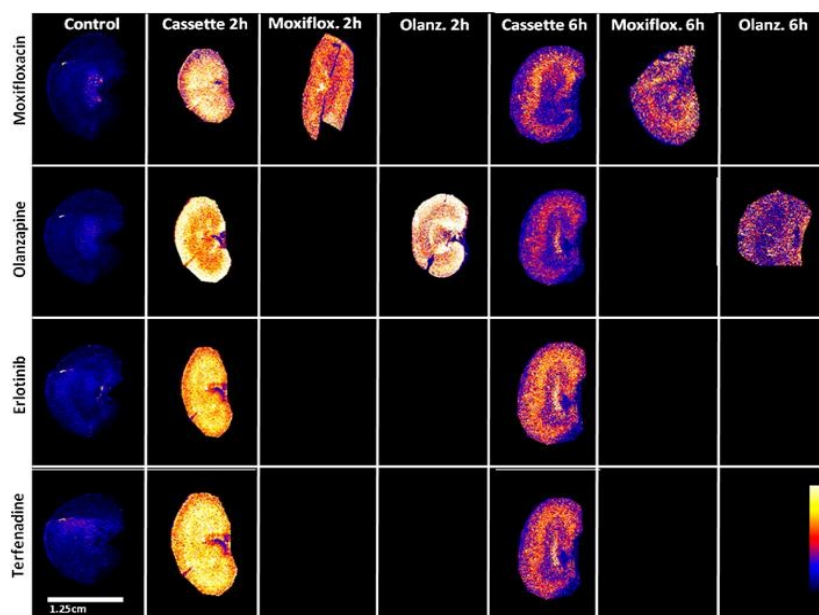


**Figure 2.** MSI abundance distributions of cassette- and discrete-dosed compounds in rat kidney sections ( $14\ \mu\text{m}$ ) at 2 and 6 h post dose. Moxifloxacin and olanzapine distributions are comparable at the two time points validating the cassette approach.

a dopamine  $D_2$  antagonist, bufuralol, a  $\beta$ -adrenoceptor antagonist, and midazolam, a GABA antagonist, were chosen at random; no data about prior MSI analysis has been published to date. Clozapine, a serotonin antagonist that has been used in several in-house studies and is known to be detectable by MALDI MSI, was added to the intravenous cassette to mitigate the risk of failing to detect all compounds in the pilot study by our primary analytical technique.

A further four compounds were selected for a more extensive oral cassette dosing experiment. Terfenadine, an  $H_1$  receptor antagonist, has been analyzed by MSI following a 50 mg/kg dose (single oral dose) using a hybrid quadrupole–time-of-flight (QqTOF, QStar Pulsar, Applied Biosystems)<sup>20</sup> and at the same dose by LESA profiling (QTRAP 5500, AB Sciex).<sup>13</sup> Erlotinib, a tyrosine kinase inhibitor, was detected using a hybrid quadrupole–time-of-flight (QqTOF, QStar XL, AB/MDS Sciex)<sup>21</sup> following 5 mg/kg oral dose. Olanzapine, a dopamine  $D_2$  antagonist, was orally dosed at 8 mg/kg and detected using a MALDI time-of-flight (Autoflex, Bruker).<sup>22</sup> The final compound in the cassette was moxifloxacin, a DNA gyrase inhibitor, detected on a FlashQuant QTRAP (AB Sciex) following oral dose at 25 mg/kg.<sup>23</sup>

**Intravenous (iv) Dosing.** An initial intravenously dosed pilot study consisting of cassette-dosed, discrete-dosed, and vehicle-dosed animals was performed in order to confirm the proof of principle that cassette dosing and discrete dosing show a similar relationship in terms of relative distribution across different tissues. Animals were euthanized at 15 min post dose, with brain, kidney, liver, and lung samples dissected and snap-frozen in 2-methylbutane postmortem.

**Distribution of Intravenously Dosed Compounds by MALDI MSI.** Brain, kidney, liver, and lung sections ( $14\ \mu\text{m}$ ) were thaw-mounted onto ITO-coated microscope slides. Sections were arranged, as stated in the Materials and Methods

section, to minimize intra-analysis variability caused by matrix applications and interanalysis variability. Typically three brain sections representing cassette-dosed, discrete-dosed, and control were mounted on the same slide. Positive ion MALDI MSI (MALDI Synapt Q-TOF, Waters, Manchester, U.K.) was employed to analyze brain and liver sections. DHB and CHCA were used as standard MALDI matrixes with limited success. Haloperidol, bufuralol, and midazolam were not detected with either matrix from either tissue type even though initial ionization testing in the absence of tissue had been positive using both matrixes (data not shown). This poor response could be due to various factors such as ionization suppression from endogenous components and salts in the tissue and could be rectified by using an alternative MALDI matrix, solvent system, or by carefully optimized slide washing of the tissue prior to matrix application<sup>24</sup> and analysis. Clozapine was detected on both tissue types using CHCA as the MALDI matrix; the relative distribution of clozapine at 15 min post dose in a sagittal brain section can be seen in Figure 1, normalized by total ion count, at a spatial resolution of  $100\ \mu\text{m}$ .

**Additional MSI Analysis by LESA-MS/MS and DESI-MS.** The failure of MALDI MSI to detect several of the intravenously dosed compounds presented an opportunity to highlight the value of orthogonal analysis by other techniques. Figure 1 shows images of intravenously dosed sagittal brain sections analyzed by LESA-MS/MS ( $1\ \text{mm}$  spatial resolution) and coronal brain sections analyzed by DESI-MS ( $150\ \mu\text{m}$  spatial resolution). LESA-MS/MS detected all of the compounds in the sagittal brain sections. Relative distribution of the compounds was largely around the frontal cortex with little distribution into the rear left and right hemispheres of the cerebrum. Cassette-dosed and discrete-dosed comparisons of haloperidol in the brain sections by LESA-MS/MS (Figure 1) highlighted some differences in distribution. This is due to the

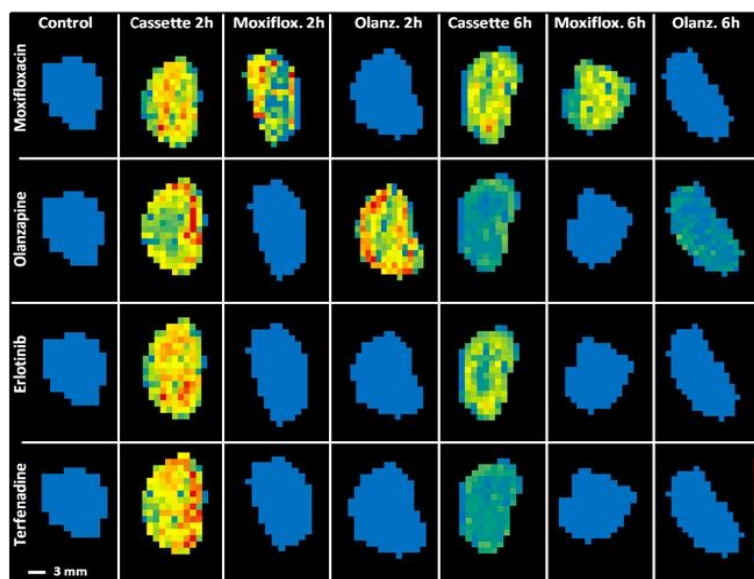


**Figure 3.** LESA-MS/MS abundance distributions of cassette- and discrete-dosed compounds in rat kidney sections ( $14\ \mu\text{m}$ ) at 2 and 6 h post dose. This data mirrors the MALDI MSI data showing comparable distributions of moxifloxacin and olanzapine dosed discretely and by the cassette approach.

in-house imaging program applying a rainbow scale to a narrow drug intensity window across the two sections; the actual distribution was relatively homogeneous throughout the tissue. Coronal brain tissue sections ( $14\ \mu\text{m}$ ) were thaw-mounted onto standard glass slides for accurate mass DESI-MS analysis. Due to the requirement to place DESI-MS samples onto nonconductive glass slides, additional tissue sections were cut by cryostat and thaw-mounted. It was necessary to use a brain from a different animal (dosed and sacrificed under same conditions) as the first brain fractured during the remounting process. While this prevents intersample consistency it does allow the coronal DESI analysis to show symmetry in detected analytes and endogenous compounds. Detection of haloperidol, bupropion, and clozapine at (mass  $\pm$  ppm)  $376.1468 \pm 1.6217$ ,  $262.1795 \pm 2.4945$ , and  $327.1366 \pm 1.5254$  Da, respectively, was achieved (Figure 1). Midazolam could not be detected with sufficient mass accuracy ( $326.0850$  Da) from the tissue sections using DESI-MS.

**Oral (po) Dosing.** A larger, more comprehensive study was designed to compare cassette dosing to discrete dosing after oral administration. Plasma analysis by LC-MS/MS revealed that cassette- and discrete-dosed animals were exposed to the test substances in all instances. Comparative plasma concentrations post dose for moxifloxacin and olanzapine were equivalent in cassette-dosed versus discrete-dosed animals (Figure S-1, Supporting Information), indicating that plasma exposures were not adversely affected by drug–drug interactions. PK parameters for each compound are listed in Table S-1, Supporting Information. The parameters exhibit reproducibility between orally administered cassette- and discrete-dosed moxifloxacin and olanzapine and provide an initial indication that the cassette dosing approach is valid.

**Distribution of Orally Dosed Compounds by MALDI MSI.** Brain, kidney, liver, and lung tissue sections ( $14\ \mu\text{m}$ ) were

thaw-mounted onto ITO-coated microscope slides and were arranged in a similar order as the intravenously dosed sections to maintain a consistent approach; where possible five sections were mounted per slide, representing cassette dose 2 and 6 h, discrete dose 2 and 6 h, and control tissue. The mass spectrometer source was rigorously cleaned after every two analytical runs to limit the risk of any observed variation in relative abundance being as a result in loss of analyzer sensitivity during the course of the analysis. Positive ion MALDI MSI (MALDI Synapt Q-TOF, Waters, Manchester, U.K.) was employed to analyze the kidney sections and produced high-quality MS images (Figure 2), normalized by total ion count, at a spatial resolution of  $100\ \mu\text{m}$  and signal thresholding consistent across samples. The spatial distribution and relative abundance of the test substances at the 2 h time point were homogeneous throughout the kidney tissue. Moxifloxacin and olanzapine distributions were relatively consistent between cassette- and discrete-dosed animals, with some minor differences which could be attributed to pharmacokinetic interanimal variability (supported by the differences in plasma PK levels, Supporting Information Table S-1) or the depth at which the section was cut from the kidney sample. At the 6 h time point the relative abundance of the test substances in the cassette-dosed kidneys was approximately 6-fold lower in abundance than the 2 h time point for moxifloxacin. A reduction was also detected for olanzapine (30-fold lower), erlotinib (8-fold reduced), and terfenadine (3-fold diminished). This drop in relative abundance reflects the decrease in concentrations observed in the plasma samples between the two time points but was not directly comparable in terms of the drop in response in tissue versus the drop in concentration in plasma. Erlotinib and terfenadine were distributed in both the cortex and medulla of the kidney, with greater intensity in the medullary region,

whereas moxifloxacin and olanzapine were more localized in the medulla of the kidney. The consistent relative abundance between the images for moxifloxacin and olanzapine at each time point for cassette and discrete dosing provides further validation of the cassette dosing approach. Liver and brain sections were also analyzed by MALDI MSI to confirm detection of the test substances in the various tissue types (data not shown).

**Analysis of Orally Dosed Tissues by LESA-MS/MS.** An advantage of tissue sectioning is that, from each sample, multiple, nearly identical tissue sections can be taken, allowing analysis such as LESA-MS/MS and DESI-MS to be performed in addition to MALDI MSI. LESA-MS/MS is based upon nano-electrospray ionization, a proven, robust technique that is capable of ionizing a wide variety of different chemical species. The combination of the ionization technique with sensitive tandem mass spectrometry offers a complementary method of analysis to MALDI MSI. MALDI by contrast is a much more complex process, subject to subtle changes in ablation, ionization, and sensitivity due to matrix choice, matrix crystal size, preparation conditions, and endogenous interferences from material in the tissue such as salts. These limitations of the technique lead to a lower than ideal success rate when working in a high-throughput environment. LESA-MS/MS and other direct ionization techniques such as DESI-MS provide a way of bridging that gap, enabling MSI scientists to pass on meaningful distribution data to project teams. Kidney sections were analyzed by LESA-MS/MS (QTRAP 5500, ABSciex, Framingham, MA, U.S.A.) to generate low spatial resolution (1 mm) mass spectrometry images. Figure 3 displays the images from the LESA-MS/MS analysis of the orally cassette-dosed and discrete-dosed sections. The images are generated using in-house-developed software that creates a heat map of the mean ion intensity data from each LESA extraction (~125 extractions per kidney section). The LESA imaging data correlate well with the observations of the MALDI MSI data, showing a clear difference in the relative abundance of the test substances at 2 and 6 h post dose and good reproducibility in terms of spatial distribution between cassette- and discrete-dosed compounds.

**High-Resolution MSI.** Lung sections were analyzed by high mass resolution MS (12 T Solarix FTICR, Bruker Daltonics, Billerica, MA, U.S.A.) for confirmation of the presence of the test substances. Sample spectra are shown in Figure S-2, Supporting Information; the presence of moxifloxacin, olanzapine, erlotinib, and terfenadine at  $m/z$  402.1824, 313.1481, 394.1761, and 472.3210 is confirmed by accurate mass and comparison of each compound with a vehicle-dosed sample.

High spatial resolution MSI is a powerful tool that allows near-cellular resolution. The higher spatial resolution images can be used to identify regions of tissue structure within organ tissue sections. Figure 4 shows a high spatial resolution image (20  $\mu\text{m}$ , UltrafleXtreme MALDI-TOF/TOF MS, Bruker Daltonics) of dosed lung section. Olanzapine ( $m/z$  313), represented in green, is distributed throughout the lung tissue, while a blood vessel can be clearly seen in the optical image and is reflected in the MSI image as an area of high heme abundance ( $m/z$  616). High spatial resolution MSI can highlight distribution of test substances into localized areas of tissue to demonstrate drug presence at the site of action and could be expanded further to confirm target engagement via changes in endogenous disease markers.

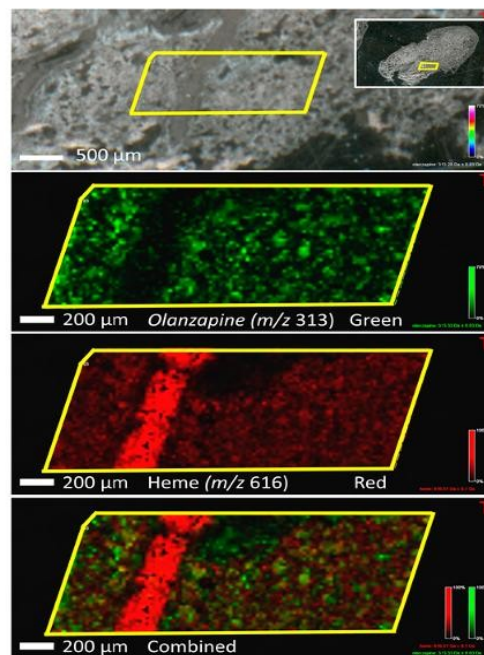


**Figure 4.** High spatial resolution MSI (15  $\mu\text{m}$ ) of orally cassette-dosed lung tissue showing an optical image describing the region of interest and MSI images of olanzapine (green) and heme (red). A blood vessel can be clearly seen with the compound being homogeneously distributed over the rest of the tissue, highlighting the power of high-resolution MSI.

## CONCLUSIONS

Cassette dosing is a widely adopted practice within pharmaceutical discovery research for plasma PK analysis. Here we have demonstrated for the first time its utility in PK tissue distribution studies using mass spectrometry imaging techniques. Cassette dosing fundamentally increases throughput, in this case by 4-fold, greatly reducing what has traditionally been an analytical bottleneck. The combination of cassette-dosed PK and drug distribution studies has many advantages; ethically the technique reduces the number of animals used, typically by around 75%; the combination also leads to a wealth of pharmacokinetic and distribution data being available at a much earlier stage of drug discovery and can lead to a much greater confidence that compounds are present at the pharmacological site of action. It is also possible to measure and monitor compound abundance target tissue in response to dose or time.

Mass spectrometry imaging covers a variety of relatively new and exciting technologies that can be used to study the regional abundance of xenobiotics within tissues, while also simultaneously measuring endogenous molecules. A single technique is yet to emerge that can successfully analyze the full scope of chemistries encountered in drug discovery, at sufficient sensitivity and with high spatial resolution. MALDI MSI was successfully used to analyze orally cassette-dosed tissue sections at 100  $\mu\text{m}$  and at higher spatial resolution (15  $\mu\text{m}$ ). LESA-MS/MS was validated against the MALDI MSI data. The success of MALDI MSI to analyze the compounds in the oral cassette-dosed study was contrasted against an intravenously dosed

cassette study in which the technique had less success. LESA-MS/MS and DESI-MS were used to profile the relative distribution of the intravenously dosed compounds, at lower spatial resolution, but with a higher success rate.

The cassette dosing strategy has been shown to be a successful approach to obtain early, combined pharmacokinetic and distribution data. Mass spectrometric imaging techniques have an increasingly important role to play in pharmaceutical R&D, with techniques being developed to provide more quantitative data and the expansion of MALDI MSI, in particular, into areas of targeted and untargeted metabolomics.

## ■ ASSOCIATED CONTENT

### 📄 Supporting Information

Additional information as noted in text. This material is available free of charge via the Internet at <http://pubs.acs.org>.

## ■ AUTHOR INFORMATION

### Corresponding Author

\*E-mail: [john.swales@astrazeneca.com](mailto:john.swales@astrazeneca.com). Phone: +44 0 7818 523 771.

### Notes

The authors declare no competing financial interest.

## ■ REFERENCES

- (1) Bass, A. S.; Cartwright, M. E.; Mahon, C.; Morrison, R.; Snyder, R.; McNamara, P.; Bradley, P.; Zhou, Y.; Hunter, J. J. *Pharmacol. Toxicol. Methods* **2009**, *60*, 69–78.
- (2) Berman, J.; Halm, K.; Adkison, K.; Shaffer, J. J. *Med. Chem.* **1997**, *40*, 827–829.
- (3) Alien, M. C.; Shah, T. S.; Day, W. W. *Pharm. Res.* **1998**, *15*, 93–97.
- (4) Olah, T. V.; McLoughlin, D. A.; Gilbert, J. D. *Rapid Commun. Mass Spectrom.* **1997**, *11*, 17–23.
- (5) Frick, L. W.; Adkison, K. K.; Wells-Knecht, K. J.; Woollard, P.; Highton, D. M. *Pharm. Sci. Technol. Today* **1998**, *1*, 12–18.
- (6) Manitpisitkul, P.; White, R. E. *Drug Discovery Today* **2004**, *9*, 652–658.
- (7) White, R. E.; Manitpisitkul, P. *Drug Metab. Dispos.* **2001**, *29*, 957–966.
- (8) Swales, J. G.; Wilkinson, G.; Gallagher, R.; Hammond, C.; O'Donnell, C.; Peter, R. *Int. J. High Throughput Screening* **2010**, *1*, 1–14.
- (9) Madden, S.; Patterson, A.; Stevenson, K. *Drug Metab. Rev.* **2012**, *44*, 63–63.
- (10) Stoeckli, M.; Chaurand, P.; Hallahan, D. E.; Caprioli, R. M. *Nat. Med.* **2001**, *7*, 493–496.
- (11) Solon, E. G.; Schweitzer, A.; Stoeckli, M.; Prideaux, B. *AAPS J.* **2010**, *12*, 11–26.
- (12) Stegemann, C.; Drozdov, I.; Shalhoub, J.; Humphries, J.; Ladroue, C.; Didangelos, A.; Baumert, M.; Allen, M.; Davies, A. H.; Monaco, C. *Circ. Cardiovasc. Genet.* **2011**, *4*, 232–242.
- (13) Eikel, D.; Vavrek, M.; Smith, S.; Bason, C.; Yeh, S.; Korfmacher, W. A.; Henion, J. D. *Rapid Commun. Mass Spectrom.* **2011**, *25*, 3587–3596.
- (14) Parson, W. B.; Koeniger, S. L.; Johnson, R. W.; Erickson, J.; Tian, Y.; Stedman, C.; Schwartz, A.; Tarcza, E.; Cole, R.; Van Berkel, G. J. *J. Mass Spectrom.* **2012**, *47*, 1420–1428.
- (15) Blatherwick, E. Q.; Van Berkel, G. J.; Pickup, K.; Johansson, M. K.; Beaudoin, M.; Cole, R. O.; Day, J. M.; Iverson, S.; Wilson, I. D.; Scrivens, J. H. *Xenobiotica* **2011**, *41*, 720–734.
- (16) Goodwin, R. J.; Pitt, A. R. *Bioanalysis* **2010**, *2*, 279–293.
- (17) Goodwin, R. J. *J. Proteomics* **2012**, *75*, 4893–4911.
- (18) Sugiura, Y.; Setou, M. *J. Neuroimmune Pharmacol.* **2010**, *5*, 31–43.
- (19) Goodwin, R. J.; Dungworth, J. C.; Cobb, S. R.; Pitt, A. R. *Proteomics* **2008**, *8*, 3801–3808.
- (20) Hsieh, Y.; Chen, J.; Knemeyer, I.; Crossman, L.; Korfmacher, W. A. *Drug Metab. Lett.* **2008**, *2*, 1–4.
- (21) Signor, L.; Varesio, E.; Staack, R. F.; Starke, V.; Richter, W. F.; Hopfgartner, G. *J. Mass Spectrom.* **2007**, *42*, 900–909.
- (22) Hamm, G.; Bonnel, D.; Legouffe, R.; Pamelard, F.; Delbos, J.; Bouzom, F.; Stauber, J. *J. Proteomics* **2012**, *75*, 4952–4961.
- (23) Prideaux, B.; Dartois, V.; Staab, D.; Weiner, D. M.; Goh, A.; Via, L. E.; Barry, C. E., III; Stoeckli, M. *Anal. Chem.* **2011**, *83*, 2112–2118.
- (24) Shariatgorji, M.; Källback, P.; Gustavsson, L.; Schintu, N.; Svenningsson, P.; Goodwin, R. J.; Andren, P. E. *Anal. Chem.* **2012**, *84*, 4603–4607.
- (25) Campbell, D. I.; Ferreira, C. R.; Eberlin, L. S.; Cooks, R. G. *Anal. Bioanal. Chem.* **2012**, *404*, 389–398.



## 11 $\beta$ -Hydroxysteroid dehydrogenase type 1 contributes to the balance between 7-keto- and 7-hydroxy-oxysterols *in vivo*

Tijana Mitić<sup>a</sup>, Steven Shave<sup>b</sup>, Nina Semjonous<sup>c</sup>, Iain McNae<sup>b</sup>, Diego F. Cobice<sup>a</sup>, Gareth G. Lavery<sup>c</sup>, Scott P. Webster<sup>a</sup>, Patrick W.F. Hadoke<sup>a</sup>, Brian R. Walker<sup>a</sup>, Ruth Andrew<sup>a,\*</sup>

<sup>a</sup> Endocrinology, University/British Heart Foundation Centre for Cardiovascular Science, The Queen's Medical Research Institute, University of Edinburgh, Edinburgh, EH16 4TJ, UK

<sup>b</sup> Institute of Structural and Molecular Biology, King's Buildings, University of Edinburgh, Edinburgh, EH9 3JR, UK

<sup>c</sup> Centre for Endocrinology, Diabetes and Metabolism, School of Clinical & Experimental Medicine, University of Birmingham, Birmingham, B15 2TT, UK

### ARTICLE INFO

#### Article history:

Received 18 December 2012

Accepted 4 February 2013

Available online 13 February 2013

#### Keywords:

7-Oxysterols

7 $\beta$ -Hydroxycholesterol

7-Ketocholesterol

Glucocorticoids

11 $\beta$ -Hydroxysteroid dehydrogenase 1

Corticosterone

### ABSTRACT

11 $\beta$ -Hydroxysteroid dehydrogenase 1 (11 $\beta$ HSD1; EC 1.1.1.146) generates active glucocorticoids from inert 11-keto metabolites. However, it can also metabolize alternative substrates, including 7 $\beta$ -hydroxy- and 7-keto-cholesterol (7 $\beta$ OHC, 7KC). This has been demonstrated *in vitro* but its consequences *in vivo* are uncertain. We used genetically modified mice to investigate the contribution of 11 $\beta$ HSD1 to the balance of circulating levels of 7KC and 7 $\beta$ OHC *in vivo*, and dissected *in vitro* the kinetics of the interactions between oxysterols and glucocorticoids for metabolism by the mouse enzyme.

Circulating levels of 7KC and 7 $\beta$ OHC in mice were  $91.3 \pm 22.3$  and  $22.6 \pm 5.7$  nM respectively, increasing to  $1240 \pm 220$  and  $406 \pm 39$  nM in *ApoE*<sup>-/-</sup> mice receiving atherogenic western diet. Disruption of 11 $\beta$ HSD1 in mice increased ( $p < 0.05$ ) the 7KC/7 $\beta$ OHC ratio in plasma (by 20%) and also in isolated microsomes (2 fold). The 7KC/7 $\beta$ OHC ratio was similarly increased when NADPH generation was restricted by disruption of hexose-6-phosphate dehydrogenase.

Reduction and oxidation of 7-oxysterols by murine 11 $\beta$ HSD1 proceeded more slowly and substrate affinity was lower than for glucocorticoids. *in vitro* 7 $\beta$ OHC was a competitive inhibitor of oxidation of corticosterone ( $K_i = 0.9 \mu\text{M}$ ), whereas 7KC only weakly inhibited reduction of 11-dehydrocorticosterone. However, supplementation of 7-oxysterols in cultured cells, secondary to cholesterol loading, preferentially slowed reduction of glucocorticoids, rather than oxidation.

Thus, in mouse, 11 $\beta$ HSD1 influenced the abundance and balance of circulating and tissue levels of 7 $\beta$ OHC and 7KC, promoting reduction of 7KC. In health, 7-oxysterols are unlikely to regulate glucocorticoid metabolism. However, in hyperlipidaemia, 7-oxysterols may inhibit glucocorticoid metabolism and modulate signaling through corticosteroid receptors.

© 2013 Elsevier Inc. Open access under CC BY license.

### 1. Introduction

Intracellular generation of active glucocorticoids (cortisol in humans, corticosterone in mice) is catalyzed by 11 $\beta$ -hydroxysteroid dehydrogenase (11 $\beta$ HSD) type 1 (EC 1.1.1.146). The potential for 11 $\beta$ HSD1 to regulate fuel metabolism has been demonstrated in murine models, in which disruption of the enzyme protects from metabolic dyshomeostasis [1,2] and, more recently, in humans in

whom specific 11 $\beta$ HSD1 inhibitors improve hyperglycaemia [3]. In murine models, inhibition of 11 $\beta$ HSD1 also offers atheroprotection [4–6]. Therefore inhibition of the reductase activity of 11 $\beta$ HSD1 is a tractable target for drug development, but to fully understand the spectrum of actions and side-effects of such drugs, effects on other substrates of 11 $\beta$ HSD1 must be considered. This is, as yet, unexplored *in vivo*, either in genetically modified mice or following selective pharmacological manipulation.

In addition to metabolizing glucocorticoids, 11 $\beta$ HSD1 can catalyze the inter-conversion of 7-keto- and 7 $\beta$ -hydroxy-sterols and steroids (Fig. 1a) (e.g. 7-oxygenated metabolites of dehydroepiandrosterone [7] and highly cytotoxic cholesterol metabolites, the 7-oxysterols [8,9]). 7-Oxysterols are formed from cholesterol both enzymatically and by auto-oxidation [10]. They accumulate in atherosclerotic plaques, a site of 11 $\beta$ HSD1 expression [11], with 7-ketocholesterol (7KC) being the most abundant, closely followed

\* Corresponding author. Tel.: +44 131 242 6763; fax: +44 131 242 6779.

E-mail addresses: [Tijana.mitic@bristol.ac.uk](mailto:Tijana.mitic@bristol.ac.uk) (T. Mitić), [s.shave@ed.ac.uk](mailto:s.shave@ed.ac.uk) (S. Shave), [nina\\_sem@hotmail.com](mailto:nina_sem@hotmail.com) (N. Semjonous), [Iain.McNae@ed.ac.uk](mailto:Iain.McNae@ed.ac.uk) (I. McNae), [d.f.cobice@sms.ed.ac.uk](mailto:d.f.cobice@sms.ed.ac.uk) (D.F. Cobice), [g.g.lavery@bham.ac.uk](mailto:g.g.lavery@bham.ac.uk) (G.G. Lavery), [scott.webster@ed.ac.uk](mailto:scott.webster@ed.ac.uk) (S.P. Webster), [patrick.hadoke@ed.ac.uk](mailto:patrick.hadoke@ed.ac.uk) (Patrick W.F. Hadoke), [b.walker@ed.ac.uk](mailto:b.walker@ed.ac.uk) (B.R. Walker), [r.andrew@ed.ac.uk](mailto:r.andrew@ed.ac.uk) (R. Andrew).

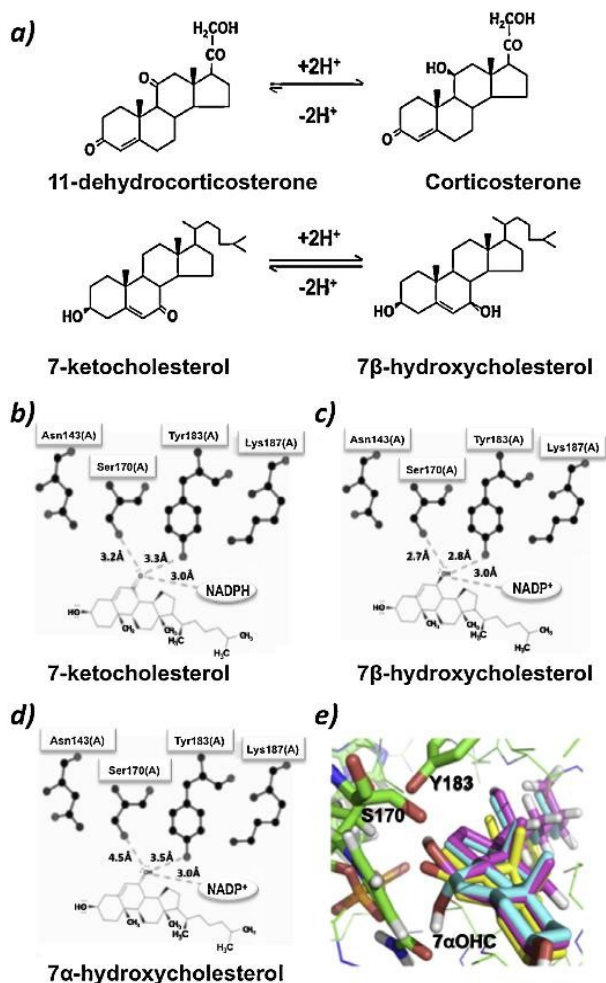


**Fig. 1.** (a) Interconversion of glucocorticoids and 7-oxysterols catalyzed by 11 $\beta$ -hydroxysteroid dehydrogenase type 1 (11 $\beta$ HSD1). The equilibrium of interconversion of inert 11-keto and active 11 $\beta$ -hydroxy forms of glucocorticoids (shown here as 11-dehydrocorticosterone and corticosterone, the principle rodent glucocorticoids) favors predominant reduction. 11 $\beta$ HSD1 can also interconvert 7-keto and 7 $\beta$ -hydroxycholesterol but the favored equilibrium position between the two reactions is not understood. (b)–(e) *In Silico* modeling of interactions between 7-oxysterols and residues in the active site of murine 11 $\beta$ -hydroxysteroid dehydrogenase 1 (m11 $\beta$ HSD1). 2D Modeling of the active site of m11 $\beta$ HSD1 (retrieved from PDB 1Y5 M) using LigPlot. Hydrogen bond lengths of interactions between (b) 7-ketocholesterol and (c) 7 $\beta$ -hydroxycholesterol and the critical residues of catalytic tetrad are shorter than those for (d) 7 $\alpha$ -hydroxycholesterol (7 $\alpha$ OHC). (e) 3D modeling of interactions between active site residues Serine 170 (S170) and Tyrosine 183 (Y183) of m11 $\beta$ HSD1 and the 7-oxygenated moieties using PyMOL. Positioning of 7 $\beta$ OHC (pink) or 7KC (yellow) into the active site demonstrated their more favorable orientation over 7 $\alpha$ OHC (turquoise), for hydrogen bonding with key amino acids of m11 $\beta$ HSD1 active site.

by 7 $\beta$ -hydroxycholesterol (7 $\beta$ OHC) [12]. Early reports [13,14] revealed that 11 $\beta$ HSD1 converted 7 $\beta$ OHC to 7KC in hepatic microsomes from all vertebrates tested (human, guinea-pig, rat, hamster and chicken) and that rat hepatic 11 $\beta$ HSD1 also reduced 7KC to 7 $\beta$ OHC. However, this has not been studied in other species and it remains unclear whether enzymes other than 11 $\beta$ HSD1 also catalyze interconversion of 7 $\beta$ OHC and 7KC.

11 $\beta$ HSD1 is a bi-directional enzyme (Fig. 1a) and both dehydrogenase (inactivating glucocorticoids) and reductase

(regenerating glucocorticoids) activities can be measured in tissues [15,16]. The prevalent direction of 11 $\beta$ HSD1, with respect to metabolism of glucocorticoids, is reduction and is dependent on the availability of endogenous co-factor (NADPH), which is generated by hexose-6-phosphate dehydrogenase (H6PDH) within the endoplasmic reticulum (ER) [17]. Mice lacking H6PDH are unable to regenerate glucocorticoids by 11 $\beta$ HSD1 [18] but it is unclear if NADPH supply physiologically regulates the balance between reductase and dehydrogenase activities and the contribution of H6PDH *in vivo* has not been investigated for 7-oxysterols. Pharmacological inhibition of 11 $\beta$ HSD1 in rats caused hepatic accumulation of 7KC [9] suggesting that, as with glucocorticoids, the predominant direction of metabolism of 7-oxysterols by 11 $\beta$ HSD1 *in vivo* is reduction. Tissue-specific differences in the equilibrium position of metabolism of glucocorticoids by 11 $\beta$ HSD1 may indeed be due to the presence of competitive substrates, as some reports have suggested that 7-oxygenated compounds inhibit metabolism of glucocorticoids by 11 $\beta$ HSD1 [19]. For example, 7KC and 7 $\beta$ OHC inhibit 11 $\beta$ HSD1 activity in mouse adipocyte (3T3-L1 and 3T3-F442) cell lines [20] and in differentiated human THP-1 macrophages [21], modulating the downstream actions of glucocorticoids.

We hypothesized that 11 $\beta$ HSD1 is a key determinant of the balance of 7 $\beta$ OHC and 7KC *in vivo*. Depending on their levels in the circulation and tissues, 7KC and 7 $\beta$ OHC may differentially inhibit either reduction or dehydrogenation of glucocorticoids, respectively. Since these oxysterols accumulate in tissues that express 11 $\beta$ HSD1 [10] (e.g. macrophages, foam cells, adipose, atherosclerotic plaques [11]), the relative proportion of 7KC to 7 $\beta$ OHC may influence the amount of active glucocorticoid within cells. To address this hypothesis we investigated the balance of 7KC and 7 $\beta$ OHC in mice with transgenic disruption of 11 $\beta$ HSD1 and H6PDH, and abilities of these 7-oxysterols to influence the equilibrium between the dehydrogenase and reductase activities of glucocorticoid metabolism by murine 11 $\beta$ HSD1.

## 2. Materials and methods

Unless otherwise stated, solvents were HPLC grade (Fisher, Hemel Hempstead, UK) and contained an anti-oxidant (0.01%w/v butylated hydroxytoluene (BHT)). Steroids and oxysterols were from Steraloids (Newport, Rhode Island, USA), derivatization reagents from Fluka (Buchs, Switzerland), tissue culture reagents from Lonza (Reading, UK) and other chemicals from Sigma-Aldrich (Poole, UK). Tritiated 11-dehydrocorticosterone (11-DHC) was synthesized [22] from [1,2,6,7- $^3$ H]<sub>4</sub>-corticosterone (GE Healthcare, Bucks, UK). Deuterium-labeled internal standards [25,26,26,26,27,27,27- $^2$ H]<sub>7</sub>-7KC, [25,26,26,26,27,27,27- $^2$ H]<sub>7</sub>-7 $\beta$ OHC and [25,26,26,26,27,27,27- $^2$ H]<sub>7</sub>-cholesterol were from CDN Isotopes (Essex, UK). Protein concentrations were quantified using a Bio-Rad kit (Hemel Hempstead, UK).

### 2.1. Animals

Male mice (10–16 weeks,  $n = 6$ –8/group [2,23]) with disruption of 11 $\beta$ HSD1 (*Hsd11b1*<sup>-/-</sup>) or H6PDH (*H6pdh*<sup>-/-</sup>) or both (*Hsd11b1*<sup>-/-</sup>/*H6pdh*<sup>-/-</sup>) and their wild-type littermate controls (15 weeks) were maintained on chow diet and tap water ad libitum, under a 16 h/8 h light/dark cycle at 21–24 °C. Male *ApoE*<sup>-/-</sup> mice (in-house colony, 8 weeks;  $n = 6$ ) were maintained on a western Diet (D12079B, Research Diets, USA) for 14 weeks. All licensed procedures were performed under accepted standards of humane animal care, as outlined in the UK Home Office Ethical Guidelines. Animals were culled by cervical dislocation at 10:00 h. Tissues and fluids were snap-frozen and stored at –80 °C.

## 2.2. Cell culture

HEK293 cells stably expressing full-length murine 11 $\beta$ HSD1 (m11 $\beta$ HSD1) [24] were maintained in Dulbecco's Modified Eagle Medium (DMEM) and seeded on poly-D-lysine coated (50  $\mu$ g/mL, 5 min) plates. Medium was supplemented with glutamine (2 mM), penicillin (100 units/mL), streptomycin (100  $\mu$ g/mL), and heat-inactivated fetal calf serum (10%v/v). For assessment of kinetic parameters, stripped fetal calf serum, prepared with dextran-coated charcoal (1% w/v), was added to the cells 12 h prior to use. For manipulation of cholesterol, medium was replaced with serum free medium 1 h prior to experimentation. Cells were maintained in a humidified atmosphere (5%CO<sub>2</sub>, 95% air, 37 °C).

## 2.3. Quantitation of 11 $\beta$ HSD1 enzyme kinetics

Inter-conversion of substrates and products was quantified under conditions of first order kinetics. Three forms of murine enzyme ( $n=6$ /group) were used: (1) a truncated form of recombinant m11 $\beta$ HSD1 protein (N23 $\Delta$ , gift from Dr Webster), (2) enzyme contained within murine hepatic microsomes and (3) a full-length m11 $\beta$ HSD1 protein expressed in stably transfected HEK293 cells [24].

### 2.3.1. Metabolism by purified and microsomal murine 11 $\beta$ HSD1

Recombinant (14–28  $\mu$ g/mL) or murine hepatic microsomal (240–260  $\mu$ g/mL [19]) protein was incubated (30 min, 37 °C) with 7-oxysterols (0.02–20  $\mu$ M) in potassium phosphate buffer (0.1 M, 0.1 mM EDTA, 20 mM cysteamine hydrochloride, pH 7.4), or with steroids (0.02–20  $\mu$ M) in Krebs-Ringer buffer (containing 5 mM glucose), and the relevant cofactor (2 mM) for oxidation (NADP<sup>+</sup> or NAD<sup>+</sup>) or reduction (NADPH or NADH). Similar experiments were performed in hepatic microsomes from *Hsd11b1*<sup>-/-</sup> mice [2] (substrate 0.2  $\mu$ M) with and without induction of cationic permeability by alameticine (0.25 mM, 1–2 h). Reactions did not proceed in the absence of either protein or the co-factor.

Following incubation, internal standards (epi-cortisol for steroids or 19-hydroxycholesterol (19OHC, 100 ng) and 4 $\alpha$ -cholesten-7 $\alpha$ -ol-3-one (50 ng) for oxysterols) were added after stopping the reaction with addition of ethyl acetate (steroids; 10 vol) or petroleum ether (oxysterols; 10 vol). Organic extracts were reduced to dryness under oxygen free nitrogen (60 °C) or argon (room temperature), respectively, and the residues stored at –20 °C until analysis by HPLC.

### 2.3.2. Metabolism by recombinant murine 11 $\beta$ HSD1 expressed in stably transfected cells

HEK293 cells, stably transfected to produce m11 $\beta$ HSD1, were seeded onto a 5 cm dish and incubated overnight with 7KC, 7 $\beta$ OHC or 7 $\alpha$ OHC (1  $\mu$ M), or with steroid (30 nM) for 45 min. Following addition of internal standard, as above, oxysterols were extracted from the medium into 2-propanol:hexane (40:60, 9 mL, 50  $\mu$ g/mL BHT) [25]. Dried organic residues were stored at –20 °C until analysis by gas chromatography mass spectrometry (GCMS). Reactions did not proceed in non-transfected HEK293 cells.

## 2.4. Competition between 7-oxysterols and glucocorticoids for metabolism by 11 $\beta$ HSD1

Recombinant protein (20  $\mu$ g/mL) was incubated, as above, in the presence of 11-DHC (0.5–10  $\mu$ M) or corticosterone (0.025–0.2  $\mu$ M) and 7KC (0.02–20  $\mu$ M) or 7 $\beta$ OHC (0.02–10  $\mu$ M). Murine hepatic microsomes (260  $\mu$ g/mL) were incubated, as above, with steroid (0.2  $\mu$ M) in the presence of 7 $\beta$ OHC or 7KC (0.1 nM–5  $\mu$ M).

The velocity of metabolism of steroids (0.02–5  $\mu$ M) was further assessed in the presence of 7-oxysterols at their IC<sub>50</sub> concentration (vehicle, 0.01% v/v ethanol). HEK293 cells expressing m11 $\beta$ HSD1 were cultured, as above, and incubated with [<sup>3</sup>H]<sub>4</sub>-labelled (5 nM) and unlabelled (25 nM) steroid and 7 $\beta$ OHC or 7KC or other oxysterols (7 $\alpha$ -, 19-, 22R- or 27-OHC; 1 nM–5  $\mu$ M, 0.01% v/v ethanol control).

## 2.5. Supplementation of cholesterol in stably transfected cells

To enrich cellular cholesterol and 7-oxysterol content, HEK293 cells stably expressing m11 $\beta$ HSD1 were incubated (37 °C, 30 min) with cholesterol-loaded methyl- $\beta$ -cyclodextrin (1:6, 10 mM in DMEM) [26]) and kinetic experiments performed within 24 h. Following manipulation, cells were washed with DMEM (37 °C) followed by phosphate buffered saline, and then incubated ( $5 \times 10^6$  cells/well, 1 h) in serum-free DMEM containing either [<sup>3</sup>H]<sub>4</sub>-corticosterone or [<sup>3</sup>H]<sub>4</sub>-dehydrocorticosterone (30 nM). Products of metabolism were quantified in medium by HPLC. Following incubation, cells were washed with ice-cold PBS and then lysed by gently rocking with NaOH (200  $\mu$ M, 0.6 mL/well, 15 min, 4 °C) [27]. An aliquot of lysate was retained for quantitation of protein. To the remaining cellular lysate, internal standards [<sup>2</sup>H]<sub>7</sub>-7KC, [<sup>2</sup>H]<sub>7</sub>-7 $\beta$ OHC (50 ng) and [<sup>2</sup>H]<sub>7</sub>-cholesterol (1  $\mu$ g) were added and oxysterols and cholesterol were immediately extracted into methanol:hexane (2:5, 7 mL, 50  $\mu$ g/mL BHT, 2 mM EDTA). The dried organic extract was dissolved in chloroform: methanol (2:1) and processed for quantitation by GCMS. All final measurements were expressed as a ratio of the total protein content in the cells.

## 2.6. Quantitation of circulating and tissue levels of 7-oxysterols

7-Oxysterols were quantified in plasma (0.4–1 mL) prepared from trunk blood collected (pooled if necessary) in EDTA-coated tubes from mice ( $n=8$ /group). Plasma was prepared from blood collected in EDTA-coated (1.6 mg/mL) vials. The effects of disruption of *Hsd1b1*, *H6pdh* or both were explored in hepatic microsomes and cytosol (0.05–0.5 mg/mL protein) from mice homozygous for the disrupted allele ( $n=6$ /group) versus their littermate controls. All samples were flushed under argon prior to extraction and BHT (45 mM, in ethanol) added before 7-oxysterols were extracted and converted to their trimethylsilyl derivatives [28] prior to analysis by GCMS [29].

## 2.7. Quantitation of steroids and oxysterols by HPLC

Substrates and products in *in vitro* extracts were analyzed by HPLC (Dionex SUMMIT<sup>®</sup> system, Camberley UK) with online radioscintillation detection (LB509<sup>®</sup>  $\beta$ -scintillation counter, Berthold Technologies GmbH & Co, Germany). 7-Oxysterols were eluted from a SUNFIRE<sup>®</sup> column (C18, 15 cm, 4.6 mm, 5  $\mu$ m; Waters, Edinburgh, UK) with acetonitrile:water (95:5), at 1 mL/min, 24 °C and quantified at selected wavelengths (195 nm (7KC, 4 $\alpha$ -cholesten-7 $\alpha$ -ol-3-one), 237 nm (hydroxycholesterols)). Glucocorticoids were separated using a SYMMETRY<sup>®</sup> C8 column maintained at 35 °C (15 cm, 4.6 mm, 5  $\mu$ m, Waters) using a mobile phase of water:acetonitrile:methanol (60:15:25) flowing at 1 mL/min. Unlabelled steroids were detected at 240 nm. Unlabelled oxysterols and steroids were quantified by interpolation onto a standard curve of peak area divided by that of the internal standard vs concentration, prepared from calibration standards processed simultaneously. Abundances of tritiated steroids were quantified by on-line liquid scintillation counting (2 mL/min; GOLDFLOW<sup>®</sup>, Meridian, Surrey, UK).



### 2.8. In silico modeling of interactions between 7-oxysterols and residues in the active site of murine 11 $\beta$ -hydroxysteroid dehydrogenase 1 (m11 $\beta$ HSD1)

3D Macromolecular structural information about m11 $\beta$ HSD1 was obtained from the Research Laboratory for Structural Bioinformatics Protein Data Bank. 1Y5M represented a dimeric m11 $\beta$ HSD1 bound with NADP<sup>+</sup> and 1Y5R represented m11 $\beta$ HSD1 bound with NADP<sup>+</sup> and corticosterone [30]. The structure of 7 $\alpha$ -hydroxysteroid dehydrogenase (EC1.1.1.159, 7 $\alpha$ HSD, PDBID 1FMC) in complex with 7-oxoglycochenodeoxycholic acid [31] was a template for modeling the steric orientation of 7 $\alpha$ OHC, allowing alignment of 7 $\alpha$ - and 7 $\beta$ -hydroxyl and 7-keto groups into the active site, when 7 $\alpha$ HSD and 11 $\beta$ HSD1 were subsequently superimposed. Energy maps for all ligand atoms around the active site were generated using the virtual screening program LIDAEUS (Ligand Discovery At Edinburgh University). Energy minimization routines were used to aid the positioning of substrate within the active site of 11 $\beta$ HSD1. 2D Representations of protein-ligand complexes from modeled structures were created using LigPlot (Cambridge, UK), the output of which was then augmented by 2D representations of substrates generated by MARVINVIEW<sup>®</sup> (ChemAxon, Budapest, Hungary) to distinguish between the steric orientation of 7 $\alpha$ - and 7 $\beta$ OHC. Visualization of 3D structures was performed using PyMOL (open source, DeLano Scientific LLC).

### 2.9. Analysis of kinetics and statistics

$V_{max}$ ,  $K_m$  and  $K_i$  values were determined, using global nonlinear regression, from data generated by measuring reaction velocity across a range of substrate concentrations in the absence and presence of competitor. In addition, using recombinant protein, Dixon Plots were generated as the reciprocal of the reaction velocity using four substrate concentrations [S] against four inhibitor concentrations [I]. All data are presented as mean  $\pm$  SEM. Non-linear regression and statistical comparisons were made using GRAPHPAD PRISM<sup>®</sup> software v5.0 (GraphPad Software Inc. San Diego, USA) by 1 or 2-way ANOVA (with Tukey post hoc tests), or unpaired or paired Student's *t*-tests as appropriate.

## 3. Results

### 3.1. Disruption of 11 $\beta$ HSD1 or H6PDH in vivo impairs reduction of 7-oxysterols

7-Oxysterols were present in plasma from wild-type, littermate control mice in concentrations of 91.3  $\pm$  22.3 (7KC) and 22.6  $\pm$  5.7 (7 $\beta$ OHC) nM [29]. Levels increased more than 10 fold (1240  $\pm$  22 (7KC) and 406  $\pm$  39 (7 $\beta$ OHC) nM) in *ApoE*<sup>-/-</sup> mice on an atherogenic, western diet. Following disruption of *Hsd11b1*, there was a trend ( $p = 0.08$ ) for an increase in concentrations of 7KC (133.8  $\pm$  16.8 nM) but not 7 $\beta$ OHC (23.6  $\pm$  2.2 nM) [29]. However, the ratio of

7KC/7 $\beta$ OHC in plasma significantly increased in the *Hsd11b1*<sup>-/-</sup> (5.4  $\pm$  0.5) vs. control mice (4.1  $\pm$  0.4,  $n = 9$ ,  $p < 0.05$ ).

Both 7KC and 7 $\beta$ OHC were detected in microsomes from control mice. Disruption of *Hsd11b1* caused a profound reduction in hepatic microsomal concentrations of both oxysterols (Table 1), with an increase in the 7KC/7 $\beta$ OHC ratio. In the cytosols from control murine liver, only 7KC (25.3  $\pm$  13.4 ng/mg protein) was detected, but following disruption of 11 $\beta$ HSD1, levels of 7KC became undetectable. Disruption of *H6pdh*, or both *H6pdh* and *Hsd11b1* also lowered the levels of 7 $\beta$ OHC and 7KC in the hepatic microsomes compared with littermate controls (Table 1). The 7KC/7 $\beta$ OHC ratio increased with disruption of *H6pdh* and disruption of both *H6pdh* and *Hsd11b1* did not have any further effect over lack of 11 $\beta$ HSD1 alone (Table 1).

#### 3.1.1. Oxysterols Inhibit oxidation and/or reduction of glucocorticoids

Competition between 7-oxysterols and glucocorticoids for metabolism by 11 $\beta$ HSD1 across physiological and pathophysiological concentration ranges was investigated using three preparations of murine enzyme. In all preparations, 7 $\alpha$ OHC was not accepted as a substrate and not generated upon reduction of 7KC (not shown).

#### 3.1.2. Murine 11 $\beta$ HSD1 stably transfected into HEK293 cells

Both oxidation and reduction of glucocorticoids were detected *in vitro*, and reduction was the preferred direction (0.79  $\pm$  0.15 (oxidation) vs. 3.86  $\pm$  0.27 (reduction) pmol/mg/min, respectively, with 30 nM substrate). Both oxidation of 7 $\beta$ OHC and reduction of 7KC, were observed, at similar velocities, which were considerably slower than those measured for glucocorticoids. For example, substrate concentrations of 1  $\mu$ M were required to achieve rates of oxidation of 7 $\beta$ OHC and reduction of 7KC of 0.90  $\pm$  0.31 vs 0.74  $\pm$  0.04 pmol/mg/min, respectively. Inhibition of metabolism of glucocorticoids by a range of endogenous oxysterols was assessed in both reductase and dehydrogenase directions. 7KC caused the most marked inhibition of reduction of all oxysterols tested, although still only by 40% at the highest concentration used (100  $\mu$ M; Fig. 2a) and further kinetic analysis was not performed. Of the different oxysterols tested, only 7 $\beta$ OHC inhibited oxidation of corticosterone, with a  $K_i$  of 1.77  $\pm$  0.09  $\mu$ M (Fig. 2b).

#### 3.1.3. Murine recombinant 11 $\beta$ HSD1

Although both oxidation and reduction of glucocorticoids were detected using recombinant 11 $\beta$ HSD1, reduction of 11-DHC was the favored reaction (lower  $K_m$  and higher  $V_{max}$ , Table 2). Oxidation of 7 $\beta$ OHC and reduction of 7KC were also detected but proceeded with slower maximal rates and these substrates had poorer affinity (higher  $K_m$ s; Table 2) than glucocorticoids. 7KC inhibited reduction of 11-DHC (Fig. 2c) with a  $K_i$  of 7.33  $\pm$  1.76  $\mu$ M, and 7 $\beta$ OHC inhibited dehydrogenation of corticosterone with a  $K_i$  of 0.91  $\pm$  0.05  $\mu$ M. (Fig. 2d). In both cases, the nature of inhibition was competitive, indicated by the regression lines of the Dixon Plots intercepting above the *x*-axis.

**Table 1**  
Effect of disruption of *Hsd11b1* or *H6pdh* on 7-oxysterol concentrations in hepatic microsomes.

	Control	<i>Hsd11b1</i> <sup>-/-</sup>	<i>H6pdh</i> <sup>-/-</sup>	<i>Hsd11b1</i> <sup>-/-</sup> / <i>H6pdh</i> <sup>-/-</sup>
7 $\beta$ OHC	84.45 $\pm$ 27.55	16.10 $\pm$ 5.20**	12.12 $\pm$ 2.34**	21.44 $\pm$ 3.50*#
7KC	22.45 $\pm$ 8.20	10.01 $\pm$ 2.85*	7.78 $\pm$ 1.68*	14.76 $\pm$ 2.64*#
7KC/7 $\beta$ OHC	0.31 $\pm$ 0.14	0.65 $\pm$ 0.04*	0.63 $\pm$ 0.01*	0.68 $\pm$ 0.04**

Disruption of either 11 $\beta$ -hydroxysteroid dehydrogenase 1 (*Hsd11b1*<sup>-/-</sup>) or hexose-6-phosphate dehydrogenase (*H6pdh*<sup>-/-</sup>) reduced levels (ng/mg protein) of 7 $\beta$ -hydroxycholesterol (7 $\beta$ OHC) to a greater extent than 7-ketocholesterol (7KC) in hepatic microsomes compared with littermate control (C57BL/6) mice. Disruption of both enzymes (*Hsd11b1*<sup>-/-</sup>, *H6pdh*<sup>-/-</sup>) did not have any additional effect on the levels of 7-oxysterols over lack of 11 $\beta$ HSD1 or H6PDH alone. Data are mean  $\pm$  SEM, compared using 1-way ANOVA, and Tukey's post hoc test,  $n = 4-6$ .

\*  $p < 0.05$ .

\*\*  $p < 0.01$  vs. control.

#  $p < 0.05$  compared with *H6pdh*<sup>-/-</sup>.

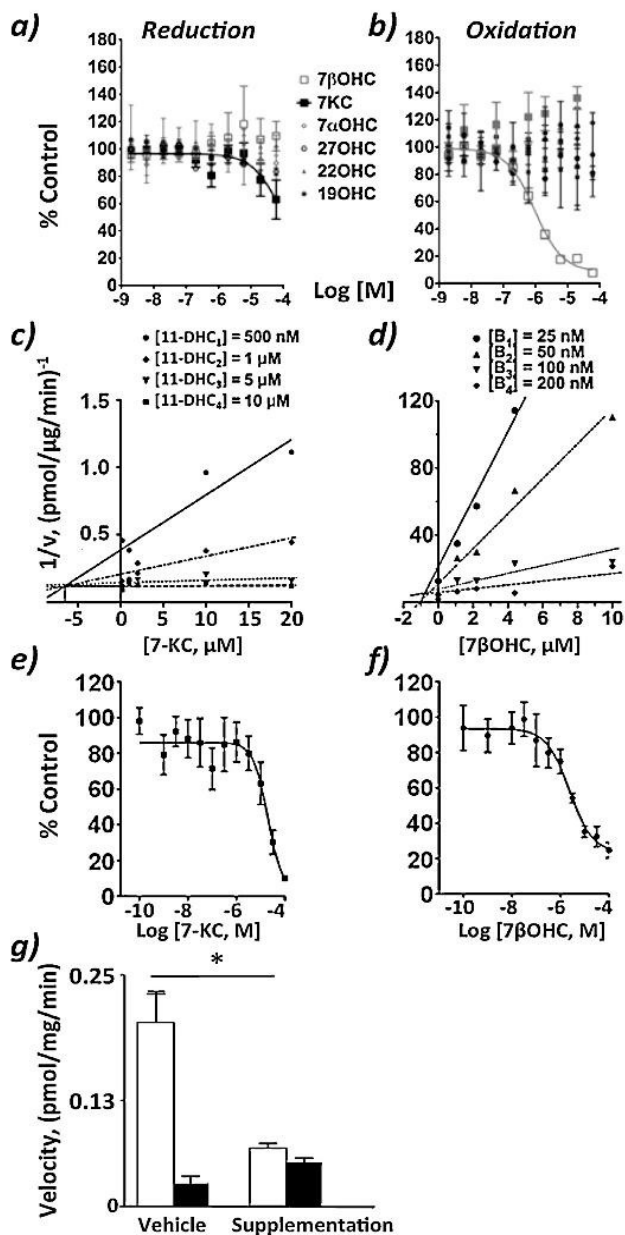


**Fig. 2.** 7-Oxysterols inhibit the metabolism of glucocorticoids by 11 $\beta$ -hydroxysteroid dehydrogenase 1 (11 $\beta$ HSD1). (a) and (b): The velocities of (a) reduction of 11-dehydrocorticosterone (11-DHC) to corticosterone and (b) oxidation of corticosterone to 11-DHC were quantified following incubation of HEK293 cells (stably transfected to generate murine 11 $\beta$ HSD 1) with a range of concentrations of oxysterols. Non-linear regression was used to assign IC<sub>50</sub> values. 7-Ketocholesterol (7KC) only inhibited the reduction of 11-DHC by ~40%. 7 $\beta$ -Hydroxycholesterol (7 $\beta$ OHC) completely inhibited oxidation of corticosterone; other oxysterols did not have an effect. Data (mean  $\pm$  SEM) are % control (absence of oxysterol),  $n = 6$  for 7-oxysterols and  $n = 3$  for other oxysterols. OHC = hydroxycholesterol. (c)–(f) 7-Oxysterols inhibited metabolism of glucocorticoids by recombinant and microsomal 11 $\beta$ HSD1; in both cases they inhibited dehydrogenation more potently than reduction. Competitive inhibition of (c) reduction of 11-DHC to corticosterone in the presence of 7KC and (d) oxidation of corticosterone to 11-DHC in the presence of 7 $\beta$ OHC, by recombinant 11 $\beta$ HSD1, demonstrated by Dixon Plots (meandata). Inhibition of (e) reduction of 11-DHC to corticosterone in the presence of 7KC and (f) oxidation of corticosterone to 11-DHC in the presence of 7 $\beta$ OHC by microsomal 11 $\beta$ HSD1,  $n = 3$ –7. (g) Supplementation of cholesterol impeded reduction of glucocorticoids by 11 $\beta$ HSD1. The velocity of reduction of 11-DHC (open bars) by 11 $\beta$ HSD1 stably transfected in HEK293 was suppressed when 7-oxysterol levels were supplemented by delivery of a

### 3.1.4. 11 $\beta$ HSD1 in murine hepatic microsomes

Both oxidation and reduction of glucocorticoids were detected using microsomal 11 $\beta$ HSD1 with reduction being the preferred direction (lower  $K_m$  and higher  $V_{max}$ , Table 2). In contrast, only oxidation of 7 $\beta$ OHC could be measured, forming 7KC at the same rate in the presence of either NAD<sup>+</sup> or NADP<sup>+</sup> (e.g.  $1.25 \pm 0.2$  vs.  $1.35 \pm 0.4$  pmol/ $\mu$ g/min respectively; 20  $\mu$ M substrate,  $n = 3$ ). This reaction was dependent on the presence of 11 $\beta$ HSD1, as 7 $\beta$ OHC was not converted to 7KC by hepatic microsomes from *Hsd11b1*<sup>-/-</sup> mice, with either cofactor. Again, 7-oxysterols demonstrated poorer affinity than glucocorticoids for 11 $\beta$ HSD1. The  $K_m$  for oxidation of 7 $\beta$ OHC was approximately three orders of magnitude higher than that for glucocorticoids (Table 2), although the maximal velocities achieved were similar for glucocorticoids and 7-oxysterols. Reduction of 7KC could not be demonstrated, even following the addition of the permeabilisation agent, alameticine, or use of NADH as an alternative cofactor [32]. 7KC weakly inhibited reduction of 11-DHC with an IC<sub>50</sub> of  $19.4 \pm 1.2$   $\mu$ M (Fig. 2e) and further kinetic analysis was not performed. 7 $\beta$ OHC inhibited oxidation with an IC<sub>50</sub> of  $2.2 \pm 0.4$   $\mu$ M (Fig. 2f).

### 3.2. Supplementation of cellular content of cholesterol and 7-oxysterol impedes reduction of glucocorticoids by 11 $\beta$ HSD1

The effect of cholesterol loading was assessed on the equilibrium of 11 $\beta$ HSD1 stably transfected into HEK293 cells. 7KC ( $19.4 \pm 1.08$  pmol/mg) and 7 $\beta$ OHC ( $4.37 \pm 1.90$  pmol/mg) were present in cells treated with vehicle. Cholesterol loading significantly ( $p < 0.05$ ) increased the levels of 7KC ( $39.48 \pm 3.01$  pmol/mg) and 7 $\beta$ OHC ( $17.6 \pm 2.4$  pmol/mg), associated with a slower velocity of reduction of glucocorticoids by 11 $\beta$ HSD1 compared with vehicle-treated cells (Fig. 2g).

### 3.3. In silico modeling

#### 3.3.1. 2D modeling

A representation of m11 $\beta$ HSD1 (PDB structure 1Y5R) was created to predict proximity of interactions of steroids and 7-oxysterols with resident cofactor (NADP<sup>+</sup>/NADPH) and the tyrosine (Tyr183) and serine (Ser170) residues of the catalytic tetrad (Tyr183-Ser170-Lys187-Asn143) (Figs. 1(b)–(d)) [33]. Distances of hydrogen bonds from the active C7 oxygen on 7-oxysterols to Ser170 and Tyr183 residues were shortest for 7 $\beta$ OHC (2.7, 2.8 Å respectively), longer for 7KC (3.2, 3.3 Å) and longest for 7 $\alpha$ OHC (4.5, 3.5 Å). Distances of 7 $\beta$ OHC and 7KC were comparable to those of glucocorticoids (B, 3.0, 3.2; A, 2.8, 2.6 Å respectively). Interactions with the co-factor were similar for all three 7-oxysterols (all 3.0 Å; corticosterone 3.9, 11-DHC, 3.3 Å).

#### 3.3.2. 3D in silico modeling

7-Oxysterols have not been co-crystallised with 11 $\beta$ HSD1. Thus, to establish the spatial orientation of the oxygenated residues at the C7 position, the structure of the closely related 7 $\alpha$ HSD in complex with 7-oxoglycochenodeoxycholic acid (1FMC) was used. Tyrosine residues in the active sites of 7 $\alpha$ HSD (1FMC) and m11 $\beta$ HSD1 (1Y5R) could be superimposed, allowing the 7 $\alpha$ -hydroxyl group of 1FMC ligand to overlay the 11 $\beta$ -hydroxyl group of corticosterone docked within 1Y5R. Thus, the 3D structure of 7 $\alpha$ OHC was created to resemble that of 7-oxoglycochenodeoxycholic acid, allowing the positions of the 7 $\beta$ -hydroxyl and 7-keto groups of 7 $\beta$ OHC and 7KC respectively to be orientated. 7-Oxysterols were docked into the active site of 1Y5R and 3D representations shown in Fig. 1e. The A-ring of 7-oxysterols (as opposed to the D-ring of glucocorticoids) was orientated toward

complex of cholesterol and methyl- $\beta$ -cyclodextrin (1:6). \* $p < 0.01$  compared by 2 way ANOVA with Bonferroni post-test,  $n = 6$ .

**Table 2**Kinetic parameters describing metabolism of 7-oxysterols and glucocorticoids by murine 11 $\beta$ -hydroxysteroid dehydrogenase 1 (11 $\beta$ HSD1).

Substrate		$K_m$ ( $\mu$ M)	$V_{max}$	$V_{max}/K_m$
<b>Recombinant protein</b>				
11-Dehydrocorticosterone	Reduction	0.20 $\pm$ 0.25	8.56 $\pm$ 4.06	42.8
7-Ketocholesterol	Reduction	1.269 $\pm$ 282	0.12 $\pm$ 0.03	9 $\times$ 10 <sup>-5</sup>
Corticosterone	Oxidation	1.78 $\pm$ 0.56	4.82 $\pm$ 0.65	2.7
7 $\beta$ -hydroxycholesterol	Oxidation	327.60 $\pm$ 98.50	0.010 $\pm$ 0.001	3 $\times$ 10 <sup>-5</sup>
<b>Microsomes</b>				
11-Dehydrocorticosterone	Reduction	1.30 $\pm$ 0.54	1.19 $\pm$ 0.18	0.9
7-Ketocholesterol	Reduction		Product not detected	
Corticosterone	Oxidation	4.20 $\pm$ 2.01	0.04 $\pm$ 0.01	0.01
7 $\beta$ -hydroxycholesterol	Oxidation	3.500 $\pm$ 326	0.03 $\pm$ 0.001	9 $\times$ 10 <sup>-6</sup>

Velocities of metabolism of substrates by murine recombinant or microsomal 11 $\beta$ HSD1 were assessed and kinetic parameters ( $K_m$ ,  $V_{max}$  and  $V_{max}/K_m$ , true or apparent) assigned following Lineweaver-Burke transformation of data fitted to Michaelis-Menten kinetics. The velocities were quantified; for reduction of 11-dehydrocorticosterone or 7-ketocholesterol in the presence of NADPH or oxidation of corticosterone or 7 $\beta$ -hydroxycholesterol in the presence of NADP<sup>+</sup>. Data are mean  $\pm$  SEM, obtained from at least three independent experiments.  $V_{max}$  expressed as pmol/ $\mu$ g/min.  $V_{max}/K_m$  expressed as L/ $\mu$ g/min  $\times$  10<sup>-6</sup>.

the interior of the 11 $\beta$ HSD1 active site. Interactions between 7 $\beta$ OHC and Ser170 and Tyr183 of the catalytic tetrad had the shortest bond distances (2.7, 2.8 Å respectively), followed by those of 7KC (3.2, 3.3 Å) and then 7 $\alpha$ OHC (4.5, 4.8 Å; for comparison corticosterone 3.1, 2.8 Å [30]; 11-DHC 2.8, 2.6 Å respectively) When 7 $\beta$ OHC and 7KC were docked, the Tyr183 residue was 5.1 Å from the nicotinamide C4 and Lys187 was 3.2 Å from the hydroxyl group on the cofactor. When 7 $\alpha$ OHC was docked, the Tyr183 residue was 4.20 Å from the nicotinamide C4 and Lys187 was 3.2 Å from the hydroxyl group on the cofactor.

#### 4. Discussion

These data demonstrate that reduction of 7KC to 7 $\beta$ OHC is the preferred direction of metabolism of 7-oxysterols by 11 $\beta$ HSD1 *in vivo* in mouse. Metabolism of 7-oxysterols (at least dehydrogenation) was not detected in microsomes of 11 $\beta$ HSD1 null mice, supporting the notion that it is the only enzyme catalyzing this reaction. While 7-oxysterols were competitive inhibitors of metabolism of glucocorticoids by 11 $\beta$ HSD1, it is unlikely that in health [34] they will be sufficiently potent to exert this effect. Inhibition may become important in hyperlipidaemia [10], or at sites where oxysterols accumulate, such as in adipose and atherosclerotic lesions.

Structural modeling of the murine protein confirmed the potential for interactions of 7-oxysterols with the catalytic tetrad of the enzymatic active site. 7-Oxygenated substrates, in contrast to steroids, interact with 11 $\beta$ HSD1 with their A-ring orientated toward the interior of the binding pocket, in agreement with models in other species [21,30,35]. The higher  $K_m$  values describing metabolism of 7-oxysterols compared with glucocorticoids, however, indicated they were poorer affinity substrates. Circulating concentrations of 7-oxysterols in the mouse were comparable in magnitude to those in other species [34] and increased in hyperlipidaemia [10]. However, it is likely metabolism by 11 $\beta$ HSD1 would not proceed at maximal velocity in the presence of the endogenous concentrations reported here or by others [34,36].

While disruption of 11 $\beta$ HSD1 only tended to alter circulating 7-oxysterol levels subtly [29], it substantially lowered the levels in hepatic sub-cellular fractions. Oxysterols can be synthesized from spontaneous oxidation of cholesterol and are derived in large part from dietary sources [10]. Therefore the reduction in absolute levels may arise because *Hsd11b1*<sup>-/-</sup> mice have an improved metabolic profile with lower circulating cholesterol concentrations [37], and thus less precursor for auto-oxidation. The specific contribution of 11 $\beta$ HSD1 to the proportions of 7-keto and hydroxy oxysterols was revealed in the increase in the ratio of 7KC/7 $\beta$ OHC ratio in plasma and microsomes, following targeted disruption of *Hsd11b1*, suggesting that 11 $\beta$ HSD1 catalyses reduction of 7KC *in*

*vivo*. This corroborates previous studies in rats in which hepatic 7KC accumulated following administration of the non-specific 11 $\beta$ HSD inhibitor carbenoxolone [9]. Lack of NADPH supply due to genetic disruption of *H6pdh* again increased the 7KC/7 $\beta$ OHC ratio, confirming *in vitro* findings [38] that H6PDH promotes catalysis of 7KC to form 7 $\beta$ OHC *in vivo*, similarly to glucocorticoids. Indeed, H6PDH appeared to be the only source of co-factor, as double knockout of *H6pdh* and *Hsd11b1*, yielded the same ratio of 7-oxysterols, as with disruption of *H6pdh* alone.

11 $\beta$ HSD1 may therefore play a similar role in regulating actions of 7-oxysterols *in vivo* as it does glucocorticoids. The importance of metabolism of glucocorticoids by 11 $\beta$ HSD1 is readily apparent since the 11-keto steroid is inert and the hydroxy form is active. However, distinct biological roles for 7KC and 7 $\beta$ OHC are not established and a target receptor has not been defined, although there are a number of reports of subtle differences in their actions (e.g. 7 $\beta$ OHC has a greater ability than 7KC to induce apoptosis in human umbilical vein endothelial cells [39]). However 7-oxysterols can be subject to further metabolism and recent reports suggest that the 25- and 27-hydroxy metabolites of 7 $\alpha$ - and 7 $\beta$ OHC play potential roles in regulating the immune response via the novel G-protein coupled receptor, EB12 [40,41]. Interestingly there is one report showing that 7KC but not 7 $\beta$ OHC limits SCAP exit from the ER within cells [42], which further prevents excess synthesis of cholesterol. Hence, it follows that the increased proportion of 7KC to 7 $\beta$ OHC upon inhibition of 11 $\beta$ HSD1 *in vivo* may exert a brake on cholesterol synthesis. Other oxysterols modulate nuclear hormone signaling pathways, but the possibility of activation of LXR, at least, by 7-oxysterols has largely dismissed [20].

Work with cells stably transfected to express human 11 $\beta$ HSD1 or with adipocytes [20] has shown that 7-oxysterols (in keeping with other 7-hydroxylated substrates [7]) may compete differentially with glucocorticoids for metabolism by 11 $\beta$ HSD1 and thus modulate glucocorticoid action. Inhibition appears cell-type specific, potentially explained by differential metabolism, accumulation or export of oxysterols [10]; adipocytes and macrophages sequester oxysterols readily [10] whereas macrophages export 7KC and other oxysterols via the ABCG1 transporter [43]. Balázs et al. did not detect any inhibition of human 11 $\beta$ HSD1 reductase activity in lysates or HEK293 cells by 7KC or 7 $\beta$ OHC, but showed an inhibition of 11 $\beta$ HSD1-reductase activity by 7KC (IC<sub>50</sub> 8.1  $\pm$  0.9  $\mu$ M) in differentiated THP-1 macrophages [21]. Inhibition of glucocorticoid metabolism by co-incubation with 7-oxysterols was investigated here using three models of murine 11 $\beta$ HSD1, in all of which reduction of glucocorticoids was favored. Our data concur with the proposal that 7-oxysterols compete with glucocorticoids for metabolism, with 7KC being consistently less effective at inhibiting 11-DHC reduction by isolated enzyme *in vitro*, than 7 $\beta$ OHC was at preventing oxidation. Taking into account the IC<sub>50</sub> values, inhibition

of glucocorticoid metabolism is unlikely to be important in health. However, at concentrations in the low micromolar range, as seen in atherosclerosis [44,45], 7 $\beta$ OH or 7KC may compete for oxidation preventing glucocorticoid inactivation or reduction, respectively.

7 $\beta$ OH is highly abundant in fatty streaks in developing lesions [46,47] and the 7 $\beta$ OH/7KC ratio is increased. If 7 $\beta$ OH dominates to inhibit glucocorticoid oxidation, the cells in the lesion and adjacent normal intima may become exposed to increased local glucocorticoid levels, with adverse consequences [48]. However, when endogenous 7-oxysterols were enriched secondary to cholesterol loading in cultured cells, the predominant effect was to suppress reduction of glucocorticoids, suggesting protection from excess glucocorticoid. These findings concur with reduction of 7KC being the major route of metabolism of 7-oxysterols *in vivo*.

In conclusion, 7KC and 7 $\beta$ OH are poor affinity substrates for murine 11 $\beta$ HSD1 and are interconverted at a slower rate than glucocorticoids. While differences exist in the patterns of *in vitro* and *in vivo* metabolism, reduction of 7KC to 7 $\beta$ OH appears the predominant reaction *in vivo*. Although it seems unlikely that the competition with oxysterols will determine predominant direction for glucocorticoid metabolism by 11 $\beta$ HSD1 in health, it may play a role in hyperlipidaemia and atherosclerosis. A greater knowledge of the actions of these 7-oxysterols is required to fully understand the consequences of inhibition or over-activity of 11 $\beta$ HSD1 pathway.

#### Acknowledgements

We are grateful to the Wellcome Trust Clinical Research Facility Mass Spectrometry Core (Mrs Alison Rutter) for technical assistance. This work was supported by grants from the Wellcome Trust (TM, RA, PWFH, SP, BRW), British Heart Foundation (RA, DC, PWFH, BW) and Medical Research Council David Philips fellowship (GGL, NS).

#### References

- [1] Kotelevtsev YV, Holmes MC, Burchell A, Houston PM, Scholl D, Jamieson PM, et al. 11 $\beta$ -Hydroxysteroid dehydrogenase type 1 knockout mice show attenuated glucocorticoid inducible responses and resist hyperglycaemia on obesity and stress. *Proc Natl Acad Sci U S A* 1997;94:14924–29.
- [2] Morton NM, Paterson JM, Masuzaki H, Holmes MC, Staels B, Fievet C, et al. Novel adipose tissue-mediated resistance to diet-induced visceral obesity in 11 $\beta$ -hydroxysteroid dehydrogenase type 1-deficient mice. *Diabetes* 2004;53:931–8.
- [3] Rosenstock J, Banarer S, Fonseca VA, Inzucchi SE, Sun W, Yao W, et al. The 11 $\beta$ -hydroxysteroid dehydrogenase type 1 inhibitor INCB13739 improves hyperglycemia in patients with Type 2 diabetes inadequately controlled by metformin monotherapy. *Diabetes Care* 2010;33:1516–22.
- [4] Hermanowski-Vosatka A, Balkovec JM, Cheng K, Chen HY, Hernandez M, Koo GC, et al. 11 $\beta$ -HSD1 inhibition ameliorates metabolic syndrome and prevents progression of atherosclerosis in mice. *J Exp Med* 2005;202:517–27.
- [5] Kipari T, Hadoke PWF, Iqbal J, Man TY, Miller E, Coutinho AE. 11 $\beta$ -hydroxysteroid dehydrogenase type 1 deficiency reduces atherosclerosis and plaque inflammation independent of risk factors: key role of the lesional environment. *FASEB Journal*; <http://dx.doi.org/10.1096/fj.12-219105>, in press.
- [6] Luo MJ, Thieringer R, Springer MS, Wright SD, Hermanowski-Vosatka A, Plump A, et al. 11 $\beta$ -HSD1 inhibition reduces atherosclerosis in mice by altering pro-inflammatory gene expression in the vasculature. *Physiol Genomics* 2013;45:47–57.
- [7] Robinson B, Michael KK, Ripp SL, Winters sj, Prough RA glucocorticoids inhibit interconversion of 7-hydroxy and 7-oxo metabolites of dehydroepiandrosterone: a role for 11 $\beta$ -hydroxysteroid dehydrogenases? *Arch Biochem Biophys* 2003;412:251–8.
- [8] Hult M, Elleby B, Shafiqat N, Svensson S, Rane A, Jornvall H, et al. Human and rodent type 1 11 $\beta$ -hydroxysteroid dehydrogenases are 7 $\beta$ -hydroxycholesterol dehydrogenases involved in oxysterol metabolism. *Cell Mol Life Sci* 2004;61:992–9.
- [9] Schweizer RA, Zurcher M, Balazs Z, Dick B, Odermatt A. Rapid hepatic metabolism of 7-ketocholesterol by 11 $\beta$ -hydroxysteroid dehydrogenase type 1: species-specific differences between the rat human, and hamster enzyme. *J Biol Chem* 2004;279:18425–34.
- [10] Brown AJ, Jessup W. Oxysterols Sources, cellular storage and metabolism, and new insights into their roles in cholesterol homeostasis. *Mol Aspects Med* 2009;30:111–22.
- [11] Morton NM. Obesity and corticosteroids: 11 $\beta$ -hydroxysteroid type 1 as a cause and therapeutic target in metabolic disease. *Mol Cell Endocrinol* 2010;316:154–64.
- [12] Brown AJ, Leong SL, Dean RT, Jessup W. 7-Hydroperoxycholesterol and its products in oxidized low density lipoprotein and human atherosclerotic plaque. *J Lipid Res* 1997;38:1730–45.
- [13] Song W, Chen J, Dean WL, Redinger RN, Prough RA. Purification and characterization of hamster liver microsomal 7 $\alpha$ -hydroxycholesterol dehydrogenase: similarity to type I 11 $\beta$ -hydroxysteroid dehydrogenase. *J Biol Chem* 1998;273:16223–28.
- [14] Maeda Y, Nagatomo H, Uchiyama F, Yamada M, Shiotsuki H, Ohta Y, et al. A comparative study of the conversion of 7-hydroxycholesterol in rabbit, guinea pig, rat, hamster and chicken. *Steroids* 2002;67:703–8.
- [15] Bujalska IJ, Walker EA, Hewison M, Stewart PM. A switch in dehydrogenase reductase activity of 11 $\beta$ -hydroxysteroid dehydrogenase type 1 upon differentiation of human omental adipose stromal cells. *J Clin Endocrinol Metab* 2002;87:1205–10.
- [16] Hughes KA, Manolopoulos KN, Iqbal J, Cruden NL, Stimson RH, Reynolds RM, et al. Recycling between cortisol and cortisone in human splanchnic, subcutaneous adipose and skeletal muscle tissues *in vivo*. *Diabetes* 2012;61:1357–64.
- [17] Draper N, Walker EA, Bujalska IJ, Tomlinson JW, Chalder SM, Arlt W, et al. Mutations in the genes encoding 11 $\beta$ -hydroxysteroid dehydrogenase type 1 and hexose-6-phosphate dehydrogenase interact to cause cortisone reductase deficiency. *Nature Genet* 2003;34:434–9.
- [18] Lavery GG, Walker EA, Draper N, Jeyasuria P, Marcos J, Shackleton CHL, et al. Hexose-6-phosphate dehydrogenase knock-out mice lack 11 $\beta$ -hydroxysteroid dehydrogenase type 1-mediated glucocorticoid generation. *J Biol Chem* 2006;281:6546–51.
- [19] McNeilly AD, MacFarlane DP, O'Flaherty EN, Livingstone DEW, MacKenzie SM, Mitić T, et al. Bile acids modulate glucocorticoid metabolism and the hypothalamic-pituitary-adrenal axis in obstructive jaundice. *J Hepatol* 2010;52:705–11.
- [20] Wamil M, Andrew R, Chapman KE, Street J, Morton NM, Seckl JR. 7-Oxysterols modulate glucocorticoid activity in adipocytes through competition for 11 $\beta$ -hydroxysteroid dehydrogenase type 1. *Endocrinology* 2008;149:5909–18.
- [21] Balazs Z, Nashev LG, Chandsawangbhuwan C, Baker ME, Odermatt A. Hexose-6-phosphate dehydrogenase modulates the effect of inhibitors and alternative substrates of 11 $\beta$ -hydroxysteroid dehydrogenase 1. *Mol Cell Endocrinol* 2009;301:117–22.
- [22] Brown RW, Chapman KE, Edwards CRW, Seckl JR. Human placental 11 $\beta$ -hydroxysteroid dehydrogenase: evidence for and partial purification of a distinct NAD-dependent isoform. *Endocrinology* 1993;132:2614–21.
- [23] Semjonov NM, Sherlock M, Jeyasuria P, Parker KL, Walker EA, Stewart PM, et al. Hexose-6-phosphate dehydrogenase contributes to skeletal muscle homeostasis independent of 11 $\beta$ -hydroxysteroid dehydrogenase type 1. *Endocrinology* 2011;152:93–102.
- [24] Webster SP, Ward P, Binnie M, Craigie E, McConnell KM, Sooy K, et al. Discovery and biological evaluation of adamantyl amide 11 $\beta$ -HSD1 inhibitors. *Bioorg Med Chem Lett* 2007;17:2838–43.
- [25] Freeman NE, Rusinol AE, Linton M, Hachey DL, Fazio S, Sinensky MS, et al. Acyl-coenzyme A: cholesterol acyltransferase promotes oxidized LDL/oxysterol-induced apoptosis in macrophages. *J Lipid Res* 2005;46:1933–43.
- [26] Klein U, Gimpl G, Fahrenholz F. Iteration of the myometrial plasma membrane cholesterol content with  $\beta$ -cyclodextrin modulates the binding affinity of the oxytocin receptor. *Biochemistry* 1995;34:13784–93.
- [27] Kritiharides L, Jessup W, Mander EL, Dean RT. Apolipoprotein A-I-mediated efflux of sterols from oxidized LDL-loaded macrophages. *Arterioscler Thromb Vasc Biol* 1995;15:276–89.
- [28] Dzeletovic S, Breuer O, Lund E, Diczfalusy U. Determination of cholesterol oxidation products in human plasma by isotope dilution-mass spectrometry. *Anal Biochem* 1995;225:73–80.
- [29] Mitić T, Andrew R, Walker BR, Hadoke PWF. Inter-conversion of 7-ketocholesterol and 7 $\beta$ -hydroxycholesterol by 11 $\beta$ -HSD1 in the mouse aortic wall: implications for vascular function. *Biochimie* 2013;95:548e555.
- [30] Zhang J, Osslund TD, Plant MH, Clogston CI, Nybo RE, Xiong F, et al. Crystal structure of murine 11 $\beta$ -hydroxysteroid dehydrogenase 1: an important therapeutic target for diabetes. *Biochemistry* 2005;44:6948–57.
- [31] Tanaka N, Nonaka T, Tanabe T, Yoshimoto T, Tsuru D, Mitsui Y. Crystal structures of the binary and ternary complexes of 7 $\alpha$ -hydroxysteroid dehydrogenase from *Escherichia coli*. *Biochemistry* 1996;35:7715–30.
- [32] Christy C, Hadoke PWF, Paterson JM, Mullins JJ, Seckl JR, Walker BR. Glucocorticoid action in mouse aorta: localisation of 11 $\beta$ -hydroxysteroid dehydrogenase type 2 and effects on responses to glucocorticoids *in vitro*. *Hypertension* 2003;42:580–7.
- [33] Filling C, Berndt KD, Benach J, Knapp S, Prozorovski T, Nordling E, et al. Critical residues for structure and catalysis in short-chain dehydrogenases/reductases. *J Biol Chem* 2002;277:25677–84.
- [34] Iuliano L, Michelatta F, Natoli S, Ginanni Corradini SIM, Elisei W, Giovannelli L, et al. Measurement of oxysterols and  $\alpha$ -tocopherol in plasma and tissue samples as indices of oxidant stress status. *Anal Biochem* 2003;312:217–23.
- [35] Odermatt A, Atanasov AG, Balazs Z, Schweizer RA, Nashev LG, Schuster D, et al. Why is 11 $\beta$ -hydroxysteroid dehydrogenase type 1 facing the endoplasmic reticulum lumen? Physiological relevance of the membrane topology of 11 $\beta$ -HSD1. *Mol Cell Endocrinol* 2006;248:15–23.

- [36] Brown AJ, Jessup W. Oxysterols and atherosclerosis. *Atherosclerosis* 1999;142:1–28.
- [37] Morton NM, Holmes MC, Fievet C, Staels B, Tailleux A, Mullins JJ, et al. Improved lipid and lipoprotein profile, hepatic insulin sensitivity and glucose tolerance in 11 $\beta$ -hydroxysteroid dehydrogenase 1 knockout mice. *J Biol Chem* 2001;276:41293–300.
- [38] Atanasov AG, Nashev LG, Schweizer RA, Frick C, Odermatt A. Hexose-6-phosphate dehydrogenase determines the reaction direction of 11 $\beta$ -hydroxysteroid dehydrogenase type 1 as an oxoreductase. *FEBS Lett* 2004;571:129–33.
- [39] Steffen Y, Wiswedel I, Peter D, Schewe T, Sies H. Cytotoxicity of myeloperoxidase/nitrite-oxidized low-density lipoprotein toward endothelial cells is due to a high 7 $\beta$ -hydroxycholesterol to 7-ketocholesterol ratio. *Free Radic Biol Med* 2006;41:1139–50.
- [40] Liu C, Yang XV, Wu J, Kuei C, Mani NS, Zhang L, et al. Oxysterols direct B-cell migration through EBI2. *Nature* 2011;475:519–23.
- [41] Hannedouche S, Zhang J, Yi T, Shen W, Nguyen D, Pereira JP, et al. Oxysterols direct immune cell migration via EBI2. *Nature* 2011;475:524–7.
- [42] Brown AJ, Sun L, Feramisco JD, Brown MS, Goldstein JL. Cholesterol addition to ER membranes alters conformation of SCAP the SREBP escort protein that regulates cholesterol metabolism. *Mol Cell* 2002;10:237–45.
- [43] Terasaka N, Wang N, Yvan-Charvet L, Tall AR. High-density lipoprotein protects macrophages from oxidized low-density lipoprotein-induced apoptosis by promoting efflux of 7-ketocholesterol via ABCG1. *Proc Natl Acad Sci U S A* 2007;104:15093–98.
- [44] Hitsumoto T, Takahashi M, Lizuka T, Shirai K. Clinical significance of serum 7-ketocholesterol concentrations in the progression of coronary atherosclerosis. *J Atheroscler Thromb* 2009;16:363–70.
- [45] Prunet C, Petit JM, Ecamot-Laubriet A, Athias A, Miguel-Alfonsi C, Rohmer JF, et al. High circulating levels of 7 $\beta$ - and 7 $\alpha$ -hydroxycholesterol and presence of apoptotic and oxidative markers in arterial lesions of normocholesterolemic atherosclerotic patients undergoing endarterectomy. *Pathol Biol (Paris)* 2006;54:22–32.
- [46] Carpenter KL, Taylor SE, van der Veen C, Williamson BK. Lipids and oxidised lipids in human atherosclerotic lesions at different stages of development. *Biochim Biophys Acta* 1995;1256:141–50.
- [47] Garcia-Cruset S, Carpenter KL, Guardiola F, Stein BK, Mitchinson MJ. Oxysterol profiles of normal human arteries fatty streaks and advanced lesions. *Free Radic Res* 2001;35:31–41.
- [48] Hadoke PWF, Macdonald LJ, Logie JJ, Small GR, Dover AR, Walker BR. Intravascular glucocorticoid metabolism as a modulator of vascular structure and function. *Cell Mol Life Sci* 2006;63:565–78.